AGARD-LS-196

AGARD-LS-196

AGARD

ADVISORY GROUP FOR AEROSPACE RESEARCH & DEVELOPMENT
7 RUE ANCELLE, 92200 NEUILLY-SUR-SEINE, FRANCE

AGARD LECTURE SERIES 196

Propagation Modelling and Decision Aids for Communications, Radar and Navigation Systems

La modélisation de la propagation et aides à la décision pour les systèmes de télécommunications, de radar et de navigation

This publication was prepared at the request of the Sensor and Propagation Panel and under the sponsorship of the Consultant and Exchange Programme of AGARD and will be presented on 4-5 October 1994 in Ottawa, Canada, 10-11 October 1994 in Lisbon, Portugal, and 13-14 October 1994 in The Hague, The Netherlands.

NORTH ATLANTIC TREATY ORGANIZATION

Published September 1994

Distribution and Availability on Back Cover

AGARD-LS-196

AGARD

ADVISORY GROUP FOR AEROSPACE RESEARCH & DEVELOPMENT
7 RUE ANCELLE, 92200 NEUILLY-SUR-SEINE, FRANCE

AGARD LECTURE SERIES 196

Propagation Modelling and Decision Aids for Communications, Radar and Navigation Systems

La modélisation de la propagation et aides à la décision pour les systèmes de télécommunications, de radar et de navigation

This publication was prepared at the request of the Sensor and Propagation Panel and under the sponsorship of the Consultant and Exchange Programme of AGARD and will be presented on 4-5 October 1994 in Ottawa, Canada, 10-11 October 1994 in Lisbon, Portugal, and 13-14 October 1994 in The Hague, The Netherlands.

17912

North Atlantic Treaty Organization
Organisation du traité de l'Atlantique Nord

The Mission of AGARD

According to its Charter, the mission of AGARD is to bring together the leading personalities of the NATO nations in the fields of science and technology relating to aerospace for the following purposes:

- Recommending effective ways for the member nations to use their research and development capabilities for the common benefit of the NATO community;
- Providing scientific and technical advice and assistance to the Military Committee in the field of aerospace research and development (with particular regard to its military application);
- Continuously stimulating advances in the aerospace sciences relevant to strengthening the common defence posture;
- Improving the co-operation among member nations in aerospace research and development;
- Exchange of scientific and technical information;
- Providing assistance to member nations for the purpose of increasing their scientific and technical potential;
- Rendering scientific and technical assistance, as requested, to other NATO bodies and to member nations in connection with research and development problems in the aerospace field.

The highest authority within AGARD is the National Delegates Board consisting of officially appointed senior representatives from each member nation. The mission of AGARD is carried out through the Panels which are composed of experts appointed by the National Delegates, the Consultant and Exchange Programme and the Aerospace Applications Studies Programme. The results of AGARD work are reported to the member nations and the NATO Authorities through the AGARD series of publications of which this is one.

Participation in AGARD activities is by invitation only and is normally limited to citizens of the NATO nations.

The content of this publication has been reproduced
directly from material supplied by AGARD or the authors.

Published September 1994

ISBN 92-836-1004-0

Printed by Canada Communication Group
45 Sacré-Cœur Blvd., Hull (Québec), Canada K1A 0S7

Abstract

In recent years, a number of powerful, flexible, modelling tools for the assessment and exploitation of propagation conditions have become available. Rapid advances in mini and microcomputer technology have put complex models with sophisticated user interfaces at the disposal of the non-specialist user. These range from system design tools to near real-time operational and tactical decision aids that include models and databases of the necessary environmental parameters. Prediction tools are required for communications, radar and navigation applications, and cover the frequency spectrum from ELF to optical.

The lectures will concentrate on the prediction tools, but will also cover [illegible]ound required to understand the models used. The emphasis will be on frequencies from HF to optical. Topics will [illegible] ionosphere, ground wave propagation, terrain diffraction, refractive effects, hydrometeors, atmospheric gases, electro-[illegible]cs and the sensing of radiometeorological parameters. Both empirical/statistical system planning methods, and more theoretically based deterministic operational decision aids will be covered.

This Lecture Series, sponsored by the Sensor and Propagation Panel of AGARD, has be[illegible]mplemented by the Consultant and Exchange Programme.

Abrégé

Au cours des dernières années, bon nombre d'outils de modélisation puissants et souples pour l'évaluation et l'exploitation des conditions de propagation sont arrivés sur le marché. Des avancées rapides en technologies mini et micro ordinateur ont mis à la disposition de l'utilisateur non spécialisé des modèles complexes, incorporant des interfaces utilisateur évoluées. Ces aides vont des outils de conception des systèmes à des aides à la décision tactique et opérationnelle en temps quasi-réel intégrant les modèles et les bases de données des paramètres de l'environnement nécessaires. Des outils de prédiction sont demandés pour des applications aux communications, aux radars et à la navigation, couvrant le spectre de fréquences du ELF à l'optique.

Les présentations se concentreront sur les outils de prédiction mais elles couvriront également les technologies de base nécessaires à la compréhension des modèles utilisés. L'accent sera mis sur la gamme de fréquences du HF à l'optique. Les sujets traités comprendont l'ionosphère, la propagation des ondes de sol, la diffraction du terrain, les effets de réfraction, les hydréométéores, les gaz atmosphériques, l'électro-optique et la détection des paramètres radiométéorologiques. Les méthodes empiriques/statistiques de planification systèmes seront discutées, ainsi que les aides déterministes à la décision opérationnelle, basées sur des considérations d'ordre théorique.

Ce cycle de conférences est présenté dans le cadre du programme des consultants et des échanges, sous l'égide du Panel de Sensor et Propagation de l'AGARD.

List of Authors/Speakers

Lecture Series Director: Dr. Ken H. CRAIG
Radio Communications Research Unit
Rutherford Appelton Laboratory
Chilton, Didcot
Oxon OX11OQX
UK

Authors/Speakers

Dr. Paul S. CANNON
Radio Propagation Exploitation Group
Space and Communications Dept.
Defence Research Agency
St. Andrews Road
Malvern
Worcs. WR14 3PS
UK

Dr. Juergen H. RICHTER
Ocean and Atmospheric Sciences Div
NCCOSC RDTE DIV 543
53570 Silvergate Ave
San Diego CA 92152-5230
USA

Dr. Anton KOHNLE
Forschungsinstitut für Optik (FfO)
Schloss Kressbach
D-72072 Tübingen
GERMANY

Dr. Jim H. WHITTEKER
Communications Research Centre
P.O. Box 11490
Station H
3701 Carling Av
Ottawa, Ontario K2H 8S2
CANADA

Mr. Herb V. HITNEY
NCCOSC RDTE DIV 543
53170 Woodward Road
San Diego, CA 92152-7385
USA

Contents

Propagation Modelling and Decision Aids for Communications, Radar and Navigation Systems

Introduction and Overview

K.H. Craig
Radio Communications Research Unit
Rutherford Appleton Laboratory
Chilton, Didcot, OX11 0QX
U.K.

1 INTRODUCTION

Any communications, radar or navigation system that relies on the propagation of electromagnetic (e.m.) waves between an emitter and a receiver is affected by the environment in which the waves propagate. An understanding of this environment, and the way in which it affects propagation, is essential for an assessment and prediction of system performance.

The medium through which the waves propagate has a direct influence on propagation. In the HF and lower frequency bands, the ionosphere (the ionised region of the atmosphere extending from about 85 to 1000 km above the Earth's surface) has the greatest effect, while at frequencies from VHF to optical, the troposphere (the non-ionised, lower part of the atmosphere, extending from the surface up to the tropopause at a height of 10–15 km) dominates. Variations in the refractive index of the medium determine how the waves deviate from the straight line paths that they would have in free space. These effects can be exploited (for example to provide communications far beyond the horizon) or can be a source of system performance degradation (as for example in the formation of radar coverage holes). Attenuation of the signal also occurs in the ionosphere and the troposphere, and scatter from particulates (such as rain, fog and smoke) can be a significant impairment, particularly on electro-optics systems.

The Earth's surface also affects system performance. The effect may be direct, by means of diffraction and scatter where the Earth's bulge or terrain features intrude into the propagation path, or it may be indirect, due to the influence of the Earth's surface on the local meteorology and hence on the refractive index structure of the lower atmosphere.

The propagation medium varies in both time and space, and on various scales. The spatial scales of interest range from thousands of kilometres for global communications via the ionosphere to less than a metre for the effects of atmospheric turbulence on optical systems. Time scales range from many years (solar cycle effects on ionospheric propagation) to hours or even minutes (the scale of weather phenomena).

These lectures address the modelling of the effects of the propagation environment on system performance. Much effort has been devoted to this task and to improving sensors for the direct or remote sensing of the environment. In recent years, the capabilities of propagation models have advanced significantly due to the ready availability of powerful mini and microcomputers:

- more complex solutions using numerical methods have been applied to a wider range of problems;
- this in turn has led to a requirement for better and more up-to-date environmental data;
- the development of sophisticated, interactive user interfaces on personal computer systems has given rise to propagation tools that can be used by non-specialists;
- propagation models have evolved into decision aids by the incorporation of system performance information. The scope of these may be quite wide, presenting tactical advice to the non-specialist user, and the propagation element may be only one part of a more complex system.

In order to model the effect of the environment on the propagation of electromagnetic waves, two components are required:

(i) an electromagnetic wave propagation model;

(ii) measurements or a model of the environment in which the waves propagate as input data for the propagation model.

2 E.M. WAVE PROPAGATION MODELS

In principle, a propagation model for any e.m. wave problem is provided by a solution of Maxwell's equations. This type of model is *deterministic* in the sense that if the propagation medium is characterised *exactly*, the solution would also be an exact description of the propagation conditions for the given path at the given time. In practice, of course, it is more complicated than this. Approximations and simplifications are required and no practical solution of Maxwell's equation (that is, one that is analytically solvable or is numerically tractable) will be applicable to all propagation problems. Different propagation mechanisms require different approximations, and this has led to the development of various methodologies throughout the e.m. spectrum. Several models and computer packages have evolved to deal with different application areas, and one of the aims of this Lecture Series is to help the user to identify the packages most relevant to his or her area of interest.

Deterministic models are particularly relevant when a prediction (or even a forecast) of the performance of a specific system is required at a specific location and time (for example, determining the best altitude at which an attack aircraft should fly to avoid detection by an enemy radar). However, it must be emphasised that the accuracy of a prediction is critically dependent of the quality (and perhaps quantity) of real-time environmental data available, the (lack of) availability of such data is usually a more serious constraint on the prediction accuracy than the accuracy of the propagation model itself.

Since the propagation environment is never known exactly, a deterministic approach to the problem may be undesirable. Indeed, a prediction may be required when no direct measurement of the environment is available. In this case, a prediction may still be possible, but it must be based either on historical data concerning the environment, or on measurements of the performance of similar systems in similar propagation conditions. This *empirical* type of model is sufficient for many applications. In general the complexity of the model is less than in the deterministic case, and this can lead to near-instantaneous predictions. Empirical models are therefore especially suitable for system planning or simulation purposes, where the requirement is more to achieve good prediction accuracy "on the average", rather than for an individual case.

Empirical models can be taken a step further by making *statistical* predictions, for example, predicting the percentage of the time that a given propagation path will be "open" for communication, or the percentage of the time that a link will be unusable because of rain. Again, the main application is in long-term system planning.

Decision aids will require system information in addition to a propagation model and environmental data. The need for performance criteria of the communications, radar or navigation system itself is obvious. However, there may be a need for other information. For example, target and background or clutter characteristics will be necessary to estimate the detection capabilities of a radar or imaging system. The human operator is also an integral part of most detection systems, and the performance of the operator should also be taken into account and modelled.

3 ENVIRONMENTAL DATA

Obtaining and assimilating information about the propagation environment is an integral part of any decision aid. In some cases the data required will be essentially static and need only be obtained once; an example would be terrain elevation data required for the modelling of terrain diffraction. However, the propagation medium itself generally varies with time and sensors must be deployed to obtain timely and representative measurements of the medium.

Direct sensing is currently the most widely available source of data in the troposphere, principally by means of radiosonde balloon ascents. However recent developments in remote sensing of the troposphere show promise for obtaining refractive index information with greater spatial and temporal resolution than is possible by radiosonde methods; ground-based remote sensors are also less prone to detection than is a radiosonde balloon. In the ionosphere, remote sensing by ionosondes has been widely employed for many years.

Real-time deterministic prediction (nowcasting) and forecasting models require a regular update of meteorological or ionospheric data. Forecasting of system performance relies on accurate forecasts of the state of the propagation medium, and improvements are closely tied to developments in numerical weather and ionospheric prediction models.

4 CONCLUSION

The main aim of these lectures is to describe the propagation models and decision aids that are available. However, in order to understand the models, and the scope of their applicability, some background on the propagation mechanisms is necessary. The major topic areas are presented in two parts, the first covering the propagation mechanisms, and the second concentrating on the propagation models and decision aids.

The lectures concentrate on frequencies from HF to optical. Although there are important system applications in the frequency bands below HF (navigation in particular), propagation modelling at the lower frequencies was extensively covered in a recent AGARD publication [1]; this publication is complementary to the present lecture series and is recommended for further reading. Reference may also be made to an AGARD Symposium publication [2] which covers recent research results and developments in operational decision aids. Another source of empirical and statistical propagation models is the Radiocommunications sector of the International Telecommunication Union (ITU-R), formerly known as the Consultative Committee International Radio (CCIR). This body publishes an extensive series of reports [3] that are used in the design of civil communications systems.

The dissolution of the Warsaw Pact and the "Partnership for Peace" accord has caused a reassessment of the role of NATO. Propagation assessment tools will be required to maximise the efficiency, effectiveness and flexibility of reduced levels of forces and weapons in the post Cold War NATO. The relevance of decision aids to the new NATO strategy and future directions for operational assessment tools are discussed further in a separate lecture.

5 REFERENCES

[1] Richter, J.H. (ed), "Radio wave propagation modeling, prediction and assessment", AGARDograph No. 326, AGARD, Paris, 1990, (ISBN 92-835-0598-0).

[2] AGARD, "Operational decision aids for exploiting or mitigating electromagnetic propagation effects", AGARD-CP-453, 1989.

[3] ITU, "Recommendations and Reports of the CCIR", XVIIth Plenary Assembly, Geneva, 1990.

Propagation in the Ionosphere - (A)

Paul S Cannon

Radio Propagation Exploitation Group
Space and Communications Dept
Defence Research Agency
Malvern, Worcs, WR14 3PS
United Kingdom

1. Introduction

The ionosphere, the ionised region of the atmosphere between about 85 km and 1000 km affects all radio signals that pass through or via it. Some of the associated radio systems can only operate because of the ionosphere, but it can also degrade radio system operation. Sometimes the effects of the ionosphere are highly significant, sometimes they can all but be ignored.

If the ionosphere were stable in time and constant in space it would be relatively easy to determine the effect of the ionisation on the radio propagation and hence on the radio system. Unfortunately, stability is not the norm, particularly in the high latitude regions [*Cannon*, 1989], and as a consequence propagation models and other decision aids have been, and are being, developed. These characterise the medium and estimate the system performance, implicitly or explicitly advising the operator on a course of action to improve system performance. By the nature of the human intervention needed to interpret the information the decision aid must be considered an off-line process.

One category of decision aid consists of the propagation model (ideally with good input and output capabilities) sometimes augmented with systems advisory information. The latter might consist, for example, of advice to change frequency. These propagation models incorporate one or more of a number of elements.

- i) An ionospheric model.
- ii) A ray tracing model.
- iii) System factors including antennas, noise etc.
- iv) A methodology to update the ionospheric model.

The propagation model is often used for long term prediction of system performance over one or more months. In such cases it is usual to provide monthly median estimates of system performance. Alternatively, forecasts (for the next few minutes, hours or days) of system performance can be generated. This is a far more difficult process requiring up-to-date ionospheric measurements and strategies for using these data.

The data used for updating ionospheric models can also be used as a decision aid in its own right. Such data may, for example, consist of actual measurements or forecasts of geomagnetic activity, or sunspot number, or even basic ionospheric parameters such as $foF2$, (the critical frequency of the ionospheric F - region). Armed with such information the decision aid can provide evidence that the system operating parameters must be adjusted to compensate for the propagation environment.

The ionospheric models and the more sophisticated of the ray tracing models can also be used together as a decision aid although it must be accepted that very skilled users are required to make best use of such systems. As an example, backscatter ionograms may be synthesised and compared with actual ionograms to aid the interpretation of the latter.

In this first of two lectures we will first introduce the physical basis for ionospheric decision aids by reference to ionospheric morphology and the basic theory of ionospheric propagation. We will then go on to review ionospheric propagation and ray tracing techniques. The second lecture will describe a number of decision aids related to the ionosphere in general and specifically to high frequency (HF) systems, meteor burst (MB) systems and satellite to ground systems. These aids provide system focused information on the current, forecast and predicted state of the ionosphere and of course the current, forecast and predicted system performance.

Since time does not permit we have elected not to address very low frequency (VLF) systems, low frequency (LF) systems and medium frequency (MF) systems.

Extensive citation of the relevant literature is given throughout this paper but the reader is referred to the excellent general texts by *Davies* [1990], *McNamara* [1991] and *Goodman* [1992]. The reader is also referred to the AGARD symposium on "Operational Decision Aids for Exploiting or Mitigating Electromagnetic Propagation Effects" [*AGARD*, 1989] and the AGARDograph on "Radio wave propagation modelling, prediction and assessment" [*AGARD*, 1990].

2. Ionospheric Morphology

2.1 Introduction

The ionosphere is a highly ionised region of the atmosphere lying in the altitude range 85 km to 1000 km, Figure 1. The ionisation of the earth's atmosphere which produces the ionosphere is caused by several mechanisms. The most important of these, at non-auroral latitudes, are the sun's extreme ultra violet (EUV), X-ray, and Lyman α together with solar cosmic rays. At high latitudes, particularly during magnetically active periods, the effects of energetic particles and electric fields are also important.

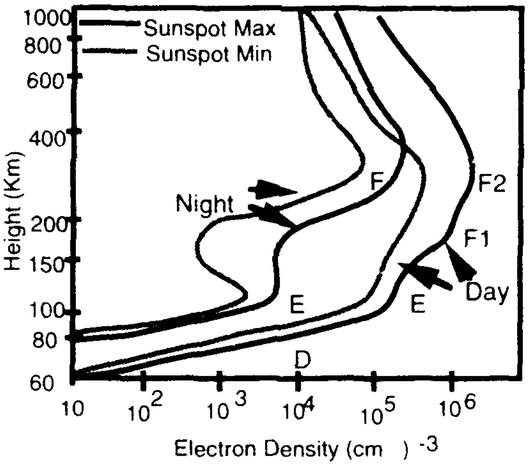

Figure 1. The ionosphere

The rates of ionisation at any altitude depends on the atmospheric composition as well as the characteristics of the incident radiation at that height. As the solar radiation propagates down through the neutral atmosphere the various frequency (energy) bands of this radiation are attenuated by different amounts. At the same time the composition of the atmosphere alters with altitude. Consequently, different ionisation processes become predominant at different heights resulting in a layered structure. The principal layers are designated *D*, *E* and *F* (see Figure 1), each being characterised by a different set of ionisation processes. Some of these regions are themselves layered or structured into the *E*, *Es*, *F1* and *F2* regions. The number of layers, their heights and their ionisation density vary with time and in space. The high latitude ionosphere is particularly complicated and will not be dealt with here but is described by *Cannon* [1989] and in the general texts referred to above.

2.2 The quiet time *D*-region

The *D*-region is the lowest layer of the ionosphere and extends from 50 km to 90 km although there is little ionisation below 85 km. Being the lowest region it is produced by the most penetrating of the ionising radiation. It is characteristically a region of very weak ionisation, the neutral density exceeding the electron density by several orders of magnitude. The electron density exhibits a strong diurnal variation being some two orders of magnitude higher during the day. The three main production sources are X-rays (wavelengths 0.1mm to 1mm) between 85 km and 90 km, Lyman α between 75km and 85 km and solar cosmic rays below 75 km.

Although the electron density is small compared to that of other regions the electron-neutral collision frequency is high due to the high neutral gas density and this leads to strong absorption. Absorption in the *D* region where the refractive index is close to unity is called non deviative. Non - deviative losses typically vary in an inverse square relationship with frequency and as a result at frequencies well above the HF band *D*-region absorption is inconsequential. Further, because *D* region ionisation is due to the sun's radiation and because recombination is rapid at these altitudes *D*-region absorption is primarily a day-time phenomenon. Two to three hours after sunset the absorption becomes negligible.

2.3 The quiet time *E*-region

The *E*-region peaks near 110 km, see Figure 1, and results from EUV radiation between 30 nm and 102.6 nm and X-rays from 1 nm to 10 nm. The *E*-region can be closely modelled as a Chapman layer and is very predictable compared to the *F2* layer above.

A large volume of vertical-incidence ionosonde data has been collected over about three solar cycles and the characteristics of the *E*-region are well known. The minimum vertical height of the *E*-region and the variation of the maximum electron density (*foE*) have been recorded as a function of time and geographical location. In the day-time the *E*-region is so regular that the distribution spread can be considered negligible (deciles at ±5%). At night there is less data but it is also reasonable to assume a small spread in values. As a guide the maximum electron density occurs during the day at ~ 110 km and the semi-thickness is ~ 20 km [*Frihagen*, 1965]. The peak electron density can be calculated from first principles or alternatively it can be estimated from statistical data bases. Usually, the *E*-layer critical frequency is determined by a semi-empirical equation involving the sunspot number and the zenith angle of the sun. An alternative approach uses numerical coefficients mapped in terms of geographic co-ordinates and universal time [*Leftin*, 1976].

Within the *E* region there also exists an ill predicted layer known as sporadic-*E* (*Es*). This layer often forms at about ~ 105 km and may be optically dense and spatially thin. In such cases it reflects radio signals well. Sporadic-*E*, however, also includes partially transparent layers and irregular patches of ionisation in which case signals may be reflected, or scattered, or little affected by the layer. The mechanisms producing sporadic-*E* are not well understood.

2.4 The quiet time *F*-region

The *F*-region consists of two regions known as the *F1*, which usually lies between 150 and 200 km altitude, and the *F2* which lies above. The *F2* region has a higher electron density and it consequently has a stronger impact on radio waves which traverse it. The *F1* layer, which is most obvious during the summer daytime, and the *F2* layer are separated by a ledge in the electron density. At night the *F1*-layer essentially disappears since it is under solar control. In the *F2* region, however, transport processes dominate due to the decreased neutral densities: ambipolar diffusion, electrodynamic drift and neutral winds determine the density distribution and maintain an ambient electron density even during the polar winter. As a consequence of the transport processes the *F2* layer is highly variable (10 to 30% from day to day).

The F-region also exhibits significant geographical variations in electron density, including the equatorial anomaly, the trough and the auroral oval. *Cannon* [1989] reviewed the *F* region in the high latitude region.

Due to the wide variation of *F*-region electron density profiles as a function of position time, averaged maps of the *F*-region electron density are generally used although other modelling approaches are now being addressed. These will be referred to later in this lecture.

3 Theory of Propagation Via the Ionosphere

The ionosphere is a dispersive medium, that is to say the refractive index of the medium varies as a function of frequency. As a consequence different frequencies travel with different speeds causing spreading of the pulse. The ionosphere is also layered, as we have described, and this leads to multi-path propagation. The earth's magnetic field introduces a further complication in as much as it renders the ionosphere anisotropic. This means that the incident ray will be split into two rays on entering the ionosphere in a manner similar to that of crystal optics. The two differently polarised rays are referred to as ordinary (*o*) and extraordinary (*x*) rays. One result of this splitting is the phenomenon of Faraday rotation of the wave polarisation plane as it traverses the ionosphere. The ionosphere, however, is above all a region where the refractive index is less than unity resulting in a group velocity which is less than that of light in free space. A consequence of this is that vertically launched rays can be reflected and oblique rays are progressively bent away from the vertical. Obliquely launched HF rays are in fact often turned back towards the ground. In these lectures a number of equations will be given describing the evaluation of specific quantities of interest. However, a fundamental equation from which the great majority can be derived is the so called Appleton-Lassen formula which describes the complex refractive index, n^2. In particular the equation is important to describe the propagation of HF waves. When collisions between the electrons and neutrals are negligible (in the *E* and *F* regions) the real part of the refractive index μ can be determined from a simplified form of the Appleton-Lassen formula:

$$\mu^2 = 1 - \frac{2X(1-X)}{2(1-X) - Y_T^2 \pm \left[Y_T^4 + 4(1-X)^2 Y_L^2\right]^{1/2}} \qquad \text{(Eq.1)}$$

where:

$X = Ne^2/\varepsilon_0 m\omega^2$, $Y_T = eB_T/m\omega$, and $Y_L = eB_L/m\omega$

The subscripts *T* and *L* refer to transverse and longitudinal components of the imposed geomagnetic flux (*B*) with reference to the direction of the wave normal of propagation. *N* is the electron density per cubic metre, *e* is the charge on the electron, *m* is the mass of the electron, ε_0 is the permittivity of free space and ω is the angular wave frequency. The plus sign above refers to the ordinary wave and the minus sign refers to the extra-ordinary wave. If the magnetic field is ignored the above reduces to:

$$\mu^2 = 1 - X = 1 - \left(\frac{f_N}{f}\right)^2 = 1 - k\frac{N}{f^2} \qquad \text{(Eq.2)}$$

where $f_N = (Ne^2/\varepsilon_0 m)^{0.5}$ and is known as the plasma or critical frequency. The constant $k = 80.5$, *N* is in electrons per cubic metre and *f* is in Hertz.

Reflection at vertical incidence occurs when $\mu = 0$ but at oblique incidence reflection takes place at finite values of the refractive index. Equation 2 demonstrates that for low frequencies such that $f<f_N$ ($<\sim$10MHz) reflection occurs for vertical incidence. At higher frequencies where $f>f_N$ the refractive index never drops to zero, reflection never occurs and the vertical ray passes through the ionosphere into space. On the other hand oblique rays which return to the ground can be supported for $f>f_N$ as described by Snell's law for total internal reflection.

4. Ionospheric Models

4.1 Introduction

The most difficult aspect of propagation modelling is the generation of the ionospheric model. The efficacy of the propagation modelling decision aid is no better than our knowledge of the underlying ionosphere. Fortunately, there have been substantial improvements in ionospheric modelling capabilities over the past few years, both as a result of improved computing facilities and, as a result of improved ground based sensors which can be used to provide real time updates.

Bilitza [1989 and 1990] provides excellent summaries of the various ionospheric models. These cover electron density, temperature, ion composition, ionospheric electric field, auroral precipitation and conductivity models. From the system users point of view the electron density distribution is paramount and we will restrict our discussions to those models only.

Both statistically based and theoretically based electron density models exist and these have been reviewed by *Davies* [1981], *Rush* [1986] and *Schunk and Szuszczewicz* [1988]. Unfortunately, the computer run times for the theoretical models are high. Typically, several hours are needed on a CRAY 1 computer to specify the global electron density [*Bilitza*, 1989]. As a consequence of these long run times the theoretical models are not appropriate for real-time or even near real-time applications.

4.2 Theoretical Simulation

Theoretical simulations are based on the self consistent solution of the *continuity, energy and momentum* equations for electrons and ions. Typical input parameters are the solar EUV radiation, the auroral particle precipitation (together with the interaction cross sections) and the atmospheric and magnetospheric boundary conditions. From those inputs and equations the plasma densities, temperatures and drifts are obtained numerically from the non-linear coupled system of equations. The most advanced computer simulations have been developed at Utah State University, USA [*Schunk et al.*, 1986], at University College London and the University of Sheffield, UK [e.g. *Fuller-Rowell et al* 1987] and at the National Center for Atmospheric Research in Boulder, Colorado, USA [e.g. *Roble et al.*, 1988].

4.3 Empirical Models

Empirical models of the electron density are currently of the most operational use. Empirical models are essentially climatological models for specified solar and/or magnetic activity levels, season, time of day, geographical area etc. The value of a number of empirical models for radio communications purpose is described by *Dudeney and Kressman* [1986] and by *Bradley* [1990].

The first three models described below are characterised in terms of a very limited number of parameters *foF2*, *foF1*, *foE* and *M(3000)* (= MUF(3000)/foF2 being related to the *F*-region peak altitude). These values can be used to generate a straight line and simple parabolic model of the electron density which is convenient for ray tracing (see section 5). Figure 2 illustrates the electron density profile as a function of height as described by the CCIR recommended *Bradley and Dudeney* [1973] model. (The CCIR, or International Radio Consultative Committee, of the International Telecommunications Union (ITU) no longer exists. However, many of its responsibilities have now been adopted by the ITU Radiocommunications Sector.)

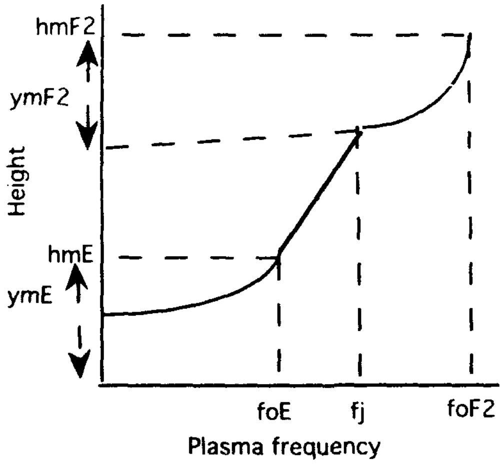

Figure 2 Bradley-Dudeney approximate model of the ionospheric electron density profile.

4.3.1 CCIR Ionospheric Maps

The most commonly used empirical model is the so called CCIR Atlas of Ionospheric Characteristics forming Report 340 [*CCIR*, 1988]. The CCIR model is a compendium of basic ionospheric characteristics which are required to determine ionospheric radio propagation. The atlas gives maps of the *F2*-layer peak critical frequency, *foF2* and the *M(3000)F2* factor.

The *E* and *F1* layer characteristics are given by a series of formulae whereas the contours of *foF2* are based on spherical harmonic and Fourier functions. The whole model consists of 34,296 coefficients. Figure 3 shows an example of the *foF2* contours for a sunspot number of 100 in September at 20 UT. It is important to note that the model lacks detail at high latitudes.

4.3.2 URSI Coefficients

It has long been known that the CCIR model is inaccurate above oceans and in the southern hemisphere where ionosonde measurements are scarce or do not exist. *Rush et al.* [1983, 1984] suggested a framework for introducing theoretical values in regions of no measurements and this lead to a new model which was adopted by the International Union of Radio Science (URSI) [*Fox and McNamara*, 1986].

4.3.3 Bent Model

The Bent model [*Bent et al.*, 1975] is important because it contains a topside model not incorporated in the previous two models. The topside is represented by a parabola and three exponential profile segments and the bottom side by a bi-parabola. The model is based on topside soundings from the Alouette and Ariel spacecraft as well as conventional bottom side ionograms. The model is often used for ionospheric corrections in satellite tracking and altimetry which rely on models of the total electron content (TEC). It does not include *D*, *E* and *F1* models and simplifies the calculation of the *F2* peak. *Brown et al.* [1991] have compared the Bent model with a number of other models, such as the IRI (see below) which include a top side model.

4.3.4 IRI

The International Reference Ionosphere (IRI) model [*Rawer and Bilitza*, 1990] gives a more detailed electron density profile between 60 and 100 km. It is divided vertically into up to seven regions, *D*, lower *E*, *E* region valley, *E/F1* intermediate, *F*, *F2* and topside. The *F2* parameters can be determined from the numerical maps of CCIR Report 340 [*CCIR*, 1988] and so are lacking detail in the high latitudes; the *F2* region parameters

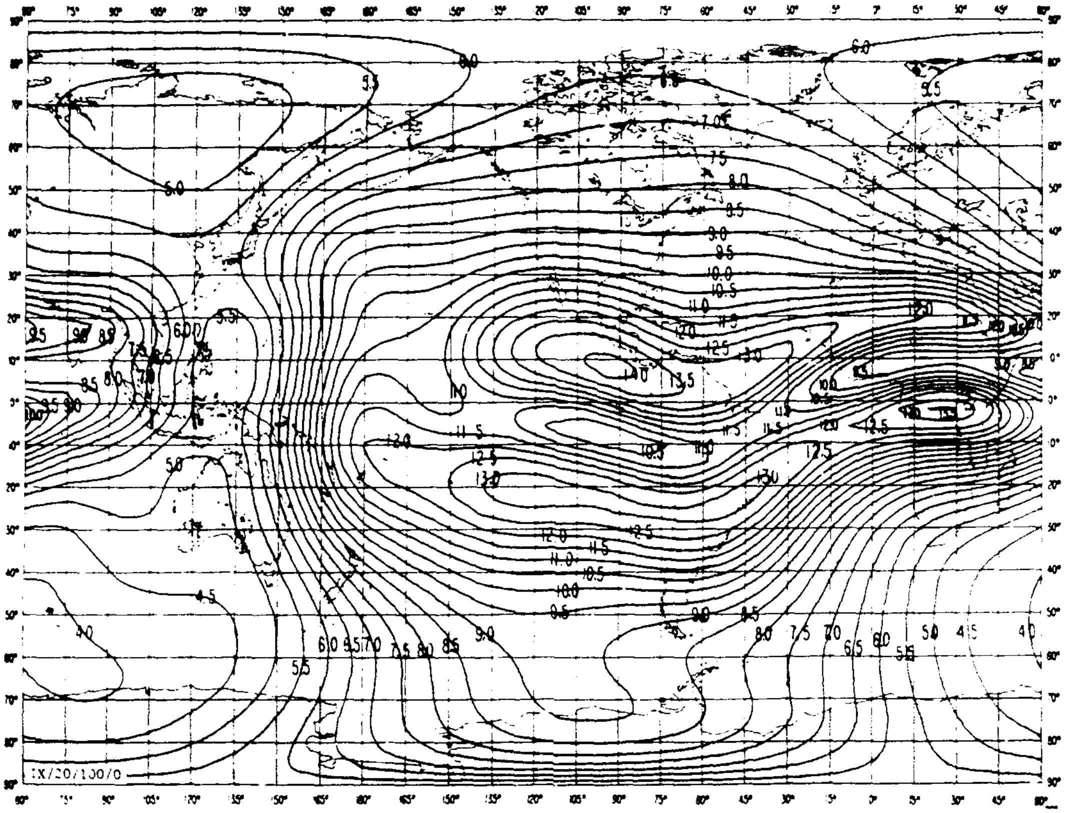

Figure 3 CCIR Report 340 map of foF2 for September at 20 UT when the sunspot number is 100.

also enter into the empirical expressions describing some of the other regions. Alternatively, the URSI coefficients or the users own coefficients can be used. Like Report 340 the model is parametric in month, universal time and sunspot number. The IRI uses a mixture of analytical calculations, iterative searches and empirical rules to provide its vertical profile. There are however, horizontal discontinuities, for example the *F1* region appears and disappears according to local time. The iterative searches are also non-linear and so it is not possible to obtain analytic derivatives of the quantities they calculate. As a consequence of these two problems the IRI cannot be used for ray tracing without modification.

4.4 Parameterised Models

We have so far described two approaches to specifying the ionospheric electron density profile, namely:

- Numerical simulations based on physical models.
- Statistical or climatological models.

Each has its advantages and disadvantages. The first is more intellectually appealing but too slow to run in real tine. The second is limited by the network of data gathering measurement stations, by averaging, and the adopted rules for extrapolation.

A third approach is the parameterised version of the physical model. Here the physical model is parameterised in terms of solar and geographical parameters. The parameterised model begins with a physical model which gives a more realistic representation of the spatial structure of the ionosphere than the statistical model can provide. (Any statistical data base inevitably averages over similar geophysical conditions resulting in a smoothed model which is unrepresentative of the instantaneous ionosphere.)

4.4.1 SLIM

The Semi-Empirical Low-Latitude Ionospheric Model (SLIM) [*Anderson et al.*, 1987] is an example of this approach where theoretical simulations of the low latitude ionosphere have been undertaken on a regular latitude-longitude grid, at various local times, times of the year and at high and low sunspot conditions. The theoretical profiles have then been parameterised in terms of modified Chapman functions using just six coefficients per profile. When the model is run the parameters can be adjusted to reflect current geophysical and solar conditions.

4.4.2 PIM

A promising global parameterised model is PIM (Parameterised Ionospheric Model). This model [*Daniell*, 1993a, and *Daniell et al.*, 1994] is itself an amalgam of a number of other models and uses either

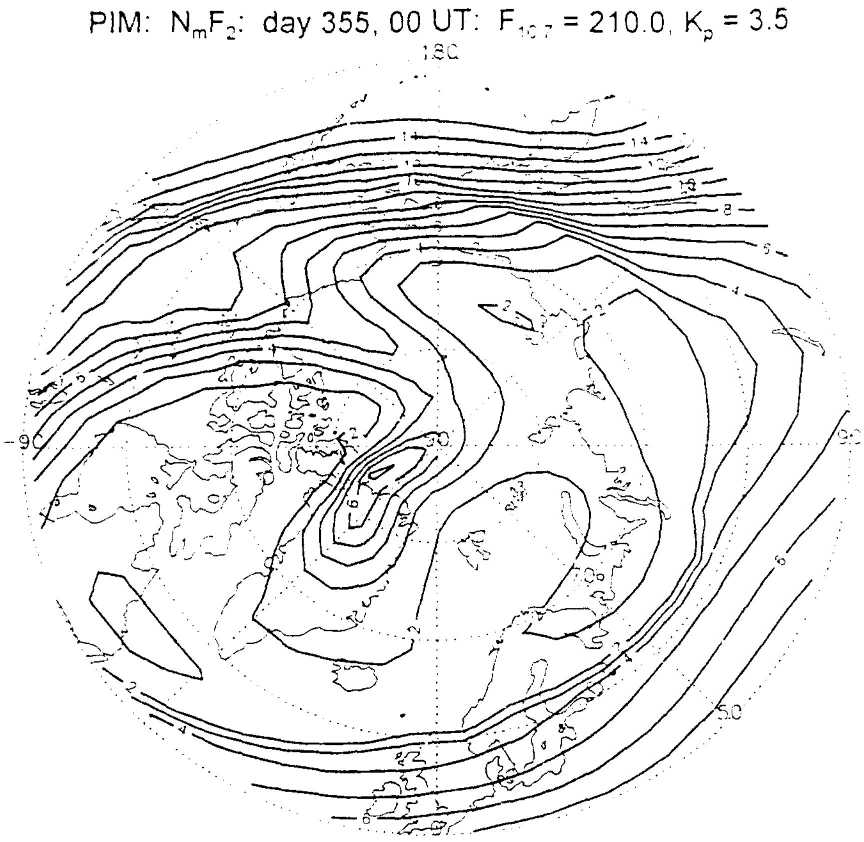

Figure 4. Contours of the maximum ionisation density in the *F2* region (in units of 10^5 cm^{-3}) in polar projection from PIM for high solar activity, moderate magnetic activity, at 00UT and at the December solstice. The "tongue of ionisation" produced by a steady convection pattern is clearly evident. Local midnight is at the bottom, from *Daniell et al.* [1994].

the *foF2* CCIR coefficients for normalisation of the electron density profiles or it uses coefficients produced by the Utah State University model. The calculation of the electron density profile is based upon the underlying neutral composition, temperature and wind together with electric field distributions, auroral precipitation and the solar EUV spectrum. Inputs to the model consist of universal time, the daily value of $F_{10.7}$ (the solar flux at a wavelength of 10.7 cm) or the solar sunspot number, the current value of *kp* (the index of solar geophysical activity) and the sign (positive or negative) of the interplanetary magnetic field *y* component. This latter factor is used to select one of two convection patterns in the high latitude region. As we will see later, however, the PIM model is at its most powerful when it is adjusted by real time inputs. Figure 4 shows typical output from PIM and illustrates the high latitude structure inherent in the model.

4.4.3 ICED

The Ionospheric Conductivity and Electron Density [ICED] model is also being developed for the USAF Air Weather Service *Tascione et al.* [1988]. This model is controlled by the sunspot number (SSN) and the geomagnetic *Q* index which is related to the better known geomagnetic *kp* index. The *kp* index is retrospectively available from a number of sources such as the Space Environment Laboratory, Boulder CO 80303, USA. In addition forecast values are available from the same and other sources for the following 24 hours, see *Cannon* [1994].

4.5 Real time updates to models

Empirical models of the non-auroral, quiet ionosphere typically describe the median monthly or seasonal conditions at every hour. Day to day *foF2* deviations from these median values can range from 10 to 30% even for quiet magnetic conditions and will be higher still during ionospheric storms. Furthermore, there are short term variations due to atmospheric gravity waves which typically have periods of 10 - 120 minutes. The difference between monthly median predicted and measured signal strengths can be up to 40 dB. Theoretical and parameterised models, do not rely on historical statistical data bases but they are reliant on accurate input data to drive the model.

In order to compensate for the temporal variations in the ionosphere it is necessary to introduce real-time values and to map these real-time values into the median, theoretical or parameterised model. Techniques for achieving this in respect to the empirical models are being addressed by the PRIME (Prediction and

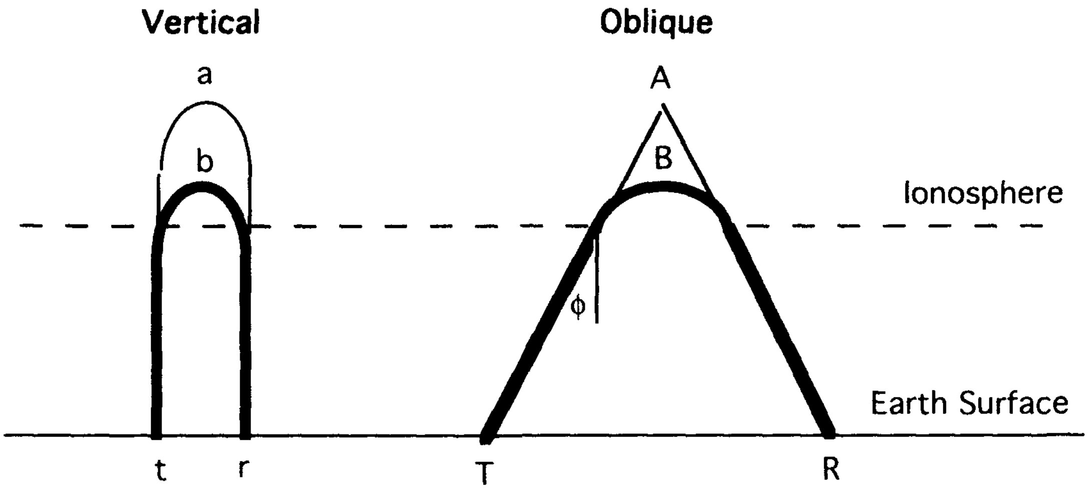

Figure 5. Geometry for ray propagation. Earth and ionosphere are plane surfaces. The transmitter and receiver are at T (t) and R (r) respectively. The true point of reflection is at B (b) and the virtual point of reflection is at A (a).

Retrospective Modelling in Europe) group in Europe [e.g. *Bradley*, 1989].

The most important developments in this field derive from the USA in support of the Air Force Space Forecast Center (AFSFC). Both the ICED and PIM models were conceived to allow for real-time updates of the input parameters from a number of sensors. ICED updates are based only on changes of the effective sunspot number SSN_{eff} and the auroral Q index whereas real-time control of PIM, via the model known as PRISM, (Parameterised Real-Time Ionospheric Specification Model) is by five input parameters as already described.

4.5.1 ICED with real time updates

Whilst ICED can be used as a stand alone model it can be driven by real time data. The model is partly updated from real-time data from a network of digital ionosondes. The *foF2* values from the ionosonde network are compared to model *foF2* values and the SSN adjusted to provide the best match. The resultant *SSN* is called the effective sunspot number, SSN_{eff}. For real time updates the Q index is used rather than *kp*. *Feldstein* [1966] related the position of the auroral oval to the Q index and the AWS reverses the procedure to obtain the Q index from DMSP satellite measurements of the position of the auroral boundary. At the US Air Force Space Forecast Center (AFSFC) the model is typically updated half hourly or hourly.

4..5.2 PRISM

PRISM can take real time data from a very extensive array of ground and space based instrumentation to adjust the parameterised model, PIM. The adjustment parameters in PRISM vary with location and consequently PRISM promises greater accuracy than ICED [*Daniell*, 1993b].

5 Ray Tracing Decision Aids

5.1 Introduction

It is often necessary to evaluate the point where an HF ray launched upward towards the ionosphere returns again to the ground and this requires a ray tracing procedure. If the ray is of sufficiently high frequency it will penetrate the ionosphere providing a satellite to ground or ground to satellite path. These too will deviate from their paths due to refraction and will suffer time and frequency dispersion; the magnitude of these effects can also be estimated by ray tracing.

5.2 Virtual Techniques

The simplest ray tracing technique is known as virtual ray tracing and it assumes that the actual propagation can be approximated by reflection from a simple horizontal mirror at an appropriate height (the secant law, Breit and Tuve's theorem and Martyn's equivalent path theorem [e.g. *McNamara*, 1991]). This approach is implemented in most HF prediction decision aids apart from a few of the most recent (e.g. AMBCOM). The major advantage of this approach is that it is computationally efficient. Its major disadvantage is that it cannot deal with a horizontally non-stratified ionosphere. It may, therefore, be considered an approximate method and more complicated ray tracing methods are necessary in certain situations. Virtual techniques are, however, well matched to a median ionospheric data base and simple ionospheric profiles. Indeed, in most circumstances the use of a more complicated model is not justified given the available ionospheric model.

5.3 Numerical Ray Tracing Decision Aids

We have discussed above the limitation of virtual techniques for *HF* systems and the possible need for numerical ray tracing techniques. Numerical ray tracing is also essential for a precise assessment of magnetic-ionic effects. These include Faraday rotation of the polarisation vector, on *satellite to ground* links and angle of arrival calculations. Typical applications are satellite navigation and altimetry systems. The standard decision aid for numerical ray tracing is the *Jones and Stephenson* [1975] program. The program is based on the solutions of a set of six coupled, first order, non-linear differential equations, in spherical co-ordinates (providing that the time dependencies of the ionosphere are neglected).

Numerical ray tracing techniques are as accurate as the ionospheric model allows but they are computationally intensive to run. In many applications the issue of ray homing is critical and several techniques to solve this problem have been reported.

5.4 Analytic Ray Tracing

A technique intermediate between the simple but inaccurate virtual technique and the complicated and accurate numerical technique also exists. The analytic technique relies on describing the ionosphere by functions that can be integrated. The technique was first pioneered by *Croft and Hoogasian* [1968] for realistic spherical earth models and was extended by *Milsom* [1985]. In its simplest form it requires the use of quasi-parabolic (QP) and linear ionospheric segments which are approximations to the true situation.

To avoid the need to resort to numerical ray tracing when a real ionosphere is used *Baker and Lambert* [1989] and *Dyson and Bennett* [1989] have more recently developed the multi-quasi-parabolic (MQP) description of the ionospheric electron density profile. In this approach an arbitrary ionospheric profile is approximated by any number of QP segments through which each ray can be analytically traced. The MQP model can also be set up using a fixed number of segments to match the scaled ionospheric parameters such as the layer critical frequency and the layer semi-thickness.

MQP techniques provide a good compromise between computational speed and performance for many applications and as a consequence they are now being employed in many of the newer HF predictions decision aids. They also provide a very useful stand alone decision aid which can be used to both ray trace single paths and simulate backscatter ionograms. The MQP analytic approach has a further significant advantages over virtual techniques; it provides an analytic determination of spatial attenuation. Unfortunately, the MQP approach only works if magnetic field effects are ignored though an estimate for their inclusion has been developed [*Bennett et al.*, 1991]. It has been estimated that neglecting the magnetic field can, in some circumstances, give rise to a 15% error in ionospheric specification at 10 MHz [*Goodman*, 1992]. At higher frequencies the error from neglecting the magnetic field diminishes.

6 Summary

This lecture has addressed ionospheric models and ray tracing models which can, at a basic level, be considered Decision Aids. In the next lecture we will address the more sophisticated Decision Aids which provide system directed advice to the operator.

7 References

AGARD, "Operational decision aids for exploiting or mitigating electromagnetic propagation effects," AGARD, Paris, 1989.

AGARD, "Radio wave propagation modelling prediction and assessment," AGARD, Paris, 1990.

Anderson, D. N., M. Mendillo and B. Herniter, A semi-empirical low latitude ionospheric model, *Radio Sci.*, **22**, 292, 1987.

Baker, D. C. and S. Lambert, Range estimation for SSL HFDF by means of a multi-quasi-parabolic ionospheric model, *IEE Proc, Pt H*, **136**, (2): 120-125, 1989.

Bennett, J. A., J. Chen, P. L. Dyson, Analytic ray tracing for the study of HF magneto-ionic radio propagation in the ionosphere, *App. Computational Electromagnetics J.* , **6**, 192-210, 1991.

Bent, R. B., S. K. Llewellyn, G. Nesterczuk and P. E. Schmid, The development of a highly successful world-wide empirical ionospheric model and its use in certain aspects of space communications and world wide total electron content investigations, Proc. Symp. on Effects of the Ionosphere on Space Syst. and Communications (IES'75), Naval Research Lab., Arlington, Virginia, USA, 13-28, US Government Printing Office, Washington DC 20402, USA, 1975.

Bilitza, D., The world-wide ionospheric data base., *Report, NSSDC/WDC-A-R&S 89-03*, National Space Science Center/World Data Center A for Rockets and Satellites, 1989.

Bilitza, D., Solar-terrestrial models and application software, *NSSDC/WDC-A-R&S 90-19*, National Space Sciences Data Center, World Data Center A for Rockets and Satellites, Goddard Space Flight Center, Greenbelt, Maryland, 1990.

Bradley, P. A., New prediction and retrospective ionospheric modelling initiative over Europe (PRIME), NRPP Research Note 114, Rutherford Appleton Laboratory, UK, 1989.

Bradley, P., *Use of electron density profiles in HF propagation assessment*, Presented at XXVIII COSPAR Plenary Meeting, The Hague, Netherlands, 1990.

Bradley, P. A. and J. R. Dudeney, A simple model of the vertical distribution of the electron concentration in the ionosphere, *J. Atmos. Terr. Phys.*, **35**, 2131-2146, 1973.

Brown, L. D., R. E. Daniell, M. W. Fox, J. A. Klobuchar and P. H. Doherty, Evaluation of six ionospheric models as predictors of total electron content, *Radio Sci.*, **26**, (4): 1007-1015, 1991.

Cannon, P. S., Morphology of the high latitude ionosphere and its implications for HF communications systems, *IEE Proc., Pt I*, **136**, (1): 1-10, 1989.

Cannon, P. S. Propagation in the Ionosphere - (B), in AGARD Lecture Series 196 on Propagation Modelling and Decision Aids for Communication, Radar and Navigation Systems, 1994.

CCIR, Atlas of ionospheric characteristics, *Report, 340-4*, Comité Consultatif International des Radiocommunications, International Telecommunications Union, Geneva, 1988.

Croft, T. A. and H. Hoogasian, Exact ray calculations in a quasi-parabolic ionosphere, *Radio Sci.*, **3**, (1): 69-74, 1968.

Daniell, R.E., W.G. Whartenby, L. D. Brown, Parameterised Real Time Ionospheric Specification Model, PRISM version 1.2, Algorithm description, Computational Physics, Inc., 385 Elliot St, Newton, MA02164, USA, 1993a.

Daniell, R.E., W.G. Whartenby, L. D. Brown, Parameterised Real Time Ionospheric Specification Model, PRISM version 1.2, Validation Report, Computational Physics, Inc., 385 Elliot St, Newton, MA02164, USA, 1993b.

Daniell, R.E., W.G. Whartenby, L. D. Brown, D. N. Anderson, M. W. Fox, P.H. Doherty, D.T. Decker, J.J. Sojka, R. W. Schunk, PRISM: A Parameterised Real-Time Ionospheric Specification Model, Submitted to *Radio Science*, 1994.

Davies, K., Review of recent progress in ionospheric predictions, *Radio Sci.*, **16**, 1407-1430, 1981.

Davies, K., "Ionospheric Radio," Peter Peregrins, London, United Kingdom, 1990.

Dudeney, J. R. and R. I. Kressman, Empirical models of the electron concentration of the ionosphere and their value for radio communications purposes, *Radio Sci.*, **21**, (3): 319-330, 1986.

Dyson, P. and J. A. Bennett, A model of the vertical distribution of the electron concentration in the ionosphere and its application to oblique propagation studies, J. *Atmos. Terr. Phys.*, 50, 3, 251-262, 1988.

Feldstein, Y. I., *Planetary and Space Sci.*, **14**, 121, 1966.

Fox, M. W. and L. F. McNamara, Improved empirical world maps of FoF2:1. The method, *Technical Report IPS-TR-86-03*, Ionospheric Prediction Service, Sidney, Australia, 1986.

Frihagen, J., Electron density profiles in the ionosphere and exosphere, Proc. NATO Advanced Study Inst., Finse, Norway, North Holland, John Wiley and Sons, New York, USA, 1965.

Fuller-Rowell, T. J., J. D. Rees, S. Quegan, R. J. Moffett and G. J. Bailey, Interactions between neutral thermospheric composition and the polar ionosphere-thermosphere model, *J. Geophys. Res*, **92**, 7744-7748, 1987.

Goodman, J. M., "HF Communications Science and Technology," Van Nostrand Reinhold, New York, 1992.

Jones, R. M. and J. J. Stephenson, A three-dimensional ray tracing computer program for radio waves in the ionosphere, *OT Report 75-76*, US Dept of Commerce, Office of Telecommunications, 1975.

Leftin, M., Numerical representation of the monthly median critical frequencies of the regular E-region (foE), *OT report 76-88*, US Government printing office, 1976

McNamara, L. F., "The ionosphere, communications, surveillance and direction finding," Strother, ed., Krieger Publishing Company, Malabar, Florida, 1991.

Milsom, J. D., Exact ray path calculations in a modified Bradley-Dudeney model ionosphere, *IEE Proc. H, Microwaves, Antennas & Propagation*, **132**, 33-38, 1985.

Rawer, K. and D. Bilitza, International Reference Ionosphere - Plasma densities: Status 1988, *Adv. Space Res*, **10**, (8): (8)5- (8)14, 1990.

Roble, R. G., T. Killeen, N. W. Spencer, R. A. Heelis, P. H. Reiff and J. D. Winningham, Thermospheric dynamics during November 21-22, 1981: Dynamics explorer measurements and thermospheric general circulation model and predictions, *J. Geophys. Res.*, **93**, 209-225, 1988.

Rush, C. M., Ionospheric radio propagation models and predictions- A mini-review, *IEEE Trans. on Ant. and Prop.*, **AP-34**, (9): 1163-1170, 1986.

Rush, C. M., M. PoKempner, D. N. Anderson, F. G. Stewart and J. Perry, Improving ionospheric maps using theoretically derived values of foF2, *Radio Sci.*, **18**, (1): 95-107, 1983.

Rush, C. M., M. PoKempner, D. N. Anderson, F. G. Stewart and R. Reasoner, Maps of FoF2 derived from observations and theoretical data, *Radio Sci.*, **19,** (4): 1083-1097, 1984.

Schunk, R. W. and E. P. Szuszczewicz, First principal and empirical modelling of the global scale ionosphere., *Annales Geophysicae*, **6,** 19-30, 1988.

Schunk, R. W., J. J. Sojka and M. D. Bowline, Theoretical study of the electron temperature in the high-latitude ionosphere for solar maximum and winter conditions, *J Geophys. Res.*, **91,** 12041-12054, 1986.

Tascione, T. F., H. W. Kroehl, R. Creiger, J. W. Freeman Jnr, R. A. Wolf, R. W. Spiro, R. V. Hilmer, J. W. Shade and B. A. Hausman, New ionospheric and magnetospheric specification models, *Radio Sci.*, **23,** (3): 211-222, 1988.

Propagation in the Ionosphere - (B)

Paul S Cannon

Radio Propagation Exploitation Group
Space and Communications Dept
Defence Research Agency
Malvern, Worcs, WR14 3PS
United Kingdom

1 Introduction

In the first paper [*Cannon*, 1994] we briefly discussed the morphology of the ionosphere and the theory of propagation through the ionosphere. This provided us with the basic tools to understand a number of ionospheric models and ray tracing techniques which follow the path of a radio ray through the ionosphere. Whilst requiring considerable skill in interpretation the ionospheric models and the ray tracing models can be considered as decision aids in their own right.

In this paper we will go on to expand our discussion on decision aids. These integrate all, or some, of the topics discussed in the first paper into (often) sophisticated computer programs or equipments. HF (high frequency) systems, satellite to ground systems and MB (meteor burst) systems will be addressed. Much of the discussion will be in the area of HF systems, this reflecting the importance of the ionospheric model and decision aid to those systems. Emphasis will be given to mature models and decision aids which provide the user (rather than the scientist) with information which can improve system operation.

This paper can be supplemented by the excellent general texts of *Davies* [1990], *McNamara* [1991] and *Goodman* [1992]. The reader is also referred to the AGARD symposium on "Operational Decision Aids for Exploiting or Mitigating Electromagnetic Propagation Effects" [*AGARD*, 1989] and the AGARDograph on "Radio wave propagation modelling, prediction and assessment" [*AGARD*, 1990].

2 Short Term Ionospheric Forecasts

Before moving on to address various systems we will first consider the short term ionospheric forecast (STIF) and geomagnetic forecast which are respectively "weather forecasts" of the electron density and the geomagnetic activity levels. In *Cannon* [1994] we emphasised the necessity of excellent ionospheric models if the system decision aids and propagation models are to provide a useful capability. Any forward estimate of system performance must consequently rely on the quality of the STIF or the geomagnetic forecast (which may indirectly act as a driver of an ionospheric model).

The Space Environment Space Center (SESC) in Boulder Colorado provides forecasts both in the USA and world-wide but forecasts are also provided by other organisations such as the Marconi Research Centre (MRC) in the UK [*Wheadon et al*, 1991]. These forecasts are communicated by fax, telex and even by satellite links. Typically, they cover geomagnetic activity, sunspot number and other ionospheric information for the immediate past, current and immediate future epochs. Such data can be used in various models.

In addition forecasts are made of HF propagation conditions. Tables 1 and 2 are typical forecasts from respectively MRC (for 1-2 February, 1994) and SESC (28-30 January, 1994). It is to be noted that the SESC forecast provides a forecast of the *effective* sunspot number specifically required by the ICED model.

A system known as DIAS (**D**isturbance **I**mpact **A**ssessment **S**ystem) has been developed by *Rose* [1993] to assess the effects of solar flares on the high latitude ionosphere in terms of sudden ionospheric disturbances, polar cap absorption, ionospheric storms, auroral zone absorption and auroral sporadic *E* and auroral *E*. This system also provides a very useful training facility.

3 HF Decision Aids

3.1 Introduction

HF communications and radar decision aids cover a number of applications. Broadcast services and HF Over The Horizon Radar (OTHR) systems require coverage patterns showing skip zones and signal strength for each operating frequency. Broadcast services are particularly constrained since they are unlikely to have many assigned operating frequencies. Within this small set the operator must provide a reliable prediction of the optimum reception frequency. Furthermore, the system designer requires a prediction method to plan for the installation of new transmission facilities. OTHR systems on the other hand are likely to have a large frequency set available to maintain coverage but the operators are very interested in where the signals go for co-ordinate registration purposes. Point-to-point HF communications operators are particularly interested in selecting the best frequency for transmission. This may be one that provides the lowest intersymbol interference, highest signal strength and lowest noise and interference level. For many applications an estimate of variability is required and this is often provided by upper and lower decile values.

3.2 Prediction Models at HF

Propagation Model Decision Aid development has largely followed the evolution of the ionospheric model and more recently the development of analytic ray tracing as described in *Cannon* [1994]. HF propagation decision aids are in fact not new, but date back to World War II. Through the years a large number of models have been developed and are still being developed. Many of the decision aids are, however, not generally available and of course a number have fallen into disuse because of the availability of the newer models. As a consequence this lecture will restrict itself to a small number of the most popular and accessible decision aids.

IONCAP [*Teters et al.*, 1983]. This is a very popular program developed by Institute of Telecommunications Sciences (ITS) in the USA and it will run on both main frame and personal computers (PC). Unfortunately, in its basic form the input of data is rather cumbersome but a number of user friendly front ends have been developed, for example the derivative VOACAP [*Lane et al.* 1993] which also makes a number of small changes to the calculations used in IONCAP. IONCAP and its derivatives use a number of approximations for the propagation model including the use of an equivalent mirror height for reflection.

FTZ [*Ochs*, 1970]. This model was developed by the Deutsche Bundespost. It includes an empirical representation of field strength. The method is based upon observations of signal level associated with a large number of circuit-hours and paths, with the majority of the paths terminating in Germany. The signal level data were analysed without accounting for the individual modes. The FTZ model is computationally very efficient and it is consequently a valuable method.

CCIR 252-2: [*CCIR*, 1970]. This model termed CCIR *Interim Method for Estimating Skywave Field Strength and Transmission Loss Between Approximate Limits of 2 and 30 MHz* was initially adopted by CCIR at the 1970 New Delhi plenary session. It was the first of three computer methods for field strength prediction which were sanctioned by the CCIR.

CCIR 252-2 *Supplement* : [*CCIR*, 1978]. A field prediction method entitled *Second CCIR Computer-based Interim Method for Estimating Skywave Field Strength and Transmission Loss and Frequencies Between* 2 *and* 30 *MHz*. The method is more complex than the method of CCIR 252-2 in a number of respects, and the machine time required reflects this additional complexity. A major change is the consideration of longitudinal gradients for the first time. A computer program was completed in 1987.

CCIR 894-1: [*CCIR*, 1982]. To assist in the World Administrative Radio Conference (WARC) HF Broadcast Conference, a rapid computational method was documented as CCIR Report 894. The CCIR approach is used for paths less than 7000 km, FTZ is used for paths greater than 9000 km, and linear interpolation schemes are applied for intermediate path lengths.

CCIR 533-3: [*CCIR*, 1992]. This computer code is derived from the method of Report 894 and includes a number of antenna models leading to improved estimates of signal level.

AMBCOM: [*Hatfield*, 1980]. This program was developed by SRI International and differs from many of the other prediction decision aids in that it employs a 2-D analytic ray-tracing routine rather than the virtual mirror approach. In addition, AMBCOM contains within its ionospheric sub-model a considerable amount of high latitude information including improved auroral absorption models. This provides for an improved prediction capability for paths through or close to the high latitude region. The program is generally slower than simpler models. AMBCOM documentation is not as widely distributed as the IONCAP or the CCIR methods.

ICEPAC: [*Stewart and Hand*, 1994]. The ICEPAC (or Ionospheric Communications Enhanced Profile Analysis and Circuit) prediction program is the latest prediction decision aid from ITS. It uses the ICED electron density model which should in particular give improved performance in the high latitude regions.

3.2.1 Typical Output from ICEPAC

ICEPAC represents one of the very newest of the HF prediction decision aids and as such it is worthy of more detailed discussion. Its outputs are very similar to IONCAP and it provides in total 29 different output options. These are listed in Table 3.

Ionospheric Descriptions, Methods 1 or 2

Methods 1 and 2 provide specialist output relating to the ionospheric parameters.

MUF output options, Methods 3 to 12 and 25-29

These methods include listings and graphical output of the basic maximum usable frequency (MUF) and frequency of optimum transmission (FOT) for the path and for individual modes *E*, *Es*, *F1* and *F2*. They also provide information on angle of take off. Method 10 (Table 4) illustrates typical output for a path from the southern UK to Ottawa, Canada for January 1994.

System Performance options, Methods 16 to 24.

The system performance outputs are largely tabular and provide system performance data. Method 16 (Table 5) illustrates typical output from ICEPAC for the path from Southern England to Ottawa, Canada. Listed at each time (UT) and frequency (FREQ) are the most reliable propagating modes (MODE), arrival angles (ANGLE), the path delay (DELAY), the virtual height (V HITE), the probability that the operating frequency will exceed the predicted MUF (F DAYS), the median system loss in decibels (LOSS), signal strength in dBm, (DBU), median signal and noise powers at the receiver input terminals in dBw (S DBW and N DBW), signal to noise ratio (SNR), the required combination of transmitter power and antenna gains needed to achieve the required reliability in decibels (RPWG), reliability, i.e. the probability that the SNR exceeds the required SNR (REL), and the probability of an additional mode within the multipath tolerances (MPROB).

Coverage area diagrams
ICEPAC can also be used to provide signal level contours over a wide geographical area. Figure 1 shows an example of such a diagram for transmissions from southern England. Such diagrams are more effective in colour but the central region close to the transmitter shows the skip or area where no signals are received. Also apparent is the result of the high latitude ionosphere which distorts the coverage area significantly.

Antenna output options, Methods 13 to 15
ICEPAC includes the antenna gain description of a number of antennas which may be specified at the transmitter and receiver. These antennas include the isotropic reference radiator, dipoles, rhombics and sloping V antennas. The radiation pattern of the antennas can be plotted and the effects of the antennas on the system performance evaluated via methods 16 to 24. This is a capability not generally available in prediction codes.

3.2.2 Application specific models

The aforementioned propagation models exhibit a general architecture which makes them useful in many applications. A number of systems have, however, been developed which take these generalised architectures and develop them for specific applications.

In the HF field one of the earliest to do this was PROPHET [*Argo and Rothmuller*, 1979; *Rose*, 1989]. It was stimulated by the availability of satellites in the early 1970s which had been developed to measure solar radiation characteristics (e.g. X-ray flux solar wind, etc.). PROPHET was developed using simple empirical ionospheric models but it has proliferated into many different versions with 500 terminals in operation. Figure 2 is a typical output showing the MUF (maximum usable frequency) FOT (frequency of optimum transmission) and LUF (lowest usable frequency). This kind of analysis and display has proved to be a very helpful decision aid for communications. A further decision aid is shown in Figure 3, MUF and LUF are displayed for a specific path (Honolulu to San Diego). The operator can choose from a library of hostile intercept stations. The solid filled areas indicate a frequency-time region for which the signal cannot be intercepted. The grey shaded region indicate the possibility of interception by just one station and consequently no position fix. The white areas indicate regions where the signal can be intercepted by a number of stations to obtain a fix.

3.3 'On Air' Decision Aids

So far we have restricted our discussions to model based decision aids but there are a number of 'on-air' decision aids. We consider off-line techniques which are distinct from embedded approaches such as those embodied in HF communication ARCS (automatic radio control systems) [*Goodman* 1992]. (ARCS were previously known by the acronym RTCE (Real Time Channel Evaluation) and ALE (Automatic Link Establishment)). An important aspect of the embedded approach is its ability to make *automatic* system changes, after characterising the HF channel, without recourse to human intervention.

3.3.1 Ionospheric Sounders

'On air' decision aids include instrumentation to measure the channel characteristics but without the *automatic* system adaptation elements characteristic of ARCS. Skilled operators sometimes combined with computer programs, are then needed to interpret the off-line measurements and appropriately adapt the system operation. One category of 'on air' decision aid is the ionospheric sounder. Ionospheric sounders (ionosondes) are essentially radars which measure the group delay of signals propagating via the ionosphere. Due to the structure of the ionosphere multiple radar returns can be obtained at a single frequency. Ionospheric sounders can be monostatic with the receiver and transmitter co-located or they can be bistatic with the transmitter and receiver separated by many tens, hundreds or thousands of kilometres. The former produce vertical ionograms and the latter oblique ionograms. A further category, the backscatter sounder, will not be discussed here.

The HF Chirpsounder™ manufactured by Barry Research (USA) (sometimes known as the AN/TRQ-35) is an off-line oblique ionospheric sounder which provides HF channel (and ionospheric information) such as propagating frequencies and multipath over the path from the sounder transmitter to the sounder receiver. If the HF communications is over the same path as the sounder the latter provides an invaluable decision aid to choose the correct operating frequency. Figure 4 shows an ionogram from the ROSE (Radio Oblique Sounder Equipment) chirp ionosonde developed at the Defence Research Agency in the UK [*Arthur and Cannon*, 1994] which is compatible with the Chirpsounder™ format but which provides higher resolution with the signal amplitude colour coded. In this monochrome example an operator might choose to operate at 18 MHz where the signal level is high and where there is no multipath.

Goodman and Daehler [1988] and *Shukla and Cannon* [1994] (for example) have extended the measurements on one HF path to a broader area by comparing the scaled values of the junction frequency (JF) of the *F*-trace to predicted values over the path. (The junction frequency is, for simple propagation conditions, the highest propagating frequency and is generally given for the *F2* mode. In Figure 4 it is close to the cross hairs.) The predicted, and scaled JF values are matched by an iterative process which uses the sunspot number as a variable. This *pseudo* sunspot number (PSSN) is then used for all predictions in the local area. Figure 5 shows an application of this technique. A PSSN has been derived for the path Andøya (Norway) to Farnborough (UK), which is then used to update the J ven Island (Norway) to Farnborough (UK) path 5 top panel). The update is performed every six at which time the measured MUF obtained from a er on the path is very close to the value derived the other path. During the following six hours the difference between the actual and spatially extrapolated value increases but generally remains smaller than the difference between the measured value and the predicted value (derived using a method known as APPLAB). This improvement is quantified in Figure 5b which shows the RMS errors between the modelled and measured MUF.

Vertical looking ionosondes can also be used to derive the electron density directly over the site [*Titheredge*, 1988]. These can then be used to provide real time updates to the ionospheric models previously described. This is the method used by the US Air Weather Service to determine up to date models of the ionosphere. Electron density information can also be obtained from oblique ionogram traces although there are more inherent inaccuracies associated with this approach. The oblique ionograms must be scaled to obtain a trace representing group path versus frequency information over the path. This is a difficult process. The scaled trace is then converted to an equivalent vertical ionogram trace [*Reilly*, 1985 and 1989] from which the electron density can be extracted using the technique appropriate to vertical ionograms.

4 Space to Ground Models and Decision Aids

4.1 Introduction

A radio signal which penetrates the anisotropic ionosphere is modified in a number of ways. Both large scale changes due to the variation in electron density and small scale irregularities affect the signal. The effects include scintillation, absorption, variation in the direction of arrival, group path delay, dispersion, Doppler shift, polarisation rotation, refraction and phase advance. With the exception of the scintillation all of these effects are proportional to the total electron content (TEC) or its time derivative and inversely proportional to frequency to the appropriate power. The TEC is the total number of electrons in a column with a 1 m^2 base along the path from the transmitter to the receiver. Table 6 shows the magnitude of these effects for a specimen frequency of 1 GHz.

AGARD [1990] describes the relationship between the magnitude of the effects and the TEC. In all cases, the working frequency is assumed to be much greater than the critical frequencies of the ionosphere.

Group Path Delay
The excess time delay, over the free space transit time, in trans-ionospheric propagation is given by:

$$\Delta t = \frac{40.3}{cf^2}\ \mathrm{TEC}\ (\mathrm{s}), \tag{Eq 1}$$

where TEC is the total number of electrons in a column with a 1 m^2 base along the path from transmitter to receiver, c is the velocity of light in ms^{-1} and f is the operating frequency in Hz. A plot of time delay versus system frequency for TEC values from 10^{16} to 10^{19} el/m^2 is given in Figure 6 [*CCIR, 1986*].

RF Carrier Phase Advance
The phase ϕ of the carrier of the radio frequency transmission is changed by the ionosphere: it is advanced with respect to the phase in the absence of the ionosphere. The importance of this effect is manifested when determining space object velocities by means of range rate measurements. The phase increase may be expressed as:

$$\Delta\Phi = \frac{1.34\times 10^{-7}}{f}\quad \mathrm{TEC}\ (\mathrm{cycles}) \tag{Eq 2}$$

Doppler Shift
With frequency being the time derivative of the phase, an additional Doppler shift (on top of geometric shift) results from the changing TEC, and may be expressed by:

$$\Delta f = \frac{d\Phi}{dt} = \frac{1.34\times 10^{-7}}{f}\frac{dTEC}{dt}\ (\mathrm{Hz}) \tag{Eq 3}$$

Faraday Polarisation Rotation
When a linearly polarised radio wave traverses the ionosphere, the wave undergoes rotation of the plane of polarisation. At frequencies above about 100 MHz, the polarisation rotation may be described by :

$$\Omega = \frac{k}{f^2} B_L \bullet TEC\,(\mathrm{rad}) \tag{Eq 4}$$

where $k = 2.36\times10^{-5}$ and B_L is the magnetic field component parallel to the wave direction, taken at a mean ionospheric height.

The Faraday effect has been widely used by the scientific community to measure TEC with emissions from orbiting and geostationary satellites. The Faraday rotation may result in no signal on a linearly polarised receiving antenna positioned to receive linearly polarised satellite-emitted signals, unless the receiving antenna is properly aligned.

Angular Refraction
The refractive index of the earth's ionosphere is responsible for the bending of radio waves from a straight line geometric path. The bending produces an

apparent elevation angle higher than the geometric elevation. The angular refraction may be expressed by:

$$\Delta E = \frac{(R + r_o \sin E_o) r_o \cos E_o}{h_i(2r_o + h_i) + r_o^2 \sin^2 E_o} \cdot \frac{\Delta R}{R} \text{ (rad)}, \quad \text{(Eq 5)}$$

where E_0 is the apparent elevation angle, R is the geometric range, r_o is the earth's radius and h_i is the height of the centroid of the TEC distribution, generally between 300 and 400 km. ΔR, the excess range over the geometrical range, is computed from:

$$\Delta R = (40.3 / f^2) \text{ . TEC. (metres).} \qquad \text{(Eq 6)}$$

Distortion of Pulse Waveforms

Dispersion, or differential time delay due to the ionosphere, produces a difference in pulse arrival time across a bandwidth Δf of:

$$\Delta t = \frac{80.6x10^6}{cf^3} \Delta f . TEC(s) \qquad \text{(Eq 7)}$$

When the difference in group delay across the bandwidth of the pulse is the same magnitude as the width of the pulse. The latter will be significantly disturbed by the ionosphere.

Absorption

In general, at a frequency greater than 10 MHz, the absorption on an oblique path, with angle of incidence at the ionosphere i, varies in proportion to $\sec(i)/f^2$ Enhanced absorption occurs due to increased solar activity and due to polar cap and auroral events.

Table 6 estimates maximum values for ionospheric effects at a frequency of 1GHz. It is assumed that the total zenith electron content of the ionosphere is 10^{18} electrons m^{-2}. A one way traversal of waves through the ionosphere at 30° elevation angle is also assumed.

4.2 TEC Based Models and Decision Aids

The TEC is normally determined by integration through the monthly median models discussed in *Cannon* [1994].

A algorithm for an approximate 50% correction to the world-wide TEC, for use in single frequency global positioning satellite (GPS) has been developed by *Klobuchar* [1987] and evaluated by *Feess and Stephens* [1987]. The model fits monthly average TEC at those times of the day when TEC is the greatest. The diurnal variation in TEC is modelled as the positive portion of a cosine wave during the daytime but is held constant at night. The latitude dependency is modelled by holding the night-time and cosine phasing terms constant and by using third order polynomials to depict cosine amplitudes and periods as functions of the geomagnetic latitude. Polynomial coefficients are chosen daily from sets of constants that reflect the sensitivity to solar flux, and seasonal variations. No attempt to account for day-to-day variability is made. Only eight coefficients are used to represent the amplitude and period of TEC on a global scale.

The US Airforce is procuring [*Bishop et al.*, 1989] a fully automated trans-ionospheric sensing system (TISS). This will consist of a global network of stations making real-time measurements of the time delay of the ionosphere, its rate of change and its amplitude and phase scintillation. NAVSTAR-GPS signals will be used. Such data will feed into the ICED and WBMOD ionospheric scintillation (see later) model to provide them with near real-time updates. This will greatly improve the specification of propagation effects on specific paths. This future capability to generate near real-time reports will allow system operators to adjust operating modes to mitigate trans-ionospheric effects.

4.3 Scintillation Based Predictions and Decision Aids

Ionospheric scintillation is the fluctuation of amplitude, phase, polarisation, and angle of arrival produced when radio waves pass through electron density irregularities in the ionosphere. The irregularities vary in size from metre to kilometre scales. Scintillation can be severe and present problems to radio systems ranging in operating frequencies from 20 MHz to about 10 GHz. A review of ionospheric scintillation theories is given by *Yeh et al* [1982] and a review of the global morphology of ionospheric scintillation is given by *Aarons* [1982]. Figure 8 shows the global picture of scintillation morphology for L-band (1.6 GHz) signals after *Basu et al.*, [1988]. Scintillation is worse in tropical regions, during the evenings around the equinoxes and in the auroral zones.

A global model of scintillation has been developed to assess its impact on systems [*Fremouw et al.* 1978]. The model is known as WBMOD and it permits the user to specify an operating scenario including frequency, location, local time, sunspot number and planetary geomagnetic index, *kp*. The user must also specify the longest time the system needs phase stability. The model output includes, the spectral index p for the power law of phase scintillation, a spectral strength parameter (T), the standard deviation of the phase variations and the scintillation index S_4.

The spectral index, p describes the power law which characterises the scintillating irregularities where the scintillation power spectrum, $P(\upsilon)$ is given by:

$$P(v) = Av^{-p} \qquad \text{(Eq 8)}$$

where A is a constant and ν is the frequency. A typical example is given in Figure 9.

The S_4 index describes the standard deviation of the received power divided by the mean value of the received power, i.e.:

$$S_4 = \frac{\left(\sum (P-\overline{P})^2\right)^{0.5}}{\overline{P}} \qquad \text{(Eq 9)}$$

Weak scintillation corresponds to low values of the scintillation index (e.g. $0< S_4< 0.3$). Strong scintillation (e.g. $S_4>0.6$) is generally associated with the presence of multiple scattering.

Whilst, the WBMOD scintillation model provides predictions which are useful for planning, the model does not provide real-time estimates of scintillation unless provided with the necessary real-time data as described by *Bishop et al.* [1989].

An alternative technique to mitigate the fading effects of scintillation is the provision of diversity reception of signals.

5 Meteor Burst Models and Predictions

5.1 An introduction to Meteor Scatter Propagation and Meteor Scatter Systems

Meteor burst (MB) communication can provide robust and reliable beyond line of sight (BLOS) communications over distances from about 200 to 2000 km. This technique exploits the ephemeral ionised meteors as they burn up in the atmosphere. Individually these trails possess only fleetingly short lifetimes, of the order of a second or less, but this is sufficient to give effective scattering of high frequency (HF) and very high frequency (VHF) radio signals (usually in the range 20 120 MHz). Although this may not appear promising from a communications viewpoint, such vast numbers of trails are formed each day in the earth's atmosphere (some 10^{10} or more) that successive trails suitable for radio communication may occur at intervals of only a few seconds. This constitutes a viable, yet intriguing, intermittent radio communication medium which has been reviewed by *Cannon and Reed* [1986].

Meteor scatter communications requires less power than ionoscatter, is less subject to degradation by ionospheric disturbances than is HF, and requires no frequency management in order to maintain viable communication. Furthermore, meteor burst systems are less vulnerable and far less costly than satellite communication, while the former's inherent security and resistance to jamming can also be advantageous.

5.2 Basic Models for Received Signal Level.

Scattering at the meteor trails is approximately specular and successful communication may be achieved when a trail axis is tangential to any ellipsoid which has the transmit and receive locations as foci. This condition can be fulfilled by many trail positions and this in combination with the distribution of trail radiants and altitudes (85-110 km) results in certain parts of the sky being favoured over others. The zone around the mid-point of the great circle path joining two terminals is itself a region of rather low probability of finding suitable trails, since here they would need to be oriented parallel to the ground, a rather rare occurrence! Instead, the regions where there is greatest probability of finding suitable trails, the so-called "hot spots", lie approximately 50 to 100 km to either side of the great circle path between the two terminals.

Meteor scatter communications is primarily a weak signal system because the losses associated with the scattering process are high. For example, at 40 MHz the transmission loss over a 1000 km link is some 170-180 dB, substantially higher than the spatial attenuation (approximately 125 dB) over the same length path, but rather less, by some 20dB, than would be found over a comparable ionoscatter link.

For underdense trails the received signal level as a function of time can be described by the following equation:

$$RSL = \frac{P_T G_T G_R \lambda^3 q^3 r_e^2 \sin^2\alpha}{16\pi^2 R_R R_T (R_R + R_T)(1-\cos^2\beta\sin^2\phi)}$$

$$\exp-\left(\frac{8\pi^2 r_0^2}{\lambda^2\sec^2\phi} + \frac{32\pi^2 Dt}{\lambda^2\sec^2\phi}\right) \qquad \text{(Eq 10)}$$

where

RSL= received signal level (watts)
P_T = transmitter power (watts)
G_T = transmitter antenna gain (rel. isotropic)
G_R = receiver antenna gain (rel. isotropic)
R_T = distance from the transmitter to the trail (m)
R_R = distance from the receiver to the trail (m)
λ = wavelength (m)
q = electron line density (electrons/metre)
r_e = classic radius of the electron (2.818×10^{-15} m)
D = Diffusion constant which is a function of height
S = polarisation coupling factor
ϕ = propagation angle formed by vectors R_T, R_R
β = angle of the trail real-time to the plane formed by R_T and R_R
α = angle between the trail and vector from the trail to the receiver

This expression shows that the received power varies as the cube of the wavelength and is very dependent on the path geometry (for each trail) via the terms α, β and ϕ.

The received power varies with time since the trail expands radically by diffusion from the moment of its formation. Typical values for the diffusion constant, *D*, lie in the range 1-15$\mathrm{m^2s^{-1}}$. As the trail diameter increases, scattering occurs from different places within the trail with the result that the signal contributions at the receiver suffer progressively from destructive interference. The two exponential terms in equation 9 reflect this process. The first accounts for the trail having a finite initial radius by the time the scattering process commences while the second term shows the subsequent exponential decay in the received signal strength.

5.3 Sophisticated MB Models

Meteor burst (MB) communications systems have performance requirements most usually quantified by the concepts of message waiting time and average data throughput. The former can vary from an acceptable value of a few seconds up to a few hours. An acceptable data throughput may be as slow as 10 bps (bits per second) or may be as high as 1000 bps. The meteor burst operating performance is controlled by a number of factors including transmitter power, antenna gain, the sporadic meteor radiant density map, and the shower meteor radiant density map. The sporadic meteor radiant density map and shower meteor radiant density map recognise the astronomical variation of apparent meteor sources as a function of time of day, month and year. Retrospective assessment of system performance, extrapolation of the path performance to another location or time of year, the design of a new system to meet certain waiting time and average throughput criteria all need a MB decision aid in the form of a model.

MB decision aids have been developed with two distinct philosophies. The first is the reference model approach which computes the waiting time and duty cycle on one path, by scaling the known performance of another experimental path. The reference model approach provides a simplified algorithm for rapid prediction of link performance. Reference based MB decision aids should be accurate for modelled links which are similar to the reference link but as the modelled link deviates more and more from the reference link the output becomes more questionable. In particular it is very difficult to account for dramatically different antenna configurations or radically different operating latitudes.

The physical modelling approach is a more computationally difficult approach but one which should provide better success. This approach considers path geometry in relation to the meteor radiant density map and corresponding velocity distribution, the power loss due to spreading, the power loss on scattering and many other system factors including noise models and antenna models. Typical outputs consist of the number of meteors detected per unit time above a certain minimum received power level (RSL), the duty cycle, or the waiting time presented as monthly, daily or hourly averages. *Schanker* [1990] describes a number of decision aids which have been developed in the USA based on the physical modelling concept. *Desourdis* [1993] describes in detail the background and mathematical basis of the METEOR LINK programs, one of a number of programs in the METEORCOM family of MB communications modelling and analysis programs.

By way of illustration we describe some output from a similar model developed in the UK [*Akram and Cannon*, 1994]. Figure 10a shows four panels for a hypothetical path with a transmitter lying on the Greenwich meridian and on the equator. The receiver is also placed on the equator but at 10° east. Horizontally polarised antenna are used at both ends of the link. In each panel the centre of the path is located at link co-ordinates (0,0) with the transmitter and receiver respectively located at ~(± 555, 0) km.

The panel labelled 'Probability Distribution' shows the probability distribution that a meteor will be correctly oriented to scatter signals from transmitter to the receiver if meteors arrived uniformly from all directions. This diagram shows a maximum over both transmitter and receiver and a minimum at the centre of the path. In reality, however, meteors arrive from a wide variety of directions but are constrained to orbits close to the ecliptic and maximise in the direction of the earth's way and at angles ~60° from that direction. Further, the probability is also controlled by the earth's inclination to the ecliptic. As a consequence the probability distribution is asymmetrical with respect to the great circle path as shown in the panel labelled 'Probability Distribution II'. Moreover this distribution varies as the day progresses as described in Figure 10b, c and d. The third panel labelled 'Trail Duration' quantifies the time that a trail will last and describes the second exponential in Equation 9. We see that this factor maximises in the centre of the path, where the probability of the trail being detected is lowest. The fourth panel addresses the 'Polarisation Coupling' loss which combines the effects of antenna polarisation, Faraday rotation [*Cannon*, 1986] and the $\sin^2\alpha$ term in equation 9. In the illustration an isotropic radiator is employed.

An obvious application of such a model is to quantify the data throughput over the path for design purposes. For example various antenna configurations can be tried to optimise the system antenna design.

6 The way ahead

A recurring theme throughout these two papers has been the adaptation of system operation by skilled personnel who have selected and interpreted the output from a computer program or experimental technique. The only exception to this rule is ARCS which operates automatically providing a transparent (to the user) decision aid. An important thrust for the future must be the further development of automatic decision aids. An artificial intelligence system [e.g. *Rose*, 1989] might replace human operator, selecting and using the models and experimental techniques to best advantage.

7 References

Aarons, J., Global morphology of ionospheric scintillation, *Proc. IEEE*, **70**, 360-378, 1982.

AGARD, "Operational decision aids for exploiting or mitigating electromagnetic propagation effects," AGARD, Paris, 1989.

AGARD, "Radio wave propagation modelling prediction and assessment," AGARD, Paris, 1990.

Akram, A. and P. S. Cannon, A meteor scatter communications system data throughput model, IEE Conf. HF Systems and Techniques, York, July 1994.

Argo, P.E. and I. J. Rothmuller, "PROPHET": an application of propagation forecasting principles", Solar-Terrestrial Predictions Proc, Vol. I, 312-321,1979.

Arthur, P. C. and P. S. Cannon, ROSE, A high performance oblique ionosonde providing new opportunities for ionospheric research, *Annali di Geofisica*, **XXXVII**, 1, 1994.

Basu, S. and E. Mackenzie, Ionospheric constraints on VHF/UHF communication links during solar maximum and minimum periods, *Radio Sci.*, **23**, 363-378, 1988.

Bishop, G. J., J. A. Klobucher, A. E. Romm and M. G. Bedard, A modern trans-ionospheric propagation sensing system, AGARD Conf. Proc. 453 on "Operational decision aids for exploiting or mitigating electromagnetic propagation effects., San Diego, USA, 1989.

Cannon, P. S. Polarisation rotation in meteor burst communication systems, 21, 3, 501-510, 1986.

Cannon, P. S., Propagation in the ionosphere - (A), Propagation modelling and decision aids for communication, radar and navigation systems, AGARD Lecture Series 196, AGARD, 1994.

Cannon, P. S. and A. P. C. Reed, The evolution of meteor burst communications systems, *J. Inst. Elec. Rad. Eng*, **57**, (3): 101-112, 1987.

CCIR XIIth Plenary Assembly, New Delhi, "CCIR Interim Method for Estimating Sky-Wave Field Strength and Transmission Loss at frequencies between the approximate limits of 2 and 30 MHz", Report 252-2, Geneva, Int. Telecomm Union 1970.

CCIR XIVth Plenary Assembly, Kyoto, "Second CCIR Computer-based interim method for estimating sky-wave field strength and transmission loss at frequencies between 2 and 30 MHz, Supplement to Report 252-2, Geneva, Int. Telecomm Union 1978.

CCIR, XVth Plenary Assembly, Geneva, "Propagation prediction methods for high frequency broadcasting, Report 894" Propagation in Ionized Media, Recommendations and Reports of the CCIR, 1982, Vol. VI, Geneva, Int. Telecomm Union, 1982.

CCIR, XVIth Plenary Assembly, Dubrovnik "Ionospheric effects upon earth-space propagation"; Report 263-6 in "Propagation in ionized media", Vol. VI, Geneva, International Telecomm. Union, 1986.

CCIR "CCIR HF Propagation Prediction Method, Report 533" Propagation in Ionized Media, Recommendations and Reports of the CCIR 1992, Vol. VI, Geneva Int., Telecomm Union 1992.

Davies, K., "Ionospheric Radio," Peter Peregrins, London, United Kingdom, 1990.

Desourdis, R. I., "Modelling and Analysis of meteor burst communications," Meteor burst communications-Theory and practice, Schilling, ed. Wiley- Interscience Publication, New York, 1993.

Feess, W. A. and S. G. Stephens, Evaluation of GPS ionospheric time delay model, *IEEE Trans. Aeros. and Electr. Systems*, **AES-23**, 332-338, 1987.

Fremouw, E. J., R. L. Leadabrand, R. C. Livingston, M. D. Cousins, C. L. Rino, B. C. Fair and R. A. Lonng, Early results from the DNA wideband satellite experiments - Complex signal scintillation, *Radio Sci.*, **13**, 167-187, 1978.

Goodman, J. M. and M. Daehler, Use of oblique incidence sounders in HF frequency management, IEE 4th International Conference on HF radio systems and techniques, London, 66-70, IEE, 1988.

Goodman, J. M., "HF Communications Science and Technology," Van Nostrand Reinhold, New York, 1992.

Hatfield, V. E., HF Communications predictions, 1978 (An economical up-to-date computer code (AMBCOM), Solar predictions proceedings, 4: D2 1-15, 1980.

Klobucher, J. A., Ionospheric time-delay algorithm for single frequency GPS users, *IEEE Trans Aeros. and Electr. System*, **AES-23**, 325-331, 1987.

Lane, G., F. J. Rhoads and L. DeBlasio, Voice of America coverage analysis program, (VOACAP) A guide to VOACAP, *B/ESA Technical Report 01-93*, US Information Agency, Bureau of Broadcasting, Washington, D. C. 20547-0001, 1993.

McNamara, L. F., "The ionosphere, communications, surveillance and direction finding," Strother, ed., Krieger Publishing Company, Malabar, Florida, 1991.

Ochs, A., The forecasting system of Fernmeldetechnischen Zentralamt (FTZ), NATO AGARD EPP Symposium, CP-49: Paper 43, 1970.

Reilly, M. H., Ionospheric true height profiles from oblique ionograms, *Radio Sci.*, **20**, (3): 280-286, 1985.

Reilly, M. H., A method for real height analysis of oblique ionograms, *Radio Sci.*, **24**, (4): 575-583, 1989.

Rose, R. B., A high latitude ionospheric disturbance assessment system, *Radio Sci.*, **28**, (1): 97-104, 1993.

Rose, R. B., Operational decision aids for exploiting or mitigating electromagnetic wave propagation effects in PROPHET and future signal warfare decision aids, AGARD Conf., San Diego, USA, Proc 453: 8-1 to 8-4, 1989.

Schanker, J. Z., "Meteor burst communications," Artech, Boston, USA, 1990.

Shukla, A. K. and P. S. Cannon, Prediction model updating using ionospheric sounders at mid and higher latitudes, IEE HF Conference, York, IEE, 1994.

Stewart, F. G. and G. Hand, Technical description of the ICEPAC Propagation prediction program, *Private Communication*, Institution of Telecommunications Sciences, 1994.

Teters, L. R., J. L. Lloyd, G. W. Haydon and D. L. Lucus, Estimating the performance of telecommunications systems using the ionospheric transmission channel: Ionospheric Communications Analysis and Prediction Program (IONCAP) User's manual, *NTIA report 83-127, NTIS order no N70-24144*, NTIA, Springfield, VA, USA, 1983.

Titheridge, J. E., The real height analysis of ionograms: A generalized formulation, *Radio Sci.*, **23**, (5): 831-839, 1988.

Wheadon, N. S., J. D. Milsom and R. Larsen, The research and development of a fully automated daily short-term ionospheric forecasting service, Conf on HF Radio Systems and Techniques, Heriot-Watt University, Edinburgh, 113-116, IEE, 1991.

Yeh, K. C. and C. H. Liu, Radio Wave scintillation in the ionosphere, *Proc. IEEE*, **70**, 324-360, 1982.

Table 1. MRC Ionospheric forecast

```
SHORT TERM IONOSPHERIC FORECAST FOR EUROPE

**BULLETIN BOARD 0245 76233 (7E1 75/1200)
FORECAST ISSUED 15[illegible]T  :  01 Feb 1994

GEC PAST SUMMARY 1[illegible] [illegible] UT 31 Jan-01 Feb
--------------------------------------------------------------
HF SKYWAVE MUF VARIATIONS
             12-18         18-24            00-06           06-12 UT
             95-110        65-120           75-95           95-100
DAYTIME LUF                     :  NORMAL
SHORTWAVE FADES                 :  NONE
GEOMAGNETIC ACTIVITY    :  31 Jan
A  =  12 ( UNSETTLED )
SUNSPOT NUMBER                  :  81
10 CM FLUX VALUE                :  98

FAIR TO NORMAL HF RADIO CONDITIONS
PREVAILED FOR THE PAST 24 HOURS .

FORECAST  1800-1800 UT 01 Feb-02 Feb
------------------------------------------------------
SKYWAVE VARIATION MUF VARIATIONS
             18-24            00-06           06-12         12-18 UT
            NORMAL    NORMAL      NORMAL     NORMAL
DAYTIME LUF                             :  NORMAL
SWF PROBABILITY                     :  8 PERCENT
GEOMAGNETIC ACTIVITY      :  02-04 Feb
A = 11/23/14  ( UNSETTLED )

FAIR TO NORMAL HF RADIO CONDITIONS
ARE EXPECTED FOR THE NEXT 24 HOURS .
```

Table 2. SESC Ionospheric forecast

```
SUBJ:  HF RADIO PROPAGATION REPORT
JOINT USAF/NOAA BULLETIN PREPARED AT THE AIR FORCE SPACE
FORECAST CENTER, FALCON AFB, COLORADO.
PRIMARY HF RADIO PROPAGATION REPORT ISSUED AT 28/0525Z JAN 94.

PART I.   SUMMARY   28/0000Z  TO  28/0600Z  JAN 94/
                 FORECAST   28/0600Z  TO  28/1200Z  JAN  94.
                                                                  QUADRANT
                                         I            II           III       IV
                                     0 TO 90W    90W  TO 180     180 TO 90E          90E TO 0
 REGION         POLAR                    N4           N4             N5                N5
                AURORAL                  N3           N3             N4                N4
                MIDDLE                   N6           N6             N7                N7
                LOW                      N7           N7             N7                N7
                EQUATORIAL               N7           N7             N6                N7

PART II.
GENERAL DESCRIPTION OF HF RADIO PROPAGATION CONDITIONS
OBSERVED DURING THE 24 HOUR PERIOD ENDING 27/2400Z, AND FORECAST CONDITIONS FOR THE NEXT 24 HOURS.
CONDITIONS WERE GENERALLY NORMAL, EXCEPT FOR SOME DEGRADATIONS REPORTED IN THE TRANSITION SECTORS OF THE
AURORAL ZONE.  THE DEGRADATIONS WERE MOSTLY SPREAD-F AND NON-DEVIATIVE ABSORPTION.
FORECAST:  EXPECT MOSTLY NORMAL CONDITIONS EXCEPT FOR THE AURORAL SECTORS, ESPECIALLY THE TRANSITION SECTORS,
WERE MINOR PROBLEMS SUCH AS INCREASED SPREAD-F AND NON-DEVIATIVE ABSORPTION CAN BE ANTICIPATED.

PART III.  SUMMARY OF SOLAR FLARE INCLUDED IONOSPHERIC DISTURBANCES WHICH MAY HAVE CAUSED SHORT WAVE FADES IN
THE SUNLIT HEMISPHERE DURING THE 24 HOUR PERIOD ENDING 27/2400Z JAN 94  . . . .
               START                  END                 CONFIRMED             FREQS AFFECTED
               0508Z                  0531Z                  NO                  UP TO 13 MHZ
PROBABILITY FOR THE NEXT 24 HOURS  . . . . SLIGHT

PART IV.  OBSERVED/FORECAST  10.7 CM FLUX AND K/AP.
THE  OBSERVED 10.7 CM FLUX FOR 27 JAN 94 WAS 120.
THE FORECAST  10.7 CM FLUX FOR 28, 29, AND 30 JAN 94
ARE 120, 115, AND 110.
THE OBSERVED K/AP VALUE FOR 27 JAN 94 WAS  03/16.
THE FORECAST K/AP VALUES FOR 28, 29, AND 30 JAN 94
ARE 03/18,  02/10,  AND 03/15.
SATELLITE X-RAY BACKGROUND:  B3.5  (3.5 E MINUS 04 ERGS/CM S Q/SEC).
THE EFFECTIVE SUNSPOT NUMBER FOR 27 JAN 94 WAS 062.0.
```

Table 3. **Available Output Methods in ICEPAC**

Method	Description of method
1	Ionospheric Parameters
2	Ionograms
3	MUF - FOT lines (nomogram)
4	MUF - FOT graph
5	HPF - MUF - FOT graph
6	MUF - FOT - Es graph
7	MOT - MUF table (full ionosphere)
8	MUF - FOT graph
9	HPF - MUF - FOT graph
10	MUF - FOT - ANG graph
11	MUF - FOT - Es graph
12	MUF by magnetic indices, K (not implemented)
13	Transmitter antenna pattern
14	Receiver antenna pattern
15	Both transmitter and receiver antenna patterns
16	System performance (S.P.)
17	Condensed system performance, reliability
18	Condensed system performance, service probability
19	Propagation path geometry
20	Complete system performance (C.S.P.)
21	Forced long path model (C.S.P.)
22	Forced short path model (C.S.P.)
23	User selected output lines (set by TOPLINES and BOTLINES)
24	MUF-REL table
25	All modes table
26	MUF - LUF - FOT (nomogram)
27	FOT - LUF graph
28	MUF - FOT - LUF graph
29	MUF - LUF graph

Table 4 **ICEPAC Method 10 output**

```
CCIR COEFFICIENTS         METHOD 10   ICEPAC  Version ITS.01

  JAN    1994          SSN =  62.     Qeff= 3.0
  Cobbett Hill, UK    CRC, Ottawa, Canada   AZIMUTHS          N. MI.      KM
  51.27 N    .63 E - 45.40 N  75.92 W      294.97   53.87    2934.6   5434.4
  MINIMUM ANGLE   3.00  DEGREES


  XMTR  2-30 CCIR.000    ISOTROPE +   .0 dBi  Azim=295.0 OFFaz=360.0    .500kW
  RCVR  2-30 CCIR.000    CCIR  /ISOTROPE      Azim=   .0 OFFaz= 53.9


            MUF(....)       FOT(XXXX)       ANG(++++)

   00  02  04  06  08  10  12  14  16  18  20  22  00
 MHZ+-+-+-+-+-+-+-+-+-+-+-+-+-+-+-+-+-+-+-+-+-+-+-+-+MHZ
40-                                                   -40
  -                                                   -
38-                                                   -38
  -                                                   -
36-                                                   -36  GMT   MUF   FOT   ANG
  -                                                   -
34-                                                   -34  1.0   9.0   7.5   9.6
  -                                                   -    2.0   8.7   7.3   9.7
32-                                                   -32  3.0   8.9   7.3   9.7
  -                                                   -    4.0   9.1   7.5   9.7
30-                                                   -30  5.0   8.8   7.2   9.6
  -                                                   -    6.0   7.4   6.1   9.3
28-                                                   -28  7.0   7.2   5.9   8.4
  -                                                   -    8.0   7.9   6.6   8.9
26-                               .                   -26  9.0   9.0   7.1   7.9
  -                             .   .                 -   10.0  10.7   8.4   7.1
24-                                                   -24 11.0  13.7  10.8   6.3
  -                                   .               -   12.0  18.1  14.3   5.7
22-                           .   X                   -22 13.0  22.4  16.8   5.6
  -                                 X                 -   14.0  25.2  18.9   5.6
20-                                                   -20 15.0  26.0  21.8   5.7
  -                             X     X .             -   16.0  24.6  20.7   6.4
18-                         .                         -18 17.0  22.7  19.1   6.5
  -                           X                       -   18.0  19.3  16.2   7.0
16-                                     X .           -16 19.0  15.9  12.4   7.3
  -                                                   -   20.0  13.2  10.3   8.1
14-                       . X                         -14 21.0  11.6   9.1   8.5
  -                                         .         -   22.0  10.5   8.2   8.8
12-                                       X   .       -12 23.0   9.6   8.1   9.5
  -                     . X                           -   24.0   9.2   7.8   9.7
10- + + + + + +                             X   . . + -10
  - . . . . . . +   + .                       X + + . -
08- X X           + . + X                   + + X X X -08
  -     X X X X . . X X +               + +           -
06-             X X       + + + + + + +               -06
  -                                                   -
04-                                                   -04
  -                                                   -
02-                                                   -02
  -                                                   -
 MHZ+-+-+-+-+-+-+-+-+-+-+-+-+-+-+-+-+-+-+-+-+-+-+-+-+MHZ
   00  02  04  06  08  10  12  14  16  18  20  22  00
                 UNIVERSAL TIME
```

Table 5. ICEPAC Method 16 output.

```
   CCIR COEFFICIENTS          METHOD 16    ICEPAC  Version ITS.01   PAGE   1

JAN     1994             SSN =  62.      Qeff= 3.0
Cobbett Hill, UK    CRC, Ottawa, Canada   AZIMUTHS             N. MI.       KM
51.27 N      .63 E - 45.40 N   75.92 W    294.97   53.8[illegible]     2934.6   5434.4
MINIMUM ANGLE   3.00  DEGREES
XMTR  2-30 IONCAP     Const 10dB                Azim=295.0 OFFaz=360.0  10.000kW
RCVR  2-30 CCIR.000   CCIR  /ISOTROPE           Azim=    .0 OFFaz= 53.9
3 MHZ NOISE = -136.0 DBW      REQ. REL = .90     REQ. SNR = 44.0 DB
MULTIPATH POWER TOLERANCE = 10.0 DB   MULTIPATH DELAY TOLERANCE =   .850 MS

14.025.2  2.0  4.0  6.0  7.0  9.0 11.0 13.0 15.0 17.0 19.0 21.0 FREQ
 2F2  5 E  4 E  4 E  4F2  3F2  3F2  2F2  2F2  2F2  2F2  2F2 MODE
      5.6  5.0  3.2  3.7 19.4 13.2 11.1  4.8  4.0  4.0  4.1  4.3 ANGLE
     18.9 18.4 18.3 18.4 20.0 19.4 19.1 18.8 18.7 18.7 18.7 18.8 DELAY
      290   71   75   81  287  288  251  269  248  248  251  254 V HITE
      .50 1.00 1.00 1.00 1.00 1.00 1.00  .99  .98  .95  .90  .80 F DAYS
      162  291  241  214  177  161  153  147  144  143  144  146 LOSS
       13 -138  -82  -27  -10    8   17   25   28   29   29   28 DBU
     -122 -251 -201 -149 -134 -118 -111 -105 -103 -102 -104 -106 S DBW
     -162 -131 -139 -144 -146 -149 -152 -154 -155 -157 -158 -159 N DBW
       40 -120  -61   -5   12   31   41   49   53   54   55   53 SNR
       30  176  118   63   46   27   20   11   10   11   15   16 RPWRG
      .41  .00  .00  .00  .00  .07  .35  .66  .73  .73  .70  .68 REL
      .00  .00  .00  .00  .00  .00  .09  .00  .00  .00  .00  .00 MPROB

15.0 26.0  2.0  4.0  6.0  7.0  9.0 11.0 13.0 15.0 17.0 19.0 21.0 FREQ
      2F2  5 E  4 E  4 E  4F2  3F2  3F2  2F2  2F2  2F2  2F2  2F2 MODE
      5.7  5.0  3.2  3.9 18.3 11.9 10.9  4.0  4.0  4.0  4.1  4.3 ANGLE
     18.9 18.4 18.3 18.4 19.9 19.2 19.1 18.7 18.7 18.7 18.7 18.8 DELAY
      291   71   75   83  271  265  248  249  247  249  251  256 V HITE
      .50 1.00 1.00 1.00 1.00 1.00 1.00 1.00 1.00 1.00  .98  .94 F DAYS
      162  301  250  222  180  163  154  147  144  143  142  142 LOSS
       14 -147  -91  -30  -13    6   16   25   29   31   32   32 DBU
     -122 -261 -210 -153 -137 -120 -112 -104 -102 -101 -101 -102 S DBW
     -162 -131 -139 -144 -146 -149 -152 -154 -155 -157 -158 -159 N DBW
       40 -130  -71   -9    9   29   40   49   53   56   57   57 SNR
       29  183  124   62   44   24   14    5    1    0    0    5 RPWRG
      .42  .00  .00  .00  .00  .05  .32  .75  .87  .91  .89  .82 REL
      .00  .00  .00  .00  .00  .00  .08  .38  .51  .00  .00  .00 MPROB

16.0 24.6  2.0  4.0  6.0  7.0  9.0 11.0 13.0 15.0 17.0 19.0 21.0 FREQ
      2F2  5 E  4 E  4F2  3F2  3F2  2F2  2F2  2F2  2F2  2F2  2F2 MODE
      6.4  5.0  3.4 18.3 13.4 11.0  4.0  3.9  4.0  4.0  4.2  4.6 ANGLE
     19.0 18.4 18.3 19.9 19.4 19.1 18.7 18.7 18.7 18.7 18.8 18.8 DELAY
      309   71   77  271  292  249  248  245  248  248  254  263 V HITE
      .50 1.00 1.00 1.00 1.00 1.00 1.00 1.00 1.00  .99  .97  .88 F DAYS
      160  284  242  187  174  160  150  146  143  142  141  142 LOSS
       15 -130  -75  -22   -7    9   21   27   30   32   32   32 DBU
     -120 -243 -194 -144 -131 -117 -107 -103 -101 -100 -101 -102 S DBW
     -161 -131 -139 -144 -146 -149 -152 -154 -155 -157 -158 -159 N DBW
       41 -112  -55    0   15   32   44   51   55   57   58   57 SNR
       29  164  105   51   35   19    6    1   -3   -4   -2    5 RPWRG
      .44  .00  .00  .00  .00  .08  .52  .88  .96  .96  .94  .82 REL
      .00  .00  .00  .00  .00  .01  .21  .46  .51  .00  .00  .00 MPROB
```

Table 6. Estimated maximum ionospheric effects at 1GHz for elevation angles of about 30°; one-way traverse to a geostationary orbit.

Effect	Magnitude	Frequency dependence
Faraday rotation	108°	f^{-2}
Propagation delay	0.25 µs	f^{-2}
Refraction	<0.017 mrad	f^{-2}
Variation in direction of arrival	0.2 min of arc	f^{-2}
Polar Cap Absorption	0.04 dB	f^{-2}
Dispersion	0.4 ns/MHz	f^{-2}
Scintillation	-	f^{-3}

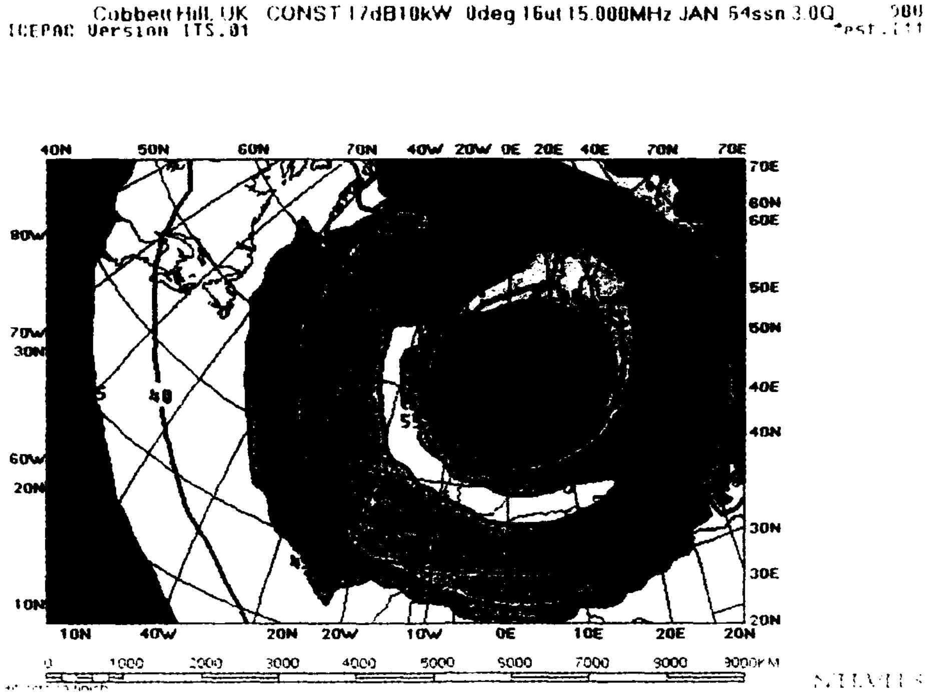

Figure 1. ICEPAC coverage area for a transmitter located in southern England for the specified operating conditions.

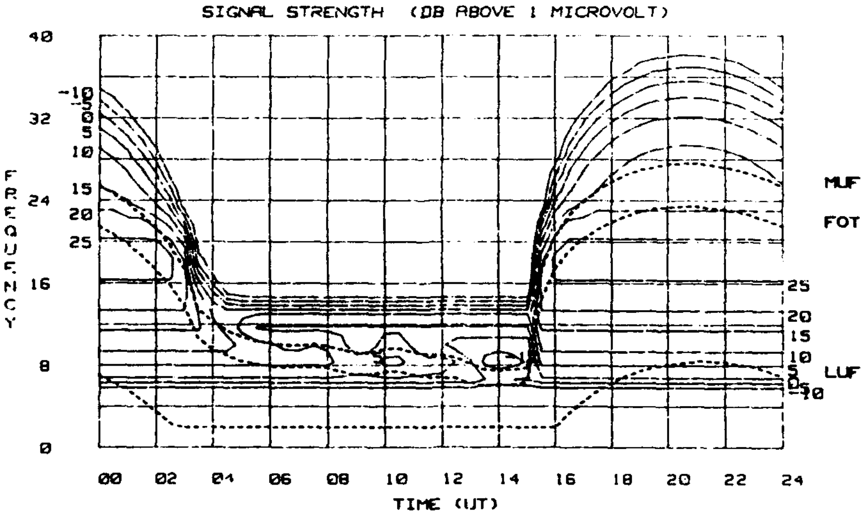

Figure 2. 24-hour PROPHET signal strength contours for the Honolulu to San Diego path.

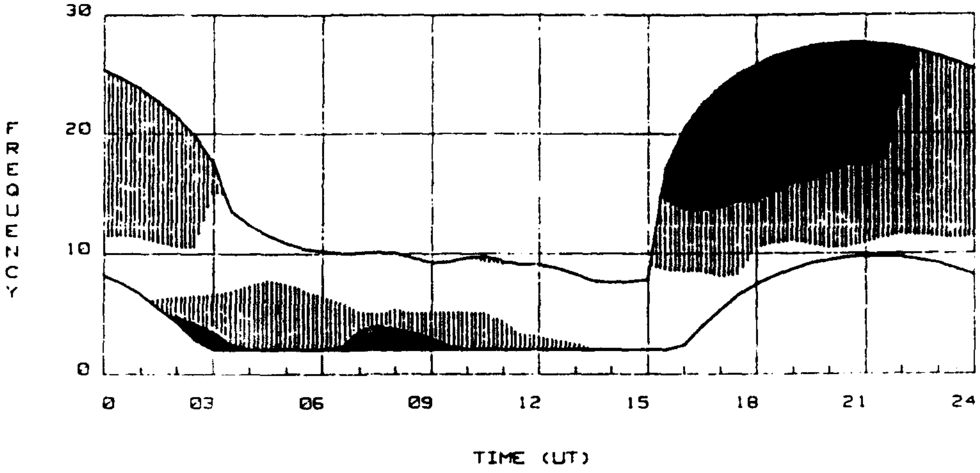

Figure 3, 24-hour secure communications display.

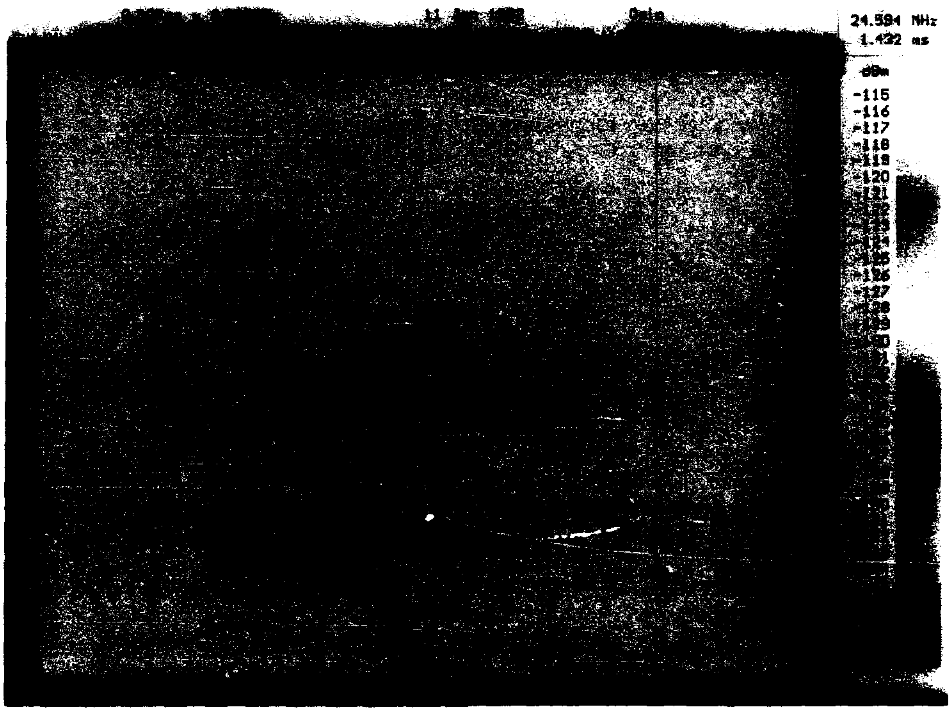

Figure 4. Monochrome ROSE ionogram for the path from Oslo, Norway to Southern England

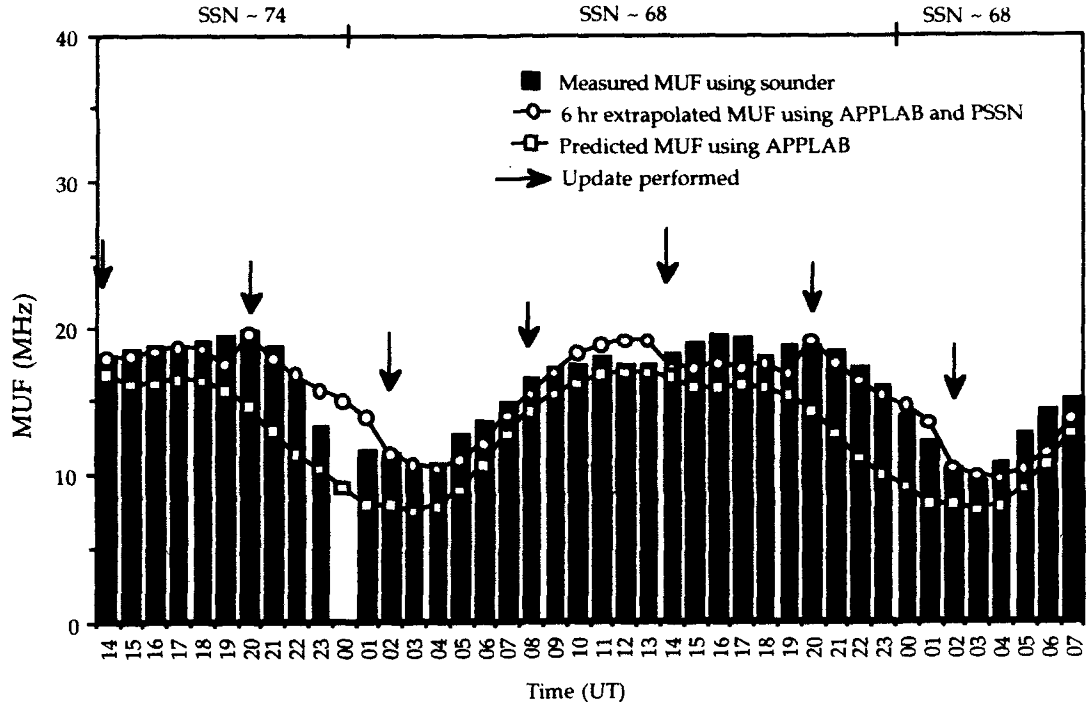

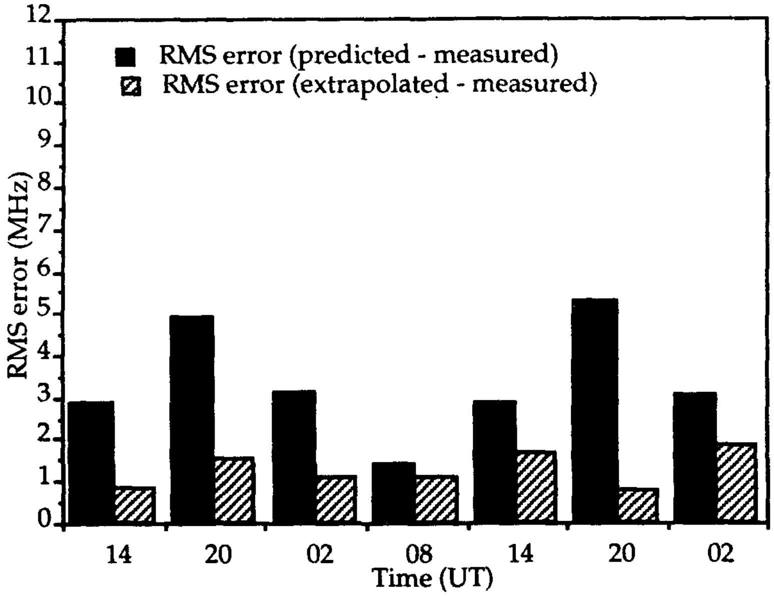

Figure 5. The application of pseudo sunspot numbers to update ionospheric predictions. Top panel; measured predicted and extrapolated values. Bottom panel; RMS errors.

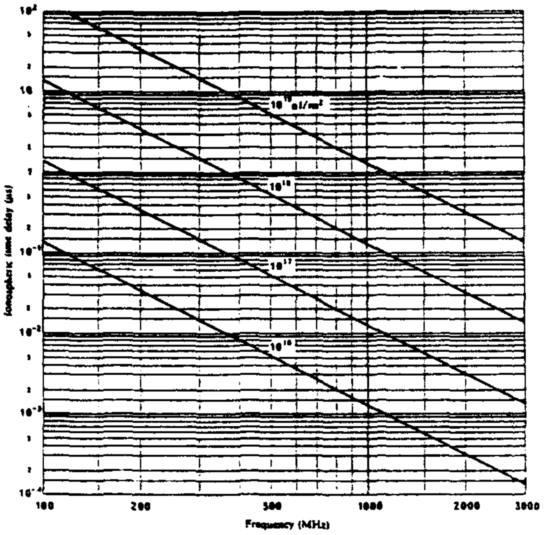

Figure 6. Ionospheric time delay versus frequency for various values of electron content.

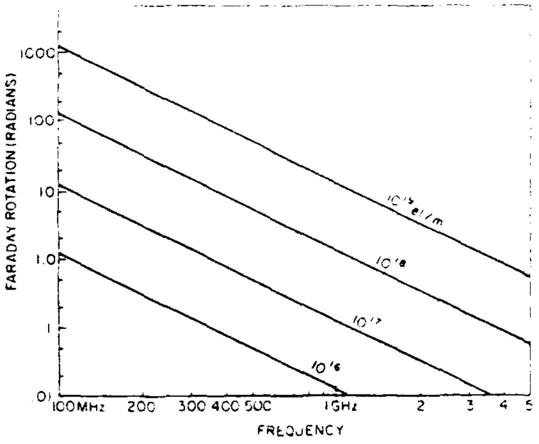

Figure 7. Faraday rotation versus frequency for various values of TEC.

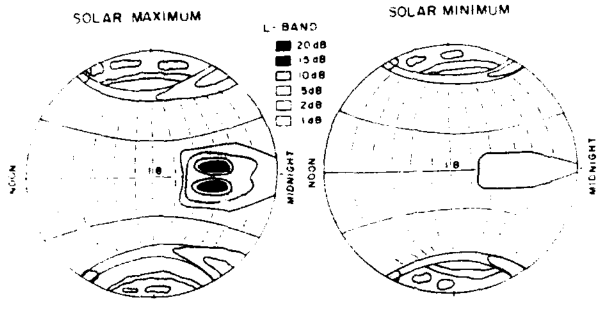

Figure 8. Global picture of scintillation morphology for L-Band (1.6 GHz) signals (after *Basu et al.* 1988)

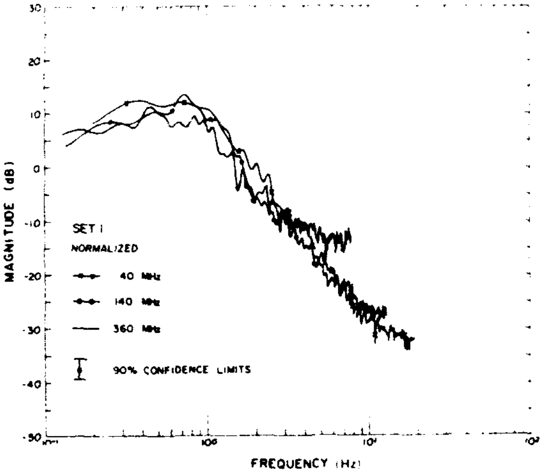

Figure 9. Power spectrum of ATS-6 signals at Boulder

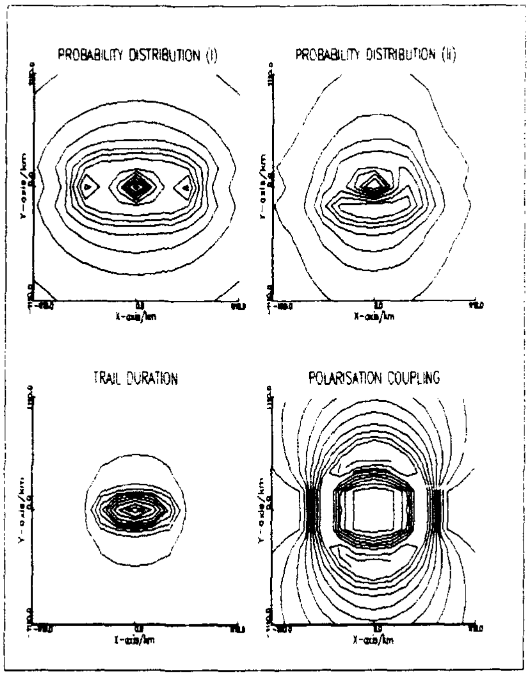

Figure 10a Typical graphical output from the computer model in the form of contour plots. The panels illustrate the behaviour of an equatorial link running East-West at 0600 hours local time.

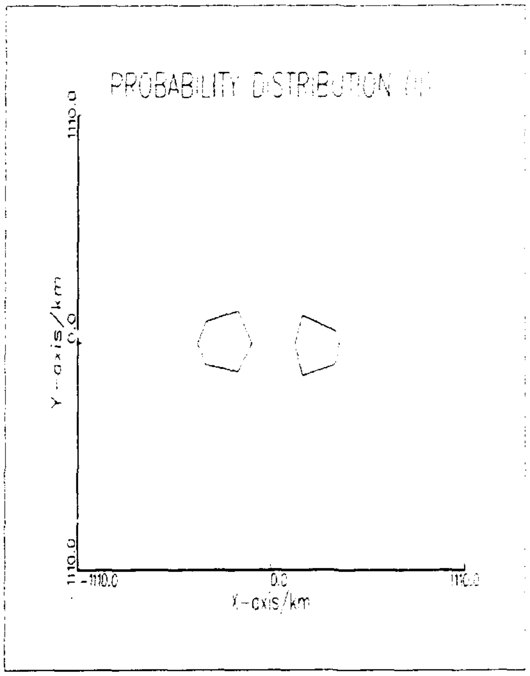

Figure 10c Plot of the probability of meteor scatter at 1800 LT for the equatorial East-West link.

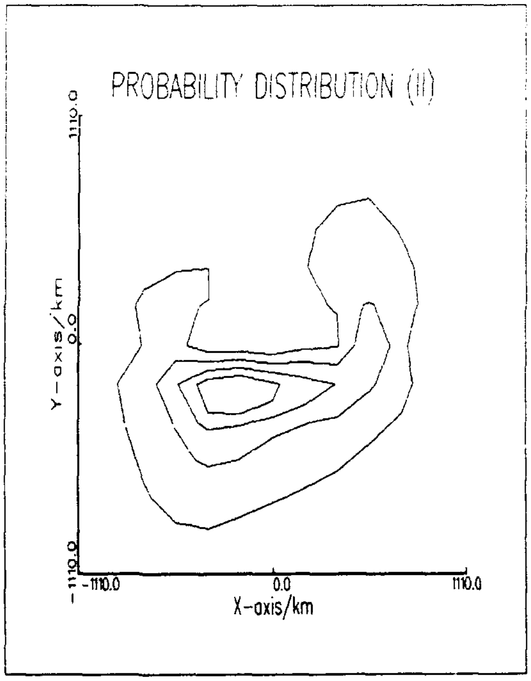

Figure 10b Plot of the probability of meteor scatter at 1200 LT for the equatorial East-West link.

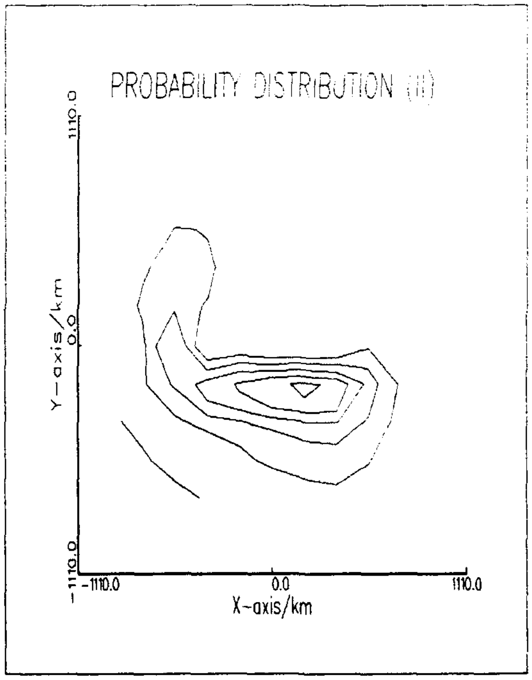

Figure 10d Plot of the probability of meteor scatter at 0000 LT for the equatorial East-West link.

Ground Wave and Diffraction (A)

J.H. Whitteker
Communications Research Centre
3701 Carling Ave.
Ottawa, Canada K2H 8S2

SUMMARY

The two lectures on ground wave and diffraction review the effect of the ground and of trees and buildings on the propagation of radio waves. The first lecture (A), concentrates on the physical models and basic mathematical methods used to describe ground-wave propagation and terrain diffraction. The discussion progresses from methods appropriate to smooth and uniform terrain, to those appropriate to irregular terrain surmounted with trees and buildings. At the same time, the radio frequencies of interest tend to progress from HF and below to higher frequencies. The second lecture (B) describes a range of tools, most but not all of them computer-based, that can be used to plan systems that are affected by these phenomena. These planning tools range from simple equations and graphs to computer programs that do intensive calculations based on detailed terrain data. They may be empirical or theoretical, or a mixture.

1.0 INTRODUCTION

The subject of this lecture is the attenuation of a radio signal resulting from its interaction with the ground (and in some cases with objects on the ground). There is no sharp division between the terms 'ground wave' and 'terrain diffraction', but the term 'ground wave' is usually used at HF and below, particularly for ranges short enough that the earth can be considered flat, and 'diffraction' is usually used for a curved earth and at VHF and above. At the lower frequencies, the electrical characteristics of the ground are very important and the height variations less so, while at the higher frequencies, the opposite is true. At the lower frequencies, the wave is usually vertically polarized, since antennas are close to the ground in terms of wavelengths, and a horizontally polarized wave tends to be shorted out by the conductivity of the earth. At the higher frequencies, both polarizations are used, and at the highest frequencies, it makes little difference which is used.

A previous AGARD lecture on this subject was given by Palmer (1982). King and Page (1973) give an earlier review of diffraction. A monograph by Meeks (1982) includes some material on diffraction, and an extensive bibliography up to that date. A text by Boithias (1987) covers some basics of ground wave and diffraction. A recent AGARDograph (Richter, 1990) includes material on ground wave and diffraction, as does CCIR Recommendation 526-1 (1990).

Figure 1 illustrates the diffraction of waves over a somewhat simplified hill. The diagram shows the wave fronts, and perpendicular to them, the wave normals, which indicate the local direction of propagation. The amplitude of the field is indicated by the density of the wave normals. The calculation used to plot the diagram was done by one of the methods to be discussed later, under the assumption that the ground is perfectly conducting. Here, it is intended only to illustrate how waves can diffract over a hill.

2.0 BASIC IDEAS AND CONVENTIONS

2.1 Phase

Phase can be assumed to increase with time and decrease with distance along the wave normal, giving a field variation of exp $i(\omega t - kx)$ or to decrease with time and increase with distance giving exp $i(kx - \omega t)$. Here, $\omega = 2\pi f$, where f is frequency, and $k = 2\pi/\lambda$, where λ is wavelength. An author may use either convention, and usually says which is being used, but not always, and it may not be immediately obvious which is in use, since the exp $\pm i\omega t$ factor is usually suppressed. Which convention is used makes no difference to any physical result, pro-

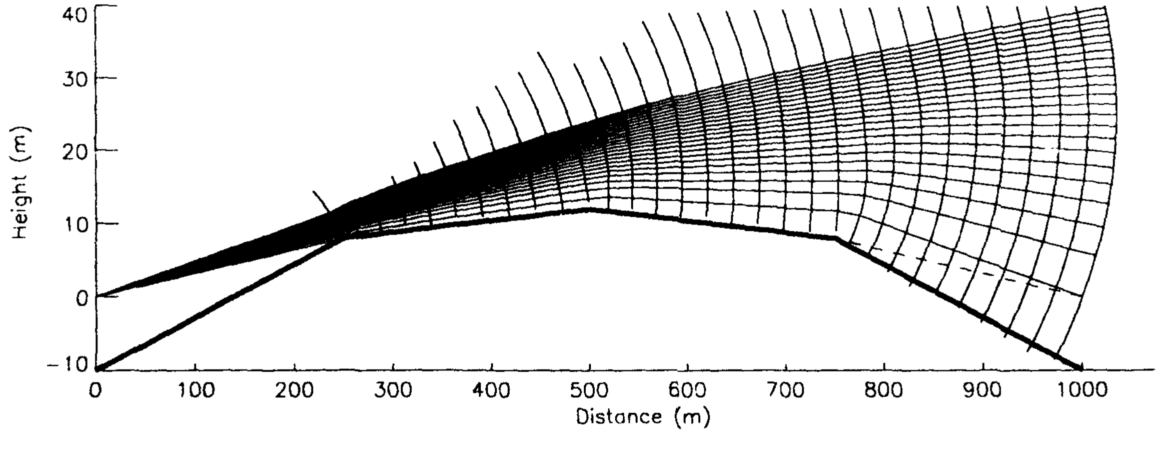

Figure 1. Wave front and wave normals for a 50-MHz wave diffracting over a hill constructed of perfectly reflecting planes.

vided one is used consistently, but any quantity calculated with one convention will be the complex conjugate of that calculated with the other. The first convention seems to be more common in recent years, and that is what is used here. The quantity $\sqrt{-1}$ can be denoted by either i or j. Neither choice is likely to cause confusion.

2.2 Reciprocity

The reciprocity theorem states that the transmission loss when A is transmitting to B is the same as when B is transmitting to A. There are exceptions, but only in ionized media permeated by a steady magnetic field (Monteath, 1973, p.137). For our purposes, the theorem can be regarded as absolute. However, the theorem does not allow us to interchange antennas, although it would usually make little difference, and certainly does not allow us to interchange antenna towers. A particular consequence of reciprocity is that for radar, at least when the transmitter and receiver are in the same place, the path loss to the target is the same as the path loss on the return trip.

2.3 Transmission loss and field intensity

According to CCIR Recommendation 341-2 (1990), the basic transmission loss of a radio link is the transmission loss that would occur if the antennas were replaced by (hypothetical) isotropic antennas with the same polarization as the real antennas, and that convention will be followed here. (Sometimes dipole antennas are used as a standard.) If we take it as given that the effective capture area of an isotropic antenna is $\lambda^2/4\pi = \pi/k^2$ (Jull, 1981, p.44), it is easy to find the free-space loss. Since the area of the sphere with radius r is $4\pi r^2$, the fraction of radiated power that is captured is $1/(4k^2r^2)$. That is, the ratio of power transmitted to power received for isotropic antennas in free space is

$$\frac{P_t}{P_r} = (2kr)^2 \qquad (1)$$

This is one version of the well-known inverse square law of radiation. The relationship between received power and r.m.s. electric field E is determined by the fact that the power density (power per unit area) of radiation in free space is E^2/Z_0, where $Z_0 = \sqrt{\mu_0/\varepsilon_0}$ is the impedance of free space, often approximated as 120π ohms. (The exact value is $4\pi 10^{-7} \times 299792458$, where the 9-digit number is the speed of light in a vacuum.) The received power is found by multiplying the power density by the effective capture area. For an isotropic receiving antenna, it is

$$P_r = \frac{\pi}{k^2 Z_0} E^2 \qquad (2)$$

2.4 Atmospheric effects

Atmospheric effects are dealt with in another lecture in this series. Usually, for the purposes of studying ground wave and diffraction, the atmosphere is ignored, except for one simple artifice: If it is assumed that the rate of change of the refractive index of the air with height, dn/dz, is constant, then we may pretend that there is a vacuum above the earth, and that instead of its true radius a, the earth has a modified radius Ka, where

$$\frac{1}{Ka} = \frac{1}{a} + \frac{dn}{dz} \qquad (3)$$

The real atmosphere varies with time and location, but for diffraction purposes, the value $K = 4/3$ is usually adopted, commonly called a '4/3 earth'.

3.0 INTERACTION WITH SMOOTH GROUND

3.1 Plane-wave reflection

Consider a plane wave incident on flat ground (Figure 2).

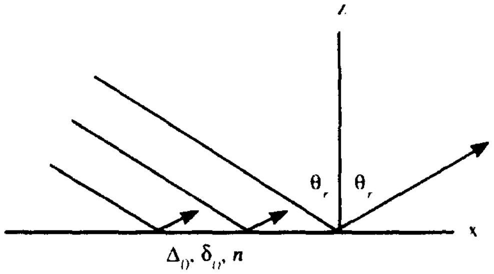

Figure 2. A plane wave incident on a horizontal reflecting surface.

The angle of incidence and of reflection is θ_r. In the notation of Maclean and Wu (1993, p.106), the reflection coefficient is

$$R_v = \frac{\cos\theta_r - \Delta_0}{\cos\theta_r + \Delta_0} \qquad (4)$$

for vertical polarization, and

$$R_h = \frac{\cos\theta_r - \delta_0}{\cos\theta_r + \delta_0} \qquad (5)$$

for horizontal polarization, where

$$\Delta_0 = \frac{1}{n^2}\sqrt{n^2 - \sin^2\theta_r} \qquad (6)$$

and

$$\delta_0 = \sqrt{n^2 - \sin^2\theta_r} \qquad (7)$$

where n is the complex refractive index of the ground, defined by

$$n = \sqrt{\frac{\varepsilon}{\varepsilon_0} - \frac{iZ_0\sigma}{k}} = \frac{Z_0}{Z} \qquad (8)$$

where ε and ε_0 are the permittivities of the ground and of free space, σ is the conductivity of the ground, and Z and Z_0 are the impedances of the ground and of free space. Usually, the magnitude of the refractive index of the ground is much greater than unity, so that $\Delta_0 \approx 1/n$ and $\delta_0 \approx n$. Because of their relationship to impedances, the quantities Δ_0 and δ_0 are known (Maclean and Wu, p.23) respectively as the normalized surface impedance and normalized surface admittance.

3.2 Leontovich Boundary condition

Now, given a reflection coefficient R, the field E above the ground due to the postulated incident and reflected plane wave is given by

$$\frac{E}{|E_0|} = e^{ikz\cos\theta_r} + Re^{-ikz\cos\theta_r} \qquad (9)$$

where $|E_0|$ is a constant and z is the vertical coordinate, as indicated in Figure 2. By differentiating, it is easy to discover that at the surface, where $z = 0$,

$$\frac{1}{E}\frac{\partial E}{\partial z} = ik\Delta_0 \qquad (10)$$

for vertical polarization, and

$$\frac{1}{E}\frac{\partial E}{\partial z} = ik\delta_0 \qquad (11)$$

for horizontal polarization. All the foregoing refers to plane waves and a flat earth.

An important generalization known as the Leontovich boundary condition states that equations (10) and (11) hold for any wave and any surface ($\cos\theta_r$ is set to unity). This condition is not exact, but for an earth that has a large refractive index, and is not too rough, it is a very good approximation. It is (or can be) used in the derivation of most of the ground-wave results that follow.

3.3 Flat earth - simple solution

An object does not have to block the line of sight to be an obstacle to radio propagation. The flat earth can be considered an obstacle, particularly if the antennas are low or the wavelength is great, and it will serve as our first path-loss calculation. First a little geometry: consider Figure 3.

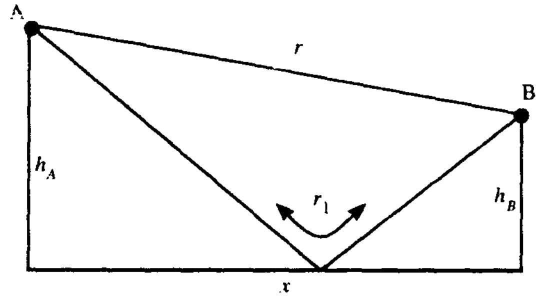

Figure 3. Antennas at A and B, separated by horizontal distance x, on towers of heights h_A and h_B on a plane earth.

We want to know the difference in length between the direct path AB and the reflected path. The direct path length is $[x^2 + (h_A - h_B)^2]^{1/2}$. The reflected path length is the same as if the path came from the image of A or went to the image of B. That is, it may be found by negating h_A or h_B, and is $[x^2 + (h_A + h_B)^2]^{1/2}$. In terrestrial propagation problems, the antenna heights can almost always be assumed to be much smaller than the path length. Therefore the reflected path is approximately $x + (h_A + h_B)^2/2x$, and similarly for the direct path, and the difference between them is

$$r_1 - r \approx \frac{2h_Ah_B}{x} \approx \frac{2h_Ah_B}{r} \qquad (12)$$

This is a useful formula to remember when ground reflections are considered. If the antennas are not too low, and the wavelength not too great, the propagation from A to B can be described in terms of rays following the two paths just discussed. If the propagation constant is $k = 2\pi/\lambda$, the field at B due to a unit source at A is given by

$$E = \frac{e^{-ikr}}{r} + R\frac{e^{-ikr_1}}{r_1} \qquad (13)$$

where R is the reflection coefficient. For most terrestrial paths we can put $r_1 \approx r$ in the denominator of the last term (but not in the exponent, since kr is a large number). This leads to

$$E \approx \frac{e^{-ikr}}{r}\left[1 + R\cos k(r_1 - r) - iR\sin k(r_1 - r)\right] \qquad (14)$$

where we can use equation (12) for $r_1 - r$. If we let r increase, and let R approach the value -1 (which it will do for grazing incidence), we find that the quantity in square brackets approaches $i2kh_Ah_B/r$. The power that would be received in free space given in eqn. (1), is reduced by the magnitude of this quantity squared, which means that the ratio of power transmitted to power received is, for isotropic antennas over a plane earth at sufficiently great distances,

$$\frac{P_t}{P_e} = \left(\frac{r^2}{h_Ah_B}\right)^2 \qquad (15)$$

This is equation (9) of Bullington (1977), which exhibits an often-quoted power dependence of $1/r^4$. The formula is remarkably simple; the path loss depends only on the path length and the antenna heights, not on frequency. Its validity depends on a number of assumptions, as we have just seen. Particularly at microwave frequencies, real terrain may be often too rough for the reflection coefficient to become close to -1. The variation of field amplitude with distance according to eqn. (14) is illustrated in Figure 4.

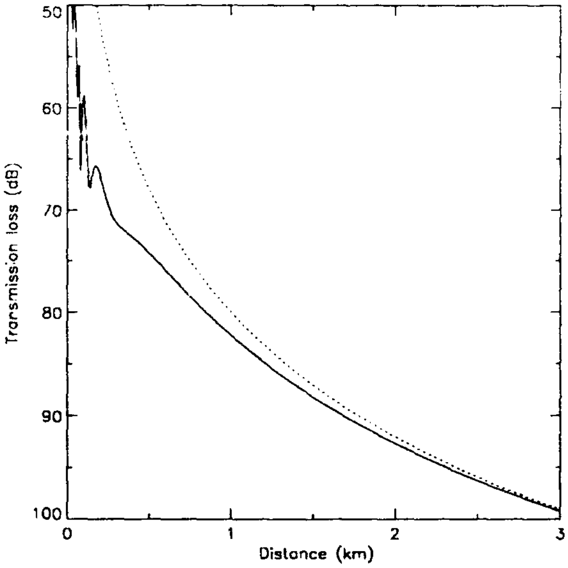

Figure 4. Path loss at 300 MHz as a function of distance over a plane earth with relative permittivity 30, conductivity 0.04 siemens/m, and antenna heights 50 m and 2 m. The solid line is from eqn. (14), while the dotted line is the inverse fourth power curve of eqn. (15).

3.4 Flat earth - rigorous solution

This is not the end of the flat earth problem. Suppose one or both of the antennas is close to the ground or even on the ground, as is usually the case at the longer wavelengths. This is the famous Sommerfeld problem. For $\sin\theta_r \approx 1$, the solution may be written in the following form (Maclean and Wu, 1993, p. 105; Wait, 1964):

$$E = \frac{e^{-ikr}}{r} + R\frac{e^{-ikr_1}}{r_1} + (1-R)F(w)\frac{e^{-ikr_1}}{r_1} \qquad (16)$$

That is, it is the simple approximate solution given above with an added term. The two original terms constitute what is often called the space wave, while the third one is usually called the Norton surface wave. It is important only close to the surface because the field due to the space wave is small there. The function F is defined in detail elsewhere (Maclean and Wu, 1993, p.106), but when its argument w is large, it has the simple form $F \approx -1/(2w)$. The dimensionless quantity w, known as the numerical distance, is proportional to the number of wavelengths in distance r_1, modified by certain factors, i.e.

$$w = -\frac{ikr_1}{2\sin^2\theta_r}(\cos\theta_r + \Delta_0)^2 \qquad (17)$$

for vertical polarization. For horizontal polarization, Δ_0 is replaced by δ_0. Usually, $\sin^2\theta_r \approx 1$ and $\cos\theta_r$ is small, so that the factors multiplying r_1 depend mostly on the electrical constants of the earth.

In contrast to the highly simplified result expressed by equation (15), the field predicted by (14) or by (16) does not continue to decrease to zero as the ground is approached, but is roughly constant from the ground up to some height. In mathematical form, if the transmitting antenna is not too high, the field close to the ground for vertical polarization is (Maclean and Wu, 1993, p.104)

$$E = E_g(1 + ik\Delta_0 z) \qquad (18)$$

where E_g is the field on the ground. This may be obtained directly from the Leontovich boundary condition, eqn. (10). Because the second term on the right side is mostly imaginary, this means that the magnitude of E does not vary much up to a height of about $h_1 = 1/|k\Delta_0|$ for vertical polarization, sometimes called the minimum effective antenna height. For horizontal polarization, the corresponding height is $h_1 = 1/|k\delta_0|$.

When must you use the Sommerfeld result and when is the simple one of equation (14) adequate? This can be answered by comparing the magnitude of the surface wave with the magnitude of the space wave. From equations (4), (16), and (17) and using $F \approx -1/(2w)$, we can find, approximately, for small values of $\cos\theta_r$, that the ratio of the amplitude of the space wave to that of the surface wave is

$$\frac{h_A h_B}{h_1^2} - i\frac{h_A + h_B}{h_1} \qquad (19)$$

The simple theory will be sufficient if the absolute value of this ratio is somewhat larger than unity. This will be so if either antenna height is much greater than h_1. Figure 5 is a plot of the heights h_1 as a function of frequency for various types of ground. The variation of field amplitude with height is illustrated in Figures 6 and 7. In these examples, the parameters are identical except for the electrical constants of the earth. There are some obvious differences in the results: The characteristic height h_1 is about 10 m in one case and 100 m in the other. Close to the surface, the field is much greater over sea than over land. The simple theory (eqn. 14) is accurate over land at this frequency, but it is beginning to fail over seawater, where the very simple eqn. (15) becomes wildly inaccurate.

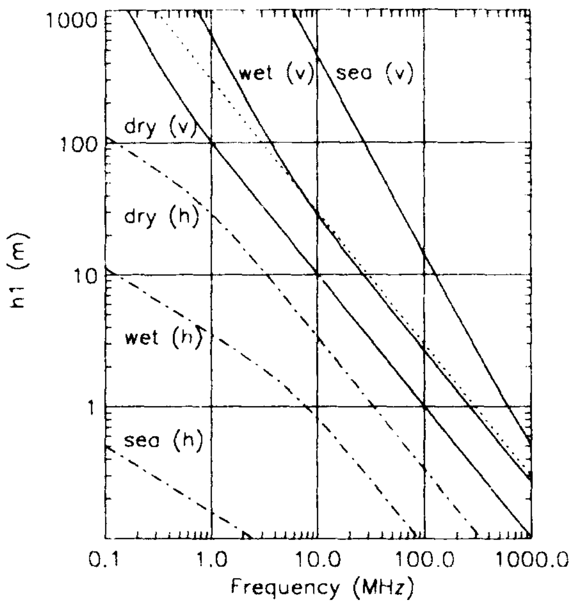

Figure 5. The 'minimum effective antenna height' h_1 for very dry and for wet earth, and for the sea, for vertical (v) and horizontal (h) polarization, using CCIR electrical constants for these types of ground. The dotted line indicates the wavelength at each frequency.

The conclusion to be drawn from Figures 5, 6, and 7 is that for horizontal polarization, the simple theory is valid under all conditions at VHF and UHF at least, whereas for vertical polarization, it may not be valid under all conditions, particularly for VHF and lower frequencies over sea water.

3.5 Spherical Earth

The next great problem in diffraction theory for radio transmission was propagation over a spherical earth. The problem was solved by use of the Watson transformation which results in the so-called residue series (the word 'residue' comes from the theory of complex variables). The solution for the magnitude of the field may be written as follows (Boithias, 1987, p.176; Bremmer, 1949, p. 75; Wait, 1964, p.178):

$$\frac{E}{2E_0} = (-2\pi iX)^{1/2}\sum_{n=1}^{\infty}\frac{f_n(h_A)f_n(h_B)e^{-i\tau_n X}}{2\tau_n - 1/\delta^2} \qquad (20)$$

where E_0 is the free-space field, X is a dimensionless quantity proportional to path length, and δ is another dimensionless quantity depending on the radius of the earth and the surface impedance of the ground. The numbers τ_n are fixed for each n. Each f_n is a height gain function. For reception points well beyond the horizon, the terms of the series decrease rapidly as a function of n, and at sufficiently great distances, only the first term is required. In that case, the equation shows that at a constant height, field strength decays almost exponentially with distance. The variation with height is described by Boithias: The field is approximately constant up to the characteristic

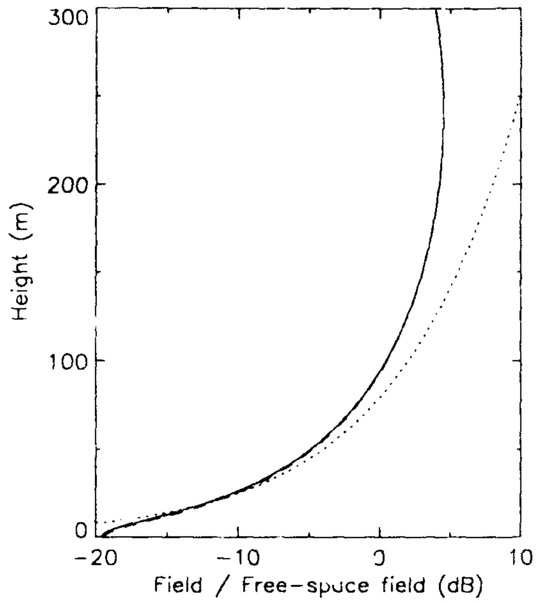

Figure 6. Field as a function of height over wet ground $\varepsilon_r = 30$, $\sigma = 0.01$, due to a 30 MHz transmitter, vertically polarized, 10 km away, with an antenna height of 100 m. The solid and broken curves (almost superimposed) represent respectively the rigorous and simple (eqn. 14) solutions, while the dotted curve represents the even simpler solution of eqn. (15).

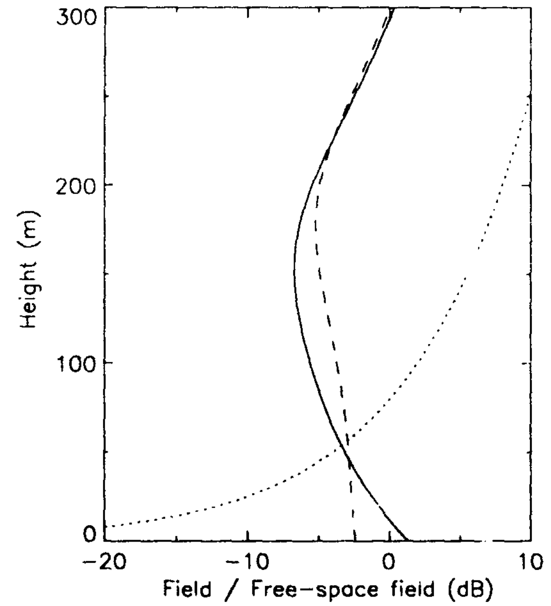

Figure 7. Field as a function of height over sea water $\varepsilon_r = 70$, $\sigma = 5.$, due to a 30 MHz transmitter, vertically polarized, 10 km away, with an antenna height of 100 m. The solid and broken curves represent respectively the rigorous and simple (eqn. 14) solutions, while the dotted curve represents the even simpler solution of eqn. (15).

height h_1 already mentioned, then increases linearly up to a second characteristic height h_2 that depends only on the earth's radius and the frequency. Above that, it increases exponentially. Of course, the field eventually stops increasing, as it approaches the free-space value, but by then it is no longer described by the first term of the residue series.

An example of field as a function of height is shown in Figure 8. At 100 MHz over sea water, $h_1 \approx 10$ m, and $h_2 \approx 100$ m. The region up to 10 m where the field does not change much is obvious, but the transition from a linear variation (6 dB for each doubling of height) to an exponential one (7 or 8 dB per doubling) is very gradual.

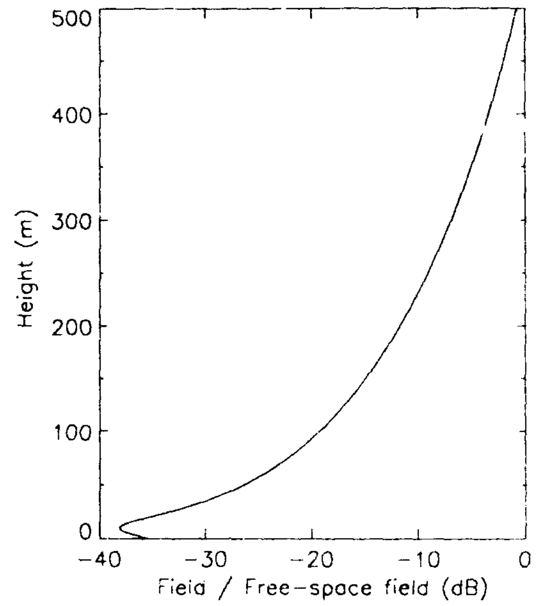

Figure 8. Field as a function of height over sea water $\varepsilon_r = 70$, $\sigma = 5.$, due to a 100 MHz transmitter, vertically polarized, 80 km away, with an antenna height of 100 m.

We have discussed the field at ranges short enough that the earth may be considered flat, and also in the deep shadow of a curved earth. There is an awkward region in between, where neither approach works very well. That is, the earth can no longer be considered flat, but on the other hand, the residue series converges very slowly. For this region, Bremmer (1958) and Hill and Wait (1980), give an extension of the flat earth theory in the form of two series in which the first term is the flat earth expression. Which series is used depends mainly on the ground impedance.

4.0 INHOMOGENEOUS AND IRREGULAR GROUND

The next step towards realism and complexity is to entertain the possibility that the earth may not be homogeneous and smooth. Inhomogeneities in electrical constants are relatively important at the lower frequencies, while the height and shape of obstacles are relatively important at VHF and UHF.

4.1 Rough ocean (or earth)

Suppose next that the surface is flat or spherical on a large scale, but rough or corrugated on a scale comparable with or smaller than a wavelength. Barrick (1971a,b) discusses this situation, and finds that the theory already discussed here can be employed, with the effect of the roughness being expressed as a modified surface impedance. The new surface impedance, applicable particularly to the ocean, depends on the height spectrum of the surface. A rough ocean can reduce the field strength considerably, as indicated in Figure 9 (Barrick, 1971b, p.532), although at 50 MHz a useful ground-wave signal does not go beyond a few hundred kilometres in any case. A physical picture of what happens is that wave energy is scattered upward by the irregularities, and is removed from the coherent wave close to the ground.

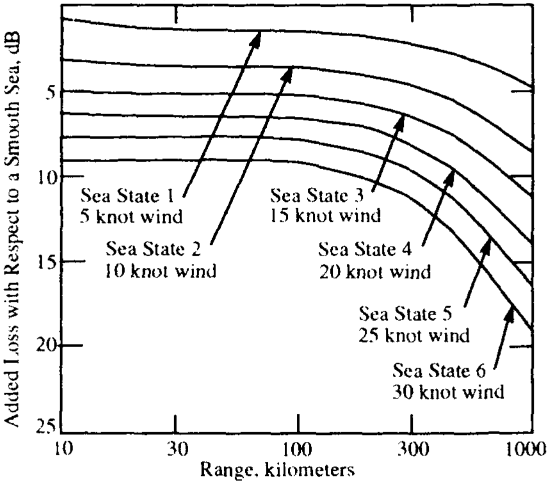

Figure 9. Added transmission loss due to sea state at 50 MHz. Figure 9 of Barrick (1971b).

4.2 Inhomogeneous ground

The surface may be smooth but with electrical parameters that vary along the path. At LF to HF, propagation (vertical polarization) is much better over sea than over land. Wait (1980) describes two methods for dealing with mixed paths. One is based on the compensation theorem. See section 4.4 below. The other method is mode-matching. The terms of the residue series already mentioned can be considered to be propagation modes, somewhat similar to modes in a waveguide. Suppose a path passes over land and then sea. There is a particular set of modes on the land part, and, one supposes, a different set of modes on the sea part. If backscatter is neglected, the modes on the first part are known, since they are not influenced by the second part. The modes on the second part are not known at first, but they can be found by making them consistent with the electrical constants of the second part and demanding that the fields as a function of height match at the boundary between the two parts of the path. It turns out that both approaches lead to exactly the same result.

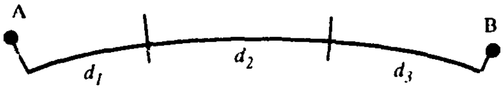

Figure 10. An inhomogeneous path. The electrical constants of the earth are different for the segments of lengths d_1, d_2, and d_3.

There is also a simple approximate method due to Millington (1949), and outlined in CCIR Report 717-3 (1990) that is widely used, and is considered accurate enough for most purposes. The idea is first to find the received field amplitude over the whole path, assuming it to be homogeneous with the electrical constants of the last segment. Then this value is corrected for the different electrical constants of the first part of the path by finding the difference between the fields found when the first part of the path is done with the correct constants, and when it is done with the constants of the last segment. If the first part of the path is itself mixed, the process continues in the same way. Then the same thing is done starting with the first segment, and the two results averaged, so that the result is reciprocal. If $E_n(d)$ is the field calculated for distance d using the ground constants of the n'th segment, the first field found is

$$E_R = E_1(d_1) - E_2(d_1) + E_2(d_1 + d_2) - E_3(d_1 + d_2) + E_3(d_1 + d_2 + d_3) \tag{21}$$

where the distances d_1, a_2, and d_3 are indicated in Figure 10. The corresponding field E_T is then found by interchanging the subscripts 1 and 3, and the final result is the average of E_T and E_R.

4.3 Irregular terrain - ground wave

Finally, suppose that the terrain along the propagation path varies in both electrical properties and in height. Much of the rest of this lecture will be devoted to this situation. How it is treated depends on the frequency in question. The discussion begins with methods appropriate to the lower frequencies, in which there are two main approaches: the compensation theorem (Maclean and Wu, 1993) and an integral equation for fields on the surface of the terrain (Ott, 1992).

4.4 Compensation theorem

The compensation theorem approach is related to the reciprocity theorem. It is assumed that the antennas at both ends of the transmission path are emitting. Begin with an unperturbed ground, say a plane surface with constant electrical characteristics, that is simple enough to allow the fields to be calculated in a straightforward way, as illustrated in Figure 11.

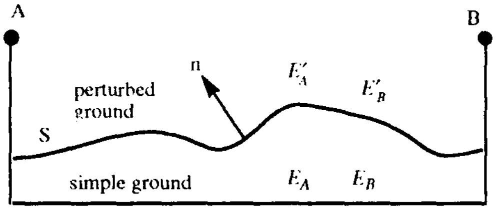

Figure 11. Compensation theorem, with simple and perturbed ground between antennas A and B.

For this unperturbed (simple) ground, the electric and magnetic fields on the ground due to antenna A are E_A and H_A respectively, and those due to antenna B are E_B and H_B. When the ground is perturbed (irregular), the corresponding (unknown) fields are E'_A and H'_A. If antenna B is a horizontal magnetic current element of strength $I_{mB}dl$ (equivalent to a vertical electric current element), then the compensation theorem (Maclean and Wu, p.168) states that

$$H'_A(B) = H_A(B) - \frac{1}{I_{mB}dl}\iint_S [H_B \cdot (n \times E'_A) - H'_A \cdot (n \times E_B)]\, dS \tag{22}$$

where the vector $\boldsymbol{n}$ is the unit vector normal to the ground, and integration is over the ground. The fields in this equation are to be regarded as vectors. In the integrand, electric and magnetic fields can be related to each other in terms of surface impedance. If the perturbed ground is not much different from the simple ground, then E'_A and H'_A can be replaced by their unprimed counterparts in the integral, and it will not make much difference to the answer. (This is the idea of a perturbation theory.) Otherwise, (eqn 22) becomes an integral equation that must be solved somehow, numerically in the general case.

4.5 Green's theorem

The other approach (Hufford, 1952; Ott, 1992) begins with Green's theorem, which relates the field on a closed mathematical surface to the field in the interior of the surface. Here, part of this surface coincides with the surface of the ground. The result is an integral equation. Hufford's version is the easier to understand. The basic equation involves an (electric or magnetic) field $\psi(B)$ at point B, and its value $\psi_0(B)$ in free space. The equation is

$$\psi(B) = 2\psi_0(B) - \frac{ik}{2\pi}\iint_S \psi(Q)\frac{e^{-ikr}}{r}\left(\Delta_0 + \frac{\partial r}{\partial n}\right)dS \quad (23)$$

where r is the distance QB, Δ_0 is the surface impedance defined in (6), and the integration is over the ground. The geometry is illustrated in Figure 12.

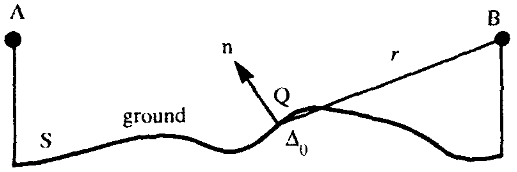

Figure 12. Irregular ground between antennas A and B, and the integral equation resulting from Green's theorem.

This equation is something like Huygens' principle (more on this later) in which each point on the ground radiates with an amplitude proportional to the field $\psi(Q)$, and the resulting wave arrives at B with a free-space propagation factor $\exp(-ikr)/r$. Before integration, the equation is made one-dimensional, and the effect of points beyond B (backscatter) is neglected. The field on the surface is not known initially, but eqn. (23) can be applied to points on the surface as well as to elevated points. Therefore the field at any point on the surface can be found in terms of the field along the path up to that point. It turns out that this equation is not easy to integrate numerically, except at very low frequencies. However, Ott and Berry (1970) replaced the free-space propagation factor with one resembling the solution to the Sommerfeld plane-earth problem. The resulting integral equation is similar to the one resulting from the compensation theorem. With it, they have been able to integrate the equation, in the most recent instance (Ott, 1992), for frequencies up to 100 MHz.

4.6 Furutsu

Furutsu (1982) has generalized the residue series approach for a curved earth to include paths on which the electrical constants and the elevation are different on several sections of the path, but uniform within a section. There may also be a narrow ridge, or knife edge, at the boundary between any two sections. The type of path profile is illustrated in Figure 13.

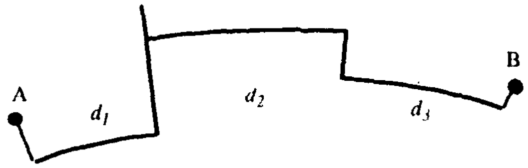

Figure 13. A path composed of homogeneous sections with discontinuities between the sections and a knife edge at one discontinuity.

The solution is expressed in terms of a multiple residue series, according to the number of terrain sections. The method of solution is an iterative one, and not all possible terms are kept, an approximation equivalent to a Kirchhoff approximation previously made by Wait (1968). The solution is a complex one, is based largely on rigorous theory, and it can be expected to be accurate provided the terrain can be reasonably modelled in the way required.

5.0 DIFFRACTION AT VHF AND HIGHER

5.1 Fresnel zones

The concepts and methods that tend to be used at VHF and higher are quite different from those used at the lower frequencies. The emphasis is less on a close interaction with the ground, and more on things simply being in the way.

A concept that is very often used is that of Fresnel zones. Consider the direct path (a straight line) from A to B, and consider also the path of a wave scattered by some terrain feature (the dotted path indicated in Figure 14). If the difference in the two path lengths happens to be exactly one half wavelength, then the terrain feature is at the edge of the first Fresnel zone. If the difference is one wavelength, it is at the edge of the second Fresnel zone, and so on in half-wavelength steps.

It is the first Fresnel zone that is of most interest. If the first Fresnel zone is not obstructed anywhere along the path, then the path may be considered to be a clear line-of-sight path. Sometimes the criterion 0.6 of the first-Fresnel-zone radius is used instead. This is because a wave passing over a knife edge with 0.6 Fresnel-zone clearance has about the same amplitude as an unobstructed wave. Using the full Fresnel-zone radius is a more conservative criterion. The first Fresnel zone is circular in cross section perpendicular to the line of sight, and its radius is given by

$$R_1 = \sqrt{\frac{\lambda d_A d_B}{d_A + d_B}} \quad (24)$$

where the distances d_A and d_B are indicated in Figure 14. Over the whole path, considered in three dimensions, the boundary of the first (or any other) Fresnel zone traces an ellipsoid, something like a very elongated balloon attached at the ends to the antennas, as illustrated in Figure 14.

A vertical cross section of a Fresnel ellipsoid is a circular Fresnel zone. On the other hand, a horizontal section is a very elongated ellipse. Therefore, when the interaction of the wave with the ground is considered, the area of ground that must be taken into account is of the order of R_1 in width transverse to the propagation path, but very much longer along the path, par-

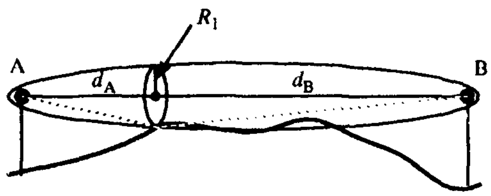

Figure 14. The first Fresnel ellipsoid between antennas A and B. A Fresnel zone has radius R_1. In this illustration, the terrain penetrates the ellipsoid only a little. The line AB need not be horizontal.

ticularly if the terrain is flat or gently curved. At the lower frequencies, it may cover almost all of the propagation path.

If obstacles penetrate into the first Fresnel zone, the attenuation depends on how much of it is blocked (and on the shape of the obstacle). The simplest example is a sharp transverse ridge (modelled as a knife edge) that blocks exactly half of the first Fresnel zone. In that case, the field amplitude is reduced by half, with a power loss of 6 dB. An obstruction that is broad in the direction of propagation would cause greater attenuation.

At VHF and higher frequencies, the simplest problem to consider is perhaps the same as at lower frequencies, namely the plane earth, but only the simple solution is used, since the wavelength is short, and the antennas are usually higher than the characteristic heights shown in Figure 2. The next simplest problem is the knife edge, discussed next.

5.2 Knife edge - physical optics

If the propagation path is obstructed by a single hill that is narrow in the direction of propagation, it can be idealized as a vertical screen with a straight-edge top. The screen does not have any particular electrical properties, but is supposed to simply absorb any radiation incident on it. This is the realm of physical optics. The wavelength is assumed to be much shorter than any part of the propagation path, if the propagation path is divided into parts by knife edges or other discrete objects. However, the wavelength is not so short that geometric optics applies. That is, we are still thinking in terms of waves, not rays. One of the basic ideas of physical optics is Huygens' principle. It states that the field at any point in space can be considered as a point source of radiation. More precisely, in the configuration indicated in Figure 15, the field E at any point B is given by (Beckmann and Spizzichino, 1987, p.181; Whitteker, 1990)

$$E(B) = \frac{ik}{4\pi}\iint_S (\cos\theta_1 + \cos\theta_2) E \frac{e^{-ikr}}{r} dS \qquad (25)$$

where the angles θ_1 and θ_2, the distance r, and the surface S of integration, are indicated in Figure 15.

In the integrand, E is the field at the Huygens point source, and the wave is modified by the factor $\exp(-ikr)/r$ on its way to B. Ordinarily, the horizontal distances are much longer than vertical ones, so the cosines can be set to unity. To solve the knife-edge problem in a simple way, we assume that the field E in the space above the knife edge is just the free-space field from the source, which is of the form $\exp(-iks)/s$, where s is the distance from the source.

The field relative to the free-space field E_0 is then

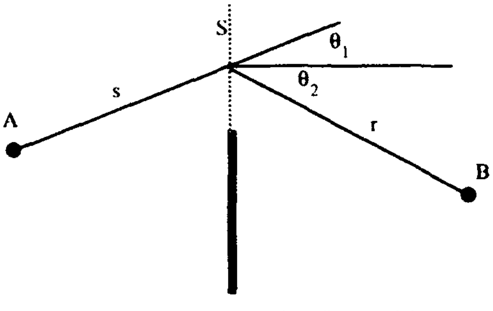

Figure 15. A knife edge (heavy black line) and the surface S above it over which E is integrated.

$$\frac{E}{E_0} = \sqrt{\frac{i}{\pi}} \int_{h/H}^{\infty} e^{-it^2} dt \qquad (26)$$

where the integral is one form of the well-known Fresnel integral, h is the height of the knife edge above a straight line between A and B, and H is a scale height

$$H = \sqrt{\frac{2d_1 d_2}{k(d_1 + d_2)}} = \frac{R_1}{\sqrt{\pi}} \qquad (27)$$

The variable of integration t is a dimensionless analog of the vertical coordinate in the surface S. A popular alternative form of (26) is

$$\frac{E}{E_0} = \sqrt{\frac{i}{2}} \int_{v}^{\infty} e^{i\frac{\pi}{2}t^2} dt \qquad (28)$$

where

$$v = h\sqrt{\frac{2(d_1 + d_2)}{\lambda d_1 d_2}} \qquad (29)$$

(CCIR Recommendation 526-1).

5.3 Round Hill

The solution to a single rounded hill is similar to that for the spherical earth, already considered. The residue series may be used for points deep in the shadow, but numerical integration of a complex integral representation of the field may be used for points where the residue series converges slowly (Vogler, 1985). It is not necessary to do a new calculation for every possible combination of frequency, soil type, and radius and height of hill. These quantities can be combined into three dimensionless parameters, relating mainly to the frequency and ground constants, height of the hill, and radius of the hill, and calculated once and for all. Plots (Vogler, 1985) have been made of these results. If the terrain consists of only one regularly-shaped rounded obstacle, then these curves provide a good prediction of path loss. Formulas that represent approximately attenuation over a single hill, applicable also to the spherical earth, except in the case of vertical polarization over seawater, are given in CCIR Recommendation 526-1 (1990).

5.4 Multiple Knife Edges

If terrain is rugged enough, it can be modelled as several knife edges. Even though a single knife edge leads to an easy result, several do not, at least in general. The integration of eqn. (25)

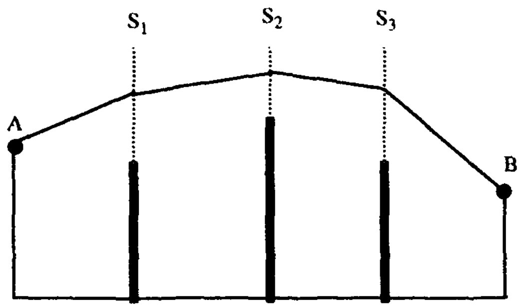

Figure 16. Three knife edges ($N = 3$) between antennas A and B. The field is integrated over the vertical surfaces indicated by dotted lines using eqn. (25). The thin segmented line connects one of many sets of integration points.

must be performed successively on surfaces S_1, S_2, S_3..., as indicated in Figure 16. Millington *et al.* (1962) worked out the attenuation due to two knife edges as a two-dimensional Fresnel integral. The formulation is fairly easy to program into a computer. It is based on exactly the same physical-optics scheme that was just outlined for a single knife edge.

For N knife edges, Vogler (1982) worked out how to evaluate the required multiple integral by expanding part of the exponent of the integrand as a power series. The series is somewhat complicated, and the time required to compute it rises very rapidly as a function of the number of knife edges, but it very nicely breaks through the N=2 barrier. The series does not converge everywhere, but the problems for which it does not converge can be transformed into problems in which it does (more on this later).

In the very special case in which the knife edges are all the same height and evenly spaced, the multiple integral for N knife edges has been worked out analytically for a few antenna positions. In a particularly simple case, where both antennas are in line with the knife edges, and separated from them by the knife-edge spacing, the field relative to the free-space field is $1/(N+1)$. Xia and Bertoni (1992) have exploited these solutions to model buildings as knife edges (see Part B of this lecture).

5.5 Heuristic schemes

There are also approximate methods of estimating the attenuation due to several knife edges that are based only partly on theory. These are much less computationally intensive than the methods just mentioned, but they are also less accurate. The best-known are those due to Epstein and Peterson (1953) and to Deygout (1966). In both schemes, a string is stretched over terrain between the antennas, and each point that supports the string is modelled as a knife edge. In the Epstein-Peterson scheme, for each knife edge, a single-knife-edge attenuation is found, for transmission between the preceding knife edge and the following one. These attenuations (in decibels) are then added. In the Deygout scheme, one knife edge is chosen as the dominant one, and the attenuation is found for this knife edge as if it were the only one between the antennas. Then attenuations are found between the dominant knife edge and the antennas on either side, and added. If many of these subdivisions are made, the calculated path loss becomes much too large. Usually only three obstacles are considered. However, Deygout (1991) has introduced an expression for correcting the calculated loss when obstacles of similar importance are close to each other, and suggests that with its use seven obstacles may be considered. Meeks (1983) introduced a modification of the Deygout method that allows two knife edges below the line of sight to be considered.

Pogorzelski (1982) analyzed these methods in terms of more rigorous types of calculation. His conclusion was that the Epstein-Peterson path-loss predictions tended to be too low, while the Deygout predictions tended to be high. He speculated that the Deygout scheme might be more accurate on average, because the tendency of the knife-edge representation to underestimate path loss would tend to cancel the overestimation of the method itself. Of course, in implementing either scheme, empirical corrections can be introduced. There are other schemes, reported by Hacking (1966) and by Gionavelli (1984), that are somewhat similar to the Epstein-Peterson, but a bit more complex, and which are designed to be similar in effect to the geometric theory of diffraction (see Section 5.9).

5.6 Multiple Round Hills

A natural step beyond modelling terrain as a series of knife edges is to model it as a series of cylindrical hills. This ia a generalization of the multiple-knife-edge model, since as the radius of a hill tends to zero, the solution approaches that of the knife-edge problem. An early model of this sort was by de Assis (1971), who simply used the Deygout construction, using the known attenuation for a hill of given radius in place of the knife-edge attenuation. It was an intuitive approach, grafted on top of the already intuitive approach of the Deygout construction. It allows a better representation of rolling terrain than a knife-edge construction, but the predicted losses become excessive if more than about three obstacles are considered, or if there is more than one with a large radius of curvature.

A more recent model (Sharples and Mehler, 1989) puts cascaded cylinders on a better theoretical basis. It combines the multiple knife edge calculation of Vogler (1982) with the cylinder diffraction results of Wait and Conda (1959) for near-grazing incidence. The combination is based on the observation that the Wait and Conda solution is composed of the knife-edge field plus a field that seems to come from a line source at or near the crest of the obstruction. The knife-edge part can be calculated by Vogler's method, and the line source on each hill crest can be treated as the transmitter in a new problem of the same type as the original one. If a cylinder is in the deep shadow region of the preceding one, then the residue series is used instead of the Wait and Conda result, in which case the calculation at that point is in the style of the geometric theory of diffraction.

5.7 Knife Edges with Reflecting Surfaces

By adding image theory to physical optics, methods developed for knife edges may be extended to solid terrain. The idea is to bridge over adjacent knife edges with a plane reflecting surface, as illustrated in Figure 17. Huygens' principle, originally applied to the aperture (dotted line) above each knife edge, can now be applied also to the image of this aperture. In this way, much of the theory and methods developed for knife edges can be applied also to solid terrain, modelled as a series of reflecting planes. For each reflecting plane, the theory already developed for a flat earth applies. That is, in eqn. (25), the free-space propagation factor is replaced by the expression in eqn. (13) to give, for one step between A and B:

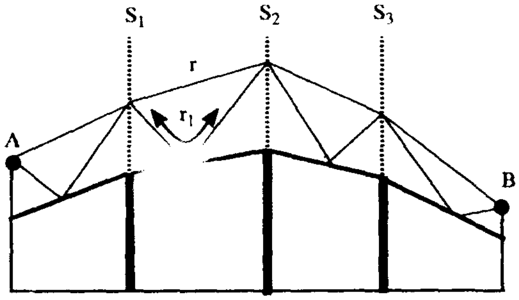

Figure 17. Three knife edges ($N = 3$) between antennas A and B, bridged over with reflecting surfaces representing the ground. The thin lines above the ground connect one of many sets of integration points by way of both direct and reflected paths.

$$E(S_2) = \frac{ik}{4\pi}\iint\limits_{S_1} E(S_1)\left[\frac{e^{-ikr}}{r} + R\frac{e^{-ikr_1}}{r_1}\right] dS_1 \tag{30}$$

That is, progressing from aperture S_1 to aperture S_2 involves the same sort of integration as for knife edges, except now there is an extra term (for the reflected path) to integrate. Using images in this way is convenient, because it avoids integrating over the surface itself, although it is less accurate than the Leontovich boundary condition if the surface is not highly reflecting. If the surfaces are considered to be imperfectly reflecting, a varying coefficient of reflection is involved, and the problem must be solved by numerical integration (Whitteker, 1990).

If the surfaces are perfectly reflecting, however, image theory is exact, and the analogy between knife edges and bridged knife edges becomes very strong. Then the knife-edge methods of Millington *et al.* (1962) and of Vogler (1982) can be used. Using bridged knife edges results in a series solution of the problem (Whitteker, 1993) that is no more difficult to compute than the multiple knife edge problem itself.

5.8 Parabolic Equations

The parabolic equation for wave propagation is a simplification of the general wave equation that takes advantage of the fact that the wavelength is much smaller than the horizontal distance between changes in terrain along the propagation path. In its general form, it can be used to calculate the progress of a wave through a medium of varying refractive index, and is the only method for modelling an irregular atmosphere and irregular terrain at the same time. This more general description is left to the lecture on refractive effects. The discussion here is limited to terrain diffraction calculations.

The wave function ψ (the waves could be acoustic or electromagnetic) is written in the form $\psi = e^{-ikx}u(x, y, z)$, where k is the propagation constant and the propagation is predominantly in the x direction. Substitution of this form in the time-independent wave equation $\nabla^2\psi + k^2\psi = 0$ leads to

$$\nabla^2 u - 2ik\frac{\partial u}{\partial x} = 0 \tag{31}$$

The approximation that is now made is to neglect $\partial^2 u/\partial x^2$ in comparison with $k\partial u/\partial x$. The assumption is that, apart from the e^{-ikx} variation, the wave does not change much in distance $1/k$. Implicit in this approximation is the neglect of backscatter (since then a rapid e^{ikx} variation would be present), and the assumption that the wave normal makes a small angle with the x axis (since otherwise the wave would not look locally like e^{ikx}). For two-dimensional problems, in which variations with y are neglected, this leaves us with

$$\frac{\partial^2 u}{\partial z^2} - 2ik\frac{\partial u}{\partial x} = 0 \tag{32}$$

This means that if the field is known as a function of z at some x, its value at a slightly larger value of x can be found.

There are two numerical methods of doing the calculation. One is the finite-difference method (Levy, 1990), in which $\partial u/\partial x$ is used directly to find the next value of u. This method is well suited for irregular terrain, since a surface impedance boundary condition can be used to take the interaction with the terrain into account. The other method is the split-step method involving Fourier transforms, which is computationally faster, but for which a terrain boundary condition is straightforward only for horizontal terrain. McArthur and Bebbington (1991) have accommodated simple irregular terrain by tilting coordinates so that the ground is effectively horizontal. Barrios (1993) has experimented with other boundary conditions.

5.9 Geometric Theory of Diffraction

A recent and accessible account of the geometric theory of diffraction is given by McNamara *et al.* (1990). At the limit of short wavelengths, radio transmission becomes almost optical. Diffraction still occurs, but it can be considered to be a local phenomenon, with free-space propagation between the isolated small regions in which the diffraction takes place. The wave starts out from an antenna and propagates as a spherical wave until it hits an obstacle. This could be a hill or a building or possibly the edge of a forest. Since diffraction is considered to be local, only the shape of the diffracting extremity of the obstacle matters. Usually obstacles are modelled as wedges, but they can also be modelled as cylinders. For example, see Figure 18.

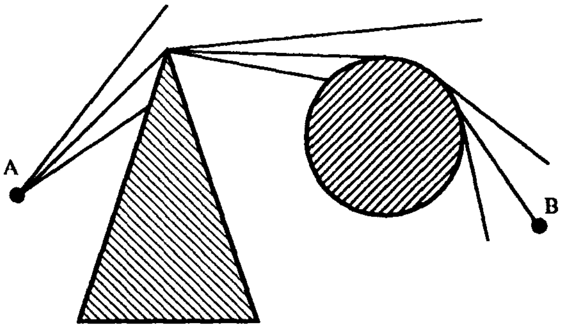

Figure 18. Diffraction over a wedge and a cylinder according to the geometric theory of diffraction. The summit of each obstacle is a source of radiation into the geometric shadow of that obstacle.

Beyond the obstacle, the wave is no longer spherical. Assuming the diffraction is over an upper extremity, the wave diverges horizontally in the same way as before, but it diverges vertically with wave normals or rays projecting back to the diffracting edge. That is, the diffracting edge acts as a line source of radiation. In calculations, a particular ray is followed, chosen because it will lead to the edge of the next obstruction or to the receiving antenna. The amplitude of the diffracted ray at the next edge is found from the solution of a standard (canonical) problem, which is to find the far field due to diffraction of a plane wave incident on a wedge or a cylinder. This solution is known as a diffraction coefficient, and since it has already been worked out, it can be put in with little computation. The process can be repeated until the receiving antenna is reached.

The method has proved extremely popular, especially for antenna design. It has also been used for terrain diffraction calculations. It has the limitation that when several diffracting edges occur along a straight line in the direction of propagation, roughly within a Fresnel zone, the assumptions behind the method are no longer valid. The Uniform version of the theory mitigates this problem, but does not eliminate it (McNamara *et al.*, 1990, p. 174). Roughly speaking, two diffracting edges close to the straight line between transmitting and receiving antennas can be dealt with, but not more (Rossi and Levy, 1992). In general, the calculation can be expected to be accurate when the first Fresnel zone is somewhat smaller than the height of the obstructions. It is particularly appropriate when buildings are to be modelled, since they are geometrically well defined and tend to cast deep shadows. It is also appropriate for three-dimensional calculations, since other detailed methods are slow in 3D.

6.0 TREES AND BUILDINGS

6.1 Trees

Radio waves may go through or around a stand of trees, as illustrated in Figure 19. The attenuation in trees is large, so that for paths of more than a few hundred metres, paths exterior to the trees are likely to dominate.

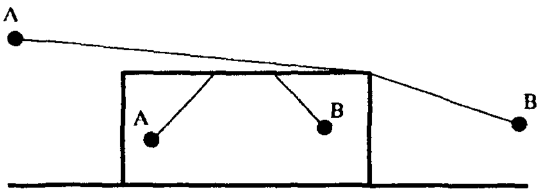

Figure 19. A stand of trees (the rectangle) with antennas either outside or inside the forest. The thin lines indicate possible wave paths, a diffracted path for antennas outside, and a lateral-wave path for antennas inside.

If both terminals A and B are outside the stand of trees, unless the stand of trees is very narrow, the problem is one if diffraction over the trees. Terminal A may be far away, in which case the forest is just part of a larger problem. The simplest way to estimate the path loss is to treat the stand of trees as if it were part of the terrain. If the terminals are inside the forest, there are two possibilities: 1. If the terminals are very close together, the signal travels directly, with exponential attenuation. 2. If the terminals are farther apart, the attenuation is too great for the signal to arrive directly, but it may go from A to the treetops, travel along the treetops as a lateral wave, then re-enter the forest to arrive at B. If only one of the terminals is inside the forest, then a combination of attenuated direct waves, lateral waves, and diffraction may be appropriate.

Tamir (1977) has worked out how to calculate the field of the lateral wave, and apply it to mixed situations. The forest is modelled as a smooth homogeneous slab of dielectric substance. A wave propagating inside at the critical angle for internal reflection emerges as a wave propagating horizontally just above the tree tops. This is a diffracted wave, similar to the Norton surface wave, mentioned in Section 3.4, which attenuates according to a $1/r^4$ power law. It re-enters by a reciprocal mechanism. This model is suitable roughly in the frequency range 2 to 200 MHz. At lower frequencies, the height of the trees is small compared to the wavelength, and the forest acts only as a perturbation on the interaction of the wave with the ground. At higher frequencies, the forest cannot be considered to be a smooth slab. Propagation still takes place over the tree tops, but it is more likely to be by means of scattering between individual trees (Campbell and Wang, 1991).

It has been observed by Weissberger (1982) and others that when both antennas are in a forest, the received power varies as $\exp(-\beta d)$ over short distances d, where β is a decay constant that depends on frequency. This describes the attenuation of radiation through a lossy medium of infinite extent, or through a collection of randomly located discrete lossy scatterers.

However, the power decreases more slowly for greater distances. For frequencies less than 200 MHz, this slower decrease corresponds to the lateral wave over the tree tops. For higher frequencies, a similar mechanism must operate, that is, over the greater distance, the wave is free to seek out the path or paths of least attenuation, whatever they may be. Empirical methods are most useful in this situation, as outlined in part B of the lecture.

6.2 Buildings

Since buildings can be considered opaque to radio waves, the mechanisms of interest are reflection from outside walls and diffraction over roofs and around the outside corners. If it is assumed that buildings are evenly spaced and of uniform height, a theoretical calculation is possible using physical optics, as mentioned in Section 5.4. If buildings are not uniform, but a detailed description of them is available, a deterministic calculation may be done using GTD (Section 5.9), or, with much longer computing times, parabolic equations (Section 5.8). Otherwise, a statistical calculation may be done, as described in part B of this lecture.

7.0 CONCLUSION

Even though the basic principles of electromagnetic radiation have been known for a long time, and even though the shape and electrical properties of the terrain may be known, no simple recipe can be given for finding the field strength in any given circumstance. The mathematical methods that must be used are usually approximate, and there is usually a trade-off between simplicity and accuracy in choosing a method. Furthermore, different methods are successful in different frequency ranges. This is because, although the basic equations are the same for all frequencies, the approximations that are made are usually appropriate to only a limited range of frequencies. As a result, a number of prediction methods must be considered for use.

8.0 REFERENCES

Note: If there is a series of papers by one author on the same subject, only the most recent may be listed.

Barrick, D.E., "Theory of HF and VHF propagation across the rough sea, 1, the effective surface impedance for a slightly rough highly conducting medium at grazing incidence", Radio Sci. 6, 517-526, 1971a.

Barrick, D.E., "Theory of HF and VHF propagation across the rough sea, 2, application to HF and VHF propagation above the sea", Radio Sci. 6, 527-533, 1971b.

Barrios, A.E., "Terrain and refractivity effects on non-optical paths", AGARD EPP Symposium, 10-1 to 10-7, Oct. 1993.

Beckmann, P., and A. Spizzichino, The Scattering of Electromagnetic Waves from Rough Surfaces, 503 pp., Artech, Norwood, USA, 1987.

Boithias, L., Radio Wave Propagation, 330 pp., McGraw-Hill, New York, 1987.

Bremmer, H., Terrestrial Radio Waves, 343 pp., Elsevier, Amsterdam, 1949.

Bremmer, H., "Applications of operational calculus to groundwave propagation, particularly for long waves", IRE Trans. Ant. Prop. AP-6(3), 267-272, 1958.

Bullington, K., "Radio propagation at frequencies above 30 Megacycles", Proc. IRE, 35, 1122-1136, 1947.

Bullington, K., "Radio propagation for vehicular communications", IEEE Trans. Veh. Tech, VT-(4), 295-308, 1977. (A reprint, with only minor changes, of the article cited above and of "Radio propagation fundamentals", in a special issue on propagation.)

Campbell, R.L., and H. Wang, "Scattered lateral wave model for UHF propagation in forest", Abstracts, URSI North American Radio Science Meeting, p. 435, June, 1991.

CCIR Rec. 341-2, "The concept of transmission loss for radio links", Recommendations of the CCIR, Vol. V, ITU Geneva, 1990.

CCIR Rec. 526-1, "Propagation by diffraction", Recommendations of the CCIR, Vol. V, ITU Geneva, 1990.

CCIR Report 717-3, "World atlas of ground conductivities" Reports of the CCIR, Vol. V, ITU Geneva, 1990.

de Assis, M.S., "A simplified solution to the problem of multiple diffraction over rounded obstacles", IEEE Trans. Ant. Prop., AP-19(2), 292-295, 1971.

Deygout, J., "Multiple knife-edge diffraction of microwaves", IEEE Trans. Ant. Prop., AP14(4), 480-489, 1966.

Deygout, J., "Correction factor for multiple knife-edge diffraction", IEEE Trans. Ant. Prop., 39(8), 1256-1258, 1991.

Epstein, J., and D.W. Peterson, "An experimental study of wave propagation at 850 Mc", Proc. IRE, 41(5), 595-611, 1953.

Furutsu, K., "A systematic theory of wave propagation over irregular terrain", Radio Sci. 17, 1037-1059, 1982.

Giovanelli, C.L., "An analysis of simplified solutions for multiple knife-edge diffraction", IEEE Trans. Ant. Prop., AP-32(3), 297-301, 1984.

Hacking, K., "Approximate methods for calculating multiple-diffraction losses", Electronics Lett., 2(5), 179-180, 1966.

Hill, D.A., and J.R. Wait, "Ground wave attenuation for a spherical earth with arbitrary surface impedance", Radio Sci., 15(3), 637-643, 1980.

Hufford, G.A., "An integral equation approach to the problem of wave propagation over an irregular surface", Quart. J. Appl. Math., 9(4), 391-404, 1952.

Jull, E.V., Aperture Antennas and Diffraction Theory, 173pp., Peregrinus, Stevenage, U.K., 1981.

King, R.W., and H. Page, "The propagation of waves over irregular terrain", AGARD Conf. Proc. No. 127, 1-1 to 1-20, 1973.

Levy, M.F., "Parabolic equation modelling of propagation over irregular terrain", Electronics Lett., 26(15), 1153-1155, 1990.

Maclean, T.S.M., and Z. Wu, Radiowave Propagation over Ground, 299 pp., Chapman and Hall, London, 1993.

McArthur, R.J., and D.H.O. Bebbington, "Diffraction over simple terrain obstacles by the method of parabolic equations", Seventh International Conference on Antennas and Propagation, ICAP 91, IEE Conf. Pub. No. 333, 1991.

McNamara, D.A., C.W.I. Pistorius, and J.A.G. Malherbe, Introduction to the Uniform Geometrical Theory of Diffraction, 471pp, Artech, Boston, 1990.

Meeks, M.L., Radar Propagation at Low Altitudes, 105pp, Artech, Boston, 1982.

Meeks, M.L., "VHF propagation over hilly, forested terrain", IEEE Trans. Ant. Prop. AP-31(3), 483-489, 1983.

Millington, G., "Ground wave propagation over an inhomogeneous smooth earth", Proc. IEE, Part III, Vol. 96(39), 53-64, 1949.

Millington, G., R. Hewitt, and F.S. Immirzi, "Double knife-edge diffraction in field-strength predictions", Proc. IEE, 109C(16), 419-429, 1962.

Monteath, G.D., Applications of the Electromagnetic Uncertainty Principle, 149 pp., Pergamon, Oxford, 1973.

Ott, R.H., "RING: An integral equation algorithm for HF-VHF radio wave propagation over irregular, inhomogeneous terrain", Radio Sci., 27(6), 867-882, 1992.

Ott, R.H., and L.A. Berry, "An alternative integral equation for propagation over irregular terrain, Radio Sci., 5(5), 767-771, 1970.

Palmer, F.H., "Ground-wave propagation characteristics of interest to the tactical communicator", AGARD Lecture Series No. 120, 2-1 to 2-16, 1982.

Pogorzelski, R.J., "A note on some common diffraction link loss models", Radio Sci., 17(6), 1536-1540, 1982.

Richter, J.H. (editor), Radio Wave Propagation Modeling, Prediction and Assessment, AGARDograph No. 326, 126 pp., 1990.

Rossi, J.-P., and A.J. Levy, "A ray model for decimetric radiowave propagation in an urban area", Radio Sci. 27(6), 971-979, 1992.

Sharples, P.A., and M.J. Mehler, "Cascaded cylinder model for predicting terrain diffraction loss at microwave frequencies, IEE Proc., 136, Pt. H, No. 4, 331-337, 1989.

Tamir, T., "Radio wave propagation along mixed paths in forest environments", IEEE Trans. Ant. Prop., AP-25(4), 471-477, 1977.

Vogler, L.E., "An attenuation function for multiple knife-edge diffraction", Radio Sci., 17(6), 1541-1546, 1982.

Vogler, L.E., "Radio wave diffraction by a rounded obstacle", Radio Sci., 20(3), 582-590, 1985.

Wait, J.R., Electromagnetic waves in stratified media, 372 pp., Macmillan, New York, 1962.

Wait, J.R., "Electromagnetic surface waves", in Advances in Radio Research, J.A. Saxton ed., vol. 1, pp. 157-217, Academic Press, London, 1964.

Wait, J.R., "Diffraction and scattering of the electromagnetic groundwave by terrain features", Radio Sci., 3, 995-1003, 1968.

Wait, J.R., "Theories for radio ground wave transmission over multisection path", Radio Sci., 15(5), 971-976, 1980.

Wait, J.R., and A.M. Conda, "Diffraction of electromagnetic waves by smooth obstacles for grazing angles", J. Res. Nat. Bureau of Standards - D Radio Propagation 63D(2), 181-197, 1959.

Weissberger, M.A., An Initial Critical Summary of Models for Predicting the Attenuation of Radio Waves by Trees, ECAC Report ESD-TR-81-101, 1982.

Whitteker, J.H., "Fresnel-Kirchhoff theory applied to terrain diffraction problems", Radio Sci., 25(5), 837-851, 1990.

Whitteker, J.H., "A series solution for diffraction over terrain modelled as multiple bridged knife edges", Radio Sci., 28(4), 487-500, 1993.

Xia, H.X., and H.L. Bertoni, "Diffraction of cylindrical and plane waves by an array of absorbing half-screens", IEEE Trans. Ant. Prop., 40(2), 170-177, 1992.

Ground Wave and Diffraction (B)

J.H. Whitteker
Communications Research Centre
3701 Carling Ave.
Ottawa, Canada K2H 8S2

1.0 PLANNING TOOLS

In choosing ground-wave or diffraction propagation tools for planning systems, it is well to keep in mind that the objects described here belong in different categories. The terminology that follows is mostly that used by Hufford *et al.* (1982). Most of the topics in Part A of the lecture are models or methods for calculating path loss. That is, you choose to represent the terrain in a certain simplified way, and having done this, you choose a theoretical technique, or perhaps a set of measurements, some approximations or generalizations, and arrive at a more or less complete recipe for doing a calculation.

An implementation is how you actually perform the calculation. The simpler methods can be implemented by nomograms, or graphs, or could be done on a hand-held calculator. The more complex ones require a computer program, which becomes the implementation. If the method has been set out in complete detail, then all implementations of it will give approximately the same answer. If (as is more common) some issues have been left unresolved, then the answers given by the implementation will depend on the details of how the implementation is done. For example, methods that model terrain as knife edges or other special shapes do not usually specify exactly how these shapes are to be identified in real terrain.

Finally, a computer implementation will usually be contained within some applications program. In some cases, the applications program will not add much to the implementation of the method, perhaps accepting input data and outputting a list of results. In other cases, the applications program may be more elaborate, with graphical input and output, and perhaps specialized tools for planning communications or broadcast systems. It is possible for an applications program to have a sophisticated user interface, but use only primitive propagation methods.

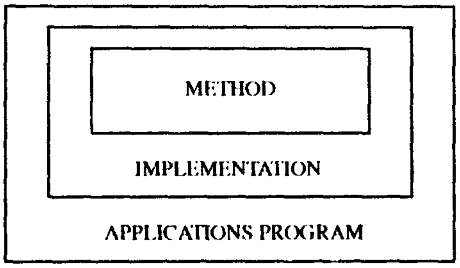

Figure 1. An hierarchy of radio-propagation planning tools.

2.0 COMPARISONS

There is no 'best' method. Comparisons have been made by Paunović *et al.* (1984), Delisle *et al.* (1985), Aurand and Post (1985), Grosskopf (1987,1988), and IEEE Vehicular Technology (1988). These comparisons are certainly useful, but it must be remembered that they are all done with a particular frequency range or service in mind. There is also the question of what is wanted. If you want to plan communications on a particular path, and you have a detailed knowledge of the terrain on that path, then a detailed, complex method will probably produce the best result. If, on the other hand, you want to plan a system in general, not knowing where in particular it will be set up (a common military requirement), then a prediction program that operates on the general features of the terrain would be more suitable. Longley and Rice (1968) and Hufford *et al.* (1982) refer to these as 'area' predictions.

Methods may be empirical or theoretical, or a mixture. The advantage of empirical methods is that all sources of attenuation are automatically taken in to account, since the predictions are based on measurements. Their disadvantage is that they are strictly valid *only in the* particular environment in which the measurements were made. For example, measurements made in one urban environment do not provide much indication of what the attenuations will be in another environment where the buildings [illegible] taller and more widely spaced, say. Theoretical methods, on the other hand, have the advantage that they do predict the dependence on these parameters, within some range. Their disadvantage is that they may be an oversimplification of the real world, and everything may not be taken into account. In practice, of course, the results of theoretical models are checked against data, to verify that they are realistic.

The greater part of this lecture is devoted to diffraction at VHF and higher frequencies rather than groundwave at HF and lower frequencies. Discussion of groundwave is confined mostly to Sections 3.1 and 6.1.

3.0 SIMPLE METHODS

3.1 Basic transmission loss

Particularly at VHF and above, the effect of the ground and other obstacles along the propagation path may usually be considered separately from the effect of the antennas. This means that the received power P_r in decibels can be found from the transmitted power P_t (in decibels) for any antennas from

$$P_r = P_t + G_t + G_r - L_b \qquad (1)$$

where G_t and G_r are the antenna gains relative to an isotropic antenna, and L_b is the basic transmission loss for the path. For example, if effective radiated power from a properly-oriented half-wave dipole is given, then $G_t = 2.15$ dB.

Sometimes, instead of the basic path loss, the electric field intensity resulting from an antenna radiating one kilowatt is given. If the field E is expressed in microvolts/metre and frequency f in megahertz, the relation between these quantities is given by

$$L_b = 137.22 + 20\log f - 20\log E \qquad (2)$$

if the one kilowatt comes from an isotropic antenna, and

$$L_b = 139.37 + 20\log f - 20\log E \qquad (3)$$

if it comes from a half-wave dipole, as is assumed, for example, in two ITU (1955, 1959) atlases. Equation (2) is the logarithmic version of eqn. (2) of Part A. These are the forms of the equation appropriate for VHF and above, and for elevated antennas at any frequency, where the concept of basic transmission loss is fairly straightforward.

At lower frequencies, antennas are often within a wavelength of the ground, and the antennas and the path cannot be so easily separated, since both the antenna impedance and pattern are influenced by the ground. The change in antenna impedance affects the power emitted for a given antenna current or dipole moment, and also affects the effective capture area of a receiving antenna. For example, for the vertically polarized transmitting dipole moment assumed by the program GRWAVE (described later), 500 watts are emitted in free space, and 1000 watts on a perfectly conducting ground plane. CCIR Recommendation 386-7 (1992) gives curves calculated with GRWAVE for both antennas on the ground. For those curves, the relationship between the field on the ground and L_b is

$$L_b = 142.0 + 20\log f - 20\log E \qquad (4)$$

for one kilowatt emitted by a short monopole (much shorter than a wavelength) on the ground. The constant 142.0 may be obtained from equation (2) by adding 1.76 dB (factor of 1.5), the gain of the short monopole assumed in the calculations, and adding also 3.01 dB (factor of 2), due to the factor of two in the effective capture area of the receiving antenna which is on the ground rather than in free space. With the effect of the ground already accounted for, the gains to be used in eqn. (1) are the free-space gains of the antennas, e.g. 1.76 dB for a short antenna or 2.15 dB for a half-wave dipole.

3.2 Free space

The simplest possible prediction is for free-space attenuation. In any case, a component of the basic transmission loss is the free-space attenuation L_{bf}, which is the loss that would occur in the absence of the earth or any other obstacles, and may be calculated as

$$L_{bf} = 32.4 + 20\log f + 20\log d \qquad (5)$$

where L_{bf} is expressed in decibels, frequency f in megahertz and distance d in kilometres. This is the logarithmic version of eqn. (1) of Part A.

In many implementations, free space is one of the models used, and the criterion for its use is whether the first Fresnel zone, or some fraction of it, is clear of all obstacles. On the other hand, if the first Fresnel zone is completely blocked, significant attenuation can be expected. The radius of the first Fresnel zone is easily calculated using eqn (24) of Part A. However, an idea of the heights involved may be obtained from Figure 2. It may be seen that at the lowest frequencies, the Fresnel zone is so large that height variations in the terrain scarcely matter, while at the highest frequencies, they are so important that an unknown small hill or grove of trees or buildings can make a field-strength prediction wildly wrong.

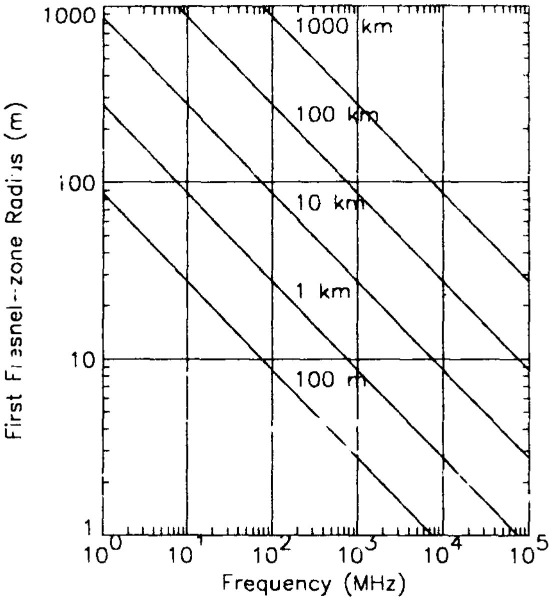

Figure 2. The radius of the first Fresnel zone at the mid point of a path of given length.

3.3 Plane earth

The next simplest method is the plane-earth, perfect-reflection approximation. The logarithmic version of eqn. (15) of Part A is

$$L_B = 120 + 40\log d - 20\log (h_A h_B) \qquad (6)$$

This is the plane-earth loss, neglecting the surface wave, assuming a reflection coefficient of -1, and assuming the path is long enough that the phase difference between the direct and reflected waves is small compared to unity. (The constant 120 dB is due to expressing d in kilometres rather than metres. Heights h_A and h_B are still expressed in metres.) According to Bullington (1977), the surface wave may be taken into account approximately by replacing the antenna height by the larger of the actual height and the minimum effective antenna height. Equation (6) has been used as the basis of several semi-empirical prediction methods, since it has been found from measurements that signal power tends to decrease roughly as $1/d^4$ under a variety of conditions, even though there may be a lot of scatter in the measured values.

3.4 Calculations based on plane earth

A formula used widely in the past is due to Egli (1957), who adopted eqn. (6), but added a term $20\log (f/40)$ to account for an empirically-observed increase in path loss with frequency above 40 MHz. There is another modification: when one antenna, say h_B, is less than 10 m above ground, the variation with height is $10\log h_B$ rather than $20\log h_B$. (Delisle *et al.* (1985) give an explicit formula.) The measurements on which the formula is based were mostly commercial television and land-mobile surveys in various parts of the U.S., with no particular characterization of the terrain except that in one area the amplitude of terrain elevation variation was about 150 m. This

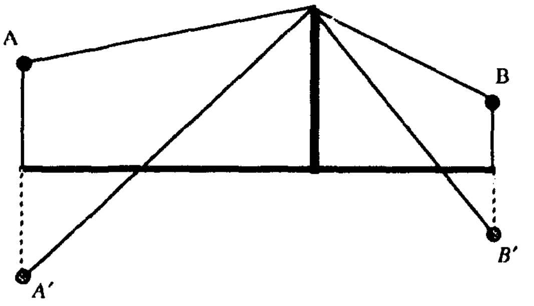

Figure 3. Plane earth with a single knife edge.

formula does have the virtue of being simple, and it might still be useful if nothing is known about the terrain, but the prediction would have to be considered a very rough one.

More recently, Ibrahim and Parsons (1983) devised a semi-empirical formula related to eqn. (6), based on land-mobile measurements made in London, and tested on measurements made in Birmingham. The model relates specifically to built-up areas on flat ground, with distances up to 10 km. They also devised an entirely empirical model, and found that the decrease with distance was roughly $40\log d$, depending on frequency. The semi-empirical formula forces the dependence on distance to be exactly $40\log d$:

$$L_B = 140 + 40\log d - 20\log\left(h_A h_B\right) + \frac{f}{40} + 0.18L - 0.34H \quad (7)$$

where L is a land-usage factor, defined as the percentage of the 500-metre-square test area around the mobile terminal that is covered by buildings, and H is the average terrain height in metres of the test area above that of the area containing the transmitter. There is also a term that applies only to the highly urbanized city centre, omitted here. This formula is also very simple, and is likely to be useful for short land-mobile paths in built-up areas if the parameters can be evaluated.

3.5 Single knife edge

If the terrain contains one narrow obstacle, it may be modelled as a single knife edge, and the resulting path loss may be found with a simple calculation, requiring only a table or approximate formula for the Fresnel integral. It is also fairly easy to take plane-earth reflections into account by doing the knife-edge calculation with images of the antennas, and adding in the reflected fields, remembering to keep track of the phases. The situation is illustrated in Figure 3. The field at B is the sum of the fields found for the paths AB, A'B, AB', and $A'B'$. In finding the fields due to reflected paths, the appropriate reflection coefficients should be included. Meeks (1982) explores this model, as well as several others.

Unfortunately, real terrain does not often look like this. If the ground where the reflections would take place is very rough, or very non-level, the reflected paths should be ignored. (Reflections from rough surfaces are covered in the lecture on refractive effects.) If the obstructions are more complex, Bullington (1977) has suggested a method of reducing them to an equivalent knife edge as illustrated in Figure 4.

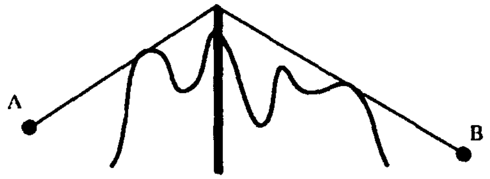

Figure 4. A complex obstacle (the irregular curve) and a Bullington equivalent knife edge (the thick vertical line).

While this construction permits a simple calculation, the resulting estimate of path loss must be considered a rough one.

3.6 Graphical implementations

The International Telecommunication Union (ITU) has published curves of field strength as a function of distance. For frequencies from 10 kHz to 30 MHz, CCIR Recommendation 386-7 (1992) gives these curves for vertically polarized antennas located on or close to the ground (the height limit is given in Note 1 of the Recommendation). The curves are theoretical, assuming a smooth earth and an exponential atmosphere. They were generated with program GRWAVE, described in section 6.1.

For the frequency ranges 30 MHz to 300 MHz and 30 MHz to 10 GHz respectively, the ITU (1955, 1959) has published atlases giving propagation curves for antennas at various heights transmitting over a spherical earth with various electrical constants. An example is shown in Figure 5. Note that in these older publications, units of conductivity are such that 10^{-11} corresponds to 1 S/m. Also, the electrical constants used do not correspond exactly to more recent soil-type categories. This is unimportant, since the categories are rough ones in any case. For the frequency range 30 MHz to 1 GHz, CCIR Report 567-4 (1990) gives curves for the terrestrial land-mobile service, and CCIR Recommendation 370-5 (1990) gives curves for the broadcasting service. The difference between the two is in the assumed height of the receiving antenna, 1.5 or 3 m in one case and 10 m in the other. The curves for broadcasting are much more numerous. In contrast to the curves for the lower frequencies, these curves are empirically based. A rough description of many of them is that, out to a distance of about 50 km, the received power decreases with distance as $1/d^4$, while beyond about 200 km it decreases exponentially. There is a smooth transition at intermediate distances. At the time of writing, work is in progress on a new ITU Recommendation to provide an empirically-based prediction method in the frequency range 1 to 3 GHz.

CCIR Report 239-7 (1990) suggests a "terrain clearance angle" correction to the curves of Recommendation 370. The correction is determined graphically from the angle subtended at the lower antenna by the horizontal and a line that clears all terrain within 16 km. Paunović *et al.* (1984) recommend this "terrain clearance angle" method from among the six methods that they tested for the land-mobile service.

A large manual by Shibuya (1987) contains many graphs for determining propagation parameters.

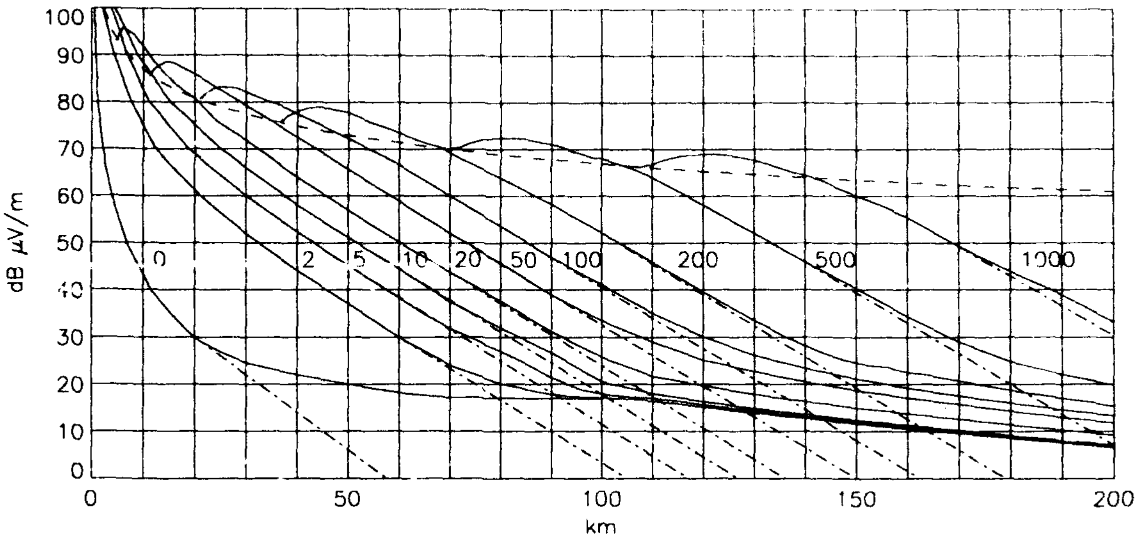

Figure 5. Field strength over a smooth earth with electrical constants $\varepsilon_r = 10$ and $\sigma = 0.01$ S/m (medium dry ground) for 1 kW at 300 MHz emitted from a horizontal half-wave dipole at a height of 100 m. The solid curves include both diffraction and tropospheric scatter, while the dot-chain curves are for diffraction only. The broken line is for free space. Adapted from ITU (1955).

4.0 EMPIRICAL METHODS

4.1 Okumura

Okumura *et al.* (1968) report on and analyze exhaustively an extensive set of measurements made in Japan at frequencies ranging from 200 MHz to 1920 MHz. The results are classified in various ways, and curves are presented for prediction purposes, intended for use in the land-mobile service. Measurements were included with the base-station height varying from 30 to about 1000 m, and with mobile heights usually at 3 m but sometimes at 1.5 m, and (from other measurements) up to 10 m. Wave polarization was vertical. Path lengths varied from 1 to 100 km. Measurements were made in the plains in and around Tokyo, and in hilly and mountainous areas to the west.

For analysis, the data were divided into intervals of 1 to 1.5 km in extent that could be classified as being urban, open etc., and these intervals were in turn divided into small sectors of about 20 m over which multipath fading could be assumed to be the dominant source of variation. Distributions of instantaneous signal strength were found in the small (20 m) sectors (Rayleigh in urban areas, but tending to log-normal in suburban areas), and the small-sector medians were found. The distribution of these small-sector medians was found for the larger intervals, and the medians of these latter distributions were used for the signal-level prediction curves.

The prediction curves were based on the urban data, with corrections for suburban and open areas. The reason for not using suburban areas as the basis was that they had a broad definition (villages, or highways scattered with trees or buildings), and so the variability was large, and the reason for not using open areas was that with their narrow definition (open fields clear of all trees or buildings within 300 or 400 m towards the base station), there were not very many of them in Japan.

Of the many results presented, two follow: (1) In an urban area, with a base station height of 140 m, the field attenuation relative to the free-space loss variation of $1/r^2$, decreases as $1/r^{0.5}$ up to about 15 km, and as $1/r^{2.3}$ beyond 40 km (Figure 11 of Okumura *et al.*). (2) For the same base station, when an urban street is in the line with the propagation path, the signal exceeds that for a perpendicular street by 6 to 10 dB.

The base predictions are for 'quasi-smooth' terrain, that is, the terrain is level within 20 vertical metres. However, corrections are given for undulating terrain, and a finer correction depending on whether the mobile antenna is near the top or bottom of an undulation. Slope corrections are also given, as are corrections for an isolated mountain and for mixed land-water paths. Okumura *et al.* define a terrain roughness parameter Δh as the interdecile height range within 10 km of the mobile terminal in the direction of the base station. (The parameter Δh is defined as the height range such that 10% of the terrain is above the range and 10% below.) They define an effective antenna height relative to average ground within 3 to 15 km. Cumulative distributions and prediction curves are also given for location variation, for both small-sector medians and instantaneous variations. The method of Okumura *et al.* is recommended for land-mobile use by Lee (1982, Section 3.6).

Since the predictions of Okumura *et al.* (1968) are contained in many graphs, they are not easy to implement in a computer program. Therefore Hata (1980) combined many of these results into a few equations that are very easy to program. At least one comparison of methods (Delisle *et al.*, 1985) has recommended their use. It should be nevertheless understood that they do not capture the full diversity of the Okumura *et al.* results. There are stated limits to their applicability; in particular they are restricted to quasi-smooth terrain. On the other hand, Löw (1986) compared the predictions of the Hata equations with the results of measurements made at 450 and 900 MHz around Darmstadt, and found that the equations could be applied beyond their stated limits, to a distance of 40 km, and to a base-station height of 800 m.

4.2 Neural networks

Neural networks, applied to radio propagation, are a way of basing predictions on measured data. Ordinarily, to use measured data, a human fits curves to the data as functions of certain parameters, guided by a general knowledge of the way radio waves propagate. There are many parameters to consider, such as path length, antenna heights, frequency, and tree or building density and height along the path. There is also the terrain elevation, with as many variables as there are terrain sample points along the path. Usually these parameters must be considered in some simplified way. The use of neural networks is an attempt to automate this process.

A neural network defines an output (the path loss in excess of the free-space loss, say) as a function of a number of parameters. The function is initially unknown, but the network can 'learn' what the function is by being given many examples in which the desired output is known. The network assigns and modifies relationships and weights to the input parameters as it learns. Eventually, it should be able to make predictions on its own, without being given the answer.

Neural nets can be designed in many ways, and the success of a net for a given application depends on the skill of the designer. Stocker *et al.* (1993) have done trials for the cities of Mannheim and Darmstadt, and the neural net seems to be able to provide reasonable estimates of path loss for the same area on which it was trained. The technique is a new one, and it is difficult to say what its future value will be.

5.0 SEMI-EMPIRICAL METHODS

5.1 Longley-Rice (Longley and Rice, 1968)

The Longley-Rice model has been, and still is, used very widely. It is a computer code for predicting long-term median transmission loss over irregular terrain for frequencies above 20 MHz. It incorporates many of the methods given in Tech. Note 101 (Rice *et al.*, 1967). Section 2.2 of Longley and Rice (1968) states that 'Transmission loss may be calculated for specific paths where detailed profiles are available, but the prediction method is particularly useful when little is known of the details of terrain for actual paths.' The authors have accumulated statistics on various types of terrain, so that the program can estimate median values of such quantities as horizon distances and elevation angles when only antenna heights and the interdecile range Δh of terrain elevations are given. For a given type of terrain, Δh increases with path length to an asymptotic value.

The diffraction loss is found in the following way: If the transmitting and receiving antennas are within the radio line of sight, two-ray optics are used, that is, a direct ray and a reflected ray. Effective antenna heights are used, relative to mean ground in the dominant reflecting plane between the antennas. In order to obtain a smooth curve as a function of distance, the attenuation is found at three points, two in the optical region, and one at the smooth-earth horizon, using diffraction techniques, and a smooth curve is drawn through these three points. If the antennas are in the diffraction region, two calculations are done, one assuming a smooth earth, and the other assuming a knife edge, and a weighted mean is taken. The weighting factors are determined empirically as a function of frequency and terrain parameters. Effective antenna heights are found relative to a smooth curve fitted to terrain visible to both antennas. If this is not possible, the effective height depends on local terrain. Finally, for long enough paths, tropospheric scatter is taken into account. An important output of the program is location variability, which is determined empirically, and which depends mainly on frequency and terrain roughness. Time variability is also given, again based on measured data.

As with any method that must make model choices, there are sometimes discontinuities as path parameters are varied. The IEEE report (1988) shows the effect of gradually raising the height of a knife-edge obstacle at 900 MHz. The discontinuities range from 3 to 17 dB. Discontinuities as a function of distance are less common.

5.2 Terrain Integrated Rough Earth Model (TIREM)

TIREM is also widely used. The program is available as part of a package distributed by NTIS (1983). It is described in a handbook by Eppink and Kuebler (1994), and in the IEEE report (1988). It takes into account atmospheric and ground constants, and requires a terrain profile. Using the terrain profile, the program decides on the type of path, and selects one of 12 propagation modes. It does this by first determining some basic parameters, such as radio horizon distances, effective antenna heights, path angular distances, and Fresnel-zone clearance. The modes include free space, line-of-sight rough earth, rough earth, knife-edge diffraction, tropospheric scatter, and various weighted combinations of the modes already mentioned.

A path is classified as line-of-sight or beyond-line-of-sight on the basis of radio horizon distances. For a line-of-sight path, if the terrain clearance of the path is greater than $1.5R_1$, where R_1 is the radius of the first Fresnel zone, the free-space loss is used. If the clearance is less than $0.5R_1$, one of two empirical rough-earth formulations is used, based on the interdecile height range Δh. These formulations, and the choice between them, are described in the IEEE report (1988). In between, a weighted combination of free-space and rough-earth is used. For a beyond line-of-sight path, if the two antennas have a common radio horizon, the obstacle is treated as a single knife edge, with ground reflections on either side. If the radio horizons are distinct but close, a Bullington equivalent knife edge is used. If they are far apart, smooth-earth diffraction theory is used. In between, a weighted combination is used.

The IEEE report (1988) remarks that the propagation data on which one of the rough-earth models is based were obtained almost entirely on point-to-point communication links, with few instances of vehicle-height antennas. When the model is used in land-mobile situations, where one antenna is much lower than the other, there is a region (line-of-sight, clearance less than $0.5R_1$), in which the predicted path loss does not change with changing base-station height. The predicted loss is also sensitive to the method used for finding the effective height of the mobile antenna. As with any program that makes model choices, discontinuities are possible, and the IEEE report found discontinuities up to 12 dB as a function of distance.

5.3 Lincoln Laboratories

Ayasli (1986) has reported on a program called SEKE, for VHF and above, intended for radar applications. Also, some of the difficulties in modelling real terrain are outlined in this paper. Three models are used: multipath (free space plus reflections), multiple knife edge diffraction, and spherical earth diffraction. The multipath model is used if the first Fresnel zone is unobstructed and one or both of the diffraction models is used if an obstruction covers more than half of the first Fresnel-zone radius. Otherwise a weighted average is taken. The choice of diffraction model is determined by how high the dominant obstruction is above a line fitted to the terrain profile. If it is more than one half a Fresnel-zone radius, knife-edge diffraction is used; otherwise spherical earth or a weighted average is used. In the multipath model, either single or multiple reflections may be chosen. For knife-edge diffraction, Deygout's (1966) method is used for a maximum of three knife edges, with a modification due to Meeks (1983). Meeks also reports on measurements of field strength as a function of height made by helicopter.

5.4 Blomquist and Ladell (1974)

This method is based on two extreme models, and a bridging formula for combining them. The first model is a smooth spherical earth. The formula they use for this is a fairly simple one. It begins with a flat-earth formula that includes the surface wave but neglects the conductivity of the ground (so that it is inappropriate over seawater). Then a correction is added that takes the curvature of the earth into account up to the distance at which the first term of the residue series becomes valid. The result is a smooth-earth propagation factor F_S. (The propagation factor is defined as the path loss in excess of the free-space loss, in decibels.) The second model is a series of knife edges that represent the terrain obstacles, neglecting any ground reflections. The Epstein-Peterson (1953) method is used to combine the path-loss functions for several knife edges. The result is a knife-edge propagation factor F_{EP}. The final result is a propagation factor

$$F = (F^2_S + F^2_{EP})^{1/2}$$

The rationale for doing this is that at low frequencies, the smooth-earth loss will be large and the knife-edge loss small, and at high frequencies, at least if the range is not great, the Fresnel ellipsoid will clear the smooth earth, leaving the knife-edge loss to dominate. Apart from this, there is not much theoretical justification for the procedure. Nevertheless, in a comparison of prediction methods for VHF broadcast at 93.8 MHz, Grosskopf (1987) found this method to be the most accurate of the eleven he tested.

6.0 IMPLEMENTATIONS OF THEORETICAL METHODS

6.1 Groundwave calculations

A summary of groundwave prediction models and prediction techniques has also been given in a recent AGARD document (Richter, 1990), including sample output from a program called PROPHET.

6.1.1 Spherical earth

For propagation over a homogeneous spherical earth with an exponential atmosphere, a commonly used program is GRWAVE, described briefly by Rotheram *et al.* (1985), and by CCIR Report 714-2 (1990). It is based on the theory of Rotheram (1981). GRWAVE is published by the ITU (1993). This program is an exception to the usual practice of accommodating the atmosphere by assuming a 4/3 earth, assuming instead an exponential atmosphere. This makes a difference for antennas elevated to great heights or for frequencies below about 3 MHz. Three different types of calculation are done, depending on wavelength λ, path length d, and antenna height h, in relation to the earth's radius a. For $d < \lambda^{1/3}a^{2/3}$ and $h < \lambda^{2/3}a^{1/3}$, extensions of the Sommerfeld flat-earth theory are used. For $h > \lambda^{2/3}a^{1/3}$ and d within the radio horizon, geometric optics is used. Beyond the radio horizon, or when $d > \lambda^{1/3}a^{2/3}$ and $h < \lambda^{2/3}a^{1/3}$, the residue series is used. Both field strengths and values of basic transmission loss L_b are given. The effect of the earth on antenna impedance is taken into account in calculating L_b, so that the ordinary free-space values of antenna gains can be used with it. According to the ITU catalogue (1993), source code is available, as well as an executable program for PC-DOS.

For propagation over a rough sea, Rotheram *et al.* (1985) describe a program called BARRICK, based on the theory by Barrick (1971a,b). It is a modification of GRWAVE. The rough surface changes the effective surface impedance, in a way that depends on the two-dimensional ocean-wave spectrum of the surface.

For propagation over an inhomogeneous spherical earth, a program called NEWBREM is described by Rotheram *et al.* (1985). It uses Bremmer's (1949) theory (residue series plus geometric optics) for homogeneous sections, and uses Millington's (1949) method to combine the results.

For propagation over earth that can be modelled as three or fewer sections, each of which is homogeneous and of constant radius (there can be discontinuities in terrain elevation between the sections), Rotheram *et al.* describe a program called FURUTSU, based on Furutsu's (1982) theory. At least one section must be a long one, but one or two sections can be short, resembling knife edges.

6.1.2 Irregular terrain

For propagation over irregular terrain, a program called WAGNER was originally developed by Ott and Berry (1970). Some results are given by Ott *et al.* (1979), and the program is described (including a Fortran listing) in Ott (1983). The original program can perform calculations at frequencies up to 30 MHz, but a recent version, program RING, described by Ott (1992) extends the frequency range to 100 MHz. In WAGNER, the choice of integration points is made by the user. Some experimentation may be required to find a spacing of points that is close enough to ensure convergence of the calculation, but not too close, since the computation time increases as the square of the number of points. Ott (1983) gives the computation time as proportional to path length squared and frequency squared. The version of the program reported by Ott (1983) can also model forests, buildings, or snow, as a lossy dielectric slab on top of the earth.

6.1.3 Ground wave, multiple method

For general ground-wave calculations, software has been written in conjunction with the book by Maclean and Wu (1993). It calculates field strength over homogeneous and inhomogeneous flat and spherical ground, and over irregular ground. It runs on PC-DOS. As of the time of writing, this software has not yet been published.

A computer program called GWVOA (Ground Wave Voice of America), described by DeMinco (1986), implements several methods. The user selects the methods to be used. The smooth earth model uses, for short distances, one of the two approximations described by Hill and Wait (1980), as does GRWAVE, depending on the impedance of the earth. For long distances it uses the residue series, and for high antennas, geometric optics. In regions where none of these apply, it does an integration of the full wave theory. For inhomogeneous paths, it uses Millington's (1949) method. The antenna heights are set to zero for the calculations over segments, and then a height gain function is applied at the ends of the path. For irregular terrain, the program implements Ott's (1983) method. An extension of the method can model trees or buildings with user-defined properties as a dielectric slab over the earth. In this implementation of Ott's method, the spacing between integration points is selected automatically according to the local roughness of the terrain. There is also an estimate of noise level, and an antenna-gain calculation. Since some of the model implementations are time consuming, the master program estimates the running time before starting a calculation. The program is intended for use in the frequency range 0.01 to 30 MHz.

6.1.4 Application to Loran-C

Loran-C operates at 0.1 MHz. The signals are pulsed, but the final determination of position depends on the phase of the wave. When a wave travels in a dissipative medium, pulse speed and phase speed are not necessarily the same. Johler and Horowitz (1974) estimate differences up to 5 μs at a range of 3000 km. However, it is phase that must be determined most precisely, and of course, the signal amplitude must be great enough for reception. For a homogeneous path, both amplitude and phase may be obtained from a standard ground-wave calculation. For a mixed path (ocean-land, say), Wait (1980) has described two theoretical methods. However, in practice, a much simpler calculation known as the Millington-Pressy method is usually used. In this method, amplitude and phase are found by separate applications of Millington's method, as outlined in part A. See Samaddar (1979) and CCIR Report 716 (1990).

6.2 Diffraction over buildings

6.2.1 Buildings of uniform height and spacing

A relatively simple theoretical solution to the complex problem of diffraction over buildings has been given by Xia and Bertoni (1992) and Maciel *et al.* (1993). They assume that a wave is to propagate over rows of equally-spaced buildings of uniform height. The buildings are modelled as diffracting screens (knife edges). The source may be either above or below roof-top level, and may be either close to the first row of buildings or at a distance. The authors take advantage of the fact that mathematical expressions already exist for equally-spaced knife edges of uniform height, for certain source positions. The field is found at the top of the final building of the series, using these expressions, and then the field at street level is found from this roof-top field in the manner of the geometric theory of diffraction (GTD). The direct ray from the roof top is used, and also a ray reflected from a building on the other side of the same street (amplitude assumed equal to that of the direct ray). No ground-reflected ray is used. The calculation along the rooftops is based on physical optics, and is one that cannot be done with GTD, which fails when several edges are aligned.

6.2.2 Satellite navigation

The GPS (Global Positioning System) system operates at 1227 and 1575 MHz. GPS transmissions are from satellites, and diffraction losses are usually unimportant, but not always. When the receiving antenna is mounted on a vehicle, the signal may be blocked by obvious things like buildings, bridges, trees, and tunnels.

6.3 Geometric Theory of Diffraction

The geometric theory of diffraction, in its uniform form, is increasingly being used for terrain and building diffraction calculations. Examples are computer programs reported by Luebbers (1990), Rossi and Levy (1992), and Kürner *et al.* (1993). All of these have been used for estimating the wideband characteristics (pulse response) of the radio channel as well as the diffraction attenuation. In the program described by Luebbers (1989), the terrain profile must be modelled by hand as a series of wedges, and the program takes over from there. He compares the results with measurements made as a function of height. Rossi and Levy describe a program particularly intended for an urban area for which there is a detailed data base containing the dimensions and locations of buildings. They looked critically at the impulse-response predictions, and found that the initial echoes from close-by buildings were well represented, but reflections from remote buildings were not.

Kürner *et al.* (1993) and Lebherz *et al.* (1992) describe a general-purpose program intended to find path attenuation and impulse response for both open and urban areas. It finds attenuation due to the conventional (vertical cross section) path profile, but also looks for reflections in the horizontal plane, due to both buildings and hills. The program automatically decides on how to represent the terrain as wedges, or sometimes as rounded hills. Physical optics methods are used to estimate the scattering from buildings and other objects that may be only partly illuminated and which may have rough surfaces. In areas where there is multipath, the field strength is estimated as a probability density function, and the impulse response is calculated. The success of this kind of calculation depends on very detailed terrain data.

6.4 Cascaded cylinders

Since the Sharples and Mehler (1989) calculation (described in Section 5.6 of Part A) is complicated, a simplified version has been adopted by COST 210 (1991). There are two simplifications: One is to replace the infinite summation of Vogler's method of knife edges by its first term. This produces a result similar to the method of Epstein and Peterson, but with a correction factor for the spreading losses. The other is to replace the complex integral of Wait and Conda with an approximate formula for the diffraction attenuation due to a single cylinder. The result is a computer program that is less accurate than that for the full cascaded knife edge procedure, but which runs much faster.

6.5 Physical Optics

A procedure for calculating the field by repeated numerical application of Huygens' principle (Whitteker, 1990) has been implemented in the CRC VHF/UHF prediction program, an early version of which was described by Palmer (1981). A terrain profile is used, usually obtained from a data base of elevations and ground cover types. The terrain profile is used as it is received, without any fitting of special shapes.

The most straightforward way of doing the calculation would be to proceed from point to point along the profile, finding the field as a function of height at each step, and assuming that the intervening terrain is planar. However, since terrain profiles are often defined by hundreds of points, this is very time consuming, and also risks the accumulation of numerical errors. Instead, the field is found as a function of height only at selected points, mostly on the higher ground. Between chosen points a model is made of the terrain as a rough and possibly curved reflector for calculating the field due to the reflected wave. In this way, the calculation is made much faster, with a reduction in accuracy in some cases.

Trees or buildings along the path are simply treated as part of the terrain. However, if (according to the data base) an antenna is within a forest, it is assumed that it is really in a clearing typical of a road allowance. If an antenna is within a built-up area, empirical losses are put in (Hata's equations), weighted according to how much built-up terrain there is on the path. The basic program is written in Fortran, with alphanumeric plots. Menu input and graphical output are available for PC-DOS.

6.6 Parabolic equations

Signal Science (Abingdon, Oxon, U.K.) publishes a program called FDPEM that implements the finite difference parabolic equation method. The software makes use of elevation and ground-cover data from a data base. The terrain profile is used as it is received, without any fitting of special shapes. Input is menu-driven, and graphical output is in the form of line plots or contours, or colour-filled contour plots. Since the calculations are computationally intensive, the program runs on PC-DOS equipped with an additional fast processor called a transputer. A Unix version is planned. Another program called PCPEM implements the split-step parabolic equation method. This is of less interest for diffraction purposes, since the terrain is supposed to be flat.

7.0 FORESTED AREAS

7.1 Propagation through trees

The classic work is by Tamir (1977), who models a forest as a dielectric slab through which waves can travel for a limited distance only, but which can support a lateral wave along the treetops. This model is said to be valid from 2 to 200 MHz. Above VHF, a forest is not well modelled as a continuous medium. Most of the results quoted below are empirical.

7.1.1 Temperate forests

Weissberger (1982) reported on an extensive study of models for predicting the attenuation of radio waves by trees. The traditional model for predicting the increase in loss due to propagation through trees is the exponential decay model. In logarithmic terms, the excess loss L, in decibels, due the trees is

$$L = \alpha d \qquad (8)$$

where α is a decay constant that depends on frequency, and d is the distance between antennas in metres (in contrast to the practice elsewhere in this paper of using d to denote distance in kilometres). Note that the relationship of α to the constant β of Section 6.1 of Part A is $\alpha = (10 \log e)\beta = 4.34\beta$. One particular expression for α, due to Lagrone (1960) is $0.00129 f^{0.77}$, where f is frequency in MHz. Weissberger proposed a modified exponential decay model in which the attenuation increased less rapidly as a function of distance. The parameters were found by a least-squares fit to data taken in a cottonwood forest in Colorado, U.S.A., in the frequency range 230 MHz to 95 GHz:

$$L = 0.063 f^{0.284} d \qquad 2 < d < 14\,\mathrm{m} \qquad (9)$$

$$L = 0.187 f^{0.284} d^{0.588} \qquad 14 < d < 400\,\mathrm{m} \qquad (10)$$

applicable to cases in which the ray path is blocked by dense, dry (i.e. not rained upon), in-leaf deciduous or evergreen trees in temperate-latitude forests. Exponential decay is retained up to 14 m, but the decay is slower for greater distances. This is an empirical model, and as such, takes everything into account, including the lateral wave, or whatever replaces it at frequencies greater than 200 MHz. This model does not discriminate between polarizations, because over most of its frequency range there is little difference. However, below about 500 MHz, vertically polarized waves are attenuated more strongly by a few decibels.

Brown and Curry (1982) report measured data in which the foliage attenuations are somewhat scattered, but go generally from 0.1 dB/m at 100 MHz to 1.0 dB/m at 10 GHz. This agrees roughly with the model of Weissberger (1982) for paths of 14 m or less, where the attenuation works out to 0.23 dB/m at 100 MHz, and 0.86 dB at 10 GHz.

In the frequency range 400 to 1000 MHz and for short paths, Seker and Schneider (1993) report attenuations between 0.25 and 0.35 dB/m, with little dependence on frequency in this range. These results are normalized to a very dense forest of 1000 tree stems/ha, under the assumption that specific attenuations are proportional to stem density.

Rain on trees can increase the total path attenuation by 4 dB at 400 MHz, and as much as 20 dB at 1000 MHz and higher frequencies (Weissberger, 1982). There are not many relevant measurements.

7.1.2 Tropical forests

The Jansky and Bailey empirical model is quoted by Weissberger (1982), where details may be found. Path lengths are in the range 8 to 1600 m, frequencies 25 to 400 MHz, antenna heights 2 to 7 m. Jungle attenuation was found to be 2 to 5 times greater than for a temperate forest. This model also is exponential for small distances, in this case less than about 80 m, and decays less rapidly for greater distances. At large distances, greater than about 160 m, the loss increases as 40 log d, as predicted by the lateral-wave model. However, Weissberger found the empirical model more accurate than a lateral-wave theoretical model when measured electrical parameters of the forest are used for the theoretical model. Lateral-wave models do, however, correctly predict the form of the loss variations as a function of distance, frequency, and antenna height.

7.1.3 A few trees

Rice (1971) offers a generalization of experience at VHF/UHF that is easy to apply in the field: 'Loss through a thin screen of small trees will rarely exceed 6 dB if the transmitter can be seen through their trunks. If sky can be seen through the trees, 15 dB is the greatest expected loss. Studies made at 3000 MHz indicate that stone buildings and groups of trees so dense that the sky cannot be seen through them should be regarded as opaque objects around which diffraction takes place.'

7.2 Propagation over trees

If the antennas are in clearings or above the trees, and not close to the trees, propagation will be primarily over the trees. According to Weissberger (1982), the most accurate way to find which is the appropriate mechanism is to estimate the loss for both, and choose the one that gives the smaller loss. However, he also gives the following guidelines: If at least one of the antennas is close enough to the trees that the elevation angle from the antenna to the treetops is greater than 26°, then propagation is through the trees. If the angle is less than 8°, propagation is by diffraction over the trees. For intermediate angles, both mechanisms may exist. For diffraction over trees, a knife edge is placed at the edge of the forest. Modelling studies have indicated (Weissberger, 1982, Lagrone, 1977) that the effective height of the knife edges should be chosen to be less than the true height of the trees. Height differences suggested have been 4.5 m at 83 MHz, 3 m at 485 MHz, 1.3 m at 210 and 633 MHz, 0.6 m at 1280 and 2950 Hz. Evidently the difference decreases with increasing frequency, but the numbers must be regarded only as rough indications.

The attenuation due to deciduous trees is greater when leaves are present than when they are not. Löw (1988) measured the seasonal variation of field strength at 450 and 900 MHz along roads in Germany transverse to the propagation path in a flat forested area. He found the mean range of variation between summer and winter to be 4 or 5 dB, depending on the year. CCIR Report 567-4 (1990) reports similar results in the U.S. Reudink et al (1973) found a larger seasonal variation along suburban roads with trees, amounting to a range of 10 dB at 836 MHz and up to 20 dB at 11.2 GHz.

For land-mobile paths, the presence of trees must often be taken to account along with all the other factors that affect the received signal strength. A simple method of taking everything into account has been found by Löw (1986): He compared the predictions of the Hata (1980) equations with the results of measurements made at 450 and 900 MHz around Darmstadt, and found that Hata's formulas for urban areas could also be applied to reception on roads through forested areas.

8.0 MULTIPATH

Particularly in built-up areas, but also in the presence of trees, the wave can arrive at the receiver from different directions, after reflections from these objects. The different waves create an interference pattern that can give rise to rapid fading as a mobile receiver moves through the pattern. The distance between minima of field intensity can vary from one-half wavelength upward. The half-wave spacing results from interference between two oppositely directed waves, and the larger spacings result from waves travelling at other angles with respect to each other. If there are many waves of comparable amplitudes coming from all directions, the received amplitude follows a Rayleigh probability distribution, a distribution that is often assumed in the analysis of fading. The effects of multipath fading can be reduced by increasing the transmitted power or by various diversity schemes, or in the case of digital transmission by coding and error correction.

If digital information is to be sent at a high data rate, then another effect of multipath propagation is of concern, namely the delay spread of a transmitted pulse. To visualize the effect, imagine speaking to someone in a room with a long reverberation time. After speaking each word or syllable, you must wait until the echoes die down before speaking the next one, if the message is to be understood. The radio analog of the reverberation time is the delay spread, which is a measure of the time during which strong echoes are received. If the delay spread is T, then information bits can be sent no faster than 1/T. This rate cannot be increased by increasing the power, since the power in the echoes also increases. If there is no diversity or coding to correct for the fading, the maximum rate is more like 1/8T (Lee, 1982, p.340).

Since the delay spread is a result of the different lengths of the different paths, it can be estimated roughly if the locations of the reflectors are known. Radio waves travel at 300 m/μs, so a reflector 300 m away in the direction opposite to that of the transmitter will give a delay of 2 μs relative to the time of arrival of the direct wave. A reflector the same distance in the transverse direction will give a delay of 1 μs, and reflectors at the same distance more in the direction of the transmitter will give smaller delays.

A number of measurements of delay spreads have been made. Lee (1982, p.42) suggests mean delay spreads of 1.3 μs in urban areas and 0.5 μs in suburban areas. The larger buildings in an urban area are more likely to reflect signals strongly from a distance of a few hundred metres. Bultitude and Bedal (1989) confirm typical delay spreads of about 1μs with maximum spreads up to 7μs to in urban areas, but report smaller values (< 1μs) when the base-station antenna is low, at street-lamp level. Seker and Schneider (1993) found, over a forest path of 300 m at 400, 850, and 1050 MHz, delay spreads of up to 0.6 μs for vertical polarization and up to 0.3 μs for horizontal polarization. Much longer delay times can sometimes be found. Mohr (1993) measured delays in a mountain valley of up to 30-40 μs. Ordinarily, signals with this much delay are of low amplitude, but they could be significant if the direct path were strongly attenuated.

Another effect of multipath propagation is a loss of phase coherence in the wave front, so that the gain of an antenna array, for example a collinear vertically polarized vehicle rooftop antenna, is reduced from its nominal value (Belrose, 1983).

9.0 LOCATION VARIABILITY

A radio wave received in an environment cluttered by either trees or buildings exhibits variations as the receiving antenna moves distances of the order of wavelengths, as discussed under 'multipath'. The field pattern is not predictable in detail, but it is at least possible to say something about the statistical distribution of field strengths. It is important to know this distribution if the goal is to achieve a signal level greater than a given level for a certain percentage of locations, for reliable communications, or, conversely, to have a signal level below a certain level for a certain percentage of time to avoid interference or unwanted interception of signals.

If the direct line of sight between the two antennas is blocked, and if the signal arrives by way of many reflections of comparable strength, the received power will follow a Rayleigh distribution. The cumulative distribution, i.e. the probability of the amplitude of the received signal exceeding x, is

$$P(x) = e^{-x^2/x_0^2} \tag{11}$$

where x_0 is the r.m.s. amplitude of the signal. The median of this distribution is found by setting P(x) = 0.5, giving an amplitude of $x_0\sqrt{\log_e 2}$. The Rayleigh distribution has no other free parameters. Once the median level is known, and the distribution is supposed to be Rayleigh, the distribution is entirely determined.

However, there are at least two common circumstances that require a more general distribution. (1) The direct wave, or possibly a particularly strong reflection, is substantially stronger than the other reflections. (2) As the receiving antenna moves, the median level of the received signal changes, i.e. the process generating the distribution is not stationary. To accommodate the first circumstance, the Nakagami-Rice distribution can be used. In this distribution, there is an added free parameter, namely the ratio of the received power of the direct wave to the mean power of the remaining Rayleigh-distributed wave. This parameter can vary from zero to infinity, depending on whether the signal is pure Rayleigh or pure direct wave. In forests, in the 50-150 MHz band, it has been observed (Weissberger, 1982) that the Nakagami-Rice distribution is suitable for horizontal polarization and the Rayleigh distribution for vertical polarization. For either polarization, the steady component is stronger in clearings than in the forest, and relatively weaker at higher frequencies. The Rayleigh distribution tends to occur in dense forests for frequencies greater than 100 MHz.

To accommodate the second circumstance, the distribution favored by Lorenz (1979) and by Parsons and Ibrahim (1983), except for open areas, is a combined Rayleigh and log-normal distribution, which they refer to as a Suzuki distribution. In built-up areas, at least, the distribution is considered to be Rayleigh over a small distance of say 20 m, but the median value of the signal varies over larger distances because of shadowing by various objects, and is random and log-normal up to say 100 or 200 m. Over this larger distance, the combined distribution might be used. A simpler alternative mentioned by Hagn (1980) is to use a log-normal distribution by itself for the median signal and to add a margin of 6 to 10 dB to allow for Rayleigh fading.

The Suzuki distribution is characterized by an adjustable parameter s, which, at VHF and UHF, Parsons and Ibrahim found to lie in the range 3.3 to 4.1 dB. These values were obtained from measurements in cities and forested roads in the Rhine Valley, and in London. There seems to be no way of predicting the appropriate value of the parameter in a particular place, except by observing that it is similar to some place where a distribution has been measured. However, once the parameter has been chosen, a signal level can be calculated for any chosen percentage of locations.

Figures 6 and 7 illustrate some of the distributions just mentioned. The probability density gives the best intuitive idea of the distribution of signal levels that may be expected. The log normal distribution is symmetrical on a decibel scale, while the Rayleigh distribution is skewed, including more deep fades than large enhancements. The Suzuki distribution combines the other two, and so is broader than either. The cumulative distribution is of more practical value, since it gives directly the probability of a desired signal being greater than some threshold, or of an unwanted signal being less than some value. In practice, power is usually plotted against probability on Rayleigh or log-normal paper, so that required power is easily read off for any desired probability (say 95% or 0.95). Lorenz (1979) gives such a plot for the Suzuki distribution for various values of its parameter. CCIR Report 1007-1 (1990) contains such diagrams for combined log-normal- Rayleigh, Nakagami-Rice, and other distributions. In a computer program, you just specify the probability you want, and the corresponding signal level appears in the output.

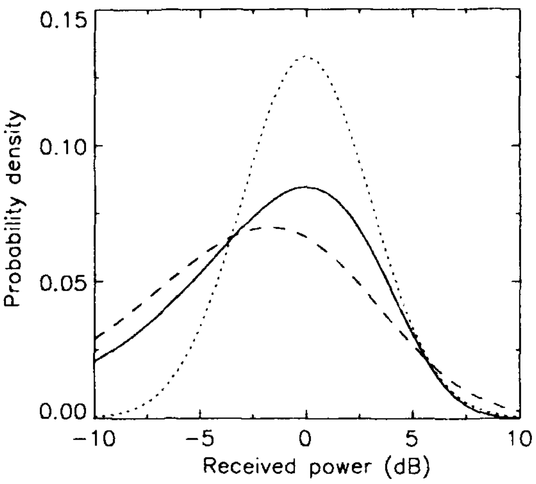

Figure 6. Probability density distributions. The solid line is Rayleigh, the dotted line is log normal with standard deviation 3 dB, and the broken line is Suzuki, also with a variance parameter of 3 dB.

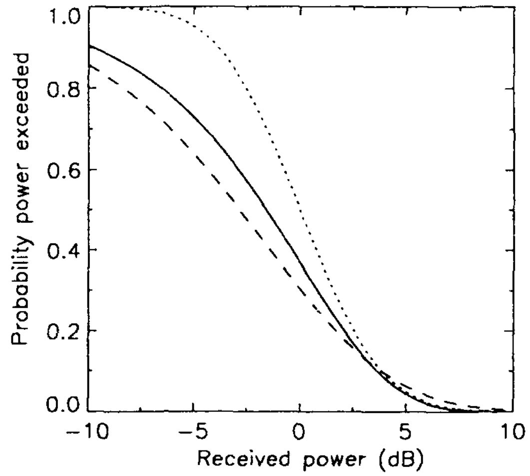

Figure 7. Cumulative probability distributions. The solid line is Rayleigh, the dotted line is log normal, and the broken line is Suzuki. The parameters are the same as in the previous figure.

10.0 ACCURACY

The accuracy of methods or implementations is difficult to assess. Average error and standard deviations are sometimes quoted, but these are difficult to interpret, because these depend so much on variables such as frequency, type of terrain, antenna heights, and whether the method was optimized on the same data set that was used for testing. For example, it is easier to make predictions for rooftop reception than for vehicle reception. It is obviously much easier in open country than in forested or suburban areas. In the VHF/UHF range, accuracy decreases with frequency since the Fresnel zone becomes smaller. The very best you can expect is a standard deviation of 5 or 6 dB for a detailed method in terrain that is not too cluttered with trees and buildings. Usually standard deviations are larger, ranging from 7 to 15 dB. Tables of prediction error are given by Preedy and Telfer (1989), Grosskopf (1989), Sandell et al (1989), and Fouladpouri and Parsons (1991). The last two are for empirical predictions.

Ideally, the probability distributions put into the program include both the location variability derived from measurements, and the error distribution of the prediction itself. It is difficult to obtain good estimates of these distributions, because they depend on all the variables mentioned in the last paragraph. Perhaps the best way to get a feeling for the accuracy of a prediction program is to compare its result with measurements that you happen to be familiar with. Figure 8 is an example of the best that can be expected at UHF in an area with

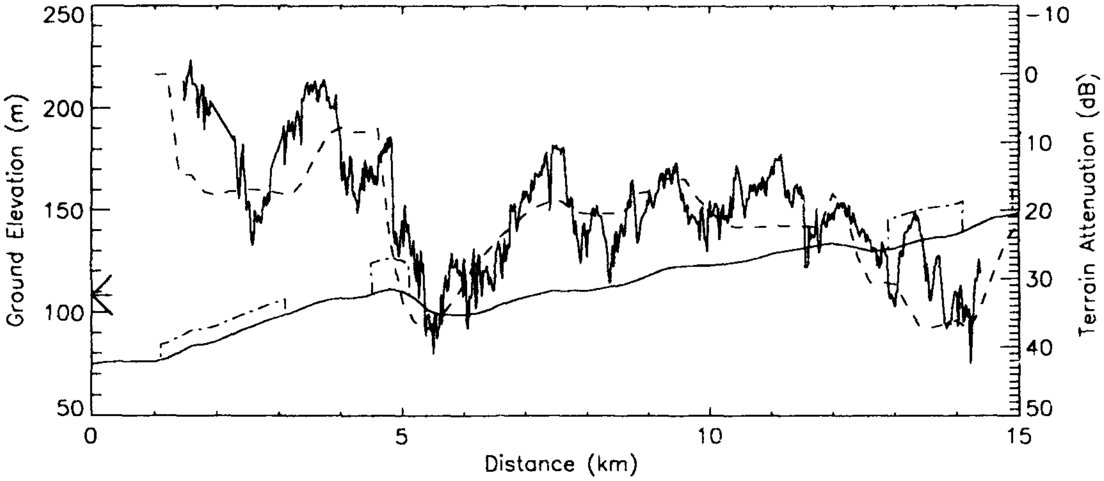

Figure 8. A terrain profile near Ottawa, and attenuation with respect to free space at vehicle height, for 910 MHz. The transmitting antenna is indicated at 110 m. On the terrain profile, suburban buildings are indicated at 2 km, and stands of trees at 5 and 13 km. The solid line is measured (20-m median) loss, and the broken line is predicted loss.

some buildings and trees. Here, the measured data are 20-metre medians, which means that most of the Rayleigh (multipath) fading has been removed. The signal is still highly variable.

11.0 APPLICATIONS PROGRAMS

Applications programs may be divided broadly into two categories. The first category includes all programs written more than a few years ago. Everything is written in Fortran. The user lets the program know what is wanted by answering questions, or perhaps creating an input file by hand, and the results of the calculation appear in tabular form or as simple graphs. In the second category are implementations in which the user lets the program know what is wanted by selecting items from menus, and typing any required numbers into labelled windows on the screen. The results appear as high-resolution graphs, usually in colour.

There is something to be said for the older format. A program written in standard Fortran (or any other standard language) is completely portable between different types of computer if the source code is made available. High resolution plots, while pretty, may mislead the user into thinking the results are more accurate than they are.

Nevertheless, programs that have menu-driven input and high-resolution graphical output are definitely the way of the future. They are easier to use, and the output can be adapted to display what you really want to know, such as detailed coverage areas, or places where there might be interference or unwanted interception of signals. With on-screen graphics, it is possible to try different options and get a visual impression of the results. Portability is becoming less of a problem with the increasing standardization of operating systems. Most specialized programs are written for PC-DOS, and some are also available for Unix, which exists in several varieties, but with some movement toward standardization. Most, but not all, of the programs described so far have been more or less of the older type. Here are examples of general-purpose programs of the newer type. (Very likely there are equally good examples that are not included, and more will appear in the future.)

Communications Data Services (Falls Church, Virginia, U.S.A.) publishes software called RFCAD™. It runs on PC-DOS, but Unix versions are available. There is a choice of methods, including Longley-Rice, Biby-C, CRC, TIREM, and Okumura. All of these have been mentioned in previous sections, except for Biby-C, which is an empirical correction to Longley-Rice that accounts for the excess attenuation due to vegetation and buildings. Multipath fading is also estimated, based on the same measurements. Coverage from one or more transmitters can be displayed on screen on a base map and printed in that form, or plotted in colour on a transparent sheet for overlaying a paper map. The software uses terrain elevations in 3-arc-second format (see next Section), and can import other formats. It also makes use of land-use data, where available.

EDX Engineering (Eugene, Oregon, U.S.A.) publishes software called SIGNAL™. It runs on PC-DOS. There is a choice of methods, including TIREM, RMD, FCC, CCIR, and Okumura. All of these have been mentioned in previous sections, except for RMD, which is described as "a simple means of including path-specific knife-edge-diffraction loss and reflections with signal level predictions based on other well-known propagation models", and FCC, which is an official broadcast and land-mobile prediction method for the U.S. There is also a ray-tracing program for microcellular radio. The user can select building and foliage blockage factors at the receive site or use a ground-cover data base. Fade margins are estimated. Multi-site coverage studies can be done, and field-strength contours can be displayed along with a base map. The software uses terrain elevations in 3-arc-second format (see next section), and can import other formats. It also makes use of land-use data, where available.

GEC-Marconi (Chelmsford, Essex, U.K.) has written software called COVMOD for area coverage and DRAW_PROFILE for fixed links. There is an on-line service. The software, which runs on a Vax computer, uses a terrain data base for the U.K., including land-cover codes. Empirical or semi-empirical methods are used. Multi-site coverage can be done.

12.0 TERRAIN DATA

Any method of predicting attenuation due to terrain diffraction requires terrain data. Terrain profiles can be obtained by hand from topographic maps, but this is very tedious. A data base is very desirable, almost necessary. Terrain elevation is the most important quantity to obtain, but terrain cover information (forest, buildings, water) is also valuable. For reasonably fast access, the data must be available as a digital elevation model, as opposed to, say, digitized elevation contours. Most elevation models are in the form of an approximately rectangular grid, although there are other possibilities. Digital terrain data are not always freely available, because they are expensive to create, because they have strategic value, and because formats differ.

However, there is a NATO standard for elevation data that has come into widespread use. It is Digital Terrain Elevation Data (DTED) Level 1, which is the subject of STANdarization AGreement 3809. In this format, an elevation is stored, as a 16-bit number, for every point in a 3-arc-second array, that is, 3″ of latitude by 3″ of longitude, except at northern latitudes, where the number of seconds of longitude is increased to 6, 9 etc. to keep the grid roughly 100-m square. Elevations are stored as profiles of 1201 points running from south to north in a 1° × 1° cell. Successive profiles go from west to east. This format was not created for radio-propagation predictions, and it is not ideal for that purpose, since to obtain elevations along a roughly east-west path that crosses a cell, all the data in the cell must be read. Nevertheless, since it appears to be the only widely-used standard, it makes sense to use it. DTED elevations exist for much of North America and much of Europe, but availability depends on the decisions of the governments involved. In the U.S., elevations derived from DTED are in the public domain and are available at low cost. Land-cover data are also available. In Canada, which is partly covered, DTED elevations are available, but at a higher price.

A much more general standard for all kinds of geographic information has recently emerged, called DIGEST (DIgital Geographic Exchange STandard). This does not have immediate application to radiowave propagation calculations, but in the future, a product suitable for these calculations could be derived from it.

There are also other forms of terrain data. In Canada, there is a 500-metre data base for the more populated areas, as well as a 7-category land-cover code. In Britain, the Ordnance Survey publishes a 50-metre data base, and a similar one is recently available also from EDX. In Germany, the German Telekom uses a 5″ × 5″ data base which includes 13 categories of land cover. In Sweden, there is a 50-metre data base, including land cover. Undoubtedly there are many more sources of data beyond those mentioned.

ITU Working Party 5B (now part of the new Study Group 3) has drafted a new Recommendation (1993b) for the contents of a terrain data base for radiowave propagation prediction purposes. However, no specific standard is proposed. Land-cover categories such as mean/maximum building height, building density, tree height, type, and density are recommended. For cities, a very detailed data base containing the shapes and sizes of buildings would be useful for some purposes.

13.0 CONCLUSION

This part of the lecture has described a number of planning tools for groundwave and diffraction propagation. These range from simple equations or graphs to sophisticated computer calculations. They are planning tools that have been described in the literature, or otherwise known to the author. There are undoubtedly many more that have not been included, particularly those that may have been written in-house by various organizations and not widely publicized or distributed. Although comments have been made in some places about the suitability of some of them, no definite recommendations have been made. The suitability of a planning tool depends very much on the particular needs of the user.

14.0 REFERENCES

Note: If there is a series of papers by one author on the same subject, only the most recent may be listed.

Aurand, J.F. and R.E. Post, "A comparison of prediction methods for 800 MHz mobile radio propagation", IEEE Trans. Veh. Tech., VT-34(4), 149-153, 1985.

Ayasli, S., "SEKE: a computer model for low altitude radar propagation over irregular terrain", IEEE Trans. Ant. Prop. AP-34(8), 1013-1023, 1986.

Barrick, D.E., "Theory of HF and VHF propagation across the rough sea, 1, the effective surface impedance for a slightly rough highly conducting medium at grazing incidence", Radio Sci. 6, 517-526, 1971a.

Barrick, D.E., "Theory of HF and VHF propagation across the rough sea, 2, application to HF and VHF propagation above the sea", Radio Sci. 6, 527-533, 1971b.

Belrose, J.S., "Vehicular antennas for 800 MHz mobile radio", Proc. 33rd IEEE Veh. Tech. Conf., 191-196, 1983.

Blomquist, A., and L. Ladell, "Prediction and calculation of transmission loss in different types of terrain", AGARD Conf. Proc. No. 144, Electromagnetic wave propagation involving irregular surfaces and inhomogeneous media, 32-1 to 32-17, 1974.

Bremmer, H., Terrestrial Radio Waves, Elsevier, Amsterdam, 343 pp., 1949.

Brown, G.S., and W.J. Curry, "A theory and model for wave propagation through foliage", Radio Sci., 17(5), 1027-1036, 1982.

Bullington, K., "Radio propagation at frequencies above 30 Megacycles", Proc. IRE, 35, 1122-1136, 1947.

Bullington, K., "Radio propagation for vehicular communications", IEEE Trans. Veh. Tech. VT-(4), 295-308, 1977. (A reprint, with only minor changes, of the article cited above and of "Radio propagation fundamentals", in a special issue on propagation.)

Bultitude, R.J.C., and G.K. Bedal, "Propagation characteristics on microcellular urban mobile radio channels at 910 MHz",- IEEE J. Selected Areas Comm., 7(1), 1989.

CCIR Rec. 368-7, "Ground-wave propagation curves for frequencies between 10 kHz and 30 MHz", Recommendations of the CCIR, Vol. V, ITU Geneva, 1992.

CCIR Rec. 570-5, "VHF and UHF propagation curves for the frequency range from 30 MHz to 1000 MHz.", Propagation in Non-ionized Media, Recommendations of the CCIR, Vol. V, ITU Geneva, 1986.

CCIR Report 239-7, "Propagation statistics required for broadcasting services using the frequency range 30 to 1000 MHz", Reports of the CCIR, Vol. V, ITU, Geneva, 1990.

CCIR Report 567-4, "Propagation data and prediction methods for the terrestrial land mobile service using the frequency range 30 MHz to 3 GHz", Reports of the CCIR, Vol. V, ITU, Geneva, 1990.

CCIR Report 714-2, "Ground-wave propagation in an exponential atmosphere", Reports of the CCIR, Vol. V, ITU Geneva, 1990.

CCIR Report 716-3, "The phase of the ground wave", Reports of the CCIR, Vol. V, ITU Geneva, 1990.

CCIR Report 1007-1, "Probability distributions in radio-wave propagation", Reports of the CCIR, Vol. V, ITU Geneva, 1990.

COST 210, Influence of the atmosphere on interference between radio communications systems at frequencies above 1 GHz, Commission of the European Communities, L-2920, Luxembourg, 1991.

de Assis, M.S., "A simplified solution to the problem of multiple diffraction over rounded obstacles", IEEE Trans. Ant. Prop., AP-19(2), 292-295, 1971.

Delisle, G.Y., J.-P. Lefevre, M. Lecours, and J.-Y. Chouinard, "Propagation loss prediction: a comparative study with application to the mobile radio channel", IEEE Trans. Veh. Tech. VT-34(2), 86-96, 1985.

DeMinco, N., "Ground-wave analysis model for MF broadcast systems", NTIA Report 86-203, 1986.

Deygout, J., "Multiple knife-edge diffraction of microwaves", IEEE Trans. Ant. Prop., AP14(4), 480-489, 1966.

Egli, J.J., "Radio propagation above 40 MC over irregular terrain", Proc. IRE, 1383-1391, October, 1957.

Eppink, D., and W. Kuebler, TIREM/SEM Handbook, U.S. Department of Defense, Electromagnetic Compatibility Analysis Center, ECAC-HDBK-93-076, 134 pp., March 1994.

Epstein, J., and D.W. Peterson, "An experimental study of wave propagation at 850 Mc", Proc. IRE, 41(5), 595-611, 1953.

Fouladpouri, S.A.A, and J.D. Parsons, "A new model for mobile radio signal strength predictions using a digitized terrain data map", Seventh International Conference on Antennas and Propagation, ICAP 91, IEE Conf. Pub. No. 333, 1991.

Furutsu, K., "A systematic theory of wave propagation over irregular terrain", Radio Sci. 17, 1037-1059, 1982.

Grosskopf, R., "Comparison of different methods for the prediction of field strength in the VHF range", IEEE Trans. Ant. Prop. AP-35(7), 852-859, 1987.

Grosskopf, R. "Comparison of field-strength prediction methods in the UHF range", EBU Review - Technical, No. 229, 102-110, June 1988.

Grosskopf, R. "Comparison of field-strength prediction methods in the UHF range", Sixth International Conference on Antennas and Propagation, ICAP 89, IEE Conf. Pub No. 301, 1989.

Hagn, G.H., "VHF radio system performance model for predicting communications operational ranges in irregular terrain", IEEE Trans. Comm. COM-28(9), 1637-1644, 1980.

Hata, M., "Empirical formula for propagation loss in land mobile radio services", IEEE Trans. Veh. Tech., VT-29(3), 317-325, 1980.

Hill, D.A., and J.R. Wait, "Ground wave attenuation for a spherical earth with arbitrary surface impedance", Radio Sci., 15(3), 637-643, 1980.

Hufford, G.A., A.G. Longley, and W. A. Kissick, A Guide to the Use of the ITS Irregular Terrain Model in the Area Prediction Mode, NTIA Report 82-100, April 1982.

Ibrahim, M.F., and J.D. Parsons, "Signal strength prediction in built-up areas Part 1: Median signal strength", IEE Proc., Pt. F, 130(5), 377-384, 1983.

IEEE Vehicular Technology Society Committee on Radio Propagation, "Coverage prediction for mobile radio systems operating in the 800/900 MHz frequency range", IEEE Trans. Veh. Tech. 37(1), 3-71, 1988.

ITU, Atlas of Ground-wave propagation curves for frequencies between 30 Mc/s and 300 Mc/s, International Telecommunication Union, Geneva, 1955.

ITU, Second Atlas, Atlas of Ground-wave propagation curves for frequencies between 30 and 10.000 Mc/s, International Telecommunication Union, Geneva, 1959.

ITU Catalogue of Software for Radio Spectrum Management, 110 pp., ITU, Geneva, 1993a.

ITU, "Digital topographic databases for propagation studies", Draft new recommendation, 1993b.

Johler, J.R., and S. Horowitz, "Propagation of a Loran pulse over irregular, inhomogeneous ground", AGARD Conference Proceedings No. 144, pp. 28-1 to 28-13, 1974.

Kürner, T., D.J. Cichon, and W. Wiesbeck, "Concepts and results for 3D digital terrain-based wave propagation models: an overview", IEEE J. Selected Areas Comm., 11(7), 1002-1012, 1993.

Lagrone, A.H., "Forecasting television service fields", Proc. IRE, 48(6), 1009-1015, 1960.

Lagrone, A.H., "Propagation of VHF and UHF electromagnetic waves over a grove of trees in full leaf", IEEE Trans. Ant. Prop., AP-25(6), 866-869, 1977.

Lebherz, M., W. Wiesbeck, and W. Krank, "A versatile wave propagation model for the VHF/UHF range considering three-dimensional terrain", IEEE Trans. Ant. Prop., 40(10), pp. 1121-1131, 1992.

Lee, W.C.Y., Mobile Communications Engineering, 464 pp., McGraw-Hill, New York, 1982.

Longley, A.G. and P.L. Rice, Prediction of Tropospheric Radio Transmission Loss over Irregular Terrain, A Computer Method - 1968, ESSA Technical Report ERL 79-ITS 67, 1968.

Lorenz, R.W., "Theoretical distribution functions of multipath propagation and their parameters for mobile radio communication in quasi-smooth terrain", AGARD Conference Proc. No. 269, Terrain Profiles and Contours in Electromagnetic Wave Propagation, 17-1 to 17-16, 1979.

Löw, K., "UHF field-strength measurements for determination of the influence of buildings and vegetation in the land mobile radio service", Proc. 36th IEEE Veh. Tech. Conf., 40-45, 1986.

Löw, K., "UHF measurements of seasonal field-strength variations in forests", IEEE Trans. Veh. Tech., 37(3), 121-124, 1988.

Luebbers, R.J., "A semiblind test of the GTD propagation model for reflective rolling terrain", IEEE Trans. Ant. Prop., 38(3), 403-405, 1990.

Maciel, L.R., H.L. Bertoni, and H.H Xia, "Unified approach to prediction of propagation over buildings for all ranges of base station antenna height", IEEE Trans. Veh. Tech. 42(1), 41-45, 1993.

Maclean, T.S.M., and Z. Wu, Radiowave Propagation over Ground, 299 pp., Chapman and Hall, London, 1993.

Meeks, M.L., Radar Propagation at Low Altitudes, 105pp, Artech, Boston, 1982.

Meeks, M.L., "VHF propagation over hilly, forested terrain", IEEE Trans. Ant. Prop. AP-31(3), 483-489, 1983.

Millington, G., "Ground wave propagation over an inhomogeneous smooth earth", Proc. IEE, Part III, Vol. 96(39), 53-64, 1949.

Mohr, W., "Wideband propagation measurements of mobile radio channels in mountainous areas in the 1800 MHz frequency range", 43rd IEEE Veh. Tech. Conf., 49-52, May 1993.

NTIS, "Master Propagation System (MPS 11) User's Manual", NTIS Accession No. PB83-178624, computer program tape: NTIS No. PB-173971, 1983.

Okumura, Y., E. Ohmori, T. Kawano, and K. Fukuda, "Field strength and its variability in VHF and UHF land-mobile service", Rev. Elec. Comm. Lab., 16(9-10), 825-873, 1968.

Ott, R.H., "Calculation of ground wave attenuation over irregular, inhomogeneous, layered media using program WAGNER", AGARD Lecture Series LS-131, 3-1 to 3-17, 1983.

Ott, R.H., "RING: An integral equation algorithm for HF-VHF radio wave propagation over irregular, inhomogeneous terrain", Radio Sci., 27(6), 867-882, 1992.

Ott, R.H., and L.A. Berry, "An alternative integral equation for propagation over irregular terrain", Radio Sci., 5(5), 767-771, 1970.

Ott, R.H., L.E. Vogler, and G.A. Hufford, "Ground-wave propagation over irregular inhomogeneous terrain: comparisons of calculations and measurements", IEEE Trans. Ant. Prop., AP-27(2), 284-286, 1979.

Palmer, F.H., "The Communications Research Centre VHF/UHF propagation prediction program: an overview", Can. Elec. Eng. J., 6(4), 3-9, 1981.

Parsons, J.D., and M.F. Ibrahim, "Signal strength prediction in built-up areas Part 2: Signal variability", IEE Proc., Pt. F, 130(5), 385-391, 1983.

Paunović, D.S., Z.D. Stojanović, and I.S. Stojanović, "Choice of a suitable method for the prediction of the field strength in planning land mobile radio systems, IEEE Trans. Veh. Tech. VT-33(3), 259-265, 1984.

Preedy, K.A., and C.R. Telfer, "Software tools for the planning of VHF, UHF and microwave systems", Sixth International Conference on Antennas and Propagation, ICAP 89, IEE Conference Publication No. 301, 382-366, 1989.

Reudink, D.O., and M.F. Wazowicz, "Some propagation experiments relating foliage loss and diffraction loss at X-band and UHF frequencies", IEEE Trans. Comm., COM-21(11), 1198-1206, 1973.

Rice, P.L., "Some effects of buildings and vegetation on VHF/UFH propagation", 1971 IEEE Mountain-West EMC Conference Record, 1-10, 1971.

Rice, P.L., A.G. Longley, K.A. Norton, and A.P. Barsis, Transmission Loss Predictions for Tropospheric Communications Circuits, National Bureau of Standards Technical Note 101, NTIS AD-687 820, (two volumes) 1967.

Richter, J.H. (editor), Radio Wave Propagation Modeling, Prediction and Assessment, AGARDograph No. 326, 126 pp., 1990.

Rossi, J.-P., and A.J. Levy, "A ray model for decimetric radiowave propagation in an urban area", Radio Sci. 27(6), 971-979, 1992.

Rotheram, S., "Ground wave propagation, part1: Theory for short distances; part 2: Theory for medium and long distances and reference propagation curves", IEE Proc. 128, Pt F (5), 275-295, 1981.

Rotheram, S., J.D. Milsom, R.N. Herring, J.M. Pielou, and R.S. Gill, "Ground-wave propagation over irregular surfaces", Fourth International Conference on Antennas and Propagation, ICAP 85, IEE Conf. Pub. No. 248, 1985.

Samaddar, S.N., "The theory of Loran-C ground wave propagation - a review", Navigation: Journal of the Institute of Navigation, 26(3), 173-187, 1979.

Sandell, R.S., C.P. Bell, and R.W. Lee, "Field strength prediction for VHF/UHF terrestrial broadcasting and mobile radio services", Sixth Int. Conference on Antennas and Propagation, ICAP 89, IEE Conference Publication No. 301, 360-366, 1989.

Seker, S.S. and A. Schneider, "Experimental characterization of UHF radiowave propagation through forests", IEE Proc. H 140(5), 329-335, 1993.

Sharples, P.A., and M.J. Mehler, "Cascaded cylinder model for predicting terrain diffraction loss at microwave frequencies, IEE Proc., 136, Pt. H, No. 4, 331-337, 1989.

Shibuya, S., A Basic Atlas of Radio-wave Propagation Systems, 778 pp., Wiley-Interscience, New York, 1987.

Stocker, K.E., B.E. Gschwendtner, and F.M. Landstorfer, "Neural network approach to prediction of terrestrial wave propagation for mobile radio", IEE Proc. -H, 140(4), 315-320, 1993.

Tamir, T., "Radio wave propagation along mixed paths in forest environments", IEEE Trans. Ant. Prop., AP-25(4), 471-477, 1977.

Wait, J.R., "Theories for radio ground wave transmission over a multisection path", Radio Sci., 15(5), 971-976, 1980.

Weissberger, M.A., An Initial Critical Summary of Models for Predicting the Attenuation of Radio Waves by Trees, ECAC Report ESD-TR-81-101, 1982.

Whitteker, J.H., "Fresnel-Kirchoff theory applied to terrain diffraction problems", Radio Sci., 25(5), 837-851, 1990.

Xia, H.X., and H.L. Bertoni, "Diffraction of cylindrical and plane waves by an array of absorbing half-screens", IEEE Trans. Ant. Prop., 40(2), 170-177, 1992.

Sensing of Radio Refractivity and Aerosol Extinction

Juergen H. Richter
Ocean and Atmospheric Sciences Division
NCCOSC RDTE DIV 54
53570 SILVERGATE AVE
SAN DIEGO CA 92152-5230
USA

1. SUMMARY

Sensing of radio refractivity has historically been accomplished with direct sensing techniques such as radiosondes. While direct sensing techniques provide good data for propagation assessment purposes, remotely sensed data would be more desirable. Various direct and remote sensing techniques and an assessment of their potential operational usefulness are reviewed. Included are radiosondes, refractometers, radar sounders, lidars, satellite-based sensors, radiometric and radio propagation techniques. The need for and feasibility ot providing three-dimensional, time-varying refractivity fields for propagation assessment are addressed.

Aerosol extinction is often the atmospheric parameter limiting electrooptical systems performance. For proper performance assessment, slant path extinction must be known. For several decades, attempts have been made to infer aerosol extinction from lidar backscatter measurements. A discussion of selected lidar techniques and their limitations is presented.

2. INTRODUCTION

Modern sensor and weapon systems rely on propagation of electromagnetic or electrooptical energy in an atmosphere with highly variable properties. For example, radars may detect targets far beyond the normal radio horizon or encounter holes in coverage dependent on the vertical refractivity structure encountered. Systems operating in the visible or infrared wave bands can be rendered totally ineffective in the presence of clouds or fogs. A quantitative assessment of the impact of the propagation medium on a system requires an adequate description of the relevant atmospheric parameters which can be obtained through sensing, numerical modeling or a combination of both. In the following, various techniques for sensing radio refractivity and aerosol extinction are described.

3. RADIO REFRACTIVITY

3.1 Structure and variability

Before addressing sensing techniques, it is important to establish *what* needs to be sensed, how *accurate* measurements ought to be and how *often* and *where* data should be taken.

Radio refractivity N ($N=[n-1]10^6$; n = refractive index) in the atmosphere is given by

$$N=77.6[P/T+4810e/T^2] \tag{1}$$

where P is the atmospheric pressure (hPa), T the temperature (K) and e the partial water vapor pressure (hPa). Under most atmospheric conditions, refractivity is primarily dependent on the partial water vapor pressure. Sensing efforts for radio refractivity are, therefore, mainly concerned with the vertical distribution of water vapor in the atmosphere.

For radio propagation assessment purposes, the absolute accuracy of N is less important than vertical refractivity gradients and their height. Based on experience in anomalous radio propagation assessment, the height of refractive layers should be known with an accuracy of some 10 m and N-unit changes across a layer to approximately one N-unit.

Answering the question of how *often* and *where* refractivity profiles should be taken requires an understanding of the temporal and spatial behavior of atmospheric refractivity. One of the best tools to visualize atmospheric refractivity structure is a special radar built for exactly that purpose (Richter, 1969). The radar is a vertically-pointing frequency-modulated, continuous-wave (FM-CW) radar which senses the turbulence structure parameter C_n^2 for the refractive index. While the relationship between C_n^2 and the refractivity profile is not simple, strong radar echoes are most often associated with steep vertical refractivity gradients. Temporal and spatial changes of radar echoes are, therefore, an excellent description of temporal and spatial variations of layers in the vertical refractivity profile. An example is shown in figure 1 where the

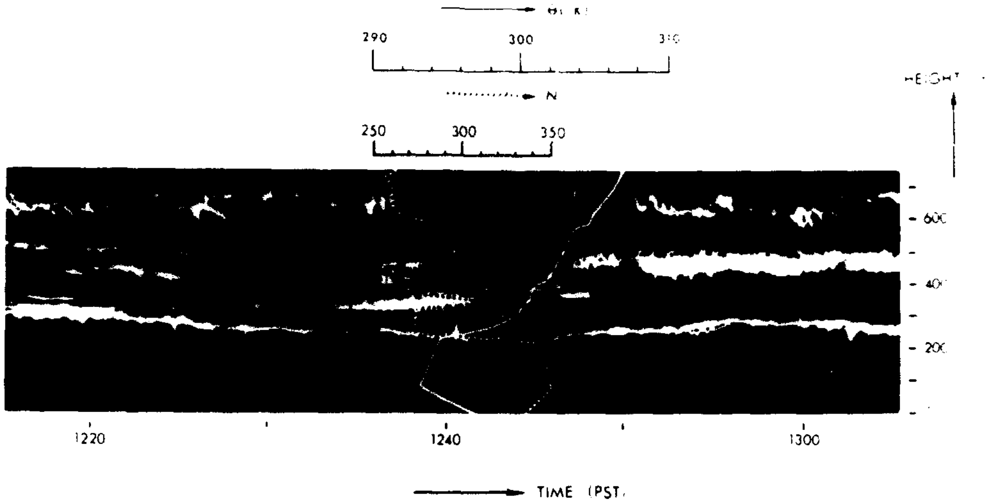

Figure 1. Atmospheric refractivity structure observed with a vertically pointing radar and concurrent radiosonde sounding (solid line is potential temperature θ, dashed line is refractivity N).

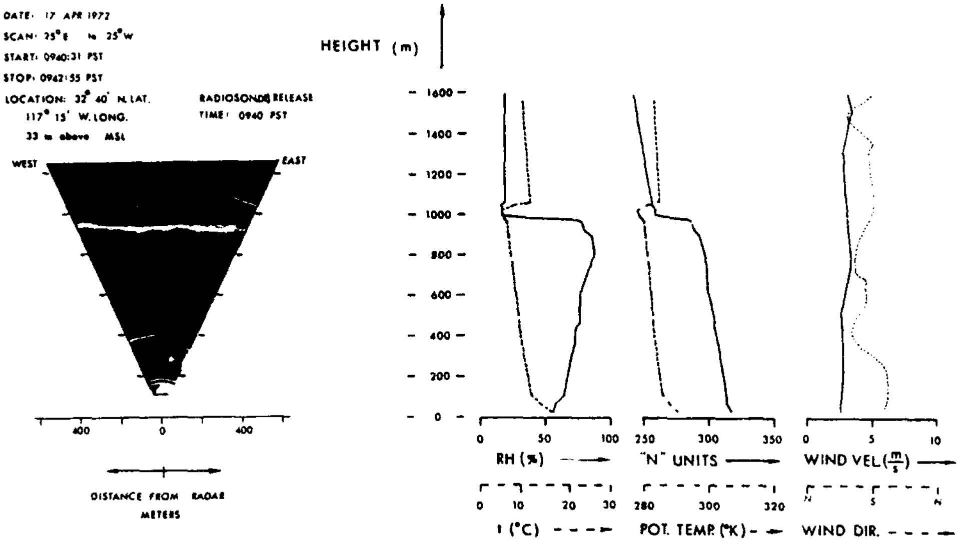

Figure 2. Scanning radar observation of refractivity structure and concurrent radiosonde data.

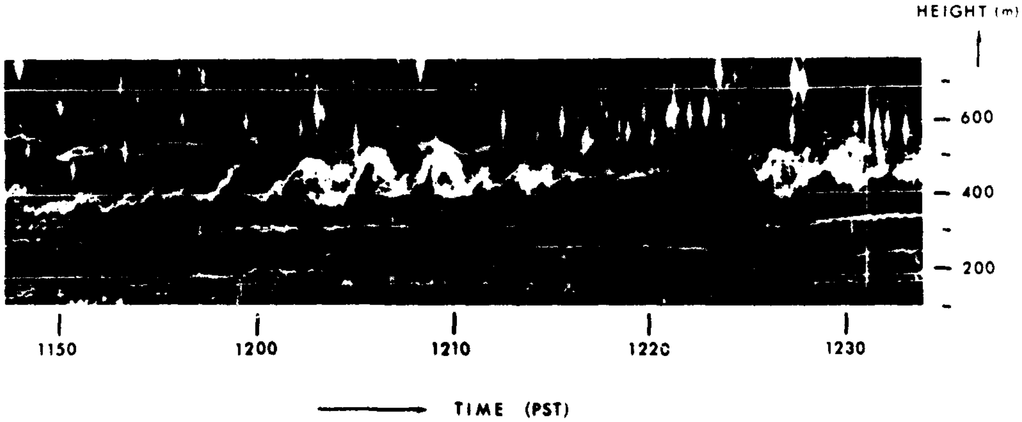

Figure 3. Dynamic atmospheric refractivity structure.

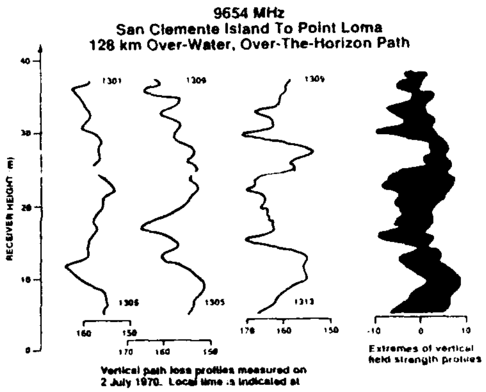

Figure 4. Vertical profiles of radio signals.

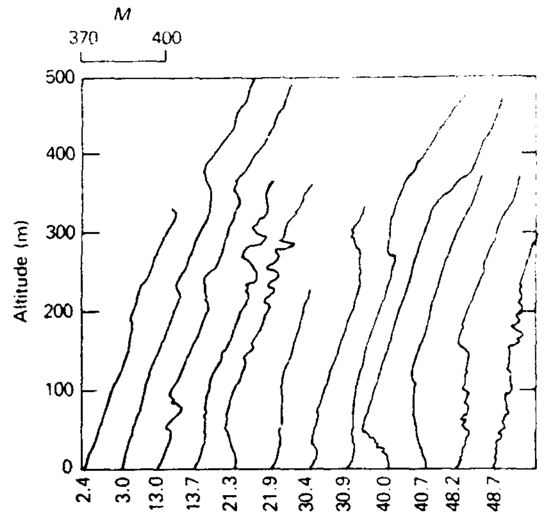

Figure 5. a) Refractivity profiles measured along a propagation path (Dockery and Konstanzer, 1987).

vertically pointing radar senses returns which are associated with strong gradients in the directly-sensed (radiosonde released at 1238 PST) refractivity profile. Several distinct layers can be seen which descend and rise with time. Another example is shown in figure 2, where a scanning FM-CW radar provides a spatial picture of an atmospheric layer which, again, coincides with the steep gradient in the directly sensed radiosonde profile (Richter et al., 1973). Figure 3 is an example of dynamic features frequently observed. There are stable layers above and below an atmospheric wave train that perturbs the upper stable layers but not the ones below, which are perturbed themselves by smaller wave motions. The vertical structures between 100 and 170 m are caused by convection in the marine layer below. Figures 1-3 convey a picture of a dynamic refractivity structure consistent with propagation measurements, which, when influenced by atmospheric refractive layers, vary (fade) with time. Figures 4-7 illustrate signal variability and suggest fundamental limitations to instantaneous signal-level predictability. Figure 4 shows 9.6 GHz signals for a 128 km over-water, over-the-horizon path measured with a receiver which was moved vertically between 5 and 38 m above the surface. The numbers at the tops and bottoms of the three individual traces indicate the start and stop time for the measurements. Acquisition of the three individual profiles took 4 minutes each. Even though the three profiles are separated by not more than 12 minutes, they have little resemblance to each other. The upper and lower envelopes of signal variability for the entire measurement period are shown on the right side of the figure indicating almost 20 dB variability. This number may be considered large and disappointing for high-fidelity assessment purposes. However, this variability is superimposed on 50 - 60 dB signal enhancements over standard atmospheric conditions (in figure 4, the transmitter was located 10 m above sea level, troposcatter loss is 215 dB; free space loss is 154 dB). This illustrates an important point: the quality of propagation and environmental models should be judged by their ability to

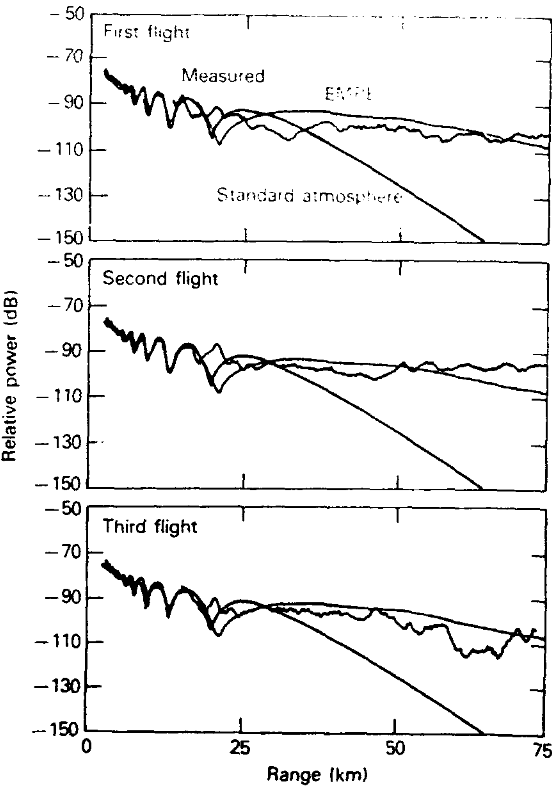

Figure 5. b) Measured and modeled received power fo the refractivity conditions of figure 5a.

predict average signal enhancements (or decreases) rather than short term fluctuations; the latter may appear large by themselves but are really small compared to the overall effect. Figure 5 (reproduced from Dockery and Konstanzer, 1987) addresses the same point using state-of-the art range-dependent refractivity measurements and range-dependent propagation models. Refractivity profiles calculated from helicopter-borne temperature and humidity measurements (figure 5a) show a variable refractivity environment along a propagation path. These profiles were used with the range-dependent propagation code EMPE (Ko et al., 1983) to calculate path loss at 5.65 GHz as a function of range. Figure 5b shows measured path loss values (from an aircraft flying at a constant altitude of 31 m), calculations based on the helicopter measurements, and, for comparison purposes, path loss for a standard atmosphere. For all three cases in figure 5b, the propagation calculations predict the general signal enhancement for beyond-the-horizon ranges but disagree at certain ranges with the measurements by as much as 20 dB.

Occasionally, the environment varies so rapidly that measuring such a variability is not feasible. Even if it were, the rapid changes would make accurate propagation predictions impossible. Two examples given by Anderson (1993) illustrate stable and variable refractivity environments. Anderson investigated low-altitude, short-range radar detection capabilities under evaporation ducting conditions. A shore-based 9.4 GHz radar at 23.5 m above mean sea level tracked a calibrated target at 4.9 m above the sea. Figure 6 shows radar data (propagation loss) for target ranges between 3-17 km. It is remarkable how closely the measurements cluster around what propagation models predict for the 7-8 m evaporation duct present (for this evaporation duct strength, signal levels between approximately 7-15 km are below those plotted for a standard atmosphere). The same radar measurements repeated on another day are shown in figure 7. Propagation loss levels show instantaneous variations of up to 20 dB. The reason for this variability was an elevated refractive layer responsible for an approximately 50 m thick surface-based duct that dominated the propagation mechanism. This elevated layer apparently fluctuated sufficiently to cause the highly-variable propagation loss values. Figure 3 serves as a reminder of possible refractivity complexity and variability. There is no way of either measuring or modeling such highly variable refractivity structures for instantaneous signal strength predictions. This means there will be situations for which an accurate instantaneous sensor performance assessment cannot be provided. Fortunately, such highly variable situations are rare (a subjective estimate is that they occur less than 10% of the time) and techniques may be developed to make the operator aware of such situations and perhaps bracket the expected variability. For the majority of the situations encountered, the assumption of horizontal homogeneity is reasonable. It was found that calculations of propagation enhancements based on a single vertical profile were correct in 86% of the cases. A similar conclusion has been reached from years of shipboard experience with the US Navy's Integrated Refractive Effects Prediction System (Hitney et al., 1985).

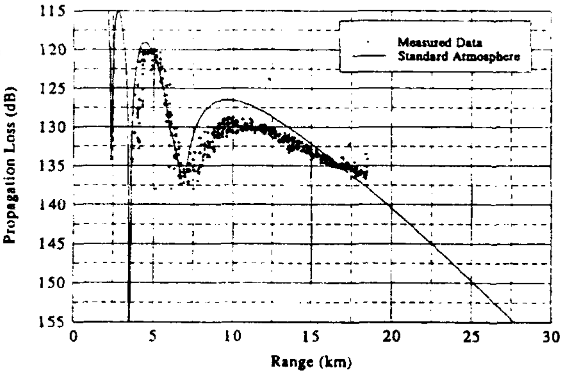

Figure 6. Propagation loss measurements under stable atmospheric conditions

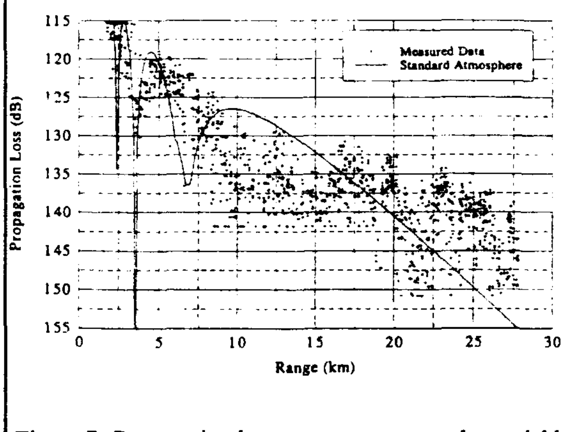

Figure 7. Propagation loss measurements under variable refractivity conditions.

Additional excellent quantitative refractivity and propagation data have recently been obtained during a program in the southern California coastal area named VOCAR [Variability of Coastal Atmospheric Refractivity, (Paulus, 1994)]. The major objective of this program is the development of a data assimilation system which provides refractivity nowcasts and forecasts based on both sensed data and meteorological numerical models. Such a data assimilation system is the only hope for an operational refractivity assessment and forecasting system. One component of VOCAR was the simultaneous and continuous measurement of a radio signal radiated from the northern tip of San Clemente Island (SCI) and received simultaneously at Pt. Mugu (133 km path) and at San Diego (127 km path). These propagation paths are

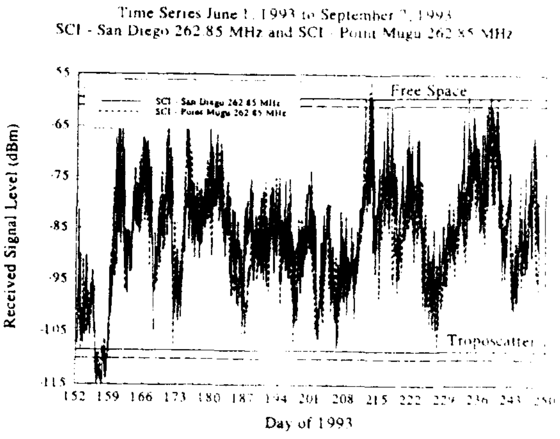

Figure 8. Signal levels for two propagation paths.

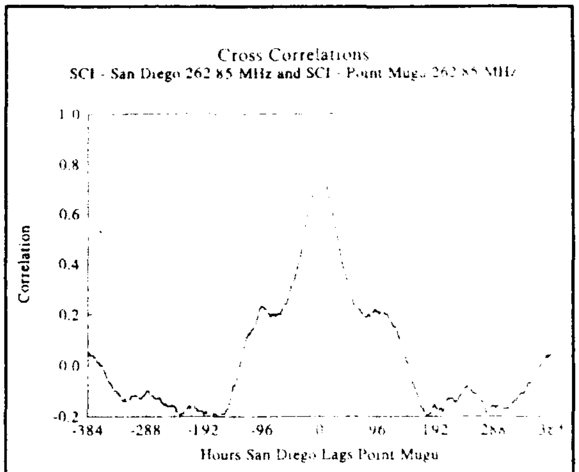

Figure 9. Cross correlation between the two signals of figure 8.

nearly identical in length but are located in different areas of the S. California Bight. Variations in signal levels over the two paths are a precise measure of path-integrated refractivity conditions and their temporal changes. Figure 8 shows over three months' of signal levels for the two paths (Rogers, 1994). Signal levels vary over six orders of magnitude which underlines the operational importance of refractivity effects and assessment. However, the variations in signal level over the two geographically different paths follow each other quite consistently. The cross-correlation of the signals along the two propagation paths is shown in figure 9 indicating a correlation factor of nearly 0.8. There is a small time-lag between the Point Mugu and the San Diego signals consistent with the notion of features advected by the prevailing north-westerly flow. One may conclude that a major benefit would be derived from a data assimilation system capable of predicting gross refractivity conditions for the S. California Bight area from which the gross signal fluctuations can be derived. Horizontal inhomogeneities over this area are probably not predictable and are usually insignificant compared to the overall assessment.

In conclusion, it is very important to realize and appreciate the temporal and spatial variability of atmospheric refractivity structure for any sensing and forecasting effort. For most applications, horizontal homogeneity is a reasonable assumption. Therefore, single profiles of refractivity measured either directly or remotely are adequate for propagation assessment purposes. Most promising is a data assimilation system, which combines sensed and numerically modeled data.

3.2 Direct Sensing Techniques

Radiosondes

Radiosondes have been, and still are, the most frequently used direct sensing technique for obtaining radio refractivity profiles. Ever since the slow-response lithium chloride humidity sensor was replaced with the carbon element some 35 years ago (thin film capacitors are used today), the radiosonde has provided satisfactory vertical humidity profiles under most conditions. A commonly used radiosonde system today consists of a Vaisala RS 80 series radiosonde and suitable receivers. The specified accuracy of the sensors is 0.5 hPa for the pressure, 0.2 °C for temperature and 2% for relative humidity (humidity lag is 1 s for 6 m/s flow at 1000 hPa, +20 °C). The radiosonde package itself weighs less than 200 g and can be launched with a 100 g balloon. The radiosonde senses temperature, humidity and pressure continuously but each of the sensors is selected in succession for relaying the information to the ground station. The duration of the measurement sequence is approximately 1.5 s. This results in non-continuous temperature and humidity profiles which can cause problems when the sonde ascends through very sharp vertical humidity gradients while transmitting other data. Such problems are not very common and rarely significant for operational assessments; they can be avoided for special applications by either more rapid switching schemes or continuous profile measurements (i.e., launching more than one radiosonde with one of the sondes transmitting humidity only). The radiosonde can also be equipped with navigation receivers (Omega or LORAN C) which permits sensing of winds. Incorrect surface values represent one problem encountered with radiosondes. The launch point may be affected by surface heating (or by a local heat source in the case of shipboard launches) and lead to systematic errors (Helvey, 1983). Shipboard-induced surface heating errors can be avoided by dropsondes (released by aircraft and descending by parachute) or by launching the radiosonde sensor package with a small rocket and obtaining the measurements during parachute descent away from the ship (Rowland and Babin, 1987). These techniques measure the profiles away from the ship down to the ocean surface. They do not, however, measure (as sometimes erroneously stated) humidity profiles responsible for evaporation ducting. Another shortcoming of radiosonde-measured profiles is the non vertical flight path of the balloon (and parachute) and the time it takes to measure one profile. Both the non vertical sampling path and temporal changes during the measurement do not necessarily provide an accurate vertical profile. This must be considered when comparing true vertical, instantaneous profile measurements (e.g., lidar profilers) with radiosonde data.

Microwave Refractometers

Unlike radiosondes, microwave refractometers measure radio refractivity directly. Ambient air is passed through a microwave cavity whose resonant frequency is a function of both the dimensions of the cavity and the refractive index of the air within the cavity. If the dimensional changes of the cavity are kept very small, the refractive index of the air within the cavity can be accurately determined from the measurement of the resonant frequency of the cavity. The operating frequency of microwave refractometers is usually around 10 GHz. Microwave refractometers have been used as early as 1952 and have been installed operationally in the US Navy's E-2C airborne surveillance aircraft (designated AN/AMH-3, Airborne Microwave Refractometer). In research operations, microwave refractometers are often deployed from helicopters. Microwave refractometers are considered the most accurate sensor for radio refractivity and have usually very rapid response times. Their disadvantages are relatively high cost and weight.

Evaporation Duct Sensors

An important ducting phenomenon over oceans is the evaporation duct. This duct is caused by a rapid decrease in humidity right above the ocean surface. A measurement of the instantaneous vertical humidity profile is difficult because humidity decreases from saturation directly at the surface (relative humidity 100%) to its ambient value within the first few centimeters above the surface. The instantaneous ocean surface is perturbed by wave motions and an average surface height is defined only when the instantaneous height is averaged over time. In addition, individually measured profiles are characterized by temporal fluctuations which are of the same order as the vertical changes of interest. Therefore, individually measured profiles are not meaningful for evaporation ducting assessment unless they are averaged over time (on the order of one minute). Lack of understanding of these basic micrometeorological properties has resulted in many inappropriate profile measurement proposals and attempts. Relationships have been developed which permit reliable evaporation duct height determination from four simple "bulk" measurements: sea-surface temperature and air temperature, relative humidity, and wind speed measured at a convenient reference height (usually 5-10 m) above the surface (Jeske, 1973). These four measurements are usually made with standard meteorological sensors (e.g., psychrometer for humidity, anemometers for wind and thermometers [thermistors, thermocouples] for temperature). For sea-surface temperature, a hand-held radiometer may provide more convenient and accurate data (Olson, 1989). Over two decades of experience in evaporation ducting assessment based on bulk measurements have provided satisfactory and consistent results. Operational assessment of evaporation ducting effects is less affected by uncertainties in relating bulk measurements to profiles than by range-variations in the duct.

3.3 Remote Sensing Techniques

Radar Techniques

Radar observations of atmospheric refractivity structures are almost as old as radars themselves (Cowell and Friend, 1937). The first radar specifically designed for the study of refractivity structure was introduced by Richter (1969). The radar provided continuous observations of atmospheric refractivity structures with an unprecedented range resolution of one meter. Observations with this radar helped settle the question of the nature of radar returns from atmospheric refractivity and revealed a detailed picture of temporal and spatial refractivity variations unknown before (Fig. 1-3). To this day, there is no other remote sensor capable of providing a more detailed picture of the dynamics and structure of atmospheric refractivity. The radar, however, does not sense the refractivity profile but rather the structure parameter C_n^2 of the structure function describing the turbulent perturbation of atmospheric refractivity. Gossard and Sengupta (1988) derived a relationship between refractivity gradient and C_n^2/C_w^2 where C_w^2 is the structure parameter of the vertical component of the turbulent wind velocity field (measured from the turbulent broadening of the Doppler spectrum). This relationship allows, in principle, retrieval of refractivity profiles from radar measurements. In practice, retrievals are limited by the presence of clouds or other particulates contaminating the radar data. Additional difficulties are that the broadening of the Doppler spectrum may be due to effects other than turbulence and the need for data with high signal-to-noise ratios. It appears that a combination of remote sensors such as radar (with Doppler capability), acoustic echo sounder, and Radio Acoustic Sounding System (RASS), may sense data which will result in accurate refractivity profiles (Gossard, 1992).

Lidar Techniques

Two lidar techniques have been used successfully to measure atmospheric profiles of water vapor: differential absorption lidars (DIAL) and Raman-scattering lidars.

DIAL uses the strong wavelength-dependent absorption characteristics of atmospheric gases. For radio refractivity, water vapor is of interest (oxygen is used for temperature profiling). A tunable laser is tuned to the resonance of an absorption line and then tuned off resonance. The ratio of the range-gated lidar signal permits determination of the atmospheric water vapor profile (Schotland, 1966; Collis and Russell, 1976; Measures, 1979).

Raman-scattering lidars utilize a weak molecular scattering process which shifts the incident wavelength by a fixed amount associated with rotational or vibrational transitions of the scattering molecule (Melfi et al., 1969; Cooney, 1970). The ratio of the Raman-scattered signal for the water-vapor shifted line to the signal from nitrogen is approximately proportional to the atmospheric water vapor mixing ratio (Melfi, 1972).

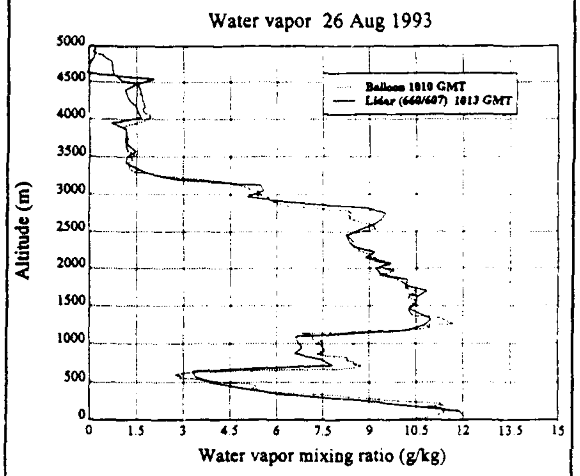

Figure 10. Water vapor mixing ratio from Raman lidar measurement (solid) and radiosonde (dashed).

An example of a water vapor profile measured with a Raman lidar is shown in figure 10 (Blood et al., 1994; Philbrick, 1994). The instrument used for measuring those data is a 532 nm, 0.6 Joule/pulse, 7 ns pulse width, 20 Hz pulse repetition frequency lidar. The lidar profiles are integrated over 30 min and the range resolution of the data set is 75 m. The solid trace in figure 10 represents the lidar and the dashed trace the radiosonde data. The agreement is excellent considering that the balloon profile is not the true instantaneous vertical profile and the lidar data are time averaged. Figure 11 shows the corresponding M-unit profile indicating a surface-based duct at 650 m.

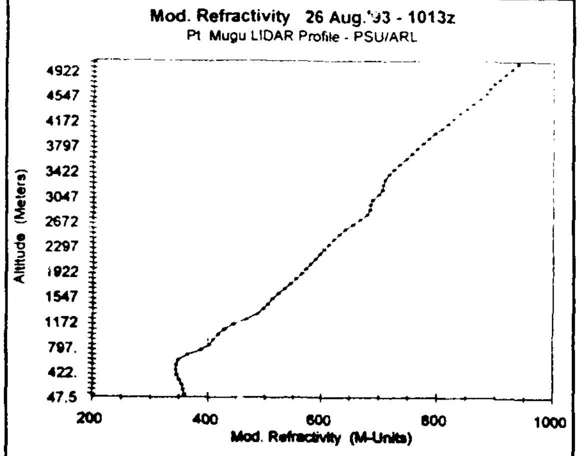

Figure 11. Modified refractivity profile for the data in figure 10.

Even though water vapor profiling based on differential absorption and Raman scattering has been demonstrated some 25 years ago, no instruments for routine ground-based use are commercially available yet. The reason is that neither technique will produce profiles reliably under all conditions. Daytime background radiation decreases the signal-to-noise ratio and so does extinction by aerosols. For cost and eye-safety reasons, there is a limit of how powerful the emitted radiation can be. For Raman-scattering lidars, various attempts have been made to use the so called solar-blind region (230-300 nm) to reduce daytime background noise (Cooney et al., 1980; Petri et al., 1982; Renaut and Capitini, 1988). Extinction by aerosols is a fundamental problem for any remote sensing technique (active or passive) using ultraviolet, visible or infrared radiation. In a marine environment the most severe ducting conditions occur when a strong temperature inversion is present. Stratus clouds form frequently when there is a strong temperature inversion. The height of the rapid humidity decrease occurs just above the top of the stratus cloud which means the laser energy has to penetrate the cloud from below and travel back to the ground-based receiver. Figure 12 shows the additional attenuation a laser signal encounters by travelling through a stratus cloud of a given thickness. The data used for calculating the extinction curves in figure 12 are based on stratus clouds having a mixture of marine and continental aerosols (Noonkester, 1985). From this graph, one can see that a vertically pointing, ground-based 530 nm lidar systems looses 43 dB in signal when penetrating a 150 m thick stratus cloud. It is doubtful that any realistic lidar could handle such

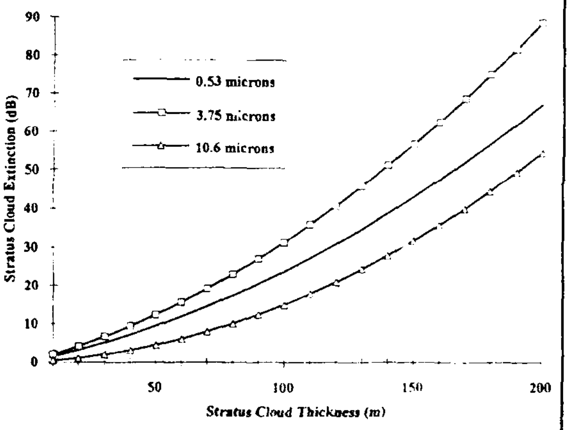

Figure 12. Two way extinction for three wavelengths for a signal penetrating a stratus cloud of a given thickness.

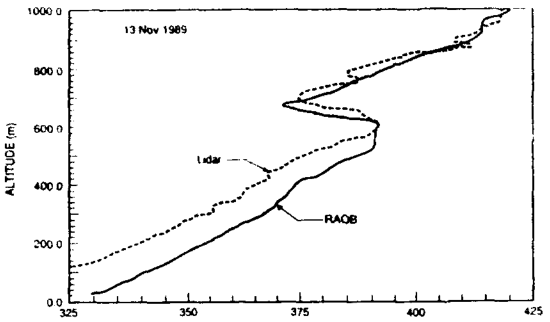

Figure 13. Refractivity profiles inferred from aerosol backscatter (dashed) and derived from radiosonde (solid).

attenuation values.

An interesting attempt to deduce water vapor profiles from lidar measurements of aerosol backscatter is described by Hughes et al. (1992). The technique is based on a correlation between aerosol dropsize distribution and relative humidity. An example of modified refractivity profiles deduced from aerosol lidar and calculated from radiosonde measurements is displayed in figure 13 showing a good agreement. This technique will also not work under high extinction (clouds) conditions.

Radiometric Techniques

Radiometric techniques are widely used in remote sensing for determining temperature and humidity profiles (Ulaby et al., 1981; 1986; Janssen, 1993). They are passive and are, therefore, ideally suited for situations where active emissions are undesirable. The downwelling sky radiometric or brightness temperature in the zenith direction $T_B(\nu)$ is related to the water vapor profile $\rho_v(z)$

$$T_B(\nu)=\int_0^\infty W_\rho(\nu,z)\rho_v(z)dz \qquad (2)$$

where the weighting function for water vapor, $W_\rho(\nu,z)$ is given by

$$W_\rho(\nu,z)=\kappa_v(z)\frac{T(z)}{\rho_v(z)}e^{-\tau_v(z)} \qquad (3)$$

$T(z)$ is the atmospheric temperature profile, τ_v the optical thickness, ν the frequency, and $\kappa_v(z)$ the absorption coefficient (which is approximately the water vapor absorption coefficient for measurements taken in the vicinity of water vapor absorption lines and under clear sky conditions). Radiometric retrieval techniques are not well suited for obtaining rapidly varying parameters. They provide better results for retrieving temperature profiles since temperature profiles have a smaller relative variability about their mean profile than humidity profiles. For anomalous radio propagation assessment, height and gradient of humidity profile changes are important; presently available microwave radiometry methods are far from producing humidity profiles with a vertical resolution suitable for anomalous propagation assessment. Figure 14 shows an example of a radiometrically retrieved water vapor profile and a radiosonde profile. The strong vertical gradient around 200 mb above the surface as well as the fluctuations below are not evident in the radiometrically sensed profile (Westwater and Decker, 1977).

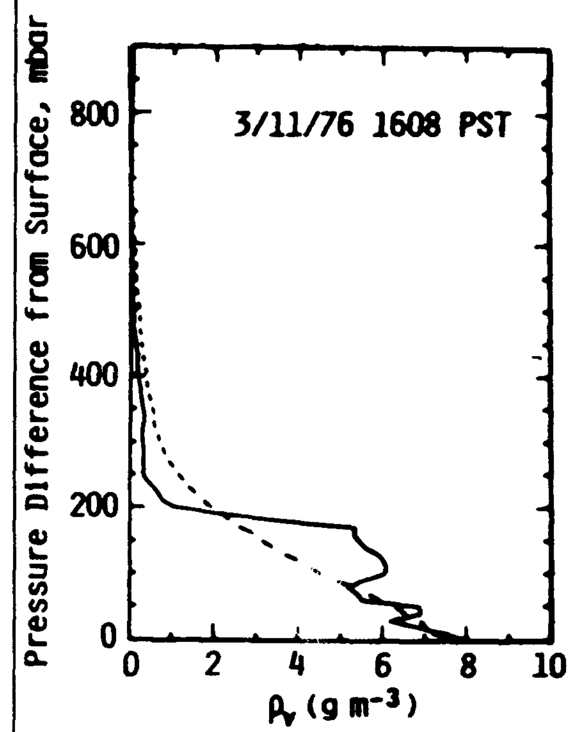

Figure 14. Radiometrically retrieved water vapor profile $\rho_v(z)$ (dashed) and radiosonde profile (solid).

Other attempts to measure humidity profiles have recently been made using a high resolution interferometer sounder (HIS) operating in the 5 - 20 μm band (Rugg, 1992). While this technique showed some minor improvements compared to microwave radiometry, it still does not produce humidity profiles with a resolution suitable for radio propagation assessment purposes. Figure 15 shows a comparison of temperature and dewpoint profiles retrieved from the HIS to radiosonde measurements (Wash and Davidson, 1994). The radiometrically retrieved temperature profile is in good agreement with the radiosonde while the radiometrically retrieved dewpoint profile misses the vertical gradients that are crucial to propagation assessment.

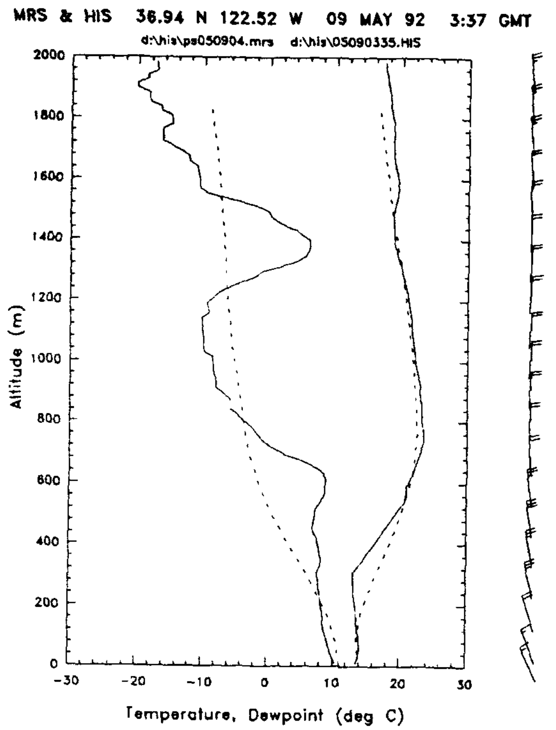

Figure 15. HIS retrieved temperature and dewpoint profiles (dashed) and MRS (Mini Rawin System) (solid).

In conclusion, microwave and infrared radiometry, *by themselves*, are presently not capable of retrieving vertical humidity profiles with an accuracy necessary for radio propagation assessment purposes. However, radiometry can play an important role as one component in a data assimilation system consisting of sensed and modeled fields.

Satellite Sensing Techniques

Because of the potential for global coverage, refractivity sensing from satellites would be very desirable. In principle, all of the above mentioned remote humidity profile (refractivity) sensors could be deployed from satellites and some already are (radiometers). Because of the limitations of the remote refractivity sensors discussed above, none are likely to provide the desired information by themselves. For determining evaporation duct heights, which require no continuous profile data but only four surface or near-surface parameters, Cook (1992) has proposed a scheme of combining satellite-sensed (ocean surface temperature, near-surface wind speed, and radiometry) data with outputs from numerical weather models in data assimilation systems. This kind of an approach is very likely to become more important in the future (Wash and Davidson, 1994). Additional interesting techniques have been proposed to use satellite data such as visible and infrared imagery to *infer* ducting conditions. Rosenthal and Helvey (1992) have pioneered subjective and objective techniques and demonstrated remarkable success in relating cloud patterns to ducting conditions in the Southern California off-shore area. Their approach assumes an inversion-dominated weather regime with low stratus or st[illegible]louds that are lowest and flattest over the eas[illegible] the subtropical oceans where the overlying inversion is lowest and strongest. They developed statistical relationships between cloud patterns and radiosonde-derived ducting conditions. They also derived an objective duct height estimate by correlating radiosonde statistics to cloud-top temperatures deduced from infrared imagery (Rosenthal and Helvey, 1994).

Radio Propagation Techniques

One remote sensing technique of high potential for operational assessment involves monitoring known radio transmitters. Especially in coastal regions, one usually finds an abundance of land-based transmitters which can be passively monitored off-shore. Signal levels of known emitters may be related to refractivity structure. Hitney (1992) used refractivity profile statistics in the S. California coastal region to derive correlations between radio signals and height of the trapping layer, which usually coincides with the base of the temperature inversion in this region. Figure 16 shows the base of the temperature inversion measured by various direct sensing techniques (filled and open circles) at various locations along a 148 km over-water propagation path between San Diego and San Pedro. The solid line is the inferred height of the base of the temperature inversion based on 547 MHz radio propagation measurements along the path (Hitney, 1992). This single-path, single-frequency

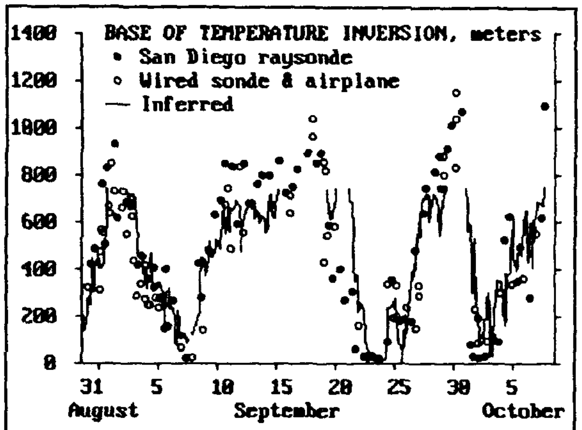

Figure 16. Base of temperature inversion from measurements (circles and dots) and inferred from radio propagation measurements (solid line).

method can undoubtedly be improved by using multiple paths and multiple frequencies. Part of the above mentioned VOCAR effort addresses remote sensing based on propagation data (Rogers, 1994).

Shipboard radars may sense returns from the sea surface and, in the presence of ducting, these sea-surface clutter returns may be modified by atmospheric refractivity. An example are clutter rings that are caused by multiple bounces of a radar signal between an elevated refractive layer (responsible for a surface-based duct) and the sea surface. In that case, the height of the reflecting layer (height of the duct) can be calculated from the geometry involved. Much more difficult is separation of the combined effects of sea-clutter enhancement and evaporation ducting. The ocean-surface properties affecting clutter (such as wind speed and direction) are not necessarily related to evaporation duct parameters and both effects are measured simultaneously. No reliable technique has been proposed to separate the two effects, which is necessary before shipboard radars may be used as evaporation duct sensors.

Another technique involves radio signals emitted from satellites in an attempt to relate refractive bending to refractivity structure. The bending effect is only significant within a few degrees of the horizon and, therefore, primarily of interest over oceans where unobstructed horizons are found. Refractivity structure may be deduced from a shift in the observed interference pattern when compared to standard conditions (Anderson, 1982). Anderson (1982) had moderate success inferring refractivity profiles but not with sufficient reliability to recommend the technique for routine use. This technique is presently being reexamined using Global Positioning System (GPS) signals which have much higher phase stability than previously available.

One very important aspect of remote sensing using radio propagation data is that the *path-integrated* effect of refractivity can be measured *instantaneously* to any degree of desired accuracy. The accuracy of data assimilation systems based on remote and direct sensors, numerical meteorological models, and other information is very difficult to verify experimentally because this requires extensive measurements in both space and time. Modelers have argued that their models are better than our present ability to measure the temporal and spatial structure of interest. That argument does not apply to careful radio propagation measurements; any data assimilation system addressing refractivity can and should be objectively and quantitatively evaluated by propagation data.

3.4 Data Assimilation Systems

It is obvious from the foregoing that there is no single sensing technique that can provide the needed refractivity information continuously and reliably. Neither can it be expected that such a technique will ever be available. Even if it were, for military applications an ability to forecast propagation conditions is as important as a nowcasting capability. Meteorological mesoscale models are presently available with 20 km horizontal grid spacing and 30 levels total in the vertical; there are ten grid points in the first 500 m with a 25 m spacing near the surface and 75 m near 500 m. Newer models being tested now have a 10 km grid spacing and a total of 36 levels in the vertical (Burk et al., 1994; Thompson et al., 1994). A data assimilation system comprising such models and utilizing remotely and directly sensed refractivity data is undoubtedly the right approach to describe and forecast refractivity conditions. A major objective of the previously mentioned VOCAR program is providing a data base to evaluate a data assimilation system under development by the US Navy.

4. AEROSOL EXTINCTION

4.1 Structure and Variability

The high emphasis on smart weapons with electrooptical (EO) sensors is putting increasing demands on assessment of atmospheric EO effects. In comparison to refractivity assessment where the spatial scales of interest are in the tens to hundreds of km, for EO applications the scales of interest are usually an order of magnitude less. Also, atmospheric variability can be much larger for EO systems than for those dependent on radio refractivity. For example, the extinction of a cloud may be many hundreds of dB above clear conditions, which poses a particularly challenging problem for real-time prediction of EO propagation conditions through broken clouds. To illustrate the complexity of EO propagation assessment, an example is presented which does not even involve clouds (Richter and Hughes, 1991). Figure 17 shows predicted and measured detection ranges for an airborne thermal imaging system (Forward Looking Infrared or FLIR) against a large ship target. The scatter in figure 17 is

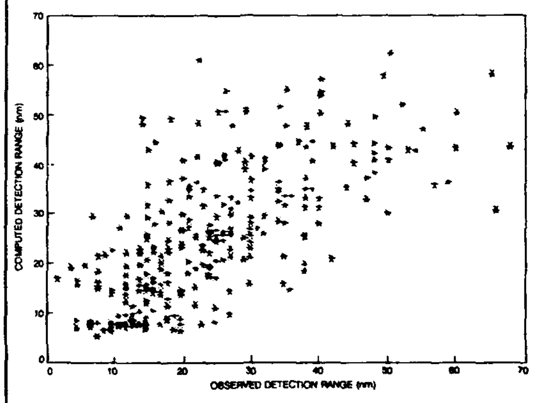

Figure 17. Observed and calculated detection ranges for a thermal imaging system.

indicative of the uncertainty in many parameters contributing to detection range calculations: there is the subjective element of the operator to call a signal on the screen a detection; the general condition and calibration of the complex hardware involved; the adequacy of meteorological data, which may come from other locations and taken at different times; the validity of models that translate observed meteorological data into parameters important for EO propagation such as aerosol extinction; and the variability of all factors affecting propagation along the path. Considering the potential contribution that each of the above uncertainties may have on the detection range calculation, the scatter in figure 17 is not unexpected. It is, however, unacceptable for the operational use of thermal imaging systems and steps need to be taken to reduce the scatter and provide more precise detection range predictions.

There are four atmospheric parameters which affect EO propagation: (a) molecular extinction; (b) turbulence; (c) refraction; (d) extinction (i.e., absorption and scattering) by aerosols. Molecular extinction by the various gases found in the atmosphere is well understood for most EO systems applications. Molecular extinction can be quite severe in certain spectral regions, which EO systems either avoid or sometimes exploit. Atmospheric turbulence may degrade the coherence of a high-resolution image or change the precise position of a laser beam and thereby limit the performance of a system. Refraction may bend the propagation of optical energy and may, for example, shorten or extend the optical horizon. In the following, only the question of sensing aerosol extinction is addressed since aerosol extinction is by far the most significant limitation for EO sensors and also it is the most difficult to measure and predict.

4.2 Direct Sensing Techniques

Detection and sizing of aerosol particles can be done by passing an air sample through a laser beam and measuring the scattered radiation. An example is the family of "Knollenberg" drop-size spectrometers available from Particle Measuring Systems. An evaluation of these devices was done by Jensen et al. (1983). Usually more than one drop-size spectrometer is needed since no single instrument is capable of measuring aerosol distributions ranging from submicron to tens of microns in diameter with number densities (numbers of aerosols per unit volume) spanning more than 12 orders of magnitude over these size ranges. Other methods to determine aerosol concentration and sizes include impaction devices, cloud chambers, electrostatic mobility devices and centrifuges. Other instruments measure the combined molecular and aerosol volume scattering (nephelometers and visibility meters) and extinction (transmissometers). The above instruments are delicate and expensive optical instruments and not suited for all applications. In particular, unlike the radiosonde, they are neither light-weight nor expendable, which limits vertical profiling to tethered balloons or aircraft. The above instruments may be impractical even for point-measurements such as the measurement of large aerosols close to the ocean, which are important for near-horizon passive infrared (IR) detection of low-flying anti-ship missiles. De Leeuw (1986a; 1986b) used a Rotorod™ impactor to collect near-surface large aerosols for analysis under a microscope. The Rotorod™ (available from Sampling Technologies, Los Altos, California) is a volumetric, rotating-arm impaction device capable of obtaining quantitative aerosol data in the 10 - 100 micron size range.

4.3 Remote Sensing Techniques

Lidars

The desire for vertical or slant-path extinction profiles prompted numerous attempts to employ lidars as described by Richter et al.(1992). The utility of a monostatic lidar system as a remote sensor for obtaining temporal and spatial information about the dynamic processes of the atmosphere is well established (Noonkester et al., 1972). By measuring the power backscattered from a laser pulse at a given range to a receiver, the movement and relative concentrations of naturally occurring aerosols, industrial pollutants or battlefield obscurants can be monitored and the bases of clouds determined. Remote mapping of wind velocities and flow patterns over large portions of the atmosphere can also be carried out. In these applications, the lidar is used as a tracer of aerosols that scatter the incident radiation rather than as a probe for studying the aerosols' optical properties.

For a given aerosol size distribution, extinction can be determined from Mie theory assuming that aerosols scatter and absorb radiation as if they were spheres of known refractive indices. For example, in the well-mixed marine boundary layer, relative humidities are usually high enough that most of the aerosols are hydrated, taking on a spherical shape. But above the boundary layer, where relative humidities are lower, aerosols may be non-spherical. In such cases, the optical properties predicted for spheres may differ by as much as an order of magnitude from those observed.

The single-scatter lidar equation is given by the relation

$$S(r)=\ln[P(r)r^2]=\ln K+\ln\beta(r)-2\int_0^r\sigma(r')dr' \qquad (4)$$

In this equation $P(r)$ is the power received from a scattering volume at range r, K is the instrumentation constant, and $\beta(r)$ and $\sigma(r)$ are the volumetric backscatter and extinction coefficients, respectively. In differential form this equation is

$$\frac{dS(r)}{dr}=\frac{1}{\beta(r)}\frac{d\beta(r)}{dr}-2\sigma(r) \qquad (5)$$

The solution of equation (5) requires knowing or assuming a relationship between $\beta(r)$ and $\sigma(r)$. However, if the atmosphere is homogeneous, the extinction coefficient can be simply expressed in terms of the rate of change of signal with range, i.e., $\sigma = -\frac{1}{2}\,[ds(r)/dr]$. A plot of $S(r)$ vs. r would then yield a straight line whose slope is -2σ.

Various authors (Klett, 1981; Kohl, 1978) have presented solutions to equation (5) by assuming a functional relationship between backscatter and extinction to be of the form

$$\beta(r)=C\sigma(r)^k \tag{6}$$

where C and k are not dependent upon r. In this case, only the aerosol number density is allowed to vary with range and not the size distribution. When the integration is performed in the forward direction from a range r_0, where the transmitted beam and receiver field-of-view overlap, to a final range r, the extinction coefficient is given by

$$\sigma(r)=\frac{\exp[S(r)]}{\dfrac{\exp[S(r_0)]}{\sigma(r_0)}-2\displaystyle\int_{r_0}^{r}\exp[S(r')]dr'} \tag{7}$$

where $\sigma(r_0)$ is the unknown contribution to extinction out to the overlap range.

The instabilities encountered in equation (7) can be overcome by performing the integration in the reverse direction from a final range, r_f, in toward the transmitter. In this case the extinction coefficient is given by,

$$\sigma(r)=\frac{\exp[S(r)]}{\dfrac{\exp[S(r_f)]}{\sigma(r_f)}+2\displaystyle\int_{r}^{r_f}\exp[S(r')]dr'} \tag{8}$$

where $\sigma(r_f)$ is the unknown value of extinction at the final range. Solutions to the single-scatter lidar equation have been presented for the reverse and forward integration cases (Bissonette, 1986) where the relationship between the backscatter and extinction coefficients is assumed to vary with range according to

$$\beta(r)=C(r)\sigma(r)^k \tag{9}$$

where k is a constant. For the forward integration case the extinction coefficient as a function of range is given by

$$\sigma(r)=\frac{\dfrac{1}{C(r)}\exp[S(r)]}{\dfrac{\exp[S(r_0)]}{C(r_0)\sigma(r_0)}-2\displaystyle\int_{r_0}^{r}\frac{1}{C(r')}\exp[S(r')]dr'} \tag{10}$$

and for the reverse integration case by

$$\sigma(r)=\frac{\dfrac{1}{C(r_f)}\exp[S(r)]}{\dfrac{\exp[S(r_f)]}{C(r_f)\sigma(r_f)}+2\displaystyle\int_{r}^{r_f}\exp[S(r')]dr'} \tag{11}$$

where the constant k has been chosen to be unity.

Klett (1981) discussed the instabilities inherent in equation (7) due to the negative sign in the denominator and the uncertainties in the boundary value $\sigma(r_0)$. In order to determine the appropriate value of $\sigma(r_0)$ from the raw lidar return, the values of C and k appropriate for the existing air mass must be known. While the value of k is usually close to unity, a critical problem is determining the proper choice of C. From the work of Barteneva (1960), a change greater than an order of magnitude can be inferred in the value of C between clear air and fog conditions. Kunz (1983) proposed that, for situations where the lower levels of the atmosphere appeared horizontally homogeneous, $\sigma(r_0)$ could be determined from the return of a horizontal lidar shot by means of the slope method, and then used as the boundary value in equation (7) for calculating the extinction in the vertical direction. The approach necessarily assumes the ratio β/σ remains constant with altitude, and that the linear decrease of return signal with range is indeed indicative of a homogeneous atmosphere. Caution must be applied in interpreting linear decreases of $S(r)$ with range as being related to homogeneous conditions. Kunz (1987a) has reported examples of vertical lidar returns beneath clouds that seemingly originated from a homogeneous atmosphere without a reflection from cloud base. In conditions where the aerosol size distribution is increasing with range, an increase in backscattered power can be balanced by a decrease in power caused by attenuation.

While equation (8) is "stable", it is difficult to use in a practical sense unless there is another independent determination of $\sigma(r_f)$. For fog conditions, the first term in the denominator of equation (8) becomes negligible, but in these situations the single scatter lidar equation is not applicable. Carnuth and Reiter (1986) used an approach to invert lidar returns beneath stratocumulus clouds by assuming $\sigma(r_f)$ to be equal to accepted values of cloud base extinction coefficient ($10\ \mathrm{km}^{-1} \le \sigma(r_f) \le 30\ \mathrm{km}^{-1}$). This approach still assumes that β/σ is invariant with altitude. Lindberg, e[illegible] 1984) have also presented measurements beneath [illegible]tus clouds in Europe. Extinction coefficients determined by the reverse integration technique agreed reasonably well with those calculated from balloon borne particle measurements and point measurements of visibility when the atmosphere was horizontally homogeneous and stable. The method by which $\sigma(r_f)$ was chosen is not clear since the authors only stated that an iteration procedure was used. Ferguson and Stephens (1983) also used an iterative scheme in an attempt to select the value of $\sigma(r_f)$. The value of $\sigma(r_f)$ at a close-in range (where the returned signal is well above the system noise) was varied until the $\sigma(r)$ determined from equation (8) allowed calculated and measured values of S(r) to agree. The chosen value of $\sigma(r_f)$ was then used as $\sigma(r_0)$ in equation (7) to integrate out from the transmitter. This procedure requires the system to be accurately calibrated and the value of β/σ to be specified and invariant with range. Hughes et al. (1985) showed the extinction coefficients calculated with this algorithm were not unique and were extremely sensitive to the chosen value of β/σ. Bissonnette (1986) pointed out that unless the system calibrations and β/σ are accurately known, this algorithm is no more stable than the forward integration solution.

Carnuth (1989) has attempted to verify the reverse integration technique (Klett's method) by making measurements of the visual range using an integrating nephelometer to obtain $\sigma(r_f)$ at the end of a slanted lidar path (7 km) up the side of a mountain. Optical depth derived from a transmissometer operated simultaneously with the lidar were in agreement with those derived from the averages of several lidar returns in cases where the path appeared homogeneous. In other cases, discrepancies were observed that the authors attributed to the variable ratio of β/σ along the path (in addition to measurement errors and the neglect of multiple scattering effects). Salemink et al. (1984) determined values of σ and β from horizontal lidar shots using the slope method when the atmosphere appeared to be horizontally homogeneous. They then presented a parameterization between values of β/σ and relative humidity (33% ≤ RH ≤ 87%). When the parameterization was used to invert visible wavelength lidar returns in the vertical direction, the derived extinction coefficient profiles (using radiosonde measurements of relative humidity) sometimes agreed reasonably well with those measured by aircraft mounted extinction meters. In contrast, de Leeuw et al. (1986) using similar types of lidar measurements did not observe a distinct statistical relationship between backscatter and extinction ratios and relative humidity. Fitzgerald (1984) pointed out that other factors such as the aerosol properties can strongly affect the relationship between β/σ and relative humidity and that the power law relationship is not necessarily valid for relative humidities less than about 80%. A unique relationship between $C(r)$ and relative humidity that is dependent on the air mass characteristics is yet to be developed.

An assumed relationship between backscatter and extinction coefficients can be eliminated by comparing the powers returned from a volume common to each of two lidars located at opposite ends of the propagation path. For this double-ended lidar configuration, the range-dependent extinction coefficient can be shown (Hughes and Paulson, 1988; Kunz, 1987b) to be related to the slope of the difference in the range compensated powers measured by the two lidars at the common range r by the equation

$$\sigma(r) = -\frac{1}{4}\frac{d}{dr}[S(r)_1 - S(r)_2] \tag{12}$$

However, the receiver gain of both lidars must be accurately known since it affects the slope characteristics of the individual S(r) curves. Although the double-ended technique has practical limitations for tactical situations, e.g., for slant path measurements at sea, it is feasible to use it in aerosol studies and to evaluate various single-ended schemes for measuring extinction. Hughes and Paulson (1988) used the double-ended lidar configuration over a 1 km inhomogeneous slant path to demonstrate that if the value of $C(r)$ varies with range, but is assumed to be a constant, neither the single-ended forward or reverse integration algorithms will allow range-dependent extinction coefficients to be determined with any assured degree of accuracy even if the initial boundary values are specified. If, however, the manner in which $C(r)$ varies is specified, both the forward and reverse single-ended inversions reproduce the double-ended measurements remarkably well.

In situations where the different layers of the atmosphere are horizontally homogeneous, the need for knowing the relationship between the backscatter and extinction coefficient can be eliminated by comparing the range compensated powers received from each altitude along two or more different elevation angles (Russell and Livingston, 1984; Paulson, 1989). Assuming extinction and backscatter coefficients to vary only in the vertical direction, the optical depth τ between any two altitudes can be shown to be

$$\tau = \frac{[S(R_3)-S(R_4)]-[S(R_1)-S(R_2)]}{2\left(\frac{1}{\sin\phi_2}-\frac{1}{\sin\phi_1}\right)} \tag{13}$$

where $S(R_1)$ and $S(R_2)$ are the range compensated powers returned along slant ranges R_1 and R_2 from an altitude h_1 with the lidar elevated at angles ϕ_1 and ϕ_2, respectively. Similarly, $S(R_3)$ and $S(R_4)$ refer to the range compensated powers returned from an altitude h_2. In principle, if the atmosphere were horizontally homogeneous, the lidar beam could be swept in elevation and the method used between closely separated angles to obtain an incremental profile of extinction and backscatter (Kunz, 1988). The smaller angular separations, however, place stringent requirements on the accuracies for measuring the range compensated powers (Paulson, 1989). Also, the works of Russell and Livingston (1984), and Spinhirne et al. (1980) concluded that the atmosphere within the convectively mixed marine boundary layer rarely, if ever, has the degree of homogeneity required. Atlas et al. (1986) presented examples of lidar returns observed from an aircraft above the marine boundary layer. Returns from within the mixed layer showed updrafts carrying aerosol-rich air upward and entrainment of aerosols from above into the mixed layer indicating a great degree of inhomogeneity of aerosol characteristics.

It has been demonstrated by Paulson (1989) that the double angle technique can be used to determine the extent to which the atmosphere is horizontally homogeneous. In these studies, data were taken beneath a thin stratus cloud layer at about 500 meters. Two calibrated visioceilometer lidars (Lindberg et al., 1984) were operated side-by-side on the west side of the Point Loma Peninsula at San Diego, California and pointed west over the Pacific Ocean. A series of nearly simultaneous shots were made with the one lidar elevated at an angle of 25° and the other at 50°. *S(r)* values for each of the lidars (determined using 5-point running averages of the raw data) showed increasing returns with increasing range that fluctuated about one another at different ranges which indicated an inhomogeneous condition. The optical depths between different altitudes determined from equation (13) are shown in table 1. The optical depth between 275 and 475 meters is only 0.15, while that from 375 to 475 meters is more than three times greater (0.49). If the data were representative of horizontally homogeneous conditions, the optical depth up to 475 meters should consistently decrease as h_l increases. These data demonstrate that, even though the magnitude of *S(r)* from a horizontal lidar return decreases linearly with range, horizontal homogeneity at higher altitudes can only be assured if optical depths, measured by the two-angle method, decrease within the boundary layer.

Lower Altitude (m)	Optical Depth
100	0.811
125	0.437
150	0.584
175	0.597
200	0.647
225	0.584
250	0.688
275	0.150
300	0.260
325	0.260
350	0.342
375	0.492

Table 1. Optical depths calculated from different altitudes up to a maximum altitude of 475 m on 17 May 1989.

Range-dependent extinction coefficients cannot be determined from single-ended lidar measurements with any assured degree of accuracy unless either the backscatter/extinction coefficient ratio is known along the propagation path or the atmosphere is horizontally homogeneous. If the conditions exist for which the forward inversion algorithm is stable, the double-ended lidar work has shown that a single-ended lidar inversion technique would be possible when augmented with a close-in measurements of extinction and measurements to relate *C(r)* to air mass characteristics and to relative humidity. While the works of Mulders (1984) and de Leeuw et al. (1986) have concluded no relationship exists between *C(r)* and relative humidity, their measurements did not account for changes in the air mass characteristics. Simultaneous lidar measurements and air mass characteristics (e.g., radon and condensation nuclei) need to be conducted to identify their relationship to relative humidity profiles. Whether or not such a relationship can ever be identified in a practical sense is yet to be determined.

For a single-ended lidar to become a useful operational tool, innovative concepts need to be pursued. A single-ended lidar technique has been proposed by Hooper and Gerber (1986; 1988) to measure optical depths when used looking down from an aircraft or satellite at the ocean surface and when the reflection properties of the surface are known. In this technique, two detectors are used: one with a narrow field-of-view, which measures the power directly reflected off the rough ocean surface and another with a wide field-of-view where the directly reflected photons are blocked (aureole detector). Bissonette and Hutt (1989) described a technique based on the simultaneous measurement of lidar returns at different fields of view. By ratioing these returns, the need for a backscatter-to-extinction relationship is eliminated. So far, none of these techniques have been widely accepted.

Finally, even if a lidar would produce reliable extinction profiles at one wavelength, the question remains of how to extrapolate the data to other wavelength bands.

Satellite Techniques

From satellites, the total spectral radiance of the upwelling light from the atmosphere can be sensed. The radiance consists of two components, the first is reflected from the surface (water or ground) and travels back through the entire atmosphere, the second never reaches the surface and is scattered by the atmosphere only. If the surface reflectance is sufficiently high and known (which is generally the case for oceans only) and the total optical depth of the atmosphere is not too high (less than 0.08) the reflected radiance exceeds the atmospheric radiance and the total optical depth of the atmosphere can be deduced (Griggs, 1975). This technique provides global data but is mostly useful over oceans; it provides no vertical structure and works only for small optical depths.

4.4 Data assimilation systems

No single sensing technique is available that provides accurate, three-dimensional, time varying aerosol extinction. Vertical aerosol distributions over water can be related to commonly observed meteorological parameters (Gathman, 1989; Gathman and Davidson, 1993). A data assimilation system which combines sensed extinction data and aerosol profiles calculated from numerical meteorological mesoscale models is presently the best approach to provide extinction data. Such systems are under development but will, initially, not have the resolution desired for EO systems performance assessment.

5. CONCLUSIONS

Direct sensing techniques for vertical refractivity (humidity) profiles are well established, are relatively easy to obtain, inexpensive, and provide useful results for propagation assessment purposes. Lidar remote sensing techniques provide excellent vertical refractivity (humidity) profiles when background noise and aerosol extinction are low. Techniques involving satellite sensors or sensing of satellite signals show promise in the future. Direct sensing of aerosol extinction is also well established even though the instrumentation is delicate and expensive. Attempts to remotely sense aerosol extinction profiles using lidar techniques have not yet resulted in generally available instrumentation that would provide data with adequate and assured accuracy. The best approach to obtaining both refractivity and aerosol extinction is the development of data assimilation systems which combine sensed data and data derived from high-resolution meteorological mesoscale models.

6. ACKNOWLEDGEMENT

This work was supported by the Office of Naval Research.

7. REFERENCES

Anderson, K.D., Inference of refractivity profiles by satellite-to-ground RF measurements, Radio Science, Vol. 17, No. 3, pp. 653-663, 1982

Anderson, K.D., Radar detection of low-altitude targets in a maritime environment, NCCOSC RDTE DIV (NRaD) TR 1630, Vol. 1 and 2, 1993

Atlas, D., B. Walter, S. Chou, and P.J. Sheu, The structure of the unstable marine boundary layer viewed by lidar and aircraft observations, J. Atmos. Sci., 43, 1301, 1986

Barteneva, O.D., Scattering functions of light in the atmospheric boundary layer, Bull. Acad. Sci. USSR Geophys., Ser. 12, 32, 1960

Bissonnette, L.R., Sensitivity analysis of lidar inversion algorithms, Appl. Opt., 25, 2122, 1986

Bissonette, L.R., and D.L. Hutt, Remote sensing of the aerosol scattering coefficient with a multi-field-of-view lidar, AGARD CP-453, pp.39.1-3913, 1989

Blood, D.W., S. McKinley, C.R. Philbrick, R.A. Paulus and L.T. Rogers, Lidar measured refractive effects in a coastal environment, Proc. IGARSS '94, 1994

Burk, S.D., W.T. Thompson, J. Cook, and G.G. Love, Mesoscale modeling of refractive conditions during the VOCAR experiment, Proc. IGARSS '94, 1994

Carnuth, W., and R. Reiter, Cloud extinction profile measurements by lidar using Klett's inversion method, Appl. Opt., 25, 2899, 1986

Carnuth, W., Verification of Klett's method by comparison of lidar and transmissometer measurements, AGARD Conference Proceedings No. 454, Paper No. 30, 1989

Collis, R.T.H., and P.B. Russell, Lidar measurement of particles and gases by elastic backscattering and differential absorption, Chapter 4 in *Laser Monitoring of the Atmosphere,* (E.D. Hinkley, ed.), Springer, 1976

Cook, J., A "Virtual Sensor" for evaporation ducts - The impact of data uncertainties, AGARD CP-502, pp. 9.1-9.10, 1992

Cooney, J.A., Remote measurements of atmospheric water vapor profiles using the Raman component of laser backscatter, J. Appl Meteor., 9, pp. 182-184, 1970

Cooney, J.A., K. Petri, and A. Salik, Acquisition of atmospheric water vapor profiles by a solar blind Raman lidar, in *Atmospheric Water Vapor,* (Deepak, Wilkerson, Ruhnke, ed.), Academic Press, New York, pp. 419-431, 1980

Cowell, R.C., and A.W. Friend, Tropospheric radio wave reflections, Science, Vol. 86, pp. 473-474, 1937

de Leeuw, G., Size distributions of giant aerosol particles close above the sea level, J. Aerosol. Sci, Vol. 17, No. 3, pp, 293-296, 1986a

de Leeuw, G., Vertical profiles of giant particles close above the sea surface, Tellus, 38 B, pp. 51-61, 1986b

de Leeuw, G., G.J. Kunz, and C.W. Lamberts, Humidity effects on the backscatter/extinction ratio, Appl. Opt.,25, 3971, 1986

Dockery, G.D., and G.C. Konstanzer, Recent advances in prediction of tropospheric propagation using the parabolic equation, Johns Hopkins APL Tech. Dig., Vol. 8., No. 4, pp. 404-412, 1987

Ferguson, J.A., and D.H. Stephens, Algorithm for inverting lidar returns, Appl. Opt., 22, 3673, 1983

Fitzgerald, J.W., Effect of relative humidity on the aerosol backscattering coefficient at .694 and 10.6 μm wavelengths, Appl. Opt., 23, 411, 1984

Gathman, S.G., A preliminary description of NOVAM, the Navy Oceanic Vertical Aerosol Model, NRL Rep. No. 9200, 1989

Gathman, S.G., and K.L. Davidson, The Navy oceanic vertical aerosol model, NCCOSC RDTE DIV, TR 1634, 1993

Gossard, E.E., and N. Sengupta, Measuring gradients of meteorological properties in elevated layers with a surface-based Doppler radar, Radio Science, Vol. 23, No. 4, pp. 625-639, 1988

Gossard, E.E., Relationship of height gradients of passive atmospheric properties to their variances: applications to the ground-based sensing of profiles, NOAA TR ERL 448-WPL 64, 1992

Griggs, M., Measurements of atmospheric aerosol thickness using ERTS-1 data, J. Air Pollut. Control Assoc., Vol. 25, pp. 622-626, 1975

Helvey, R.A., Radiosonde errors and spurious surface-based ducts, Proc. IEE, Vol. 130, Part F, No. 7, pp. 643-648, 1983

Hitney, H.V., J.H. Richter, R.A. Pappert, K.D. Anderson, and G.B. Baumgartner, Tropospheric radio propagation assessment, Proc. IEEE, Vol. 73, No. 2, pp. 265-283, 1985

Hitney, H.V., Remote sensing of refractivity structure by direct radio measurements at UHF, AGARD CP-502, pp. 1.1-1.5, 1992

Hooper, W.P., and H. Gerber, Down looking lidar inversion constrained by ocean reflection and forward scatter of laser light, Appl. Opt., 21, 689, 1986

Hooper, W.P., and H. Gerber, Monte Carlo simulations of laser-generated sea surface aureole, Appl. Opt., 27, 5111, 1988

Hughes, H.G., J.A. Ferguson, and D.H. Stephens, Sensitivity of a lidar inversion algorithm to parameters relating atmospheric backscatter and extinction, Appl. Opt., 24, 1609, 1985

Hughes, H.G., and M.R. Paulson, Double-ended lidar technique for aerosol studies, Appl. Opt., 27, 2273, 1988

Hughes, H.G., M.R. Paulson, and J.H. Richter, Radio refractivity profiles deduced from aerosol lidar measurements, AGARD CP-502, pp. 6.1-6.6, 1992

Janssen, M.A., *Atmospheric Remote Sensing by Microwave Radiometry*, Wiley, New York, 1993

Jensen, D.R., R. Jeck, G. Trusty, and G. Schacher, Intercomparison of Particle Measuring Systems, Inc.'s particle-size spectrometers, Optical Eng., Vol. 22, No. 6, pp. 746-752, 1983

Jeske, H., State and limits of prediction methods of radar wave propagation conditions over the sea, in *Modern Topics in Microwave Propagation and Air-Sea Interaction*, D. Reidel, Boston, 1973

Klett, J.D., Stable analytical inversion solution for processing lidar returns, Appl. Opt., 20, 211, 1981

Ko, H.W., J.W. Sari, and J.P. Skura, Anomalous microwave propagation through atmospheric ducts, Johns Hopkins APL Tech. Dig., 4, pp. 12-26. 1983

Kohl, R.H., Discussion of the interpretation problem encountered in single-Wavelength lidar transmission, J. Appl. Meteorol., 17, 1034, 1978

Kunz, G.J., Vertical atmospheric profiles measured with lidar, Appl. Opt., 22, 1955, 1983

Kunz, G.J., Lidar and missing clouds, Appl. Opt., 26, 1161, 1987a

Kunz, G.J., Bipath method as a way to measure the spatial backscatter and extinction coefficients with lidar, Appl. Opt., 26, 794, 1987b

Kunz, G.J., A method for measuring the vertical extinction and backscatter profile with a scanning lidar, TNO Physics and Electronics Laboratory, Report No. FEL 1988-65, 1988

Lindberg, J.D., W.J. Lentz, E.M. Measure, and R. Rubio, Lidar determinations of extinction in stratus clouds, Appl. Opt., 23, 2172, 1984

Measures, R.M., Analytical use of lasers in remote sensing, Chapter 6 in *Analytical Laser Spectroscopy*, (N. Ometto, ed.), John Wiley and Sons, 1979

Melfi, S.H., J.D. Lawrence, and M.P. McCormick, Observations of Raman scattering by water vapor in the atmosphere, Appl. Phys. Lett., 15, pp.295-297, 1969

Melfi, S.H., Remote measurements of the atmosphere using Raman scattering, Appl. Optics, 11, pp.1605-1610, 1972

Mulders, J.M., Algorithm for inverting lidar returns: comment, Appl. Opt., 23, 2855, 1984

Noonkester, V.R., D.R. Jensen, and J.H. Richter, Simultaneous FM-CW radar and lidar observations, Prepr. 15th Radar Meteorology Conf., pp.335-340, 1972

Noonkester, V.R., Profiles of optical extinction coefficients calculated from droplet spectra observed in marine stratus cloud layers, J. Atm. Sci., Vol. 42, No. 11, pp.1161-1171, 1985

Olson, J., Shipboard measurements of air-sea temperature in the evaporation duct, Naval Ocean Systems Center, TR 1313, Dec. 1989

Paulson, M.R., Atmospheric horizontal inhomogeneity effects on the optical depths determined by the double elevation angle lidar technique, Naval Ocean Systems Center Technical Document 1600, 1989

Paulus, R.A., VOCAR: An experiment in variability of coastal atmospheric refractivity, Proc. IGARSS '94, 1994

Petri, K., A. Salik, and J. Cooney, Variable-wavelength solar-blind Raman lidar for remote measurement of atmospheric water-vapor concentration and temperature, Appl. Optics, Vol. 21, No. 7, pp. 1212-1218, 1982

Philbrick, C.R., Lidar measurements of water vapor concentrations in the troposphere, Proc. IGARSS '94, 1994

Renaut, D., and R. Capitini, Boundary layer water vapor probing with a solar-blind Raman lidar: validations, meteorological observations and prospects, J. Atmos. and Oceanic Technology, 5, pp. 585-601, 1988

Richter, J.H., High resolution tropospheric radar sounding, Radio Science, Vol 4, No. 12, pp. 1261-1268, 1969

Richter, J.H., D.R. Jensen, R.A. Pappert, and V.R. Noonkester, New developments in FM-CW radar sounding, Bound. Layer Met., 4, pp. 179-199, 1973

Richter, J.H., and H.G. Hughes, Marine atmospheric effects on electro-optical systems performance, Opt. Eng., Vol 30, No. 11, pp. 1804-1820, 1991

Richter, J.H., H.G. Hughes, and M.R. Paulson, Remote sensing of aerosol extinction using single-ended lidars, AGARD CP-502, pp. 22.1-22.5, 1992

Rosenthal, J., and R. Helvey, Refractive assessments from satellite observations, AGARD CP-502, pp.8.1-8.9, 1992

Rosenthal,J., and R. Helvey, Guidance for an expert system approach to elevated duct assessment over the northeastern Pacific Ocean, Proc. IGARSS '94, 1994

Rogers, L.T., Statistical assessment of the variability of atmospheric propagation effects in the southern California coastal area, Proc. IGARSS '94, 1994

Rowland, J.R., and S.M. Babin, Fine-scale measurements of microwave refractivity profiles with helicopter and low-cost rocket probes, Johns Hopkins APL Technical Digest, Vol 8, No. 4, pp. 413-417, 1987

Rugg, S.A., An investigation of the ground based high-resolution interferometer sounder (GB-HIS) in a coastal marine environment, Thesis, Naval Postgraduate School, Monterey, 1992

Russell, P.B., and J.M. Livingston, Slant-path extinction measurements and their relation to measured and calculated albedo changes, J. Clim. and Appl. Meteor. 23, 1204, 1984

Salemink, H.W.M., P. Schotanus, and J.B. Bergwerff, Quantitative lidar at 532 nm for vertical extinction profiles and the effect of relative humidity, Appl. Opt., B34, 187, 1984

Schotland, R.M., Some observations of the vertical profile water vapor by means of a laser optical radar, *Proc. Fourth Sym. on Remote Sensing of the Propagation Environment*, U. of Michigan, Ann Arbor, 1966

Spinhirne, J.D., J.A. Ragan, and B.M. Herman, Vertical distribution of aerosol extinction cross section and inference of aerosol imaginary index in the troposphere by lidar technique, J. Appl. Meteor., 19, 246, 1980

Thompson, W.T., S.D. Burk, J. Cook, and G.G. Love, Variations in coastal atmospheric refractivity induced by mesoscale processes, Proc. IGARSS '94, 1994

Ulaby, F.T., R.K. Moore, and A.K. Fung, *Microwave Remote Sensing,* Volume I: Microwave Remote Sensing Fundamentals and Radiometry, Addison-Wesley, Reading, 1981

Ulaby, F.T., R.K. Moore, and A.K. Fung, *Microwave Remote Sensing,* Volume III: From Theory to Applications, Artech House, Norwood, 1986

Wash, C.H., and K.L. Davidson, Remote measurements and coastal atmospheric refraction, Proc. IGARSS '94, 1994

Westwater, E.R and M.T. Decker, Application of statistical inversion to ground-based microwave remote sounding, in *Inversion Methods in Atmospheric Remote Sounding* (A. Deepak, ed.), Academic Press, New York, pp. 395-428, 1977

Refractive Effects from VHF to EHF
Part A: Propagation Mechanisms

Herbert V. Hitney
Ocean and Atmospheric Sciences Division
NCCOSC RDTE DIV 543
53170 WOODWARD ROAD
SAN DIEGO CA 92152-7385
USA

1. SUMMARY

Radio wave propagation in the VHF to EHF bands at low elevation angles and near the earth's surface is almost always affected by refraction. This lecture details these effects and the various methods used to model them, from simple effective-earth-radius factors for standard refraction to parabolic-equation methods for range-dependent ducting environments. Part A of the lecture introduces and discusses refraction-related propagation mechanisms and their effects, and Part B describes propagation models and uses examples from propagation assessment systems and other propagation software to illustrate many of the effects. Frequencies from about 30 MHz to 100 GHz are considered.

Refraction and Snell's law are discussed and standard and nonstandard propagation mechanisms are defined. Standard propagation mechanisms are free-space spreading, reflection, forward scatter from rough surfaces, spherical earth divergence, optical interference, diffraction, tropospheric scatter, and absorption. Nonstandard mechanisms discussed are evaporation ducts, surface-based ducts from elevated trapping layers, elevated ducts, lateral inhomogeneity, and terrain effects.

To establish the significance of nonstandard propagation effects, some statistics on the occurrence of ducting around the world are presented. Specifically, statistics on the strength of evaporation ducts for selected areas and on the frequency of occurrence of surface-based ducts are presented.

2. INTRODUCTION

The desire to understand tropospheric radio propagation mechanisms has existed since the early days of radio. This desire became urgent soon after radars became widely available during World War II, when many unusual or unexpected propagation effects were observed. A famous early example of anomalous propagation is the sighting of points in Arabia with a 200 MHz radar from Bombay, India, 1700 miles away, reported by Freehafer [1]. The many experimental and analytical studies begun during and soon after the war greatly expanded the scientific understanding of these phenomena, and most of this information has been well documented and compiled by Kerr [2]. It was found that the most dramatic propagation anomalies usually occurred over water, where atmospheric ducting is more significant and consistent than over land. Also the evaporation duct was discovered in the mid 1940s [3] to be a persistent phenomenon found over water that is very important for microwave systems operating in a maritime environment. These mechanisms are often referred to collectively as refractive effects.

Table 1 shows the International Telecommunications Union (ITU) radio frequency bands. Radio propagation in the HF band is usually dominated by effects of the ionosphere and is not significantly influenced by the lower atmosphere. For frequencies from VHF to EHF it is frequently assumed that radio waves will propagate outwards from a transmitter in straight lines anywhere within the "line of sight." However, the propagation of radio waves in the lower atmosphere is affected by many processes that may not be readily apparent. Refractive effects imply those mechanisms directly related to the bending of radio waves, and these effects can sometimes be dramatic. However, to discuss refractive effects from VHF to EHF properly, other mechanisms must also be considered. The dominant effect on any path within the horizon is spherical spreading, which in benign environments may be the primary limitation to the performance of a system. For radio terminals near the earth's surface, the coherent interference of the direct path energy with the reflected path energy will place limits on the performance of most systems. The amount of interference is a function of the reflection coefficient of the reflecting surface, which may be affected by a rough surface, and the divergence of the reflected wave by the spherical earth. At ranges near and just beyond the horizon, the dominant mechanism in the absence of anomalous refractive effects is diffraction around the earth's surface. At ranges far beyond the horizon, the dominant mechanism is usually forward scatter from small-scale refractive inhomogenieties in the atmosphere, a process known as troposcatter. In addition to all these mechanisms, absorption by atmospheric gases and scattering by hydrometeors in the atmosphere are sometimes important.

Although this paper has a very broad title that could encompass all refractive effects, I will discuss only those propagation mechanisms that are considered or planned to be considered in the Integrated Refractive Effects Prediction

System (IREPS) [4], the Engineer's Refractive Effects Prediction System (EREPS) [5], and the Tactical Environmental Support System (TESS) [6]. This should not imply that other mechanisms are not important. Indeed, some effects not discussed, such as rain attenuation, may be the dominant effect for certain frequencies and applications. Some of these other effects are the subjects of companion papers in this lecture series. Also I will not discuss the sensing of radio refractivity, since this topic is included in another companion paper in this series. Much of the material in this paper is an update of, or taken from, Hitney, et al. [7] and AGARDograph 326 [8].

	Meaning	Frequency Band
HF	High Frequency	3 - 30 MHz
VHF	Very High Frequency	30 - 300 MHz
UHF	Ultra High Frequency	300 MHz - 3 GHz
SHF	Super High Frequency	3 - 30 GHz
EHF	Extremely High Frequency	30 - 300 GHz

Table 1. ITU Frequency Bands.

3. REFRACTION AND SNELL'S LAW

Refraction is the bending of the path taken by an electromagnetic wave due to variations in the speed of propagation in the atmosphere. The refractive index n is defined as

$$n = c/v \qquad (1)$$

where c and v are the speeds of an electromagnetic wave in a vacuum and the atmosphere, respectively. A typical value of n at the earth's surface is 1.000350. Refractivity N is defined as

$$N = (n-1)\times 10^{6} \qquad (2)$$

such that the corresponding surface refractivity value is 350. Refractivity is related to atmospheric parameters by

$$N = 77.6\left[P/T + 4810\, e/T^{2}\right] \qquad (3)$$

where P is pressure (hPa), T is temperature (K), and e is partial water vapor pressure (hPa).

A radio ray is the locus of points normal to a radio wave front that describes the path the local wave front takes moving through the atmosphere. Snell's law dictates the relationship between the angles of incidence and the refractive index of the atmosphere along a ray. If the atmosphere is considered to have a continuously varying refractive index n, composed of infinitesimal small horizontal layers, then Snell's law can be stated as

$$n\cos\alpha = n_0\cos\alpha_0 \qquad (4)$$

where α is the elevation angle at an arbitrary point along a ray, and α_0 and n_0 are the elevation angle and refractive index at one reference point along the ray. In this form, both α and α_0 are relative to the horizontal layers. Since the earth's atmosphere can be approximated by concentric spherical layers, it is appropriate to state Snell's law as

$$nr\cos\alpha = n_0 r_0\cos\alpha_0 \qquad (5)$$

where r and r_0 are radial distances from the center of the earth to the arbitrary and reference points along the ray, respectively. In this case, α and α_0 are relative to the local horizontal at their positions along the ray. Figure 1 illustrates the geometry associated with equation (5).

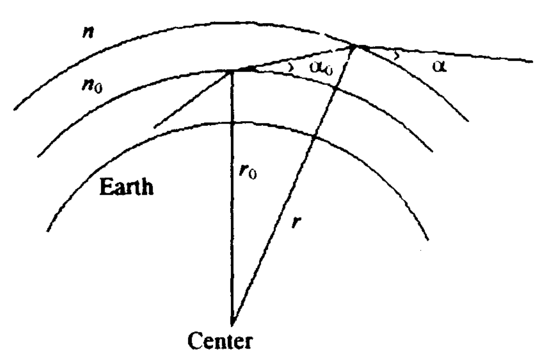

Figure 1. Geometry for Snell's law.

For a standard or normal refractivity gradient, a radio ray will refract downward toward the earth's surface, but with a curvature less than the earth's surface. Normal gradients are usually considered to be from -79 to 0 N units per km of height, which are characteristic of long-term mean refractive effects for a particular area. For example, the long-term mean gradient over the continental United States is approximately -39 N/km [9]. If the N-gradient exceeds 0 N/km in an atmospheric layer, a radio ray will bend upwards and that layer is said to be subrefractive and has the effect of shortening the distance to the horizon. If a layer's gradient is between -157 and -79 N/km, a ray will still bend downwards at a rate less than the earth's curvature, but greater than normal. The most dramatic nonstandard effects are those caused by gradients less than -157 N/km which are called trapping gradients. In a trapping layer, ray curvature exceeds the earth's curvature and leads to the formation of a radio duct which can result in propagation ranges far beyond the horizon. As a convenience in identifying trapping layers and assessing propagation effects, the modified refractivity M has been developed and is defined by

$$M = N + (h/a)\times 10^{6} = N + .157h \qquad (6)$$

where h is height above the earth's surface in meters and a is the earth's radius in meters. M is useful in identifying trapping layers since trapping occurs for all negative M gradients. Table 2 lists the four refractive conditions discussed above with their corresponding N and M gradients, and Figure 2 illustrates the relative curvature for each.

Condition	N/km	M/km
Trapping	-∞ to -157	-∞ to 0
Superrefractive	-157 to -79	0 to 78
Normal	-79 to 0	78 to 157
Subrefractive	0 to ∞	157 to ∞

Table 2. Refractive Conditions.

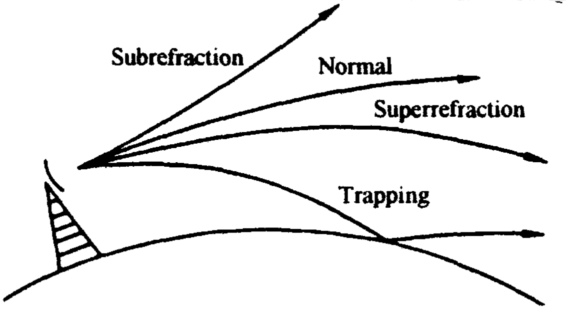

Figure 2. Refractive conditions.

The mechanisms controlling radio propagation in the troposphere can be separated into standard and nonstandard mechanisms. Standard propagation refers to a so-called standard atmosphere in which the radio refractive index decreases exponentially with increasing height. At low altitudes, this decrease with height is nearly linear [9]. The presumption of a standard atmosphere is purely for computational convenience and is based on long-term averages, usually over large continental areas. A standard atmosphere should not be automatically assumed to be the most common condition since there are many geographic areas where other significant propagation conditions prevail. Standard mechanisms also assume a smooth or slightly rough earth surface, such as the sea surface. The standard propagation mechanisms that are discussed here are spherical spreading, reflection, forward scattering from rough surfaces, divergence, optical interference, diffraction, tropospheric scatter, and absorption. Nonstandard mechanisms are evaporation ducts, surface-based ducts, elevated ducts, lateral inhomogeneity, and terrain effects.

4. LOSS DEFINITIONS

This section will define the quantities path loss, propagation loss, and propagation factor and discuss their relation to similar quantities recommended by the ITU [10]. In this paper radio wave propagation effects will be quantified in terms of propagation loss or propagation factor expressed in decibels.

Path loss is defined as the ratio of transmitted to received power between loss-free isotropic antennas. If path loss L is expressed in decibels, then

$$L = 10\,\mathrm{Log}(p_t/p_r) \tag{7}$$

where p_t and p_r are the power transmitted and power received expressed in the same units. The ITU prefers to call this quantity basic transmission loss. The two quantities are identical, and I will continue to use the former one here.

Propagation loss is defined as the ratio of the power transmitted by an antenna to the power received by another antenna but normalized to unity gain for both antennas. This definition includes the effects of antenna patterns but not the gain of those antennas, and is different from the quantity path loss. Since the antenna pattern in many cases can affect the loss observed or computed from models, propagation loss is a more accurate description. In the case of two isotropic or omnidirectional antennas, propagation loss and path loss are equal. In the case of directional antennas, even with beamwidths of only a few degrees, if those antennas are aligned towards each other, then propagation loss is very nearly equal to path loss on trans-horizon paths.

The ITU does not recommend the use of the term propagation loss, recommending instead the terms transmission loss or basic transmission loss. Transmission loss includes gains as well as patterns for both antennas, and is normally very different than propagation loss. Basic transmission loss removes the effects of both gains and patterns by substituting loss-free isotropic antennas for the actual antennas. Although these terms are fine for system engineers designing radio transmission systems, they are awkward for doing comparative studies of radio propagation. For example, propagation experiments in practice must measure transmission loss. To compare one point-to-point measurement with another, the effects of different antenna gains can be easily normalized, but the effects of antenna patterns cannot, since these effects are mixed in with other propagation effects. Thus basic transmission loss cannot in general be determined from measured data, while propagation loss can.

Propagation factor F in decibels is defined as

$$F = 20\,\mathrm{Log}[E/E_0] \tag{8}$$

where E is the field strength at a point, including antenna pattern effects but normalized to unity gain antennas, and E_0 is the field strength that would occur at that point under free space conditions if loss-free isotropic antennas were used for both the transmitter and receiver. Propagation factor is the difference between free space path loss and propagation loss. Some authors call this quantity the pattern propagation factor [2]. To summarize, both propagation factor and propagation loss include antenna pattern effects but are normalized to unity antenna gains.

5. STANDARD MECHANISMS

For purposes of illustration, consider the propagation loss between a 5 GHz transmitter and a receiver, both 25 meters above the sea surface, plotted versus range between the

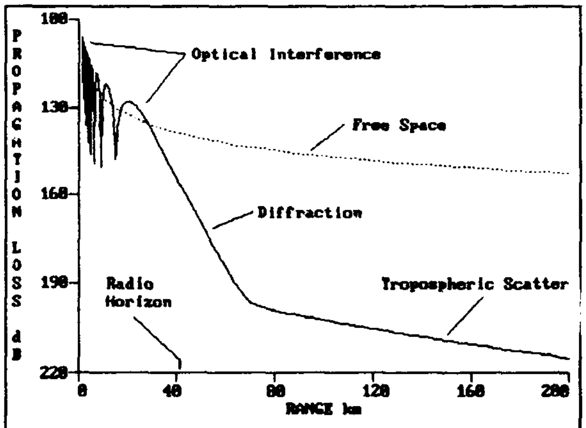

Figure 3. Standard propagation mechanisms.

terminals, as shown in Figure 3. The radio horizon is defined as the boundary within which direct paths exist between the transmitter and receiver considering the effects of standard refraction. At close ranges the propagation loss is determined by the coherent interference of the direct and sea-reflected radio waves, producing a series of relative maxima and minima in the loss. As the range approaches the radio horizon, diffraction by the earth's curved surface becomes the dominant mechanism. At much further ranges, scattering from refractive inhomogeneities high in the atmosphere becomes the most important mechanism. These standard propagation mechanisms are shown in Figure 3 relative to the propagation loss that would have been observed if the terminals were in free space, where only spherical spreading of the radio wave would occur. I will discuss each of these mechanisms in more detail in the sections following.

5.1 Spherical Spreading

Spherical spreading of a wave front is the most fundamental propagation mechanism. This mechanism is characterized by the increasing surface area of a sphere centered on the transmitter and radiating outward. Field strength at any point is inversely proportional to the square of the range between the transmitter and receiver. If both the transmitter and receiver are far removed from the earth's surface and atmosphere, that is if they are in free space, then spherical spreading is the only propagation mechanism. Free-space propagation is used throughout this lecture as a standard against which both propagation measurements and computations are compared. Free-space path loss L_f expressed as decibels is given by

$$L_f = 32.45 + 20\,\mathrm{Log}(f) + 20\,\mathrm{Log}(d) \qquad (9)$$

where f is frequency in MHz and d is distance between the transmitter and receiver in km. Free-space path loss is included in many figures of this paper as a reference for other propagation effects.

5.2 Reflection

When an electromagnetic wave strikes a nearly smooth large surface such as the ocean, some or all of the energy is reflected from the surface and continues propagating along a new path. The incident ray and the reflected ray make equal grazing angles ψ with the reflecting surface, as illustrated in Figure 4. In general, there is both a reduction in the magnitude and a change in phase of the wave on reflection. Both effects are frequently described by a full complex reflection coefficient that is the ratio of the reflected and incident complex electric fields, but in this paper I will refer to the magnitude R and phase lag φ of the reflection coefficient. The phase of the reflected field usually lags the phase of the incident field, hence the phase lag φ is normally positive. For horizontal polarization and a smooth perfectly conducting reflecting surface, R is 1 and φ is 180 degrees for all values of ψ [11]. For finite conductivity or polarization other than horizontal, the reflection coefficient can vary significantly as a function of ψ, as illustrated in Figure 5 for vertical polarization over smooth sea water at 1000 MHz.

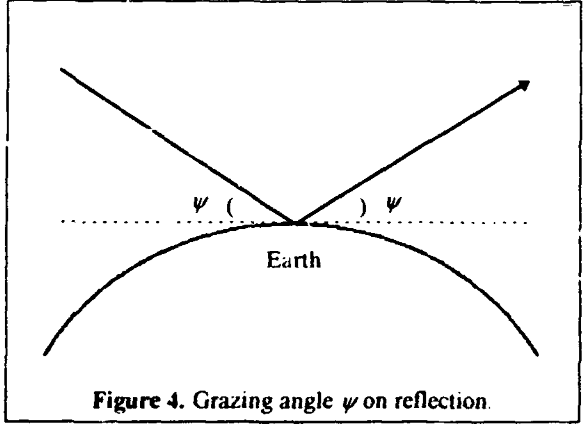

Figure 4. Grazing angle ψ on reflection.

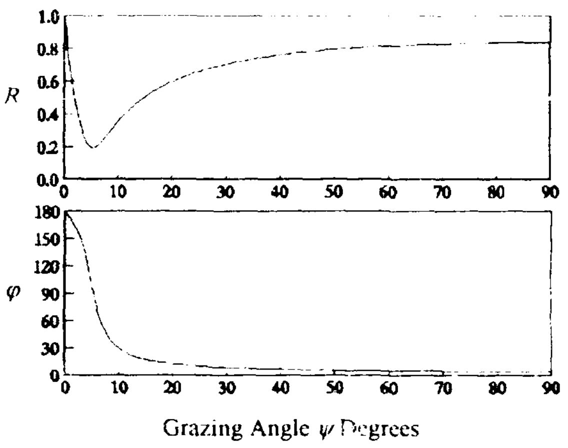

Figure 5. Reflection coefficient magnitude R and phase lag φ for vertical polarization at 1.0 GHz over sea water versus grazing angle ψ. Both φ and ψ are in degrees.

At many frequencies and polarizations, the reflection coefficient strongly depends on the electrical characteristics of the earth, in particular the conductivity and the relative permittivity. The ITU recommends using a graph to determine these characteristics which has been prepared for several conditions (sea water, wet ground, fresh water, medium dry ground, etc.).

5.3 Forward Scatter from Rough Surfaces

When a radio wave reflects off a rough surface, such as a wind-roughened sea, only part of the energy is reflected coherently in the specular direction, that is, in the same direction as for a smooth surface. The remaining energy is incoherently scattered by the various sea-wave facets into random directions. Both the coherent and incoherent, or diffuse, fields depend on the apparent ocean roughness g given by

$$g = (\sigma_h \sin\psi)/\lambda \approx \sigma_h \psi / \lambda \qquad (10)$$

where σ_h is the standard deviation of the sea surface elevation, ψ is the grazing angle, and λ is radio wavelength [12]. For $g = 0$, the rough-surface coherent reflection coefficient equals the smooth surface reflection coefficient, and the incoherent reflection coefficient is zero. As *g* increases, the coherent field decreases while the incoherent field increases up to perhaps 100 mrad, and then decreases.

The most notable effect of the rough surface is the reduction of the coherent reflected field at relatively high angles in the optical interference region. As an example, Figure 6 shows propagation loss measurements at 3 GHz for a transmitter at 21 m and a receiver at 152 m compared to a model that assumes near-perfect reflection from the sea. The disagreement between the modeled and the measured depths of the interference nulls at short ranges is clearly the result of sea roughness. Sea surface roughness can also be an important consideration under conditions of strong surface ducting, as will be described in a later section.

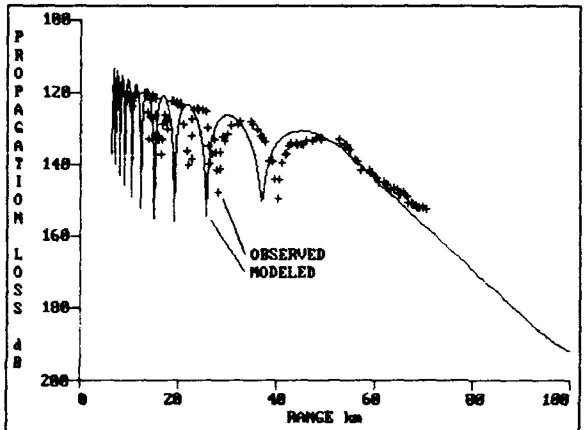

Figure 6. Rough surface effects on the depth of optical interference nulls. Model is for near-perfect reflection.

5.4 Divergence Factor

A radio wave reflecting off the spherical earth's surface at low grazing angles suffers a spreading loss in addition to the normal spherical spreading, as illustrated in Figure 7. This figure is a simplification, since a small solid angle at the transmitter should really be considered along with the effects of earth's curvature in azimuth as well as elevation.

The divergence factor is defined as the ratio of the field strength obtained after reflection from a smooth spherical surface to the field strength that would be obtained after reflection from a plane surface, with the radiated power, total axial distance, and type of surface being the same in both cases, and the solid angle at the transmitter being a small elemental angle approaching zero. This mechanism must be accounted for in addition to the smooth or rough-surface reflection coefficient to account for the total reflected energy.

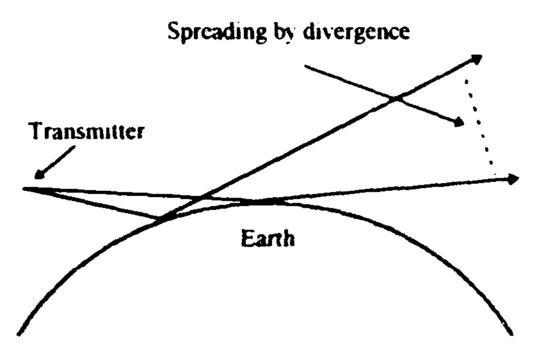

Figure 7. Illustration of spherical earth divergence.

5.5 Optical Interference

Optical interference is probably the second-most important propagation mechanism after spherical spreading, because in many applications it applies to a very large region. Consider the case of a shipboard air-search radar, for example, where the primary search volume is most of the region above the radio horizon. The radar may be able to detect targets a short distance into the diffraction region, or in some cases to large over-the-horizon distances due to ducting, but for everyday considerations the interference region represents the region of coverage for the system. In this region, propagation is determined by the coherent interference of the direct and sea-reflected waves.

In the interference region, the relative phase between the direct and reflected components is important. This phase is the combined effect of the path length difference between the two components and the phase lag of the reflection coefficient. Taken together, this phase determines the location of interference maxima and minima in this region. The magnitude of the direct wave field strength is a function of the antenna pattern for the elevation angle of the direct path, while the magnitude of the reflected wave field strength is a function of the antenna pattern for the reflected ray elevation angle, the reflection coefficient, rough surface effects, and divergence.

A coverage diagram is a height-versus-range plot of the region in which a system is expected to operate at a specified level. Figure 8 is an example of a coverage diagram for a 3 GHz radar located 10 m above the sea surface. The radar has an antenna beam 3 degrees wide pointed at 0 degrees elevation and is assumed to have a free-space range of 100 km. The shaded region in the figure

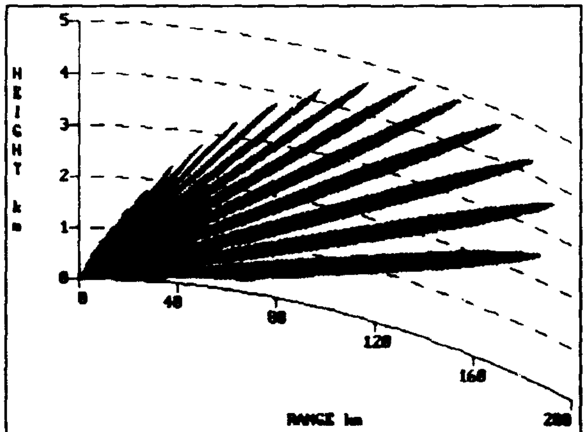

Figure 8. Vertical coverage diagram.

shows the expected coverage of this radar. The narrow lobes in the coverage diagram are the optical interference lobes, while the larger envelope to the lobes is the effect of the antenna pattern.

5.6 Diffraction

From just before to somewhat beyond the radio horizon, the dominant propagation mechanism is diffraction by the spherical earth. Diffraction is a physical optics propagation mechanism that allows energy to propagate beyond the line of sight into a shadow region. With the exception of vertical polarization for frequencies below about 300 MHz, the effects of the electrical characteristics of the earth are unimportant. However, the average effects of refraction do make a difference in this region.

Propagation in the diffraction region is characterized by an exponential decay of signal strength with increasing range, which is equivalent to a linear increase of propagation loss in dB with range. Typical values of attenuation rate for a standard atmosphere are 1 dB/km at 1 GHz and 2 dB/km at 10 GHz.

5.7 Tropospheric Scatter

Until the late 1940s it was assumed that diffraction was the only standard propagation mechanism that could contribute energy beyond the line of sight. However, theory by Booker and Gordon [13] and others, plus numerous radio experiments, have shown that energy scattered from refractive index inhomogeneities just inside the optical interference region will dominate the diffraction field at sufficiently large ranges. This mechanism is called tropospheric scatter or troposcatter, and it is most useful for communication systems where high-power transmitters and high-gain transmitter and receiver antennas can be used.

A good example to illustrate both the diffraction and troposcatter mechanisms is a radio propagation experiment reported by Ames, et al. [14]. In this experiment a 220 MHz transmitter was located 23.5 m above mean sea level and received signal was recorded in an aircraft flying an over water path during standard conditions. Figure 9 shows propagation loss results for an aircraft altitude of 152 m. Diffraction is the dominant mechanism out to about 120 km, after which troposcatter dominates with a substantially decreased attenuation rate.

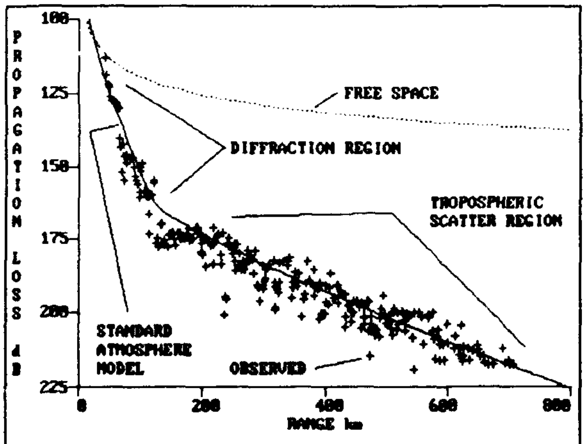

Figure 9. Example of diffraction and tropospheric scatter propagation mechanisms at 220 MHz over sea water. Terminals are 23.5 and 152 m above sea level.

5.8 Absorption

The final propagation mechanism to discuss is absorption by atmospheric gases, primarily water vapor and oxygen. This mechanism is in addition to all the previously discussed mechanisms, but it is generally not very important at frequencies below 20 GHz. The total absorption on any given path is the integrated effect along the entire path, so paths that traverse the entire atmosphere may have much more absorption at lower altitudes than at higher altitudes. For paths near the surface, Figure 10 shows attenuation rate from both water vapor and oxygen versus frequency for a temperature of 15 °C and 75% relative humidity.

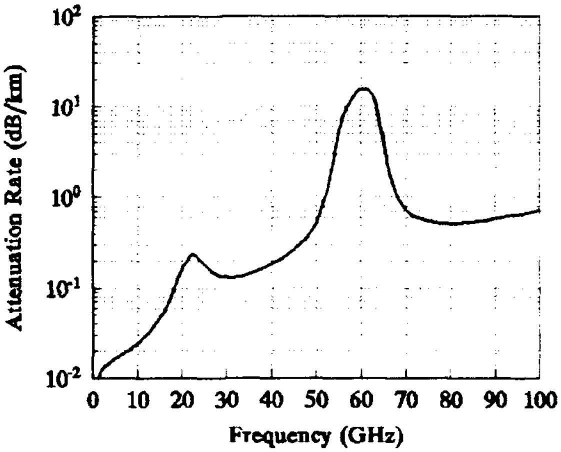

Figure 10. Attenuation rate at the ground due to oxygen and water vapor as a function of frequency for a temperature of 15°C and 75% relative humidity.

6. NONSTANDARD MECHANISMS

Nonstandard propagation mechanisms are characterized by vertical refractivity profiles that are substantially different from a standard atmosphere or by propagation paths that are located over variable terrain. The most important nonstandard refractivity profiles are those associated with ducting. Ducting occurs whenever a refractivity profile contains at least one trapping layer. The three cases of ducting that are most important in marine areas and are discussed here are evaporation ducts, surface-based ducts from elevated layers, and elevated ducts.

6.1 Evaporation Ducts

Evaporation ducts are the most persistent ducting phenomena, found nearly everywhere over the oceans and other large bodies of water. This duct is created by the rapid decrease in water vapor with altitude near the water's surface. For continuity reasons, the air immediately adjacent to the water surface is nearly saturated with water vapor and expected that such a technique will ever be available.

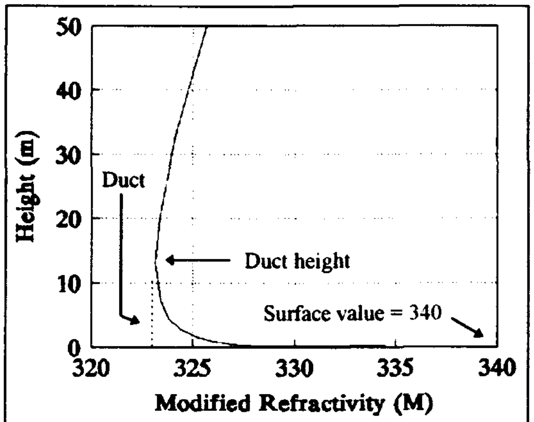

Figure 11. Modified refractivity versus height profile for an evaporation duct. The duct height is 13 m.

the relative humidity is thus nearly 100 percent. This high relative humidity decreases rapidly with increasing height in the first few meters until an ambient value is reached which depends on the general meteorological conditions. The rapid decrease in humidity creates a trapping layer adjacent to the surface as illustrated by the modified refractivity curve in Figure 11. The height at which a minimum value of M is reached is called the evaporation duct height, which is a measure of the strength of the duct. The evaporation duct itself extends down to the surface.

Since evaporation ducts are very "leaky" dielectric waveguides, they may affect radio or radar terminals significantly above as well as within the duct. The lowest frequency affected by the evaporation duct is strongly dependent on the existing evaporation duct height, and for most practical applications, the lower frequency limit is 3 GHz. Evaporation duct heights generally vary between 0 and 40 m, with a long-term mean value of about 5 m at northern latitudes, and up to 18 m at tropical latitudes. The most obvious evaporation duct effects are to give extended ranges for surface-to-surface radio or radar systems operating above 3 GHz. Evaporation ducts are very leaky, and for all frequencies above about 3 GHz, some effects from the evaporation duct will be present. As a rough guide for the duct height required to completely trap a particular frequency, refer to Table 3. The optimum frequency to achieve extended ranges via the evaporation duct appears to be around 18 GHz [15-18]. Although ducting effects extend beyond this limit, and have been measured at frequencies as high as 94 GHz [19-20], absorption by atmospheric gases and attenuation by rough surfaces counteract the trapping effects of the duct.

Frequency (GHz)	Duct Height (m)
3	25
7	14
10	10
18	6

Table 3. Full trapping evaporation duct heights.

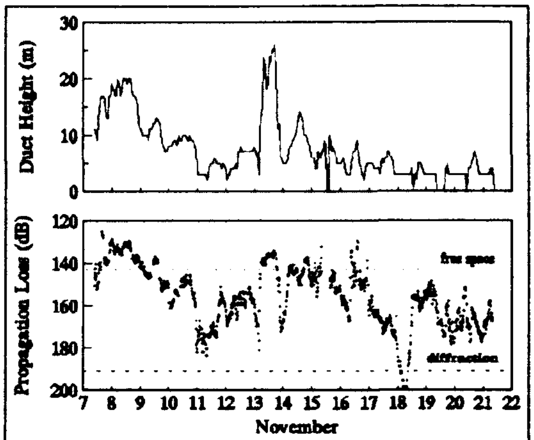

Figure 12. Evaporation duct height and propagation loss at 9.6 GHz versus time for 15 days in the Aegean Sea. Path length was 35.2 km, and the transmitter and receiver were at 4.8 and 4.9 m above mean sea level.

An example of evaporation duct effects at 9.6 GHz is illustrated by Figure 12. In this experiment propagation loss was measured between Naxos and Mykonos, Greece from 7 to 22 November 1972 [15-16]. The transmitter and receiver heights above mean sea level were 4.8 and 4.9 m, respectively, and the path length was 35.2 km. The figure shows observed propagation loss versus time and the corresponding evaporation duct height calculated from bulk meteorological measurements of air temperature, relative humidity, wind speed, and sea temperature at one end of the path, using a technique developed by Paulus [21]. This figure clearly shows how higher duct heights correspond to loss values less (signals higher) than the free space reference level, and virtually all duct heights correspond to loss values less than the diffraction reference level.

Although the evaporation duct may enhance signals on over-the-horizon paths, it can also reduce signal levels in some cases on paths within the horizon. Figure 13 is an example from an experiment performed by Anderson [22-23] in which propagation loss was derived from a 9.4 GHz

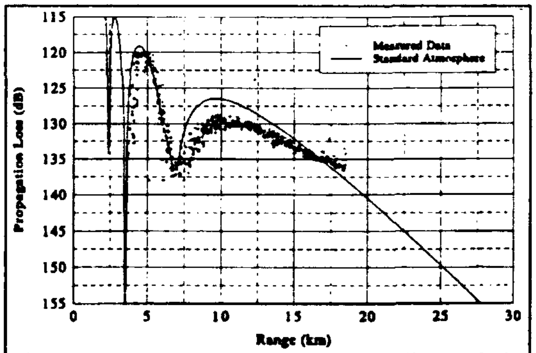

Figure 13. Low altitude propagation effects of the evaporation duct at 9.4 GHz. Radar and target heights were 23.5 and 4.9 m above mean sea level.

radar that was tracking a corner reflector on a boat. The radar and target heights were 23.5 and 4.9 m above mean sea level, respectively. This figure shows propagation loss versus range and compares the measurements to a standard atmosphere model. The evaporation duct height for this case was about 8 m, and the figure clearly shows that the measured loss was greater than standard in the vicinity of the last optical interference peak.

6.2 Surface-based Ducts

A ducting mechanism less common than the evaporation duct, but usually more dramatic when it occurs, is a surface-based duct from an elevated trapping layer. Figure 14 illustrates a typical modified refractivity profile for this type of duct. Surface-based ducts are created by trapping layers that occur up to several hundred meters in height, although they can be created by a trapping layer adjacent to the surface (sometimes referred to simply as surface ducts). A surface or surface-based duct occurs when the *M* value at the top of the trapping layer is less than the surface value of *M*. The propagation effects of these ducts are not particularly sensitive to frequency and they commonly provide for long over-the-horizon communication or detection ranges at frequencies exceeding about 100 MHz. Surface-based ducts occur with annual frequencies of up to 58% and are the type of duct responsible for most reports of extremely long over-the-horizon radar detection and communication ranges, such as the example between India and Arabia cited earlier. These ducts rarely exceed a few hundred meters in thickness.

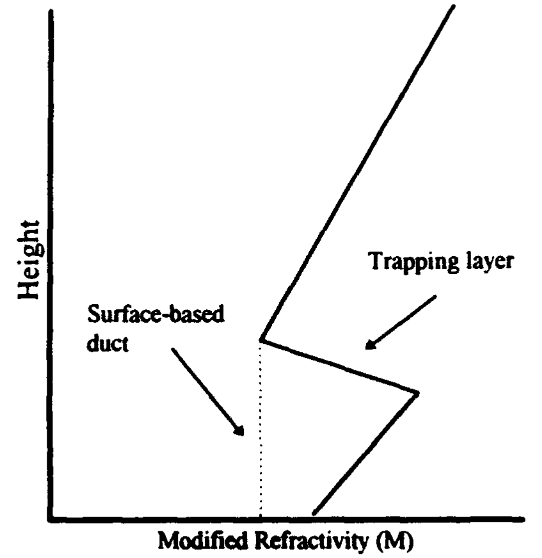

Figure 14. Modified refractivity versus height profile for a surface-based duct.

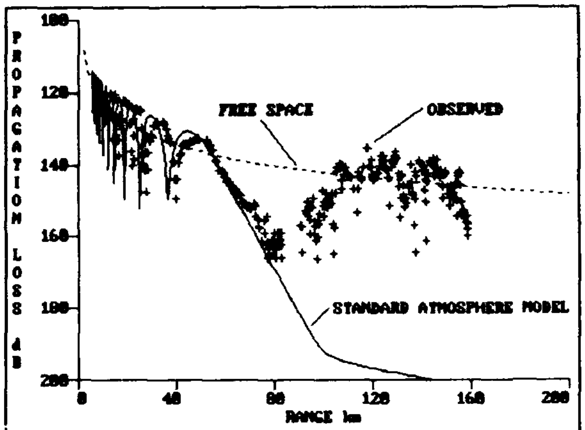

Figure 15. Propagation loss versus range in a surface-based duct for 3.0 GHz. Transmitter and receiver heights were 21 and 152 m above mean sea level.

A good example of propagation in a surface-based duct is given in Figure 15. In this experiment, the frequency was 3 GHz, and the transmitter and receiver heights were 21 and 152 m above mean sea level. The figure shows observed loss and a modeled standard atmosphere loss. At close ranges, the observations match the standard model reasonably well, but at ranges well beyond the 70 km horizon range, the observed loss is far less than the standard predictions due to the duct. An interesting feature of surface-based ducts is the "skip zone" effect illustrated by the measurements. If a radar, for example, can detect a certain target for propagation loss less than 140 dB, then in this example, a skip zone would exist from about 55 to 105 km where the target would not be seen. Figure 16 is a ray trace diagram for a surface-based duct similar to the case of Figure 15 that clearly illustrates the refractive process responsible for the creation of the skip zone.

Although surface-based ducts have the greatest impact on frequencies in excess of 100 MHz, they can also cause noticeable effects at lower frequencies, even as low as 20 MHz. Figure 17 shows path loss versus frequency from 4 to 32 MHz measured by Hansen [24] on a 235 km southern California path. No skywave signals existed on this path. Hansen found that above approximately 20 MHz the average signal levels considerably exceeded predictions based on groundwave theory. Pappert and Goodhart [25]

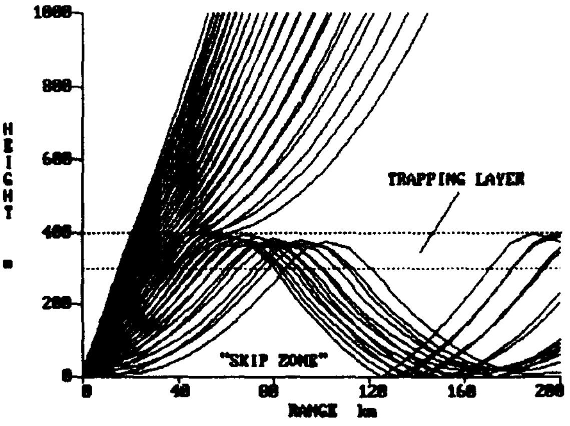

Figure 16. Ray trace diagram illustrating a skip zone created by a surface-based duct.

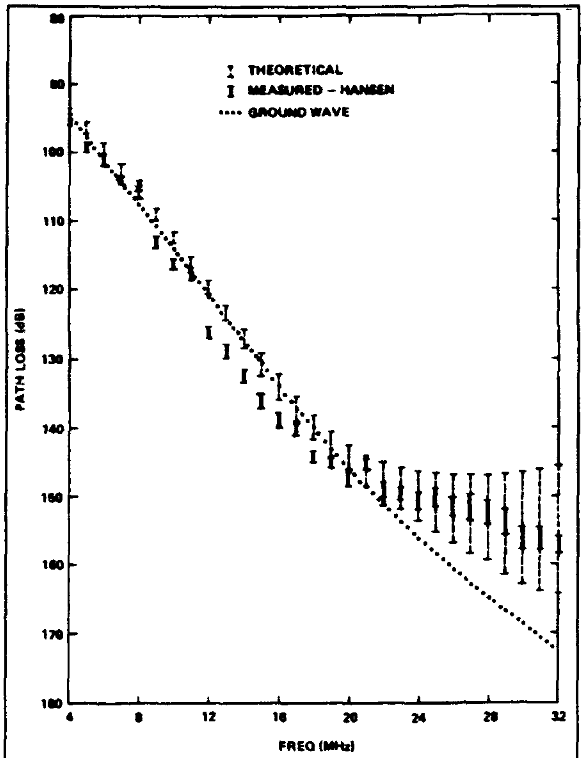

Figure 17. Path loss versus frequency showing effects of tropospheric ducting. From Hansen [24] and Pappert and Goodhart [25].

modeled the effects of ducting on this path using available refractivity profiles and their results are also shown in Figure 17 labeled as "theoretical." Even though there is a spread in the observed and theoretical results, they are in substantial agreement, and it seems clear that a case has been made that the enhanced signal levels at these very low frequencies are the result of tropospheric ducts.

6.3 Elevated Ducts

Elevated ducts are created by trapping layers in a similar manner to surface-based ducts. In surface-based ducts, the radio wave is repeatedly bent downward by the trapping layer and reflected upward by the surface. In elevated ducts, the radio wave is repeatedly bent downward by the trapping layer and then bent upward by one or more refractive layers below the trapping layer. Figure 18 illustrates a typical modified refractivity profile for an elevated duct. It is necessary that the *M* value at the top of the trapping layer be greater than the *M* value at some height below the trapping layer to form an elevated duct. The elevated duct extends from the top of the trapping layer down to the highest height at which the *M* value below the trapping layer equals *M* at the top of the trapping layer.

Figure 19 is a ray trace diagram illustrating propagation in an elevated duct. According to ray optics theory, both terminals of a radio path need to be within the duct to gain the benefit of enhanced signals from the duct. In practice, however, these ducts are leaky and some benefit can be achieved with terminals outside the duct. The thickness of these ducts can range from near zero to several hundred meters, and the frequencies affected will vary accordingly. In many cases, frequencies as low as 100 MHz will be affected. In addition to the enhanced signal levels in or near the elevated duct, there can also be an absence of ray coverage above the duct, compared to what would have been there for a standard atmosphere. This lack of coverage has often been called a radio or radar "hole" and an example of this effect is seen in Figure 19. In practice some energy does propagate into this region by physical optics processes not accounted for by ray optics theory, but the signal levels will generally be much less than for a standard atmosphere.

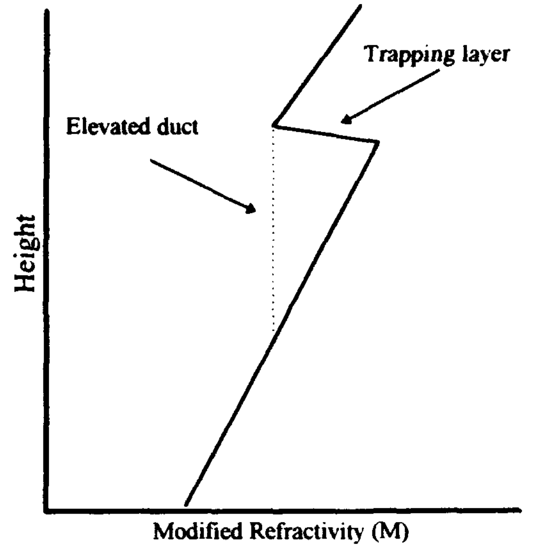

Figure 18. Modified refractivity versus height profile for an elevated duct.

A large experimental effort to investigate propagation in elevated ducts was conducted in the late 1950s and early 1960s under the name Project Tradewinds [26], which investigated the semi-permanent ducts associated with tradewind regions. One part of these experiments consisted of flying an instrumented aircraft from San Diego,

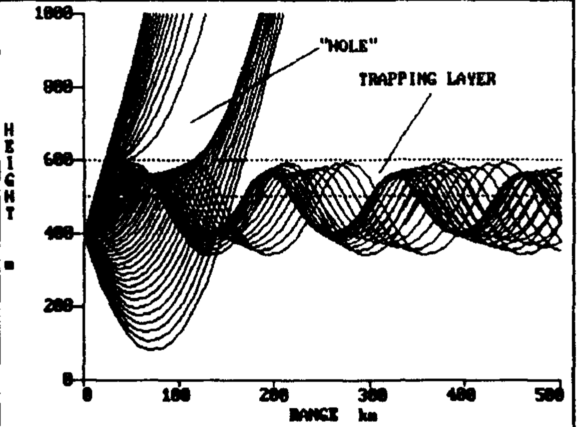

Figure 19. Ray trace diagram showing propagation in an elevated duct.

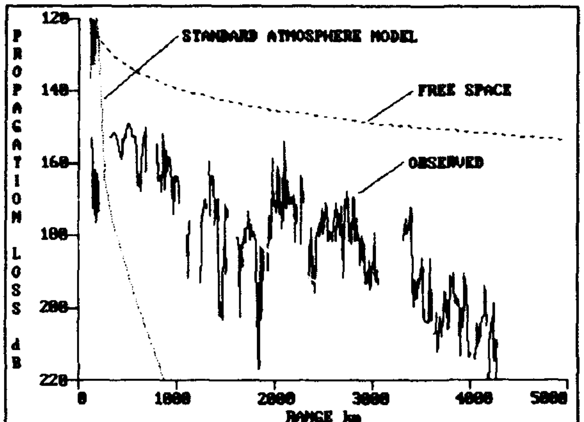

Figure 20. Propagation loss at 220 MHz between San Diego and Hawaii. From Project Tradewinds [26].

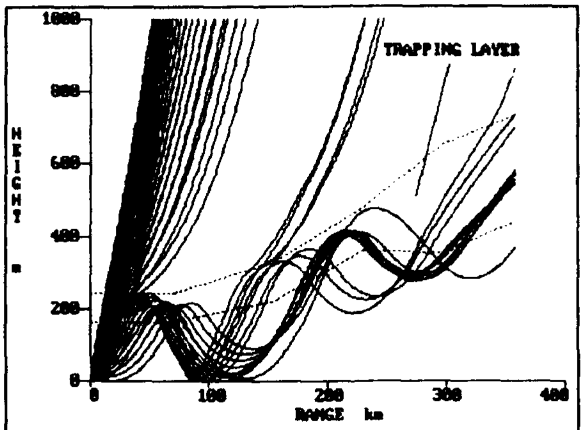

Figure 21. Ray trace diagram showing effects of lateral inhomogeneity. The trapping layer rises with range changing a surface-based duct into an elevated duct.

California to Oahu, Hawaii and recording 220 and 445 MHz signals transmitted at both ends of the path. Figure 20 shows the propagation loss for one flight for a 220 MHz transmitter at San Diego located 244 m above sea level and an aircraft altitude that varied from near 0 to about 1500 meters. The path length was about 4200 km, and for this case the signal levels were measured all along the path and were detected even after the aircraft had landed in Hawaii.

6.4 Lateral Inhomogeneity

The refractive index layers in the atmosphere are usually stratified with the vertical changes being many times greater than horizontal changes. All of the mechanisms discussed previously assume that the vertical refractivity profile is homogeneous with range. In reality, the atmosphere is never perfectly homogeneous with range, but if the actual propagation effects are equivalent to those effects that would be observed in a homogeneous environment, then the assumption of horizontal homogeneity is valid. In practice, this assumption is valid most of the time, especially over open ocean conditions. However, there are times when the vertical refractive index profile changes enough along the propagation path to alter propagation effects substantially compared to the homogeneous case. These cases are said to be subject to the effects of lateral inhomogeneity.

As an example of lateral inhomogeneity, consider the ray trace diagram of Figure 21. In this case, the vertical refractivity profile at the transmitter is characterized by a surface-based duct. As the range increases, the height of the trapping layer also increases, such that the surface-based duct becomes an elevated duct. The rays that are trapped tend to follow the trapping layer and result in enhanced signal levels at much higher altitudes than would have been the case for a homogeneous surface-based duct. This environment is a realistic one that was measured off the coast of San Diego [8].

More examples of propagation effects under conditions of lateral inhomogeneity will be given in Part B of this lecture, when propagation models are described. From a propagation assessment point of view, it has been found that the assumption of horizontal homogeneity is good about 86 percent of the time [7]. A similar conclusion has been reached by U.S. Navy users of IREPS.

6.5 Terrain Effects

The last nonstandard propagation mechanism that I will discuss is propagation over terrain. Another lecture in this series covers this topic in depth, so I will mention only a few points. When at least one part of a propagation path is over variable terrain, that terrain will normally obstruct or otherwise interfere with the radio wave. Diffraction as affected by the various high points in the terrain profile is the usual dominant propagation mechanism. In some cases, the effects of surface-based or elevated ducts may be comparable to the terrain diffraction mechanism. In other cases, ducting may be the dominant propagation mechanism, and the terrain profile along the path may reduce the efficiency of the duct.

As an example of conditions where both ducting and terrain are important, consider the following radio experiment conducted in the Arizona desert [27]. In this experiment, the primary propagation mechanism was ducting associated with the radiation temperature inversion created by nocturnal cooling of the ground. Two propagation paths 43 and 75 km long were established with 60 m towers at both ends of the paths, such that both optical and nonoptical paths could be studied. Received signal strengths from 170 MHz to 24 GHz were recorded versus time, 24 hours per day, and selected height-gain recordings were also made. The terrain features along the propagation paths differed from a smooth earth by 30 m or less in height. The experiment concluded that only the highest frequencies were affected by the radiation duct, but many measurements clearly displayed the mixed effects of ducting and terrain. In Part B of this lecture, I will show an example where one of these results is well modeled when both the terrain and the lateral inhomogeneity of the duct are accounted for.

7. STATISTICS OF DUCTING

Of the various propagation mechanisms discussed here, the surface ducting mechanisms are the most likely to substantially alter the performance of a given system. For example, an evaporation duct or a surface-based duct might extend a shipboard radar's capability to detect a low-altitude target from 20 km to several hundred km. Therefore, it is important to discuss how strong these mechanisms are and how often they exist in various parts of the world.

EREPS is an IBM/PC-compatible system that contains a Surface Duct Summary (SDS) program [5] that summarizes annualized climatological evaporation duct height in histogram form and the percent of occurrence of surface-based ducts for most ocean areas of the world. The statistics displayed by SDS are derived from two meteorological data bases, one for marine surface meteorological observations from which evaporation duct heights were derived, and one for radiosonde observations, from which statistics on surface-based ducts were derived [28].

The surface marine observations data base was assembled by the National Climatic Data Center and is named DUCT63. This data set is a 15 year subset of over 150 years of worldwide observations obtained from ship logs, ship weather reporting forms, published observations, automatic buoys, etc. The reported observations of air temperature, humidity, wind speed, and water temperature were converted into evaporation duct height using the technique described by Paulus [21]. These data are organized into 292 10-degree latitude by 10-degree longitude squares called Marsden squares located between latitudes 70° N and 60° S.

The radiosonde data base was assembled by GTE Sylvania Corporation and is called the Radiosonde Data Analysis II. This data set is based on approximately 3 million worldwide radiosonde soundings taken during a 5 year period, from 1966 to 1969 and from 1973 to 1974. This data set is organized into 399 coastal, island, and ocean weather station ship radiosonde locations.

SDS displays a world map to the user showing the locations of all Marsden squares and radiosondes in the two data bases, as illustrated in Figure 22. The user selects one or more squares or the world average, and SDS then presents the annual surface duct summary of the corresponding ducting conditions. Figure 23 is an example for the Greek islands area corresponding to the measurements presented in Figure 12. A histogram of evaporation duct height is given in 2 m intervals from 0 to 40 m. The upper right area identifies the Marsden square, shows the average evaporation duct height and wind speed, and the sample size. The lower right area identifies the radiosonde location, surface-based duct (SBD) occurrence, average SBD height, average surface refractivity (NSUBS), average effective earth radius factor (K), and sample size.

The annual average evaporation duct height can range from just a few meters to about 18 meters depending on geographic location, with lower heights occurring in northern latitudes. Table 4 shows several ocean areas and their average duct heights to illustrate this variability. Surface-based duct occurrence varies from 0 in northern latitudes to 58% in the Persian Gulf area, as illustrated by several sample locations in Table 5.

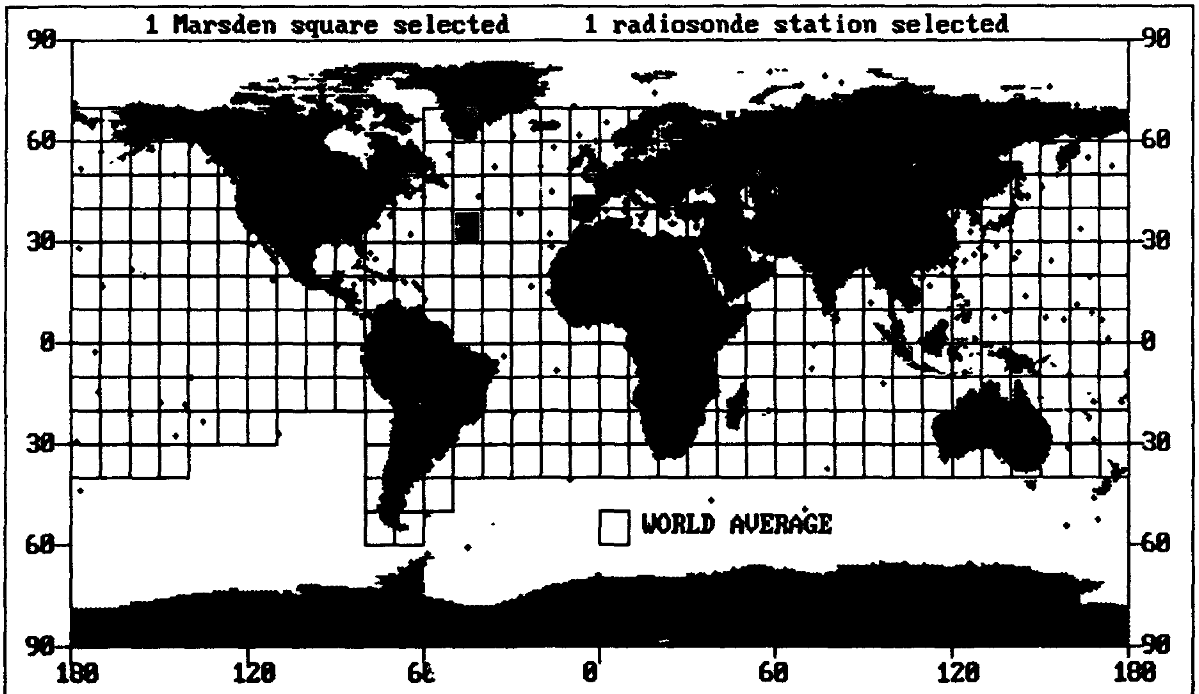

Figure 22. EREPS Surface Duct Summary display showing the locations of Marsden squares and radiosonde stations.

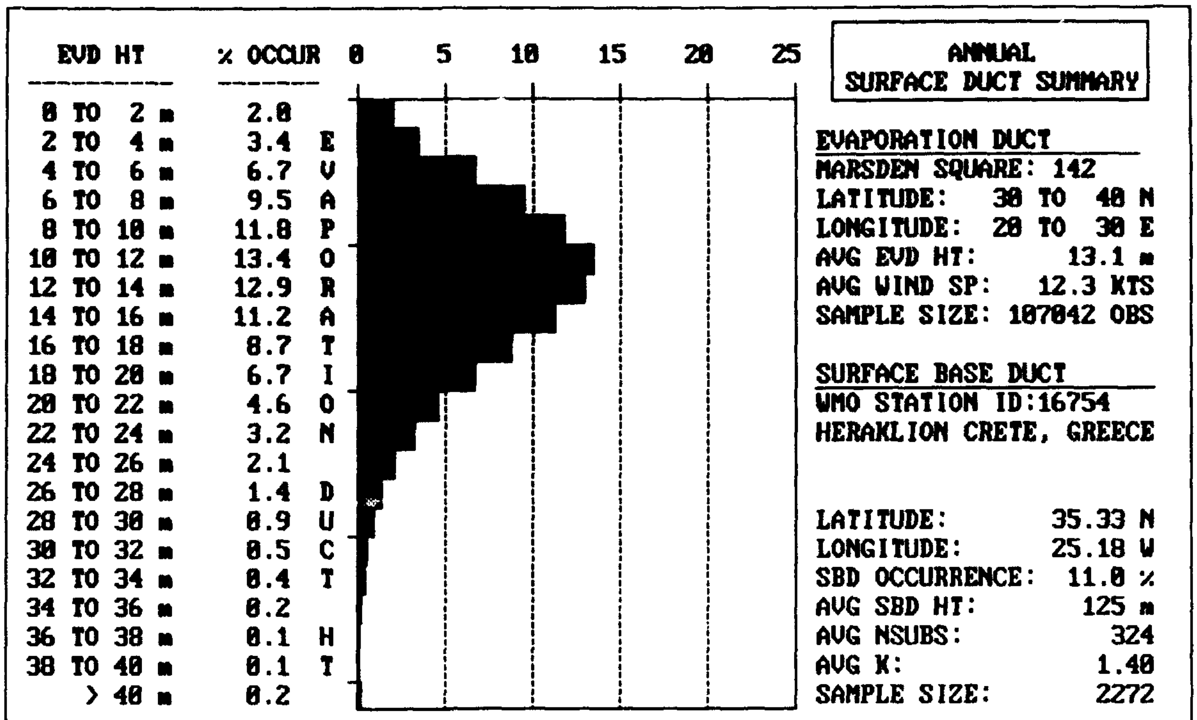

EVD HT	% OCCUR
0 TO 2 m	2.0
2 TO 4 m	3.4
4 TO 6 m	6.7
6 TO 8 m	9.5
8 TO 10 m	11.8
10 TO 12 m	13.4
12 TO 14 m	12.9
14 TO 16 m	11.2
16 TO 18 m	8.7
18 TO 20 m	6.7
20 TO 22 m	4.6
22 TO 24 m	3.2
24 TO 26 m	2.1
26 TO 28 m	1.4
28 TO 30 m	0.9
30 TO 32 m	0.5
32 TO 34 m	0.4
34 TO 36 m	0.2
36 TO 38 m	0.1
38 TO 40 m	0.1
> 40 m	0.2

ANNUAL
SURFACE DUCT SUMMARY

EVAPORATION DUCT
MARSDEN SQUARE: 142
LATITUDE: 30 TO 40 N
LONGITUDE: 20 TO 30 E
AVG EVD HT: 13.1 m
AVG WIND SP: 12.3 KTS
SAMPLE SIZE: 107042 OBS

SURFACE BASE DUCT
WMO STATION ID:16754
HERAKLION CRETE, GREECE

LATITUDE: 35.33 N
LONGITUDE: 25.18 W
SBD OCCURRENCE: 11.0 %
AVG SBD HT: 125 m
AVG NSUBS: 324
AVG K: 1.40
SAMPLE SIZE: 2272

Figure 23. EREPS Surface Duct Summary display showing a histogram of evaporation duct height, average evaporation duct height and wind speed, and percent occurrence and other parameters for surface-based ducts.

Ocean Area	Average Duct Height (m)
Labrador Sea	3.5
North Sea	6.4
Norwegian Sea	6.7
Bay of Biscay	8.2
Adriatic Sea	10.9
Aegean Sea	13.1
Arabian Sea	14.8
Gulf of Mexico	16.6
Caribbean Sea	17.6

Table 4. Annual average evaporation duct heights.

Radiosonde Location	SBD Occurrence (%)
Ship 65.7° N 2.2° W	0
Ship 45.0° N 16.0° W	2
Azores, Portugal	10
Cabo Verde, Portugal	15
Tobruk, Libya	21
San Diego, CA, USA	23
Bahrain	58

Table 5. Percent occurrence of surface-based ducts.

8. CONCLUSIONS

In this part of the lecture I have defined the basics of refractive effects from VHF to EHF and outlined the most important radio propagation mechanisms for point-to-point paths near the earth's surface. I have presented both standard mechanisms and nonstandard mechanisms such as ducting. I emphasized propagation over the sea, since this is where some of the most dramatic anomalous radio propagation events occur, and briefly discussed some statistics and geographical variability of the two most important ducting mechanisms.

In Part B of this lecture, I will build on the material presented here and discuss the various models that are used in assessing radio propagation effects. I will also discuss radio propagation assessment systems and present several application examples that illustrate the accuracy and utility of the models.

ACKNOWLEDGMENT

This work was supported by the Office of Naval Research.

REFERENCES

1. Freehafer, J.E., "Tropospheric Refraction," in "Propagation of Short Radio Waves," D.E. Kerr, Ed., New York, McGraw-Hill, 1951, pp 9-22.
2. Kerr, D.E., Ed., "Propagation of Short Radio Waves," New York, McGraw-Hill, 1951.
3. Katzin, M., R.W. Bauchman, and W. Binnian, "3- and 9-Centimeter Propagation in Low Ocean Ducts," Proc. IRE, 35, 9, Sep 1947, pp 891-905.
4. Hitney, H.V. and J.H. Richter, "Integrated Refractive Effects Prediction System (IREPS)," Nav. Eng. J., 88, 2, Feb 1976, pp 257-262.

5. Hitney, H.V., "Engineer's Refractive Effects Prediction System (EREPS)," in "Operational Decision Aids for Exploiting or Mitigating Electromagnetic Propagation Effects," AGARD CP-453, May 1989, Paper 6.
6. Phegley, L. And C. Crosiar, "The Third Phase of TESS," Bull. Amer. Meteor. Soc., 72, 7, July 1991, pp 954-960.
7. Hitney, H.V., J.H. Richter, R.A. Pappert, K.D. Anderson, and G.B. Baumgartner, "Tropospheric Radio Propagation Assessment," Proc. IEEE, 73, 2, Feb 1985, pp 265-283.
8. Richter, J.H., Ed., "Radio Wave Propagation Modeling, Prediction, and Assessment," AGARD AG-326, Dec 1990.
9. Bean, B.R. and E.J. Dutton, "Radio Meteorology," New York, Dover, 1968.
10. Recommendation 341-2, "The concept of transmission loss for radio links," in "Recommendations and Reports of the CCIR, Volume V, Propagation in Nonionized Media," ITU XVIIth Plenary Assembly, Düsseldorf, 1990.
11. Reed, H.R. and C.M. Russell, "Ultra High Frequency Propagation," second edition, Cambridge, Mass., Boston Technical Publishers, Inc., 1966.
12. Beard, C.I., "Coherent and Incoherent Scattering of Microwaves from the Ocean," IRE Trans. Antennas Propagat., AP-9, Sep 1961, pp 470-483.
13. Booker, H.G. and W.E. Gordon, "A Theory of Radio Scattering in the Troposphere," Proc. IRE, 38, 4, Apr 1950, pp 401-412.
14. Ames, L.A., P. Newman, and T.F. Rogers, "VHF Tropospheric Over-water Measurements Far Beyond the Horizon," Proc. IRE , 43, 10, 1955, pp 1369-1373.
15. Richter, J.H. and H.V. Hitney, "The Effect of the Evaporation Duct on Microwave Propagation," Naval Electronics Laboratory Center TR 1949, Apr 1975.
16. Richter, J.H. and H.V. Hitney, "Antenna Heights for the Optimum Utilization of the Oceanic Evaporation Duct," Naval Ocean Systems Center TD 1209, vols. 1 and 2, Jan 1988.
17. Anderson, K.D., "Evaporation Duct Effects on Moderate Range Propagation Over the Sea at 10 and 1.7 cm Wavelengths," Naval Ocean Systems Center TR 858, Nov 1982.
18. Anderson, K.D., "Surface-Search Radar Performance in the Evaporation Duct: Global Predictions," Naval Ocean Systems Center TR 923, Oct 1983.
19. Anderson, K.D., "94-GHz Propagation in the Evaporation Duct," IEEE Trans. Antennas Propagat., 38, 5, May 1990, pp 746-753.
20. Anderson, K.D., "Evaporation Duct Effects at Millimeter Wavelengths," in "Atmospheric Propagation in the UV, Visible, IR and mm-Wave Region and Related Systems Aspects," AGARD CP-454, Oct 1989, Paper 9.
21. Paulus, R.A., "Practical application of an evaporation duct model," Radio Sci., 20, 4, Jul-Aug 1985, pp 887-896.
22. Anderson, K.D., "Remote Sensing of the Evaporation Duct Using an X-Band Radar," in "Remote Sensing of the Propagation Environment," AGARD CP-502, Oct 1991, Paper 3.
23. Anderson, K.D., "Radar Detection of Low-Altitude Targets in a Maritime Environment," Naval Command, Control and Ocean Surveillance Center, RDT&E Division TR 1630, vols. 1 and 2, Nov 1993.
24. Hansen, P., "Measurements of basic transmission loss for HF ground wave propagation over sea water," Radio Sci., 12, 3, May-Jun 1977, pp 397-404.
25. Pappert, R.A. and C.L. Goodhart, "A numerical study of tropospheric ducting at HF," Radio Sci., 14, 5, Sep-Oct 1979, pp 803-813.
26. Guinard, N.W., J. Ransone, D. Randall, C. Purves, and P. Watkins, "Propagation Through an Elevated Duct: Tradewinds III," IEEE Trans. Antennas Propagat., 12, 4, July 1964, pp 479-490.
27. Day, J.P. and L.G. Trolese, "Propagation of Short Radio Waves Over Desert Terrain," Proc. IRE, 38, 2, Feb 1950, pp 165-175.
28. Patterson, W.L., "Historical Electromagnetic Propagation Condition Database Description," Naval Ocean Systems Center TD 1149, Sep 1987.

Refractive Effects from VHF to EHF
Part B: Propagation Models

Herbert V. Hitney
Ocean and Atmospheric Sciences Division
NCCOSC RDTE DIV 543
53170 WOODWARD ROAD
SAN DIEGO CA 92152-7385
USA

1. SUMMARY

Part A of this lecture introduced and discussed refraction-related propagation mechanisms and their effects in the VHF to EHF bands. Part B builds on the material of Part A to describe and discuss propagation models that are used to assess radio propagation effects, and uses examples from propagation assessment systems and other propagation software to illustrate many of the effects. Frequencies from about 30 MHz to 100 GHz are considered.

Both standard and nonstandard propagation models are described. The standard models are the effective-earth-radius model, the Fresnel reflection coefficient model, and models for surface roughness, divergence, optical interference, diffraction, and tropospheric scatter. Ray trace, waveguide, parabolic equation, and hybrid models are discussed to account for nonstandard effects. A brief description of three propagation assessment systems that include the various models is given, and several application examples are presented that illustrate both the propagation effects and the applicability of the models. For evaporation ducts, a statistical method is discussed that can be used for system planning purposes or engineering of new equipment. A comparison of this method to measurements is presented.

2. INTRODUCTION

Modeling radio wave propagation in the lower atmosphere is important for many reasons, including the development of decision aids for communications, radar, and navigation systems. Decision aids can be broken down into two broad categories: engineering decision aids and tactical decision aids. Engineering decision aids are most useful to electromagnetic systems engineers for the design of new systems or the evaluation of existing systems. These aids frequently consider the statistical nature of the propagation environment, such that a system's long-term performance can be evaluated. Tactical decision aids are most useful to military planners who must consider propagation effects on military sensor and weapon systems. These aids normally consider a single measured or forecast environmental condition such that propagation effects can be exploited or mitigated by altering military tactics. For example, changing an attacking aircraft's flight profile can minimize the range at which it is first detected by radar. Both categories of decision aids consider the same propagation mechanisms, and use similar radio propagation models, described in the this paper.

In the same manner as part A of this lecture, I will discuss only those propagation models that are considered, included, or planned in the Integrated Refractive Effects Prediction System (IREPS), the Engineer's Refractive Effects Prediction System (EREPS), and the Tactical Environmental Support System (TESS). Again, this should not imply that other mechanisms or models are not important, but that they are simply not considered or necessary for the systems mentioned.

3. STANDARD PROPAGATION MODELS

Standard propagation models are applicable to propagation paths over a smooth or slightly rough earth surface and conditions that can be well represented by a standard atmosphere. Although the refractive index decreases exponentially in a standard atmosphere, at low altitudes the decrease is very nearly linear. All of the models described in this section assume this linear decrease for computational simplicity, but they do allow the user to specify the gradient, which is often taken as -39 *N*/km.

3.1 Effective-earth-radius Model

Under standard or normal conditions, a radio ray curves downward with a curvature less than the earth's surface. The effective-earth-radius concept [1] replaces the earth's true radius with a larger radius such that the relative curvature between the ray and the earth's surface is maintained and the ray becomes a straight line. For small elevation angles, this transformation accurately preserves angles, heights, and ranges, and greatly simplifies the computations required to determine grazing angles and path length differences for specified terminal locations. Sometimes the effective earth radius is also referred to as the equivalent earth radius [2]. The effective earth radius a_e and the effective-earth-radius factor k are related by

$$a_e = ka \tag{1}$$

where a is the true earth radius. k can be computed using

$$k = 1\Big/\left[1 + a(dn/dh)\right] \tag{2}$$

where dn/dh is the vertical refractive index gradient. Using the mean earth radius of 6371 km and a refractivity gradient of -39 *N*/km gives k = 1.33 or about 4/3.

3.2 Fresnel Reflection Coefficient

The complex reflection coefficient for reflection of an electromagnetic wave from a smooth surface is given by the Fresnel reflection coefficient. A good description of the derivation of the following formulas is given by Reed and Russell [2]. Let R be the magnitude and φ be the phase lag of the reflection coefficient and let the subscripts h and v refer to horizontal and vertical polarization, respectively. Then the Fresnel reflection coefficients are given by

$$R_h e^{-i\varphi_h} = \frac{\sin\psi - \sqrt{n^2 - \cos^2\psi}}{\sin\psi + \sqrt{n^2 - \cos^2\psi}} \tag{3}$$

and

$$R_v e^{-i\varphi_v} = \frac{n^2\sin\psi - \sqrt{n^2 - \cos^2\psi}}{n^2\sin\psi + \sqrt{n^2 - \cos^2\psi}} \tag{4}$$

where ψ is the grazing angle and n^2 is the square of the refractive index of the reflecting surface given by

$$n^2 = \varepsilon_r - i\,60\,\sigma\,\lambda \tag{5}$$

in which ε_r is the relative permittivity, σ is the conductivity in S/m, and λ is radio wavelength in m. The electrical characteristics ε_r and σ are functions of radio frequency and the type of surface, and can be determined from multiple sources, including a figure in the *Recommendations and Reports of the CCIR* [3]. Table 1 gives example values for both parameters for sea water at a temperature of 20 °C and average salinity for a few frequencies.

Frequency (MHz)	ε_r	σ(S/m)
100	70	5
1000	70	5
10000	50	17

Table 1. Sample relative permittivity ε_r and conductivity σ for sea water at 20 °C and average salinity.

3.3 Miller-Brown Surface Roughness Model

For reflection from a wind-roughened sea, the Fresnel reflection coefficient must be modified for the effects of surface roughness. The original theory was developed by Ament [4] and validated experimentally by Beard [5], but a more recent model by Miller and Brown [6] has proven to be more complete and is given by

$$R = R_0 \exp\left[-2(2\pi g)^2\right] I_0\left[2(2\pi g)^2\right] \tag{6}$$

where R is the rough-surface coherent reflection coefficient, R_0 is the Fresnel reflection coefficient from either (3) or (4), I_0 is the modified Bessel function, and the "apparent ocean roughness" g is given by

$$g = (\sigma_h \sin\psi)/\lambda \tag{7}$$

where σ_h is the standard deviation of the sea-surface elevation, ψ is the grazing angle, and λ is the electromagnetic wavelength. The relationship of σ_h to wind speed is derived from the Phillips' saturation curve spectrum [7] and is given by

$$\sigma_h = 0.0051\,u^2 \tag{8}$$

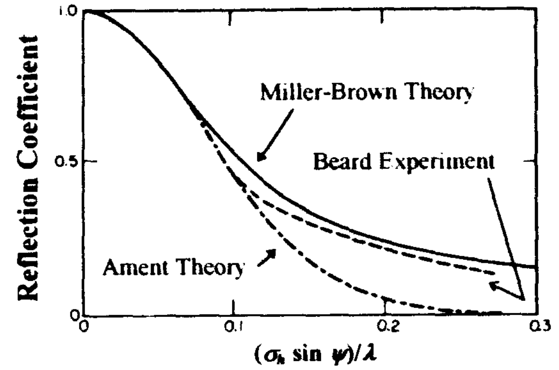

Figure 1. Rough surface reflection coefficient R/R_0 versus apparent ocean roughness.

where u is wind speed in meters per second. A very useful and quite accurate approximation to (6) that does not require computation of the modified Bessel function is given by CCIR [8] as

$$R = \frac{1}{\sqrt{3.2x - 2 + \sqrt{(3.2x)^2 - 7x + 9}}} \tag{9}$$

where $x = 0.5\,g^2$. Figure 1 illustrates R versus g for both the Ament and Miller-Brown theories compared to the measurements of Beard.

3.4 Divergence Factor

A radio wave reflecting off the spherical earth's surface at low grazing angles suffers a spreading loss due to divergence. The theory for this loss was originally worked out by Van der Pol and Bremmer [9]. The divergence factor D is defined as the ratio of the field strength obtained after reflection from a smooth spherical surface to the field strength that would be obtained after reflection from a plane surface, with the radiated power, total axial distance, and type of surface being the same in both cases, and the solid angle at the transmitter being a small elemental angle approaching zero. Referring to Figure 2, D is given by

$$D = \left[1 + \frac{2r_1 r_2}{ka(r_1 + r_2)\sin\psi}\right]^{-1/2} \tag{10}$$

where r_1 and r_2 are the ranges between the transmitter and reflection point and the reflection point and the receiver, and the other variables are as previously defined.

3.5 Optical Interference Model

In the optical interference region, the propagation factor F is determined from the coherent sum of the direct and surface-reflected field components according to

$$F = \sqrt{f_d^{\,2} + [f_r DR]^2 + 2 f_d f_r DR \cos(\Omega)}\,. \tag{11}$$

The direct and reflected antenna pattern factors f_d and f_r correspond to angles γ_d and γ_r relative to the main beam pointing angle γ_0 above the local horizontal, as illustrated in Figure 2. The antenna pattern function f is normalized to unity gain in the direction of the antenna beam maximum. D and R are the divergence factor and reflection coefficient,

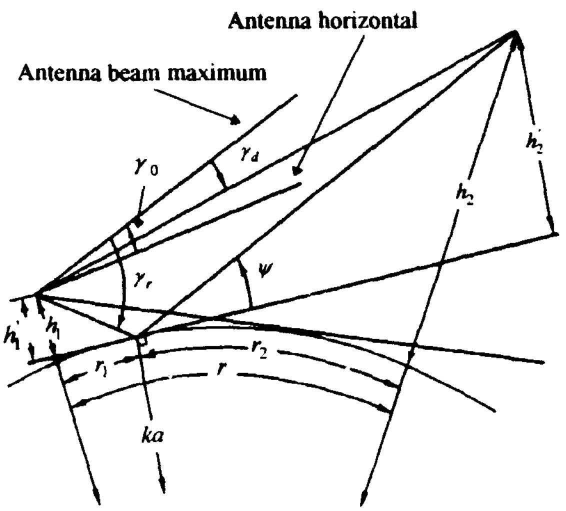

Figure 2. Geometry for optical interference region.

computed by (10) and (6), respectively, for the values of r_1, r_2 and ψ shown in Figure 2. The total phase lag Ω is the sum of the phase lag angle φ determined from (3) or (4) as appropriate and the path length difference angle δ given by

$$\delta = \frac{2\pi}{\lambda} \frac{2h_1'h_2'}{r} \quad (12)$$

where h_1' and h_2' are the effective terminal heights of the transmitter and receiver illustrated in Figure 2 and computed as

$$h_1' = h_1 - \frac{r_1^2}{2ka} \qquad h_2' = h_2 - \frac{r_2^2}{2ka} \quad (13)$$

where h_1 and h_2 are the transmitter and receiver heights above the sea, respectively. The optical region models presented here assume that the transmitter height is always less than or equal to the receiver height. If this is not the case, the transmitter and receiver heights are simply reversed, and the calculation of F will be correct according to the Lorentz reciprocity theorem [10]. The grazing angle ψ is computed as

$$\psi = h_1'/r_1 = h_2'/r_2 \quad (14)$$

and the antenna pattern angles γ_d and γ_r are computed as

$$\begin{aligned} \gamma_d &= \gamma_0 - \frac{(h_2 - h_1)}{r} - \frac{r}{2ka} \\ \gamma_r &= \gamma_0 - \frac{r_1}{ka} - \psi. \end{aligned} \quad (15)$$

The expression for F in (11) is valid provided that δ is greater than or equal to $\pi/2$ or ψ is greater than a limit described by Reed and Russell [2] below which the divergence factor calculation is in substantial error. This limit is

$$\tan\psi = (\lambda/2\pi ka)^{1/3}. \quad (16)$$

Also, the methods presented here are generally valid only for grazing angles less than about 5 degrees since many of the formulas are based on small angle approximations.

The optical region calculations are normally implemented in one of two ways. For the case in which the two terminal heights and range separation are specified, then (13) and (14) are combined to form the cubic equation

$$2r_1^3 - 3rr_1^2 + \left[r^2 - 2ka(h_1 + h_2)\right]r_1 + 2kah_1r = 0 \quad (17)$$

which can be solved for r_1 using either the formal solution found in many standard textbooks, or by a numerical iteration process such as Newton's method. A more efficient method for some applications is to specify the two terminal heights and the reflection point range r_1 and then solve (17) for r and (11) through (15) for the other quantities needed. This method avoids solving the cubic equation and is particularly useful to provide a graphical plot of F versus r when it is not necessary that specific values of r be used.

3.6 CCIR Diffraction Model

Diffraction is the dominant mechanism for propagation paths at short over-the-horizon ranges. A very useful model for diffraction that was developed for a variable effective earth radius a_e is described by CCIR [11] and is summarized here. Some of the variables have been changed from the source document to avoid conflicts with other usage. The propagation factor F is given by

$$20\log F = V(X) + G(Z_1) + G(Z_2) \quad (18)$$

where X is a normalized range between the terminals and Z_i are normalized heights for each terminal given by

$$X = \beta\left(\frac{\pi}{\lambda a_e^2}\right)^{1/3} r \qquad Z_i = 2\beta\left(\frac{\pi^2}{\lambda^2 a_e}\right)^{1/3} h_i \quad (19)$$

where β is a parameter allowing for the type of ground and polarization. β can be taken as 1 for horizontal polarization at all frequencies and vertical polarization above 20 MHz over land or 300 MHz over sea. Otherwise, it is given by

$$\beta = \frac{1 + 1.6K^2 + 0.75K^4}{1 + 4.5K^2 + 1.35K^4} \quad (20)$$

where K is determined for either horizontal (K_h) or vertical (K_v) polarization as

$$\begin{aligned} K_h &= \left(\frac{2\pi a_e}{\lambda}\right)^{-1/3}\left[(\varepsilon_r - 1)^2 + (60\lambda\sigma)^2\right]^{-1/4} \\ K_v &= K_h\left[\varepsilon_r^2 + (60\lambda\sigma)^2\right]^{1/2} \end{aligned} \quad (21)$$

and ε_r is the relative permittivity and σ is surface conductivity in S/m. In (18), V is a distance term given by

$$V(X) = 11 + 10\log(X) + 17.6X \quad (22)$$

and G is a height-gain term given by

$$G(Z) \cong \begin{cases} 17.6(Z - 1.1)^{1/2} - 5\log(Z - 1.1) - 8 & Z > 2 \\ 20\log(Z + 0.1Z^3) & 10K < Z < 2 \\ 2 + 20\log K + 9\log\dfrac{Z}{K}\left[\log\dfrac{Z}{K} + 1\right] & \dfrac{K}{10} < Z < 10K \\ 2 + 20\log K & Z < \dfrac{K}{10} \end{cases} \quad (23)$$

where K is the appropriate term from (21).

The method just described is based on a single term in a classical residue series solution, which is sufficient provided that the terminals are far enough beyond the radio horizon. The minimum range r_d at which a single term is adequate in the diffraction region has been derived from Reed and Russell [2] as

$$r_d = r_h + 230.2\left(k^2/f\right)^{1/3} \tag{24}$$

where r_h is the horizon range given by

$$r_h = 3.572\left[\sqrt{kh_1} + \sqrt{kh_2}\right]. \tag{25}$$

In (24) and (25), r_d and r_h are in km, h_1 and h_2 are in m, and f is in MHz. Ranges between the maximum range permitted in the optical interference region and the minimum range permitted in the diffraction region are said to be in the intermediate region. A computational technique frequently used for the intermediate region is "bold interpolation" described by Kerr [1]. In this technique, 20 log F is computed at both limits and then linearly interpolated with range between the two limits. As simple as this technique is, comparisons to more sophisticated models prove it to be remarkably good for standard conditions.

3.7 Yeh Troposcatter Model

At ranges sufficiently far over the horizon, tropospheric scatter, or troposcatter, will dominate the effects of diffraction. There are many troposcatter models available with various strengths and weaknesses, but one that is quite good and very easy to implement is described by Yeh [12]. Propagation loss in dB is given by this model as

$$L_p = 52.9 + 10\theta + 20\log r + 30\log f - 0.2(N_s - 310) \tag{26}$$

where θ is the scattering angle in degrees illustrated in Figure 3 and given by

$$\theta = 57.3\frac{r - r_1 - r_2}{ka}$$
$$r_1 = \sqrt{2kah_1} \quad r_2 = \sqrt{2kah_2} \tag{27}$$

where k, a, and h_t are as previously defined. For narrow-beam antennas, an aperture-to-medium coupling loss term is usually added to L_p which accounts for the reduced atmospheric volume that is common to both terminals. Also, L_p should be modified with a frequency-gain function described by Rice, et al. [13] in the case of low antenna heights, particularly if the frequency is also low. These additional terms will not be described here.

4. NONSTANDARD PROPAGATION MODELS

Nonstandard propagation models must be used to assess refractive effects when the actual atmosphere cannot be approximated by a standard atmosphere, or when the effects of terrain become important. The simplest of these models are ray trace models that illustrate the paths that radio waves take in the atmosphere, but, in general, do not compute field strength. The most successful and often used field-strength models are waveguide, parabolic equation (PE), and hybrid PE and ray-optics models. A brief description of each model follows.

4.1 Ray Trace Model

A simple yet very effective ray trace model, such as the one used in several figures in Part A of this lecture, is based on linear segmentation of the modified refractivity profile in height and classical small angle approximations to Snell's law. Since the radio refractive index is not, in general, a function of frequency, a single ray trace diagram can be considered representative of all frequencies for a given source height and atmospheric profile. A ray trace diagram consists of a height-versus-range display showing a series of individual ray paths, where each ray is characterized by a different initial elevation angle at the source. For each ray trajectory, a series of calculations is required to determine the height at a specified range, or a range at a specified height, as the ray traverses through the various linear segments of the refractivity profile. Rays that reflect from the sea surface are assumed to have equal incident and reflected angles. Although the algorithm to perform the ray trace is fairly complicated in terms of keeping track of the various layers and cases that must be considered, it is a straightforward process that can be summarized with a few cases. Referring to Figure 4, r, h, and α are the range, height, and elevation angle relative to the horizontal at the beginning of a single ray trace step, and r', h', and α' are the same quantities at the end of the step. Each step must take place in a single linear refractivity layer between the heights of H_i and H_{i+1} at which the modified refractivity values are M_i and M_{i+1}, respectively. Then define the gradient g_i for

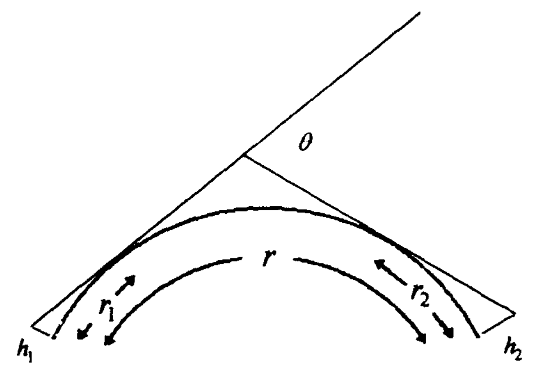

Figure 3. Geometry for troposcatter.

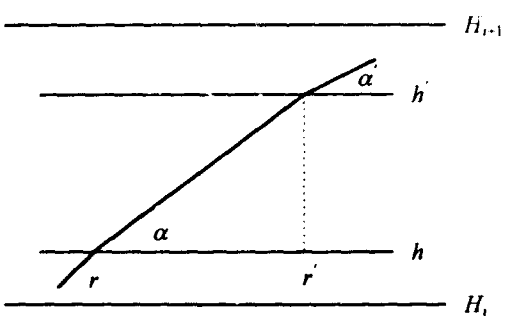

Figure 4. Geometry for ray trace computation.

this layer as

$$g_i = 10^{-6}\left(M_{i+1} - M_i\right)/\left(H_{i+1} - H_i\right) \qquad (28)$$

and consider the following 3 cases.

Case 1. h' known.

$$\begin{aligned} \alpha' &= \sqrt{\alpha^2 + 2g_i(h'-h)} \\ r' &= r + (\alpha'-\alpha)/g_i \end{aligned} \qquad (29)$$

Case 2. r' known.

$$\begin{aligned} \alpha' &= \alpha + g_i(r'-r) \\ h' &= h + \left(\alpha'^2-\alpha^2\right)/(2g_i) \end{aligned} \qquad (30)$$

Case 3. α' known.

$$\begin{aligned} r' &= r + (\alpha'-\alpha)/g_i \\ h' &= h + \left(\alpha'^2-\alpha^2\right)/(2g_i) \end{aligned} \qquad (31)$$

If the radicand in (29) is negative, then there is no solution for the specified height since the ray has reached a maximum or minimum level in the layer. When this happens, case 3 should be employed with α' set to zero. Care must also be exercised for case 1 if α is zero, since the ray will then turn upward only if $g_i > 0$, and downward only if $g_i < 0$. A complete ray trace model can be constructed using these rules and the proper combination of cases 1 through 3.

4.2 Waveguide Model

Waveguide models use normal mode theory to compute field strength under standard or nonstandard refractive conditions. These models are most useful for conditions where the vertical refractivity profile does not change along the propagation path and where results are desired at ranges well beyond the horizon, since there are fewer modes required in this case. The use of waveguide models dates back to the early 1900s when they were successfully used to explain the propagation of long wavelength radio waves around the surface of the earth in the waveguide formed by the earth and the ionosphere. A very good description of waveguide models is given by Budden [14]. The fundamental equation of mode theory is

$$R(\theta)R_g(\theta)\exp(-2ik_0h_0\sin\theta) = 1 \qquad (32)$$

where R is the complex reflection coefficient looking upward from level h_0 in the atmosphere, R_g is the complex reflection coefficient looking down (towards the ground) at level h_0, k_0 is the free space wave number given by $k_0 = 2\pi/\lambda$, and θ is the complex angle of incidence or reflection at level h_0. For tropospheric models, h_0 is often taken to be 0, such that (32) reduces to

$$R(\theta)R_g(\theta) = 1 \qquad (33)$$

and θ then refers to the angles at the ground. There are an infinite number of solutions to (32) or (33), known as eigenangles, but fortunately only a limited number are important for practical applications.

Crucial to any successful waveguide program is the determination of all significant solutions of (32) or (33). One solution to the equation is $\theta = 0$. Using this knowledge and searching the curve defined by $G = \left|R(\theta)R_g(\theta)\right| = 1$ for solutions gives one method of root extraction. An example taken from the work of Baumgartner et al. [15] is shown in Figure 5. The vertical axis is the imaginary part of θ and the horizontal axis is the real part of θ. Modes with attenuation rates less than 1.3 dB/km are shown. The insert is the modified refractivity profile used for the calculation and corresponds to $M = 0$ at $h = 183$ m. For practical purposes, the waveguide results are determined by the refractivity gradient, and translational effects from the actual refractivity profile are inconsequential. The Os in Figure 5 denote modes located on the G curve traced from the origin. The Xs denote modes found using a 2-dimensional search method described below. The mode not found using the G-trace method is a diffraction type mode with an attenuation rate of 0.868 dB/km that could be significant in some applications.

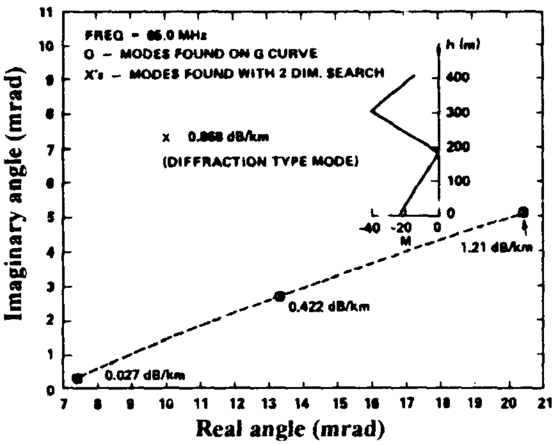

Figure 5. Eigenangle space showing location of modes.

A better method for finding the mode solutions is based on an algorithm described by Morfitt and Shellman [16] and illustrated in Figure 6. Implementation of the method requires searching the periphery of a rectangular region of the eigenangle space for 0° or 180° phase contours of the modal function, which is required to be analytic within and

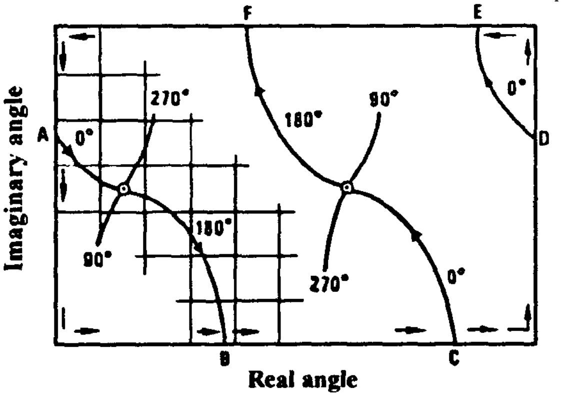

Figure 6. Schematic of root-finding method.

on the boundary of the search rectangle. This requirement guarantees that phase contours that enter the search rectangle must either terminate on zeros of the modal function or exit the search rectangle, as shown in Figure 6. A method for satisfying the analytic requirement is given by Baumgartner [17], who has put the Shellman-Morfitt root-finding algorithm to excellent use for tropospheric waveguide calculations.

Once the eigenangles are determined, the propagation factor F can be computed as

$$F = \frac{0.144r\sqrt{f}}{\sqrt{\sin(r/a)}}\left|\sum_{n=1}^{N} \Lambda_n g_n(h_1) g_n(h_2)\exp(-ik_0 r\cos\theta_n)\right| \qquad (34)$$

where f is frequency in MHz, r is range in km, a is the earth radius in km, g_n is the height-gain function normalized to unity at level h_0, h_1 and h_2 are the transmitter and receiver heights, θ_n is the nth eigenangle, and N is the total number of modes used. Λ_n is the excitation factor given by

$$\Lambda_n = \frac{\sqrt{\cos\theta_n}\left(1+R_g\right)^2}{R_g \frac{d}{d\theta}\left[RR_g\right]} \qquad (35)$$

where R, R_g, and the derivative are all evaluated at θ_n. Equations (34) and (35) are consistent with the plane wave reflection coefficient formalism of Budden [14]. The height-gain function for horizontal polarization, and to a good approximation for vertical polarization, obeys the equation

$$\frac{d^2 g_n}{dh^2} + k_0^2\left[m^2(h) - \cos^2\theta_n\right]g_n = 0 \qquad (36)$$

where m is the modified refractive index given by the relation $m = n + h/a$.

The original work of Baumgartner [17] using the methods outlined here has been expanded to include consideration of multiple refractivity levels, complete treatment of vertical as well as horizontal polarization, inclusion of the CCIR electrical characteristics for the sea, and the Miller-Brown surface roughness model. This program is now known as MLAYER, and will be used for some of the application examples later in this lecture.

As mentioned earlier, waveguide models are most useful for horizontally homogeneous refractivity environments. However, they can be applied to inhomogeneous environments as well, by breaking the waveguide up into horizontal slabs and using a technique known as mode conversion. Cho and Wait [18] and Pappert [19] have shown good success using this method, but it is much less efficient than parabolic equation models, and hence for practical applications it has not been developed any further.

4.3 Parabolic Equation Model

In 1946 Fock [20] used the parabolic equation method to describe electromagnetic propagation in a vertically stratified troposphere. In 1973 Hardin and Tappert [21] developed an efficient practical solution called the split-step Fourier method based on fast Fourier transforms (FFTs) that has been widely applied to ocean acoustic propagation starting in the mid 1970s. In the early 1980s Ko et al. [22] applied the split-step PE method to radio propagation, and since that time, many applications of the same basic method have been applied to radio propagation [23-25].

There are several advantages to the split-step PE method. First, and probably most important, it allows for efficient modeling of environments where the vertical refractivity profile changes along the propagation path. However, this method also has the advantage that it works well within the horizon, near the horizon, and over the horizon, thus allowing for single model assessments in many important applications. Another advantage of this model is that it has proven to be very robust in the sense that it works well for any practical environmental condition. However, the method also has disadvantages. Probably the biggest disadvantage is that it requires very large computer resources, both in terms of memory and run time, for applications involving combinations of high frequencies, high elevation angles, high terminals, and long maximum ranges. Another disadvantage is that rough surface effects are difficult to account for rigorously in the model.

The split-step PE model is a range step model that advances the field incrementally over fairly small range steps, which allows the refractive structure to change slowly with range. Let the complex field be represented by $u(r,h)$ and the range step be δr. Then the simplest form of the split-step PE model advances the field according to

$$\begin{aligned} u(r+\delta r,h) = {} & \exp\left\{ik_0\delta r\left[10^{-6}M(r,h)\right]\right\} \\ & \cdot\mathcal{F}^{-1}\left[U(r,p)\exp\left(-ip^2\delta r/2k_0\right)\right] \end{aligned} \qquad (37)$$

where M is modified refractivity as a function of range and height. The Fourier transform $\mathcal{F}$ of $u(r,h)$ is defined as

$$U(r,p) = \mathcal{F}\left[u(r,h)\right] \equiv \int_{-\infty}^{\infty} u(r,h)\exp(-iph)\,dh \qquad (38)$$

where $p = \kappa_0 \sin\theta$, and θ is the angle from the horizontal. Typically, a filter is applied to the upper one quarter of the field in both h and p spaces to ensure that the field reduces to zero at the top of the transforms. There are many details concerning the appropriate size of the height mesh, maximum angle, proper range step, type of filters, and starting solutions that must be considered in addition to (37) and (38), but they will not be discussed further here. One crucial issue is the method used to interpolate between successive refractivity profiles in range-dependent cases. Barrios [25] has discussed this issue in detail and shows that interpolation between height and refractivity parameters of corresponding features in the profiles is much superior to simple algebraic interpolation. A number of examples using PE models are presented in a later section.

The parabolic equation may also be solved using a finite-difference numerical solution, and this method has some advantages that are particularly important to propagation over irregular terrain, as demonstrated by Levy [26].

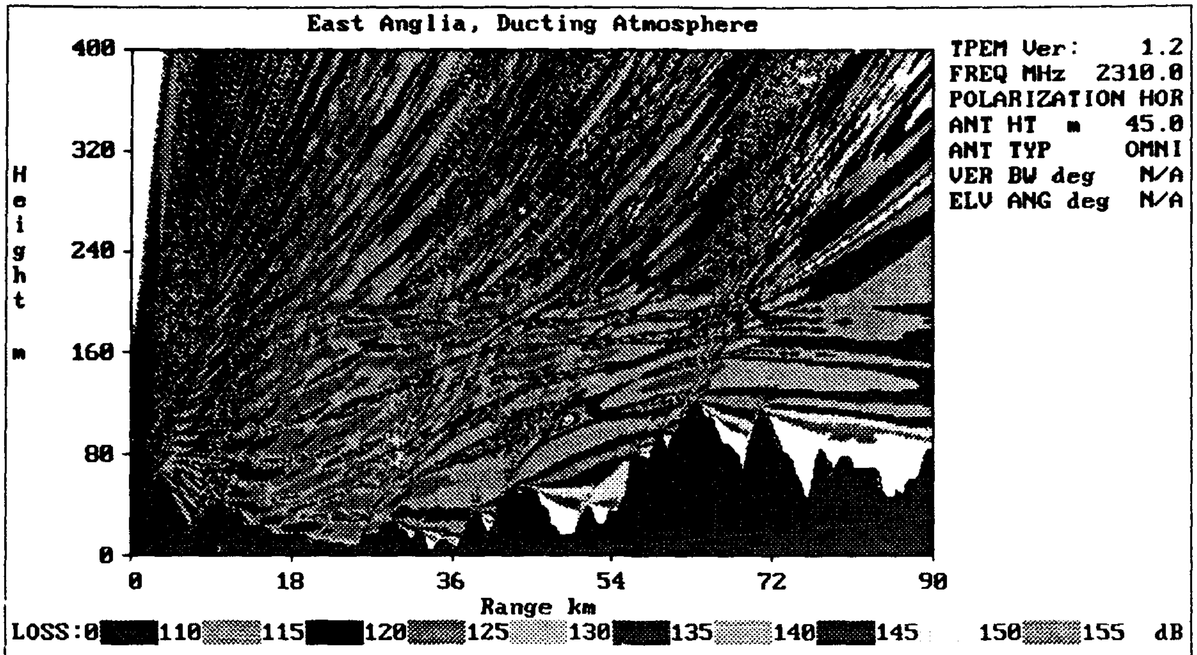

Figure 7. Sample coverage diagram from the TPEM program showing effects of ducting and terrain.

However, this method typically requires a many-fold increase in computer time compared to the split-step PE model. The split-step PE method has also been applied to propagation over terrain, as described by McArthur [27] and more recently Barrios [28]. Figure 7 is an example of this latter work for a ducting case over terrain using the Terrain Parabolic Equation Model (TPEM). The gray shades in the figure correspond to 5 dB increments of propagation loss.

4.4 Hybrid Methods

PE methods usually demand a large amount of computer time, especially if a combination of high frequencies, high elevation angles, high terminals, and long maximum ranges is desired, or if terrain must be accounted for in the model. In some cases this high computational burden can be overcome by combining the best features of various methods into a hybrid model. One example of such a hybrid model is the Radio Physical Optics (RPO) model described by Hitney [29]. In this model, a simple split-step PE model is combined with various ray optics models to create a hybrid model that can be up to 100 times faster than a pure split-step PE model for stressful cases. Ray optics models and PE models are very complementary, since the former work very well at angles above some small angle, and the latter are very efficient provided only small angles are considered.

Figure 8 illustrates the four regions, or submodels, considered in RPO. At ranges less than 2500 m and for all elevation angles above 5 degrees, RPO uses a flat earth (FE) model that ignores refraction and earth curvature effects. For the region beyond the FE region where the grazing angles of reflected rays from the transmitter are above a small limiting value, a full ray optics (RO) model is used that accounts for the effects of refraction and earth curvature. The PE model is used for ranges beyond the RO region, but only for altitudes below a maximum PE altitude determined by the maximum FFT size (1024) allowed. For ranges beyond the RO region and heights above the PE region, an extended optics (XO) method is used that is initialized by the PE model at the maximum PE altitude, and uses ray optics methods to propagate the signal to higher altitudes. Continuity of the solutions across each region's boundaries is kept to less than 0.1 dB by careful selection of the limiting RO grazing angle and the maximum PE propagation angle. A special troposcatter model [30] was developed for the PE portion of RPO such that this mechanism can be simulated efficiently in the hybrid model. This semiempirical scatter model adds a random fluctuation to the mean refractive-index value at each height considered by the PE model.

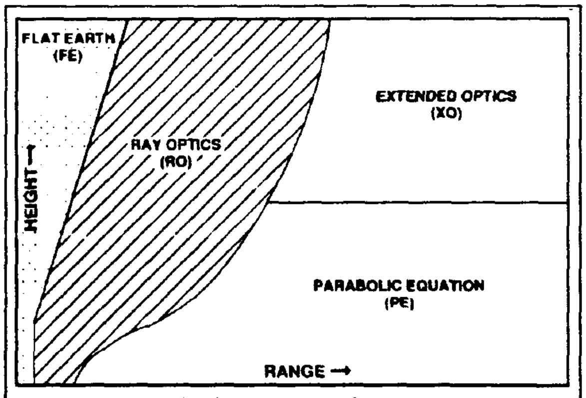

Figure 8. The four regions of the RPO model.

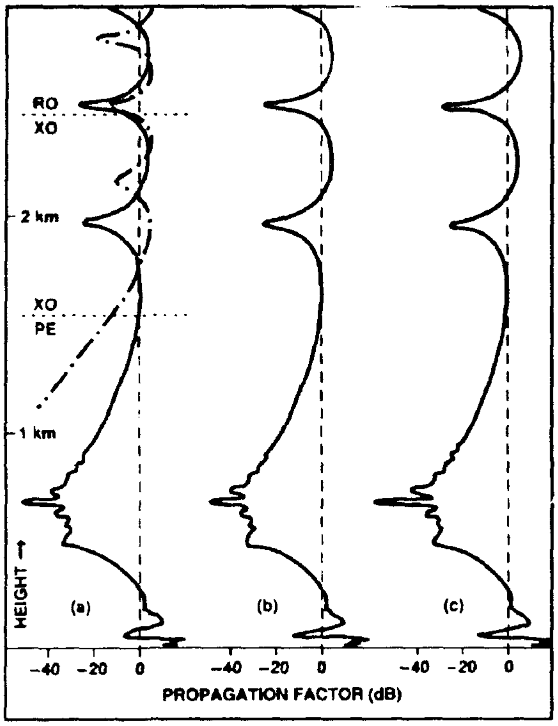

Figure 9. Comparisons of RPO (a), waveguide (b), and pure PE (c) models for a surface based duct at 3.0 GHz. Transmitter height is 30.5 m and range is 185 km.

Height (m)	Refractivity (*M* units)
0	367
267	401
465	354
3000	703

Table 2. Modified refractivity versus height profile for the surface-based ducting case of Figure 9.

Figure 9 compares the propagation factor versus altitude computed using (a) RPO, (b) waveguide, and (c) pure split-step PE models for a homogeneous surface-based duct defined by Table 2. A horizontally homogeneous case was selected for this test according to the waveguide model requirements. The frequency is 3.0 GHz, the antenna height is 30.5 meters, the range is 185 km, the polarization is horizontal, the antenna pattern is omnidirectional, and a smooth sea surface was assumed. Figure 9(a) shows the RPO results for the ducting case by a solid curve, and the corresponding standard-atmosphere case by a dot-dash curve. The dotted horizontal lines in Figure 9(a) indicate the boundaries of the PE, XO, and RO regions for the ducting case. The effects of the strong duct in all three of the RPO regions is clear from a comparison of the ducting and standard curves. The results from the waveguide and pure PE models given in 9(b) and 9(c) are virtually identical to the hybrid results from RPO. The times required to compute the ducting cases in Figure 9 on a 25 MHz IBM/PC-compatible computer were 69, 381, and 310 seconds for the RPO, waveguide, and pure PE models, respectively.

Since there is no simple way to account for surface roughness effects rigorously in PE models, a semiempirical method was developed for the PE submodel of RPO based on several sample waveguide model results [31]. This model is used only for surface ducting conditions and accounts for both vertical polarization and rough surface effects. The method computes a boundary loss factor based on (6) and (7) for the maximum grazing angle ψ that can be trapped in the surface duct. The PE model is modified by multiplying the magnitude of the lowest field point by the boundary loss factor immediately before each range step calculation. This simple method is very efficient, and results from RPO using the method match waveguide results and measured data quite well. Some examples are presented in a [illegible]ion.

The RO submodel of RPO assumes the propagation factor is constant along a ray traced from the top of the PE region to all higher altitudes. This assumption appears to be quite good for propagation over the sea, even under range dependent refractive conditions. However, in the case of propagation over terrain, such a simple model is not likely to work well, since there are typically multiple secondary sources corresponding to peaks in the terrain, etc. Two methods have been developed that should be effective for these cases. Marcus [32] has developed a hybrid model that uses a finite difference PE model at lower altitudes and Green's function solutions at higher altitudes for this application. Levy [33] has developed a horizontal PE method that can be used to project PE model results to higher altitudes. Using this model, a regular finite-difference or split-step vertical PE model is run to the maximum range of interest, thus obtaining a solution on an initial horizontal at the maximum vertical PE altitude. The horizontal PE method then requires one initial FFT at this altitude, plus one inverse FFT at each altitude of interest.

5. ASSESSMENT SYSTEMS

Refractive effects assessment systems are computer systems and associated software that allow a user to define and manipulate refractivity data, run radio propagation models on that data, and display the results in terms of expected performance on actual or proposed electromagnetic systems. Applications include radar, communications, electronic warfare, and weapons effects assessment. Assessment systems can be directed at operational assessment or at engineering assessment. Following are discussions of the three assessment systems that the author has been associated with over the last 20 years and that are primarily used by the United States Navy. There are many other similar systems in use in various countries.

5.1 IREPS

The Integrated Refractive Effects Prediction System (IREPS) was developed in the early 1970s as an operational assessment system [34]. The original system was based on Hewlett-Packard desktop computers and the programming language was HP-BASIC, but an IBM/PC-compatible version is also available that uses the C programming language. IREPS allows inputs from radiosondes or the airborne microwave refractometer on the E-2 aircraft to define a single refractivity profile that is assumed to be homogeneous in range and azimuth. The propagation models are a combination of the standard propagation models described earlier, easy-to-compute approximations to waveguide program results for evaporation and surface-based ducts, and ray trace models. IREPS considers both surface systems and airborne systems, but uses separate models for each type. Surface systems are used for applications where one terminal is within 100 m of the sea surface. Typical applications are shipboard sensors, but certain low-sited coastal applications can also be assessed by IREPS. For surface systems, the effects of the refractivity profile in the optical interference, diffraction, and troposcatter regions are accounted for, as well as effects from the evaporation duct and surface-based ducts from elevated trapping layers. Antenna pattern effects plus a radar detection model are included. The frequency limits are 100 MHz to 20 GHz. For airborne systems, a ray trace model, modified by antenna pattern effects, is used to assess the effects of elevated ducts or other refractivity features on air-to-air system coverage. However, the airborne assessments do not use a field strength propagation model, hence the displays are mostly of a qualitative, rather than a quantitative, nature.

The primary IREPS displays are propagation-loss-versus-range plots or range-versus-height coverage diagrams. By far, the most important use of the IREPS displays has been in selecting the best flight profile to penetrate an enemy's radar coverage. For example, under nonducting conditions it is best for an attack aircraft to fly a profile that is very low in altitude, since this will result in relatively short radar detection ranges. On the other hand, for surface-based ducting conditions a low flight profile may well result in radar detection ranges that greatly exceed the normal detection range. Under these conditions it is usually better to fly at an altitude slightly above the top of the duct. Note that for this application, it is only the relative performance of the radar in detecting targets at different altitudes that is most important, as opposed to absolute range predictions. The use of IREPS coverage diagrams in strike warfare flight profile selection has been verified operationally to be effective about 85% percent of the time. IREPS has been used for many other applications, but the effectiveness is normally much less than the strike warfare application, since the absolute performance thresholds of the equipment being assessed is very difficult to determine in an operational environment.

5.2 TESS

The functions of IREPS have been fully incorporated into the Tactical Environmental Support System (TESS) for use within the U.S. Navy [35]. TESS is a comprehensive environmental effects computer workstation that provides and displays information for the Navy's tactical decision makers. TESS is a direct descendent of the first IREPS which was fielded in 1979. The first phase of TESS was operational in 1985 and was based on Hewlett-Packard desktop computers similar to the original IREPS. TESS has evolved into a very capable system using Masscomp computers with multiple processors and continuous on-line electronic interfaces to satellite data and other observation and warning data. When fully deployed, TESS will be on all surface ships that have officers trained in the environmental sciences, including aircraft carriers, helicopter carriers, and amphibious assault ships, plus several shore facilities.

The capabilities and applications of TESS are very much greater than the original IREPS. They include real time satellite data, including imagery, and the ability to analyze and overlay this data with other meteorological analyses and forecasts, such as contoured grid fields. There are many aviation-related and general weather applications, such as fog probability forecasts and jet stream location displays. However, TESS also remains the host system for both ocean acoustic propagation and atmospheric electromagnetic propagation assessment.

The current radio propagation assessment models and displays in TESS are basically the same as those found in the original IREPS. By November 1994 TESS is scheduled to have a range-dependent refractive effects assessment capability based on the hybrid RPO model described earlier. Initially, this capability will consist of RPO plus meteorological driver modules that are required to match refractive structures and interpolate between measured or forecast refractivity profiles, and drivers to create a refractivity profile for the evaporation duct and merge it with upper-air refractivity profiles. The radar or other system performance models will be the same as IREPS and the displays will be single propagation loss plots or coverage diagrams. Eventually, TESS should include some form of a three dimensional coverage diagram, such that range and azimuth dependent assessments can be displayed.

5.3 EREPS

The Engineer's Refractive Effects Prediction System (EREPS) is a derivative of IREPS that is optimized for use by engineers and scientists, instead of operational tactical decision makers [36-37]. Soon after IREPS was introduced, many scientists and engineers at laboratories were using the models to simulate system performance on hypothetical or proposed systems. Since the original software was not designed for this purpose, many user-interface deficiencies in such a use were soon identified. For example, most engineers prefer to graphically compare performance results in terms of a single design parameter, such as radar pulse length. Also, in designing a new system, one is usually more interested in long-term statistical performance than in single-event performance that the tactical decision aids of IREPS were designed to assess.

The EREPS displays in many cases look similar to those of IREPS, but the capabilities of the user to edit the various parameters is greatly increased. Most displays can be overlaid on other similar displays, and there are extensive editing, labeling, and crosshair capabilities. EREPS consists of 5 IBM/PC-compatible DOS programs named COVER, PROPR, PROPH, RAYS, and SDS. COVER produces a range-versus-height coverage diagram for surface systems, PROPR produces a propagation-loss-versus-range plot, PROPH produces a propagation-loss-versus-height plot, RAYS is a range-versus-height ray trace, and SDS is the Surface Duct Summary program described in Part A of this lecture. The EREPS models are generally the same as those used in IREPS described above. In addition, the latest versions of EREPS are capable of reading binary files of propagation loss versus range and height that are generated by the RPO program, so it is possible to combine the radar system model or graphical capabilities of EREPS with a high-fidelity range-dependent propagation model. Many of the application examples presented in the next section were generated using EREPS programs.

6. APPLICATION EXAMPLES

This section consists of several examples of propagation calculations using the models presented in this paper compared to propagation measurements. In most cases, all of the input parameters needed by the models are included such that the reader may use the examples for comparisons with the results of other models. Horizontal polarization is assumed in all the examples unless stated otherwise.

6.1 Optical Interference Region

This example illustrates propagation effects for a near-standard atmosphere within the optical interference region based on one sample of a series of measurements reported by Hopkins et al. [38]. These measurements consisted of field strength recordings versus range from a high-altitude jet aircraft by a ground based receiver at 218, 418, and 1089 MHz. The paths were flown entirely over water and both vertical and horizontal polarizations were used. Measurements were made on several different days, and refractivity soundings were made at the receiver site. Figure 10 shows results at 418 MHz for vertical polarization for a case characterized by a very nearly standard refractivity profile, where the assumption that $k = 4/3$ is very good. In this case, the transmitter height was 8689 m and the receiver height was 33.2 m. Figure 10 shows the propagation factor versus range modeled by EREPS and observed. In this case, the two are in excellent agreement.

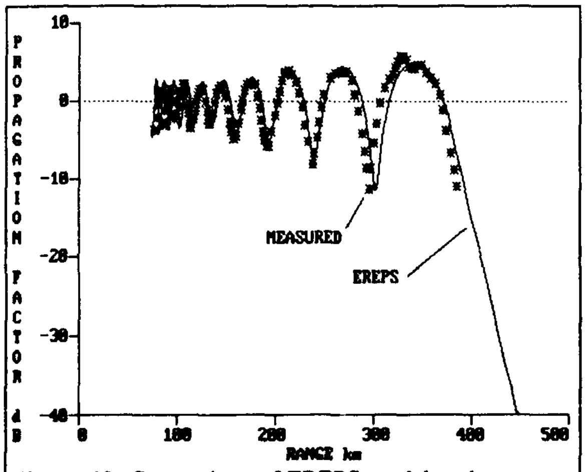

Figure 10. Comparison of EREPS model and measurements in the optical interference region for standard conditions. Frequency is 418 MHz, polarization is vertical, and terminal heights are 33.2 and 8689 meters.

6.2 Diffraction and Troposcatter

This example compares diffraction and troposcatter models to measurements reported by Ames et al. [39] at 220 MHz. Signal levels from a source 23.5 m above mean sea level were recorded in an aircraft that flew an over water path between Scituate, Massachusetts toward Sable Island. Figure 11 shows measured data recorded on 17 December 1953 and modeled results from EREPS and RPO. For the models used here, a standard atmosphere having a vertical refractivity gradient of 118 *M* units per km was assumed, corresponding to $k = 4/3$. For EREPS, a surface refractivity value of 339 *N* units was also assumed, based on long term average values for the area. The RPO model was applied both with and without its scatter model. In the diffraction region, at ranges roughly between 200 and 300 km, EREPS, RPO, and the observations are all in excellent agreement. In the troposcatter region, the Yeh model used in EREPS results in loss values about 15 dB less than observed. RPO without the scatter model clearly overestimates the loss in the troposcatter region, but with the scatter model included, the results match the observations quite well.

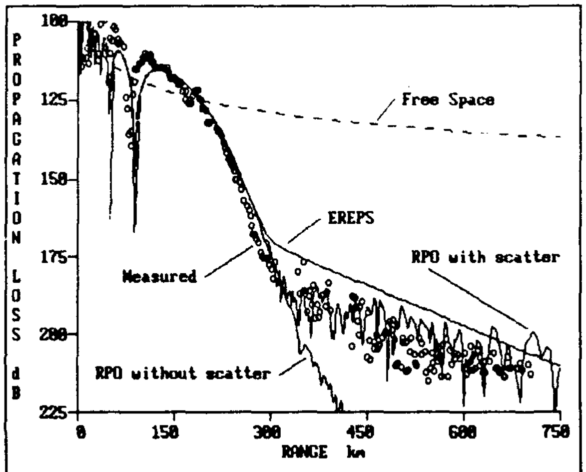

Figure 11. Comparisons of the EREPS and RPO troposcatter models to measurements. Frequency is 220 MHz, and terminal heights are 23.5 and 3048 meters.

6.3 Evaporation Duct at 9.6 GHz

This case illustrates the use of RPO to model propagation in the evaporation duct at 9.6 GHz. The measurements are taken from an experiment performed in 1972 between the Greek islands of Naxos and Mykonos and reported by

Richter and Hitney [40]. The frequencies investigated in this experiment were 1.0, 3.0, 9.6, 18.0, and 37.4 GHz, but only the 9.6 GHz case will be used in this section. The transmitter was on Naxos at a height of 4.8 m above mean sea level (msl), and the receiver was on Mykonos and switched every five minutes between heights of 4.9, 10.0, and 19.4 m above msl. The path length was 35.2 km.

Meteorological measurements were made at both ends of the path from which evaporation duct heights and profiles were computed using the methods outlined by Paulus [41]. On 10 November 1972 at 1200 at Mykonos, the wind speed was recorded as 17.5 knots, the air temperature was 17.0 °C, the sea temperature was 17.0 °C, and the relative humidity was 84%. Based on these measurements, the evaporation duct height was computed to be 10.4 m, and the corresponding refractivity profile is given in Table 3. The modified refractivity values are relative to the surface value.

Height (m)	Refractivity (*M* units)
0.0	0.0
0.135	-8.83
0.223	-9.46
0.368	-10.09
0.607	-10.71
1.000	-11.31
1.649	-11.88
2.718	-12.40
4.482	-12.83
7.389	-13.11
10.400	-13.18
12.182	-13.16
20.086	-12.83
33.115	-11.85
54.598	-9.81
90.017	-6.03
148.413	0.62

Table 3. Refractivity profile for meteorological observations at 1200 on 10 Nov 72 at Mykonos. The evaporation duct height is 10.4 meters. Profile is used by RPO for Figure 12.

The profile of Table 3 was used by RPO to compute loss versus receiver height as shown in Figure 12. Also included in Figure 12 are a free space reference and an EREPS result for a standard atmosphere. The propagation loss observed at 1200 on 10 November at the lowest height of 4.9 m is also indicated in the figure. The observed loss is much closer to RPO and free space than the standard atmosphere model. The same technique used to generate the RPO results in Figure 12 was applied each hour throughout the November measurement period and is illustrated in Figure 13. The overall fit of the observations to the RPO model is quite good, in spite of a few periods of substantial mismatch. Both RPO and the observations show increases of signal level by the evaporation duct of up to 60 dB compared to the diffraction case.

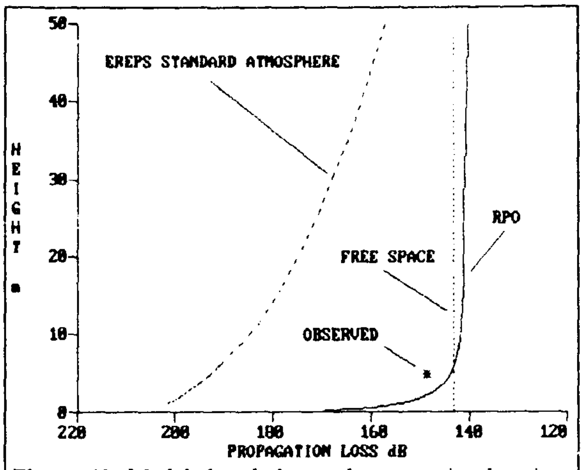

Figure 12. Modeled and observed propagation loss in a 10.4 m evaporation duct at 9.6 GHz. Transmitter height is 4.8 m and the range is 35.2 km.

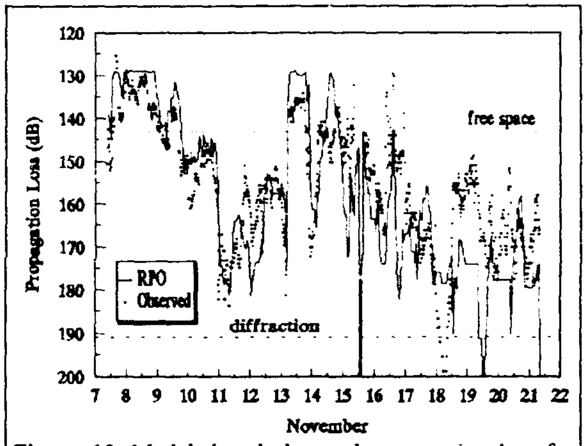

Figure 13. Modeled and observed propagation loss for 16 days at 9.6 GHz for the 1972 Greek islands experiment. Terminal heights are 4.8 and 4.9 meters.

6.4 Evaporation Duct at 37.4 GHz

This example illustrates the effects of surface roughness in a ducting environment. The measurements are also from the Greek islands experiment, but at the highest frequency of 37.4 GHz. In this case, the transmitter and receiver were 5.1 and 3.6 m above msl, respectively. Figure 14 shows modeled propagation loss versus height at 35.2 km for this case based on a 12 m evaporation duct refractivity profile given in Table 4. The most trusted model for surface roughness is MLAYER, which was run with an assumed wind speed of 10 m/s. RPO was also run for this same case, and the results are seen to compare quite well with the results from MLAYER. For comparison, RPO was also run for the smooth surface case and included in the figure. From Figure 14 it is clear that surface roughness effects can substantially reduce the increased signal levels typical of the evaporation duct at high frequencies.

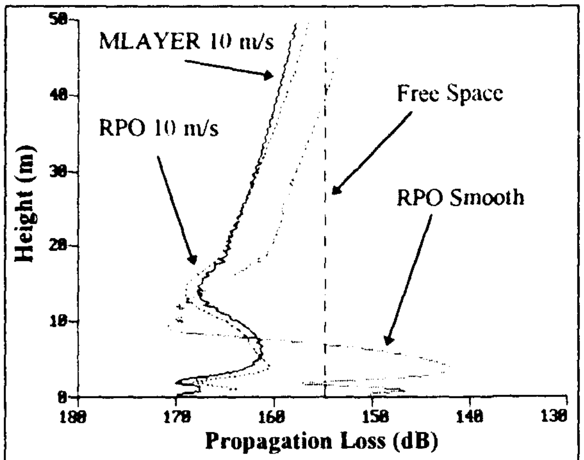

Figure 14. Comparisons of RPO and MLAYER models for a 12 m evaporation duct at 37.4 GHz. Transmitter height is 5.1 m and the range is 35.2 km.

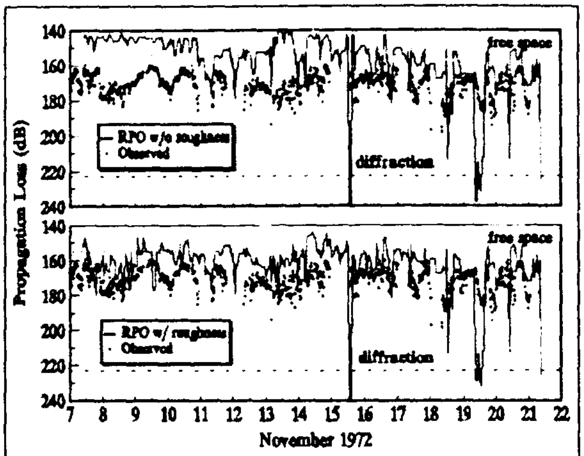

Figure 15. RPO results with and without roughness model compared to observations at 37.4 GHz. Terminal heights are 5.1 and 3.6 meters above mean sea level.

Height (m)	Refractivity (*M* units)
0.0	0.0
0.135	-10.19
0.223	-10.93
0.368	-11.66
0.607	-12.38
1.000	-13.08
1.649	-13.75
2.718	-14.37
4.482	-14.90
7.389	-15.28
12.000	-15.44
12.182	-15.43
20.086	-15.20
33.115	-14.32
54.598	-12.38
90.017	-8.71
148.413	-2.16

Table 4. Refractivity profile for 12 meter evaporation duct height used by RPO and MLAYER for Figure 14.

Figure 15 was prepared using the same methods as Figure 13 to illustrate the overall benefit of accounting for surface roughness effects. The upper panel shows RPO model results without a roughness submodel and the lower panel shows the RPO results with the roughness submodel. The roughness model is clearly superior at matching the entire data period, especially during the first few days when the wind speeds were relatively high. It should be pointed out that RPO does not include an absorption model. If it did, the modeled loss would be approximately 5 dB higher, which would fit the observations even better.

6.5 Evaporation Duct at 94 GHz

This example illustrates the combined effects of the evaporation duct, surface roughness, and absorption at 94 GHz. The measurements are from an experiment performed by Anderson [42]. The propagation path was 40.6 km long and entirely over water along the coastline just north of San Diego. The transmitter and receiver antennas were 5.0 and 9.7 m above mean low water, respectively. Meteorological support measurements were made at each end of the path. At the beginning of one measurement period in October 1986, the evaporation duct height was computed to be about 6 m and the wind speed was measured at 8 knots. Figure 16 shows modeled results from MLAYER for three conditions. The first is for a 6 m evaporation duct height, based on the refractivity profile given in Table 5, and smooth surface conditions. The second is for the same duct plus surface roughness corresponding to a wind speed of 8 knots, and the third is for a standard atmosphere and a smooth surface. The propagation loss in Figure 16 does not include absorption by atmospheric gases, which was typically 35 dB on this path. The observed propagation loss, less the computed absorption, is also shown in this figure as an asterisk. The observed loss in this case is seen to be substantially less than expected for a standard atmosphere, but not quite as low as predicted for the ducting case, either

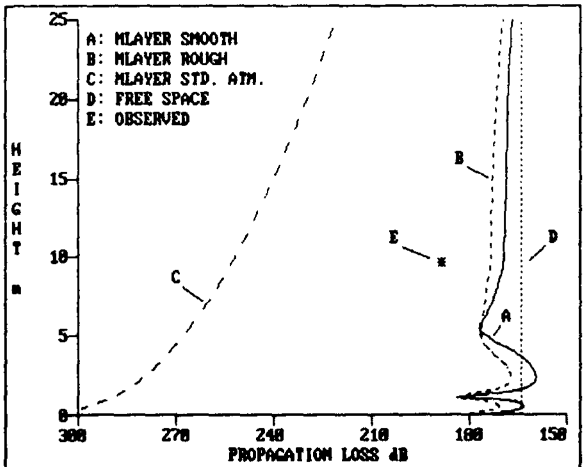

Figure 16. Modeled and observed propagation loss for a 6 m evaporation duct at 94 GHz. Transmitter height is 5 m and range is 40.6 km. Absorption not included.

with or without surface roughness. A possible reason for this discrepancy is the inability to properly assess horizontal variations of either ducting or surface roughness without meteorological measurements along the path.

Height (m)	Refractivity (*M* units)
0.0	0.0
0.135	-5.09
0.223	-5.45
0.368	-5.81
0.607	-6.15
1.000	-6.48
1.649	-6.77
2.718	-7.01
4.482	-7.17
6.000	-7.20
7.389	-7.18
12.182	-6.96
20.086	-6.34
33.115	-5.09
54.598	-2.78
90.017	1.27
148.413	8.20

Table 5. Refractivity profile for 6 meter evaporation duct height used by MLAYER for Figure 16.

Figure 17 shows propagation loss versus time for the entire two week measurement period in October 1986. The upper solid line represents loss modeled with MLAYER in the same manner as in Figure 16, including roughness effects, based on the computed duct height and measured wind speed. In Figure 17, molecular absorption is included in the model by adding on an absorption term based on the measured temperature and humidity following the methods of Liebe et al. [43]. The observed propagation loss including absorption is shown by the dots and generally follows the model very well. For comparison, the lower solid line in Figure 17 is loss modeled by diffraction and absorption. It is clear from this figure that the evaporation duct is a very significant propagation mechanism on this path, accounting for 60-80 dB increases in signal compared to diffraction.

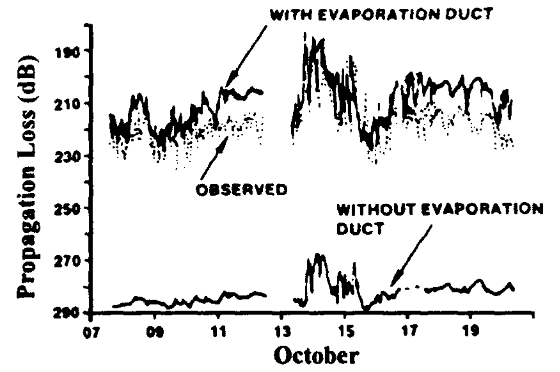

Figure 17. Modeled and observed propagation loss for a two week period at 94 GHz. Terminal heights are 5 and 9.7 m and range is 40.6 km. Absorption included.

6.6 Surface Based Duct

This case illustrates the use of RPO to model propagation in a surface based duct at 170 MHz. The measurements were made by the U.S. Navy Electronics Laboratory [44] on a 500 km over-water path between San Diego, California and Guadalupe Isle, Mexico. An aircraft was fitted with transmitters at 63, 170, 520, and 3300 MHz and receivers and recorders were located in San Diego with antennas at either 30.5 or 150 m above sea level. The aircraft flew sawtooth profiles out to about 500 km with altitude varying from near zero to 1200 m. Refractivity profiles were measured aboard the aircraft. This example will consider only the 170 MHz results with the receiver height of 30.5 m recorded on 8 April 1948. Table 6 lists the first four refractivity profiles measured on that date, reduced to a number of linear segments and a form that can be directly used by RPO. Inspection of Table 6 shows a strong surface-based duct at all ranges. The top of this duct is nearly the same at 175 and 171 m for the first two profiles, and then rises to 300 and 323 m for the last two profiles.

Range km 76		Range km 105		Range km 172		Range km 246	
m	*M*	m	*M*	m	*M*	m	*M*
0	340	0	342	0	342	0	343
107	353	112	352	205	368	224	369
175	310	171	308	300	321	323	324
295	318	311	321	458	359	469	362
368	345	395	351	554	359	639	372
1220	412	1220	415	1220	448	1220	443

Table 6. Refractivity profiles at four ranges measured on 8 April 1948. *M* represents modified refractivity in *M* units and m represents height in meters.

Figure 18 shows RPO results using the profiles of Table 6 for both an assumed homogeneous environment, using only

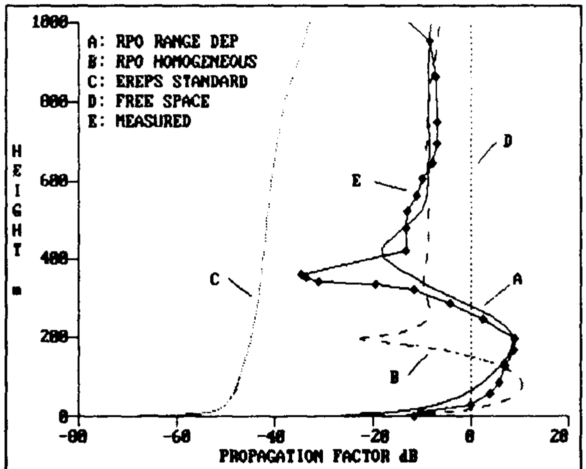

Figure 18. Modeled and measured propagation factor at 170 MHz versus transmitter height in a surface based duct. Receiver height is 30.5 m and range is 189 km. Standard atmosphere, homogeneous, and range dependent models are shown.

the profile measured at 76 km, and a range-dependent environment using all four profiles. Since the first two profiles are very much alike, the first profile was assumed to exist at the receiver site as well as at 76 km. Propagation loss versus transmitter (aircraft) height for both cases is shown in this figure, along with measured propagation loss at this range. The EREPS loss for a standard atmosphere and free space loss are also shown for comparison. It is obvious from the figure that a much better match to the measured loss is achieved when the range-dependent environment is accounted for in the model.

6.7 Elevated Duct

This example compares the RPO model to propagation measurements in an elevated duct at 3088 MHz. The measurements were performed by the Naval Electronics Laboratory Center in 1974 and are analyzed in some detail by Hitney [45]. A transmitter was established 21 m above sea level in San Diego and receivers in an aircraft recorded signal level at various altitudes as the aircraft flew towards the west entirely over water. This example considers only the measurement made on 28 May 1974 with the aircraft at 914 m above sea level. A refractivity profile was measured at the transmitter site and is listed in Table 7.

Height (m)	Refractivity (*M* units)
0	330
594	403
681	368
2000	539

Table 7. Modified refractivity profile for 28 May 1974.

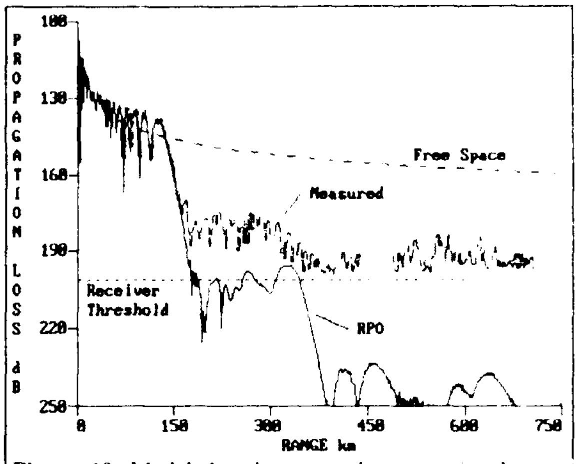

Figure 19. Modeled and measured propagation loss in an elevated duct at 3088 MHz. Terminal heights are 21 and 914 m. Duct is assumed homogeneous in range.

Figure 19 shows modeled propagation loss versus range from RPO using the profile of Table 7, assuming horizontal homogeneity, and the measurements of loss made aboard the aircraft. Free space and receiver threshold levels are also shown for comparison. The RPO model follows the measurements well within and just over the horizon, however at longer ranges the modeled loss substantially overestimates the observed loss. In the San Diego area, trapping layers are frequently observed to rise gradually in the westerly direction. Although offshore measurements of refractivity profiles were not made in this experiment, a much better match can be made to the data if the profile of Table 7 is allowed to rise at a typical rate of 1:1500 (1 meter in height for every 1500 meters in range). Figure 20 shows

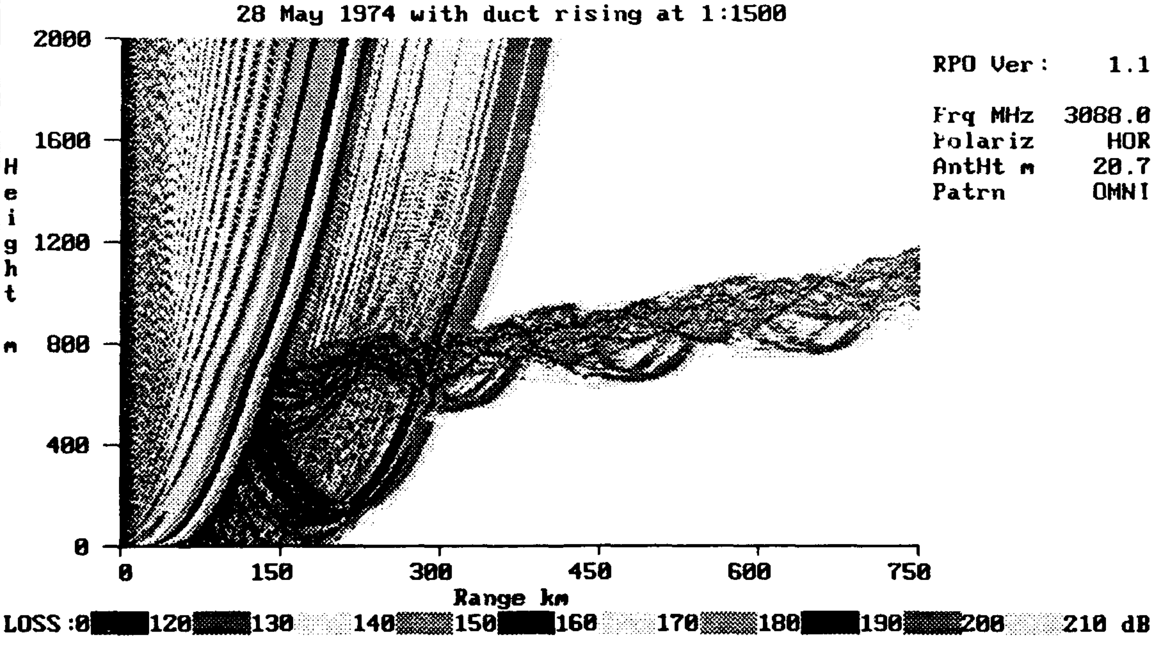

Figure 20. Coverage diagram for a hypothetical rising elevated duct.

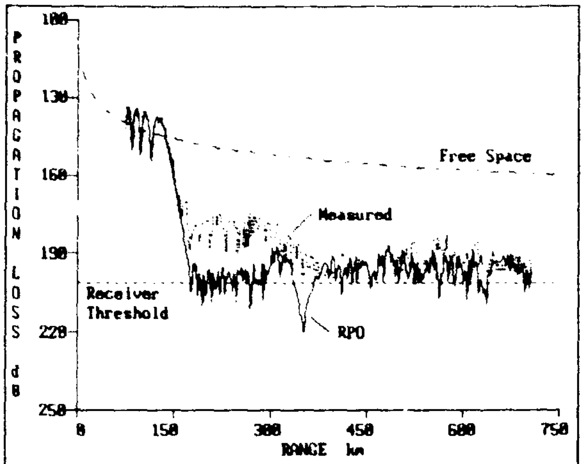

Figure 21. Modeled and measured propagation loss for the same case as Figure 19, except that the elevated duct is assumed to rise at a rate of 1:1500.

the coverage diagram from RPO for this hypothetical range-dependent case, and Figure 21 shows the corresponding loss versus range at 914 m. The RPO model is much closer to the measurements for this case than it is for the homogeneous case of Figure 19. Based on this modeling, it is concluded that the elevated duct probably did rise, such that the aircraft was in the duct at the greater ranges. Although the signal levels recorded at the longer ranges were low, the attenuation rate was nearly zero, which suggests ducted propagation sometimes referred to as whispering gallery effects.

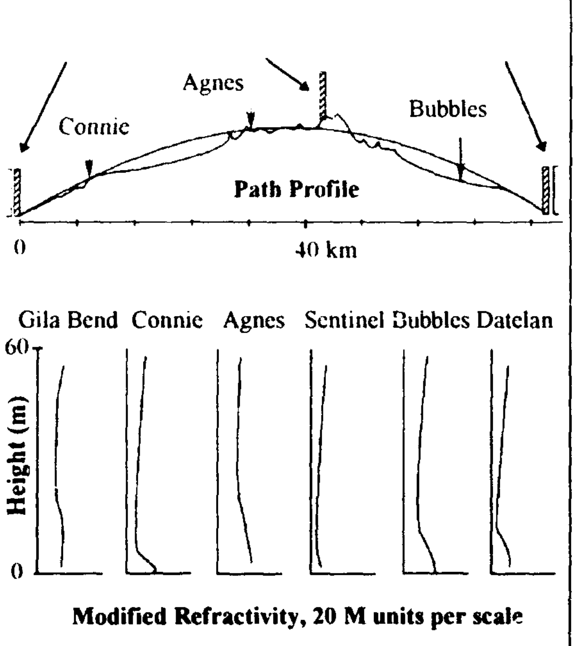

Figure 22. Terrain profile and refractivity profiles for 0300 6 Feb 1946 Arizona desert experiment.

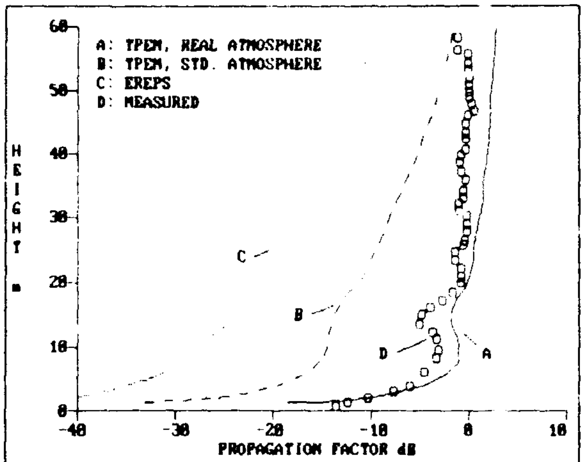

Figure 23. Modeled and measured propagation factor at 1.0 GHz over desert terrain. Transmitter height is 30.5 m and range is 43 km. EREPS assumes smooth earth and standard atmosphere. TPEM includes terrain for both standard and observed (real) refractivity cases.

6.8 Propagation Over Desert Terrain

This example illustrates the use of TPEM to model propagation over desert terrain at 1.0 GHz. The measurements were performed by the U.S. Navy Electronics Laboratory in the Arizona desert in 1946 [46]. Barrios [28] has recently compared several of these measurements to TPEM, and the example used here is taken from that work. Figure 22 shows the terrain profile of the propagation path studied and a series of refractivity profiles measured at six locations on 6 February 1946 at 0300. Transmitters were installed at Gila Bend and receivers were installed at Sentinel and Datelan on elevators in 60 m towers. Figure 23 shows propagation loss at 1.0 GHz from TPEM plotted versus receiver height for a transmitter height of 30.5 m on the 43 km Gila Bend to Sentinel path. Modeled results are shown for both the real atmosphere, as represented by the refractivity profiles of Figure 22, and a standard atmosphere. Modeled results from EREPS for a smooth surface and a standard atmosphere are also shown. Figure 23 indicates that the best model is the one that accounts for both the terrain and the refractive effects.

7. STATISTICAL ASSESSMENTS

The models presented in this lecture can in some cases be used to prepare statistical assessments of propagation effects. The evaporation duct mechanism is well suited to this technique, since its effect can be well characterized by the evaporation duct height, and good statistical distributions of duct height have been compiled as discussed in Part A of this lecture. In areas and for paths where the evaporation duct is the dominant mechanism, statistical assessments have been proven valid by comparison to measured distributions of propagation loss. The example presented here is taken from Hitney and Vieth [47] for the Aegean Sea measurements previously described.

Figure 24 shows propagation loss modeled by MLAYER versus evaporation duct height at 1.0, 3.0, 9.6, and 18.0 GHz for the highest receiver antennas in the Greek island

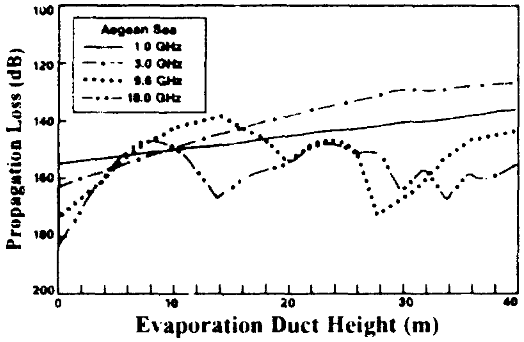

Figure 24. Propagation loss versus evaporation duct height for four frequencies used in the 1972 Greek islands experiment in the Aegean Sea.

experiment. For 9.6 GHz the terminal heights are 4.8 and 19.2 m and the path length is 35.2 km. A smooth sea was assumed in the MLAYER model since roughness effects are usually not very important below 20 GHz. The evaporation duct refractivity profiles used to prepare Figure 24 all assumed neutral stability (air temperature equal to sea temperature) since experience has shown stability to be a secondary effect compared to duct height [42, 48]. Figure 25 is an annual histogram of evaporation duct height from EREPS for the Marsden square containing the Greek islands experiment. By combining the loss versus duct height relationship of Figure 24 with the expected occurrence of duct height from Figure 25, frequency distributions of propagation loss can be easily determined. Figure 26 is an example of a modeled accumulated frequency distribution of propagation loss for 9.6 GHz compared to the measured distribution. The measured distribution combined four periods of 2-3 weeks duration each in January, April, August, and November of 1972, so it should well represent an annual expected distribution. As Figure 26 shows, the modeled and measured distributions are in excellent agreement except for loss values less than free space. These cases are probably the result of surface-based ducts or other refractive effects not modeled in the results shown in Figure 24.

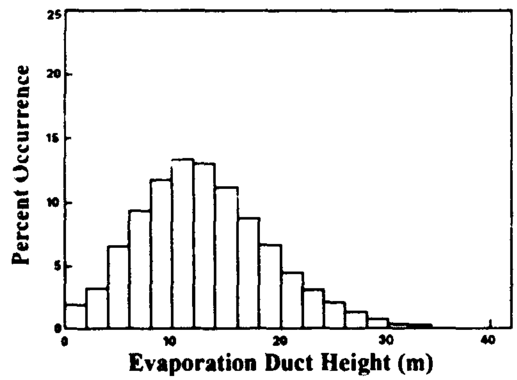

Figure 25. Evaporation duct height histogram for the area of the Greek islands experiment.

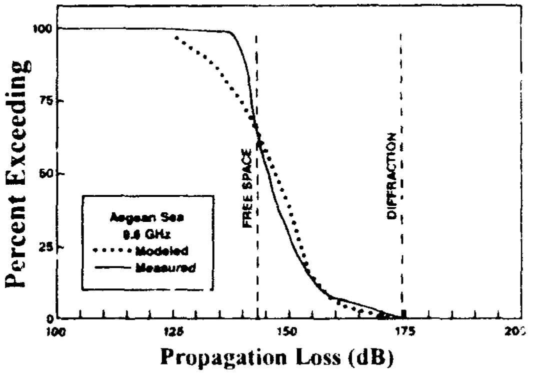

Figure 26. Modeled and measured propagation loss distribution at 9.6 GHz for the Aegean Sea. Terminal heights are 4.8 and 19.2 m above mean sea level.

It should also be mentioned that the International Telecommunications Union (ITU) has a recommendation [49] for a method to statistically assess interference of microwave stations operating between about 0.7 and 30 GHz that includes the effects of ducting. The recommendation consists of about 30 pages total and is based in part on graphical techniques.

8. CONCLUSIONS

I have presented several radio propagation models that can be used to assess refractive effects from VHF to EHF. These models range from the relatively simple effective-earth-radius model used to assess standard refractive effects, to quite complicated PE models used to assess nonstandard refractive effects over terrain. I also discussed assessment systems, presented several application examples to illustrate the accuracy and utility of the models, and briefly discussed statistical modeling of propagation effects.

ACKNOWLEDGMENT

This work was supported by the Office of Naval Research.

REFERENCES

1. Kerr, D.E., Ed., "Propagation of Short Radio Waves," New York, McGraw-Hill, 1951.
2. Reed, H.R. and C.M. Russell, "Ultra High Frequency Propagation," second edition, Cambridge, Mass., Boston Technical Publishers, Inc., 1966.
3. Recommendation 527-2, "Electrical characteristics of the surface of the Earth," in "Recommendations and Reports of the CCIR, Volume V, Propagation in Nonionized Media," ITU XVIIth Plenary Assembly, Düsseldorf, 1990.
4. Ament, W.S., "Toward a Theory of Reflection by a Rough Surface," Proc. IRE, 41, 1, 1953, pp 142-146.
5. Beard, C.I., "Coherent and Incoherent Scattering of Microwaves from the Ocean," IRE Trans. Antennas Propagat., AP-9, 5, September 1961, pp 470-483.
6. Miller, A.R., R.M. Brown, and E. Vegh, "New derivation for the rough-surface reflection coefficient and for the distribution of sea-wave elevations," IEE Proc., Pt. H, 131, 2, April 1984, pp 114-116.

7. Phillips, O.M., "Dynamics of the Upper Ocean," London, Cambridge Univ. Press, 1966.
8. Report 1008-1, "Reflection from the surface of the Earth," in "Recommendations and Reports of the CCIR, Volume V, Propagation in Nonionized Media," ITU XVIIth Plenary Assembly, Düsseldorf, 1990.
9. Van der Pol, B. and H. Bremmer, "Further Note on the Propagation of Radio Waves over a Finitely Conducting Spherical Earth," Phil. Mag., 27, Ser. 7, 182, March 1939, pp 261-275.
10. Ballantine, S., "The Lorentz Reciprocity Theorem for Electric Waves," Proc. IRE, 16, 3, 1928, pp 513-518.
11. Report 715-3, "Propagation by diffraction," in "Recommendations and Reports of the CCIR, Volume V, Propagation in Nonionized Media," ITU XVIIth Plenary Assembly, Düsseldorf, 1990.
12. Yeh, L.P., "Simple Methods for Designing Troposcatter Circuits," IRE Trans. on Comm. Systems, CS-8, 3, September 1960, pp 193-198.
13. Rice, P.L., A.G. Longley, K.A. Norton, and A.P. Barsis, "Transmission Loss Predictions for Tropospheric Communication Circuits," U.S. Dept. of Commerce, National Bureau of Standards TN 101, vols. 1 and 2, 1965.
14. Budden, K.G., "The Wave-Guide Mode Theory of Wave Propagation," Englewood Cliffs, NJ, Prentice-Hall, Inc., 1961. Also London, Logos Press, 1961.
15. Baumgartner, G.B., H.V. Hitney, and R.A. Pappert, "Duct propagation modelling for the integrated-refractive-effects prediction system (IREPS)," IEE Proc., Pt. F, 130, 7, December 1983, pp 630-642.
16. Morfitt, D.G. and C.H. Shellman, "MODESRCH, an Improved Computer Program for Obtaining ELF/VLF/LF Mode Constants in an Earth Ionosphere Waveguide," Interim Report 77T, prepared for Defense Nuclear Agency by the Naval Electronics Laboratory Center, 1976.
17. Baumgartner, G.B., "XWVG: A Waveguide Program for Trilinear Tropospheric Ducts," Naval Ocean Systems Center TD 610, June 1983.
18. Cho, S.H. and J.R. Wait, "Analysis of microwave ducts in an inhomogeneous troposphere," Pure Appl. Geophys., 116, 6, 1978, pp 1118-1142.
19. Pappert, R.A., "Propagation Modeling for Some Horizontally Varying Tropospheric Ducts," in "Operational Decision Aids for Exploiting or Mitigating Electromagnetic Propagation Effects," AGARD CP-453, September 1989, Paper 22.
20. Fock, V.A., "Electromagnetic Diffraction and Propagation Problems," New York, Pergamon, 1965.
21. Hardin, R.H. and F.D. Tappert, "Application of the Split-step Fourier Method to the Numerical Solution of Nonlinear and Variable Coefficient Wave Equations," SIAM Rev., 15, 2, 1973, p 423.
22. Ko, H.W., J.W. Sari, and J.P. Skura, "Anomalous Microwave Propagation Through Atmospheric Ducts," APL Tech. Dig., 4, 2, 1983, pp 12-16.
23. Dockery, G.D., "Modeling Electromagnetic Wave Propagation in the Troposphere Using the Parabolic Equation," IEEE Trans. Antennas Propagat., 36, 10, October 1988, pp 1464-1470.
24. Craig, K.H., "Propagation Modeling in the Troposphere: Parabolic Equation Method," Elec. Lett., 24, 18, 1988, pp 1136-1139.
25. Barrios, A.E., "Parabolic Equation Modeling in Horizontally Inhomogeneous Environments," IEEE Trans. Antennas Propagat., 40, 7, July 1992, pp 791-797.
26. Levy, M.F., "Parabolic Equation Modelling of Propagation over Irregular Terrain," Elec. Lett., 26, 15, July 1990, pp 1153-1155.
27. McArthur, R.J., "Propagation Modelling over Irregular Terrain Using the Split-Step Parabolic Equation Method," in "Radar 92," IEE Conf. Pub. 365, 12-13 October 1992, pp 54-57.
28. Barrios, A.E., "A Terrain Parabolic Equation Model for Propagation in the Troposphere," IEEE Trans. Antennas Propagat., 42, 1, January 1994, pp 90-98.
29. Hitney, H.V., "Hybrid Ray Optics and Parabolic Equation Methods for Radar Propagation Modeling," in "Radar 92," IEE Conf. Pub. 365, 12-13 October 1992, pp 58-61.
30. Hitney, H.V., "A Practical Tropospheric Scatter Model Using the Parabolic Equation," IEEE Trans. Antennas Propagat., 41, 7, July 1993, pp 905-909.
31. Hitney, H.V., "Modeling Surface Effects with the Parabolic Equation Method," in "IGARSS '94," IEEE Symposium Digest, 8-12 August 1994.
32. Marcus, S.W., "A Hybrid (Finite Difference-Surface Green's Function) Method for Computing Transmission Losses in an Inhomogeneous Atmosphere over Irregular Terrain," IEEE Trans. Antennas Propagat., 40, 12, December 1992, pp 1451-1458.
33. Levy, M.F., "Combined Effects of Atmosphere and Terrain on UHF/Microwave Paths," in "Multiple Mechanism Propagation Paths (MMPPs) Their Characterisation and Influence on System Design," AGARD CP-543, October 1993, Paper 15.
34. Hitney, H.V. and J.H. Richter, "Integrated Refractive Effects Prediction System (IREPS)," Nav. Eng. J., 88, 2, April 1976, pp 257-262.
35. Phegley, L. and C. Crosiar, "The Third Phase of TESS," Bull. Amer. Meteor. Soc., 72, 7, July 1991, pp 954-960.
36. Hitney, H.V., "Engineer's Refractive Effects Prediction System (EREPS)," in "Operational Decision Aids for Exploiting or Mitigating Electromagnetic Propagation Effects," AGARD CP-453, September 1989, Paper 6.
37. Patterson, W.L., C.P. Hattan, H.V. Hitney, R.A. Paulus, A.E. Barrios, G.E. Lindem, and K.D. Anderson, "Engineer's Refractive Effects Prediction System (EREPS) Revision 2.0," Naval Ocean Systems Center TD 1342, Rev. 2.0, February 1990.

38. Hopkins, R.U.F., J.B. Smyth, and L.G. Trolese, "The Effect of Superrefraction on the High-Altitude Coverage of Ground-Based Radar," U.S. Navy Electronics Laboratory Report 741, 12 December 1956.
39. Ames, L.A., P. Newman, and T.F. Rogers, "VHF Tropospheric Over-water Measurements Far Beyond the Horizon," Proc. IRE , 43, 10, 1955, pp 1369-1373.
40. Richter, J.H. and H.V. Hitney, "Antenna Heights for the Optimum Utilization of the Oceanic Evaporation Duct," Naval Ocean Systems Center TD 1209, vols. 1 and 2. January 1988.
41. Paulus, R.A., "Practical application of an evaporation duct model," Radio Sci., 20, 4, Jul-Aug 1985, pp 887-896.
42. Anderson, K.D., "94-GHz Propagation in the Evaporation Duct," IEEE Trans. Antennas Propagat., 38, 5, May 1990, pp 746-753.
43. Liebe, H.J., K.C. Allen, G.R. Hand, R.H. Espeland, and E.J. Violette, "Millimeter-Wave Propagation in Moist Air: Model Versus Path Data," NTIA Rep. 85-171, March 1985.
44. "Symposium on Tropospheric Wave Propagation," U.S. Navy Elec. Lab. Report 173, 25-29 July 1949.
45. Hitney, H.V., "Whispering gallery effects in the troposphere," Radio Sci., 27, 6, Nov-Dec 1992, pp 893-898.
46. Day, J.P. and L.G. Trolese, "Propagation of Short Radio Waves Over Desert Terrain," Proc. IRE, 38, 2, February 1950, pp 165-175.
47. Hitney, H.V. and R. Vieth, "Statistical Assessment of Evaporation Duct Propagation," IEEE Trans. Antennas Propagat., 38, 6, June 1990, pp 794-799.
48. Paulus, R.A., "Propagation in the Evaporation Duct: Model Predictions and Comparisons," Naval Command, Control and Ocean Surveillance Center RDT&E Division TR 1644, March 1994.
49. Recommendation ITU-R PN.452-6 (1994), "Prediction procedure for the evaluation of microwave interference between stations on the surface of the earth at frequencies above about 0.7 GHz," ITU-R Fasicule: ITU-R Recommendations, RPN Series, Propagation in Non-Ionized Media, Geneva, 1994.

Electro-optics: Propagation from IR to UV and Sensor Considerations

Part A: Propagation Theory

Anton Kohnle
FGAN-Forschungsinstitut für Optik (FfO), Doc. 1994/43
Schloss Kressbach, D-72072 Tübingen, Germany

SUMMARY

The basic propagation theory is presented in a form usable for electro-optical systems engineers. Starting with the different contributions which affect an electro-optical system under environmental conditions (background, target-signature, atmospheric propagation, sensor specifications, signal-processing) the atmospheric transmittance separated into molecular and particle contributions is discussed. Both absorption and scattering terms as well as scattering functions are given with respect to their wavelength dependence. For statistical system performance analysis extinction coefficients for Nd:YAG and CO_2 laser radiation derived from measured OPAQUE data of Southern Germany are discussed. They are given as a function of the month of the year for specific cumulative probabilities. Optical turbulence which is affecting laser systems more than broad band systems is discussed with emphasis on intensity and phase fluctuation in the atmospheric boundary layer. Nonlinear effects encountered in high-energy laser beam propagation through the atmosphere are illustrated.

1. INTRODUCTION

Atmospheric propagation of infrared (IR), visible (VIS) and ultra-violet (UV) radiation is of importance for many military systems. The increasing sophistication and complexity of these systems require an increasingly accurate and comprehensive description of the propagation environment as well as the relevant background scenario. Rapidly evolving sensor and signal processing technology has prompted novel and highly specialised systems concepts. Depending on the functional principle of such systems, propagation phenomena affect and often limit their performance. Loss of performance is often the result of several combined effects working in conjunction, e.g., molecular and aerosol absorption, emission and scattering, and optical turbulence. A thorough understanding of such effects on systems parameters and overall performance (including signal processing) is the basis for atmospheric systems adaptation and possible corrective techniques.

There are many military systems which depend on the ability either to transmit radiation through the atmosphere or to detect an object against a complex radiation background. In general such systems fall into two classes: 1. High spectral resolution systems typified by laser sources and 2. Broad band systems specified by thermal imaging systems working in the 3 - 5 µm or 8 - 12 µm spectral region. These different types of systems dictate substantially different requirements on atmospheric propagation modelling.

The main objective of atmospheric propagation modelling is to be able to predict the opacity of the atmosphere along any geometric path under any atmospheric condition at any wavelength given a set of measured or predicted meteorological parameters. The spectral range regarded here is from UV (0.2 µm) to IR (14 µm).

In order to understand the propagation characteristics of the atmosphere for radiation in this broad spectral region, it is necessary to understand the details of molecular extinction processes (both absorption and scattering) as well as details of aerosol absorption and scattering processes and of optical turbulence. These effects are wavelength dependent with the general trend for "all weather" capability with increasing wavelength.

For military systems the effective range to perform a specific task is mandatory for successfully plan and execute a mission. The system range performance depends not only on the propagation medium but also on target and background characteristics, sensor characteristics, and possible countermeasures. Conventionally weather support is normally not sufficient for forecasting system performance. Tactical decision aids (TDA) are therefore modular constructed based on up-to-date environmental information in the target area and models for targets and backgrounds, atmospheric transmittance, and for the sensor. The part A of this lecture concentrates on atmospheric propagation effects essential for system performance analysis and part B on modelling atmospheric effects for such purposes.

2. Background Signatures and Sources

Environmental conditions affect thermal signatures. Unlike reflection signatures (visual range, active laser systems), which are not greatly affected by weather effects, the thermal signature of, e.g., a vehicle depends on past meteorological conditions, the current weather situation (warming up, cooling down etc.) and the heat produced by the vehicle (motor, generators, energy consuming equipment, weapons). Extensive signature data banks exists in most NATO countries. Thermal contrast is normally fairly low around sunrise and sunset, because of the change from domination by incoming radiation during the day to outgoing radiation during the night. For the same reason, thermal contrasts are not usually very pronounced beneath extensive cloud cover.

For imaging sensors working in the UV, especially in the solar blind spectral region of the UV (230 - 290 nm) an object is regarded against a nearly radiation free and therefore homogeneous background. The background is generally weak because UV radiation emitted by the sun is absorbed by the stratospheric ozone layer so that an UV emitting object is seen against a radiation free sky background or against a non irradiated and therefore not reflecting terrestrial background. This is the reason, why for UV sensors backgrounds play a minor role, in contradiction to infrared systems where detection probabilities and false alarm rates are mainly determined by the complexity of the cluttered IR backgrounds.

For an explanation of the basic contributions to background radiances, see Fig. 2.1. This Figure shows a typical spectral sky radiance curve composed by different contributions [1]. Sky background radiation in the infrared is caused by scattering of the sun radiation and by emission from atmospheric constituents. As can be seen in Fig. 2.1, the spectrum can be separated into two regions: the solar scattering region with wavelengths shorter than 3 µm and the thermal emission region beyond 4 µm. Solar scattering is represented by reflection from a bright sunlit cloud and alternatively by a curve for clear-air scattering. The thermal region is represented by a 300 K blackbody.

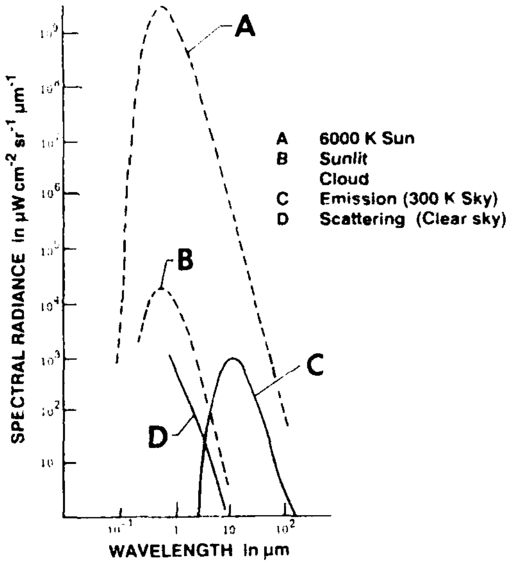

Fig. 2.1: Contributions from scattering and atmospheric emission to background radiation [1].

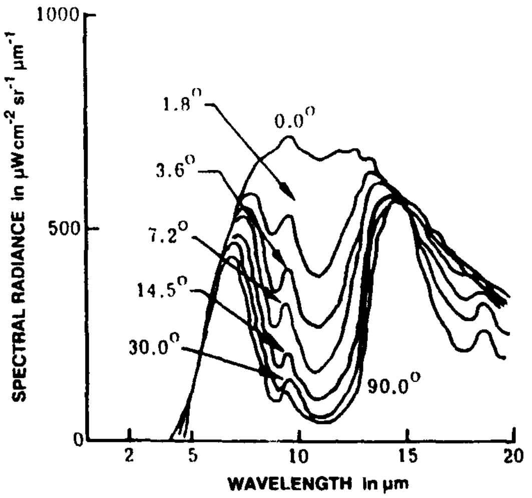

Fig. 2.2: Spectral radiance of a clear nighttime sky for several angels of elevation above the horizon [1].

This simple model is modified by absorption bands, the position of the sun, the viewing trajectory (air mass) etc. Fig 2.2 shows the spectral radiance of a clear night-time sky for several angles of elevation above the horizon [1]. For a horizontal path (0.0°) the spectral radiance is close to a blackbody curve appropriate to the ambient temperature. For a vertical path, only those regions of the spectral radiance curve correspond to a blackbody curve with ambient temperature where strong atmospheric absorption and therefore strong emission occurs. Because vision is based on radiance differences, a cloud at ambient temperature cannot be seen in these spectral regions.

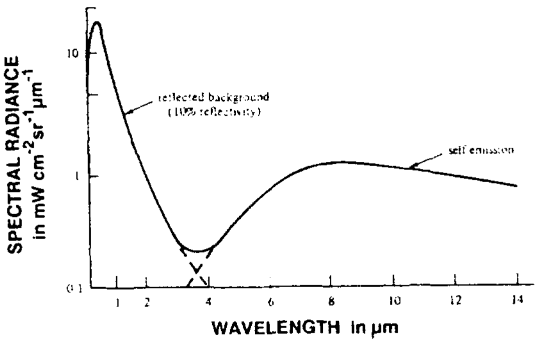

Fig. 2.3: Typical terrain spectral radiance contributions [2].

The spectral radiance of a terrain surface can be divided into two main components: reflected radiance and self-emittance.

The terrain background radiance in the daytime is dominated by reflected sunlight up to 3 μm. Self-emission is dominant for night operations and for wavelength longer than 4 μm even during the day. Fig. 2.3 gives a typical terrain spectral radiance [2]. Very much the same is true for the spectral radiance of the ocean. Fig. 2.4 shows spectral radiance curves for different sea states under daytime conditions [1].

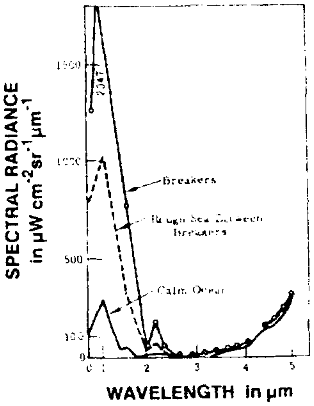

Fig. 2.4: Spectral radiance of the ocean under sunlit [1].

Besides the spectral radiance of natural backgrounds, the knowledge of the spectral signature of threat targets is essential. This is obvious because e. g. detection of an aircraft is possible at a given distance only, if enough radiance difference to the background is available for analysis within the spectral sensitivity band of the used sensor. Fig. 2.5 shows as an example the variation of aircraft spectral signatures over different aspect angles [1]. As expected, the front view radiance is the lowest one. To see a target against a given background, a contrast radiance between target and background is necessary. Fig. 2.6 shows for demonstration purposes the spectral radiance difference between a tank target and a terrestrial background under sun illumination [1]. The background radiance is composed of the low temperature soil radiation and the high temperature solar reflected radiation. Imaging sensors are sensitive in selected spectral bands matched to the spectral sensitivity of the used detectors. One of the driving questions in sensors selection is often the advantage of one wavelength band over the other for a given task. Without going into too much details here, two considerations play a major role. As can be seen in the previous source spectral radiance curves, spectral band energy ratios depend on temperature and emittance characteristics.

For the simple case of a blackbody radiator the spectral band energy ratios for a 3 - 5 μm and 8 - 14 μm band as a function of blackbody temperature are given in Fig. 2.7 [3]. This example shows that for low temperature targets, the 8 - 14 μm band has some advantage. For sensors, used in the atmosphere also the range dependence of the band ratios play an essential role. Fig. 2.8 shows such relations for 6 different band ratios [1]. The range dependence of these band ratios are quite different. Because of the strong atmospheric extinction of UV-radiation, the ratio UV / 8 - 12 μm is decreasing very fast with range. Such a combination would be ideal for passive ranging for short distances.

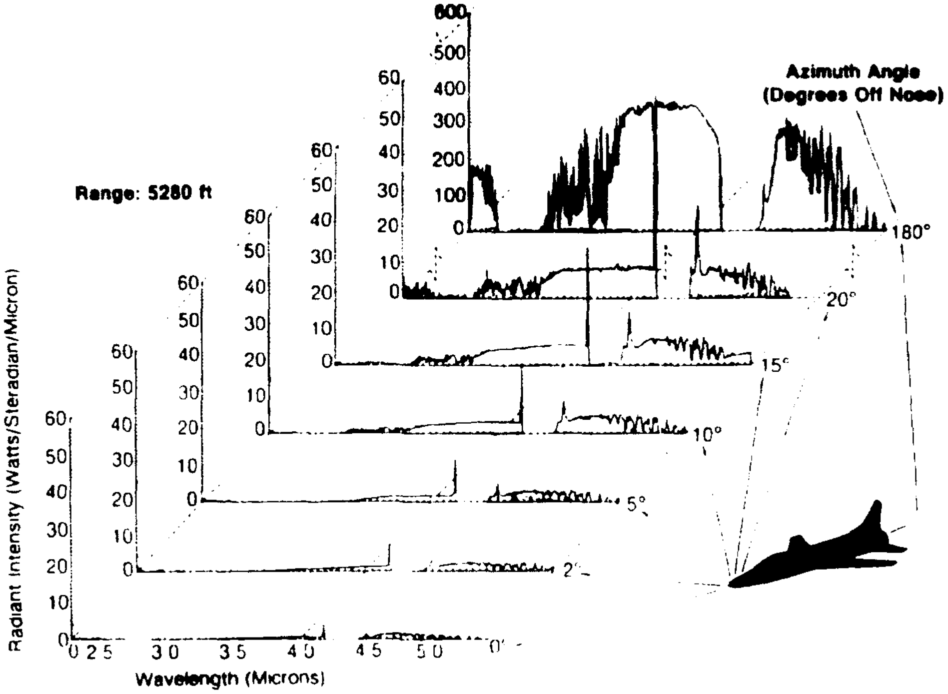

Fig. 2.5: Variation of aircraft spectral signatures over aspect angle [2].

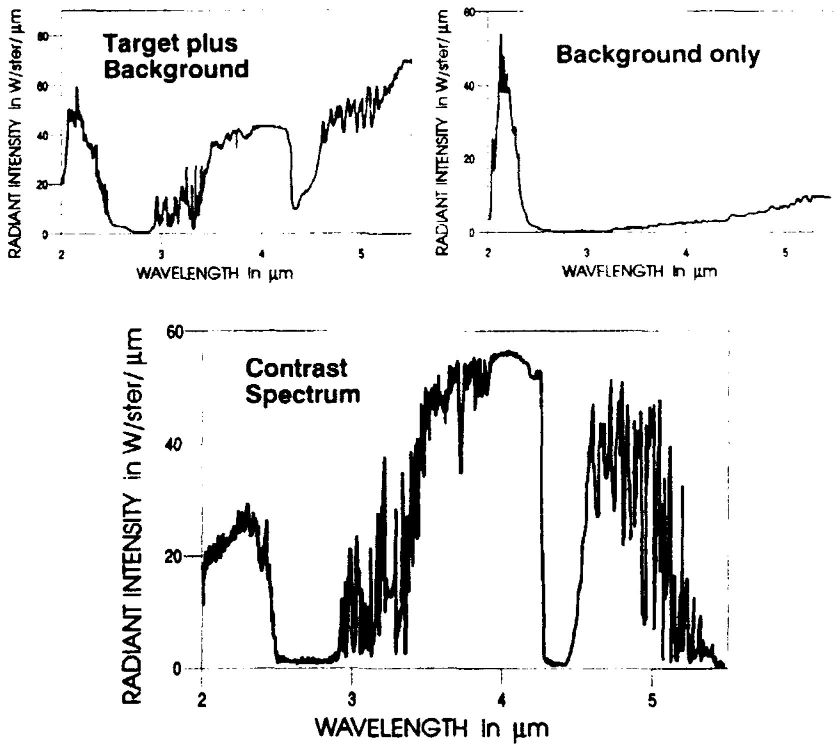

Fig. 2.6: Data example for spectral radiant intensity signature data [1].

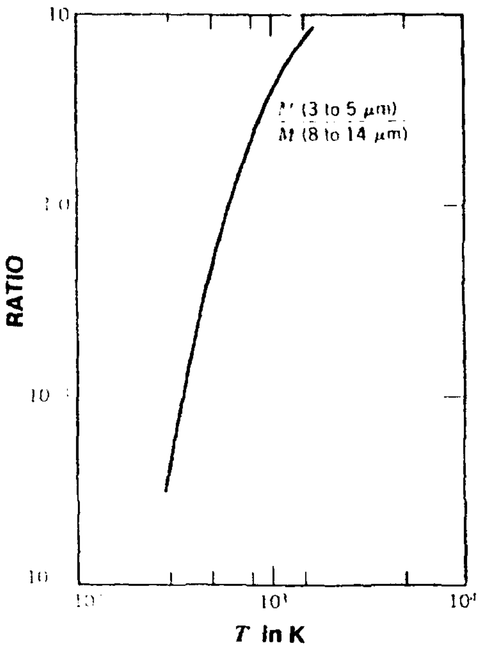

Fig. 2.7: Blackbody spectral band energy ratios [3].

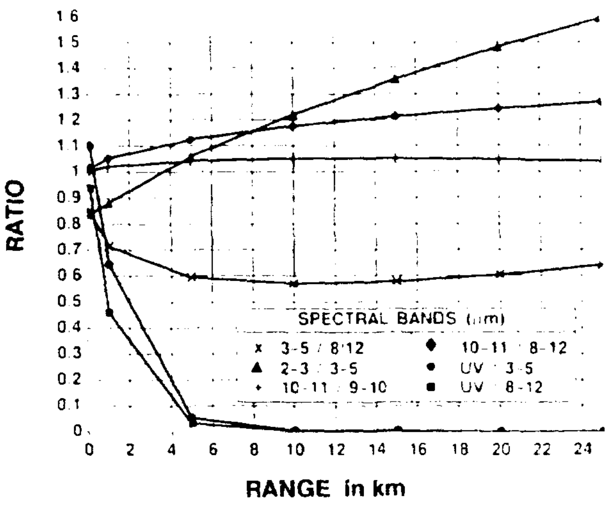

Fig. 2.8: Relative band ratios versus range [1].

3. Atmospheric Propagation

Propagation of electromagnetic radiation at ultraviolet/optical and infrared frequencies through the atmosphere is affected by absorption and scattering by air molecules and by particulates (e.g. haze, dust, fog, and clouds) suspended in the air. The earth's atmosphere is a mixture of many gases and suspended particles varying with altitude, time, and space as a function of geographical region. For the involved absorption and scattering processes also variations in pressure, temperature and concentration for gaseous constituents and in addition size distributions for particles play an essential role. Scattering by air molecules (Rayleigh scattering) plays a role only for wavelengths shorter than e.g. 1.3 μm and gets very much pronounced in the UV-region. Molecular absorption on the other hand including the so-called continuum absorption is a difficult matter and play a role for wavelength shorter (UV) and larger (IR) than for visible wavelength.

Scattering and absorption by aerosol becomes the dominant factor in the boundary layer near the earth's surface, especially in the visible, and under reduced visibility conditions at all wavelengths. These atmospheric particles vary greatly in their concentration, size, and composition, and consequently in their effects on radiation.

It is impossible to go into full depth of this complicated subject within one lecture. The intention is therefor rather to illuminate the basic relations with relevance to system performance analysis.

3.1 Atmospheric Transmission

The differential loss in spectral radiant flux $d\Phi_\lambda(r)$ along an incremental distance dr can be expressed as

$$d\Phi_\lambda(r) = -\sigma_\lambda \Phi_\lambda(r) dr, \qquad (3.1)$$

with σ_λ = spectral extinction coefficient.

Integration for a homogeneous medium (σ_λ = const.) for a distance R results in

$$\Phi_\lambda(R) = \Phi_\lambda(0) \exp - \sigma_\lambda R. \qquad (3.2)$$

Equation (3.2) is the well known exponential extinction law, sometimes called Bouguer's or Beer's Law.

The spectral transmittance τ_λ over a distance R is defined as

$$\tau_\lambda(R)=\frac{\Phi_\lambda(R)}{\Phi_\lambda(0)}=\exp-\sigma_\lambda R. \qquad (3.3)$$

The spectral extinction coefficient is additive with respect to different, independent attenuation mechanisms and constituents, expressed by

$$\begin{aligned}\sigma_\lambda &= \sigma_\lambda^M+\sigma_\lambda^P \\ &= \left(\alpha_\lambda^M+\beta_\lambda^M\right)+\left(\alpha_\lambda^P+\beta_\lambda^P\right), \qquad (3.4)\end{aligned}$$

where the separation is made for molecules (M) and particles (P) and for absorption (α) and scattering (β) contributions.

For inhomogeneous distributions of absorbing and scattering atmospheric constituents the transmission $\tau_\lambda(R)$ must be calculated by integration along path R according to

$$\begin{aligned}\tau_\lambda(R) &= \exp-\int_0^R\sigma_\lambda(r)dr \qquad (3.5)\\ &= \exp-\overline{\sigma_\lambda}R,\end{aligned}$$

where $\overline{\sigma_\lambda}$ represents the mean extinction coefficient.

For polychromatic radiation integration over the selected wavelength band $\Delta\lambda$ is necessary to calculate the broad band transmittance $\tau_{\Delta\lambda}$ expressed by

$$\tau_{\Delta\lambda}(R)=\frac{\int_{\Delta\lambda}\Phi_\lambda(0)(\exp-\overline{\sigma_\lambda}R)d\lambda}{\int_{\Delta\lambda}\Phi_\lambda(0)d\lambda}. \qquad (3.6)$$

For system analysis the spectral responsivity R_λ of the sensor has to be included as another factor in the integral to yield the effective broad band transmittance.

The relative transmission of primary constituents of the atmosphere is shown in Fig. 3.1 as a function of wavelength [4]. There are regions of high transparency (windows) at wavelength regions 1 - 2 µm, 3.5 - 5 µm and 8 - 14 µm. The curves of Fig. 3.1 have relatively poor spectral resolution. As will be shown later, the atmospheric absorption changes drastically as a function of wavelength. The influence of atmospheric spectral molecular absorption on the solar irradiance can be seen in Fig. 3.2 [4].

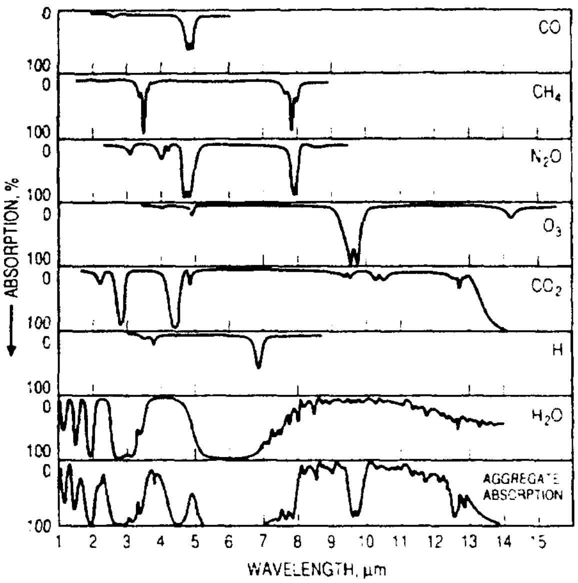

Fig. 3.1: Infrared absorption by atmospheric gases.

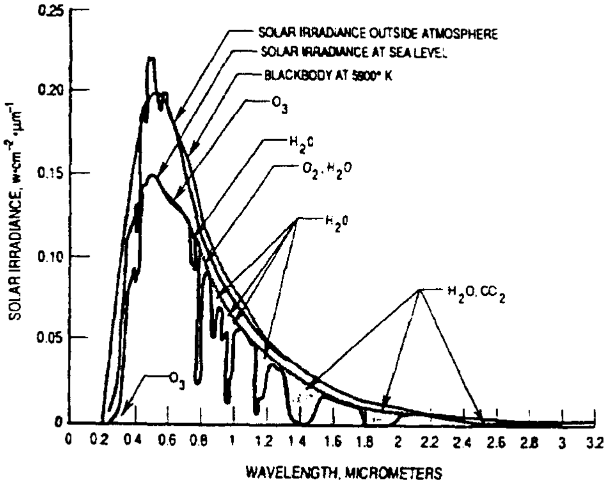

Fig. 3.2: Solar spectral irradiance at Earth's surface and outside Earth's atmosphere (shaded areas indicate absorption, at sea level, due to the atmospheric constituents) [4].

3.2 Molecular Extinction

The spectral molecular extinction coefficient σ_λ^M is composed, see Eq. (3.4)., of an absorption term α_λ^M and a scattering term β_λ^M. The molecular absorption term α_λ^M contains contributions from line absorption α_λ^{ML} and continuum absorption α_λ^{MC}. These quantities are explained in the following sections.

3.2.1 Molecular Line Absorption

A basic understanding of the molecular spectroscopy is necessary for the understanding of the location and nature of atmospheric transmittance windows.

Molecular absorption, see Fig. 3.3, is related to the discrete energy levels of molecules.

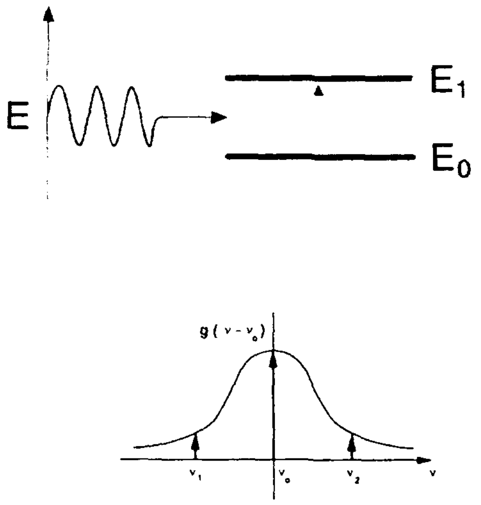

Fig. 3.3: Photon absorption in a two-level system (a) and smearing of energy levels caused by external perturbations and the resulting line shape (b).

In the most simple two-level system a photon with a frequency f_0 such that

$$f_0 = \frac{E_1 - E_0}{h}, \tag{3.6}$$

with h = Planck's constant holds is absorbed. Thus a spectral line is observed at f_0 because of the absence of energy relative to the incident photon field. The equivalent wavenumber is given as

$$\upsilon_0 = f_0\, c^{-1}, \tag{3.7}$$

with c = speed of the light.

A real spectral line has an integrated amplitude (or strength S_i) and a half-width a_i because the energy levels are not single valued, but instead have a distribution of energies caused by the Heisenberg uncertainty principle, collisions from other molecules, electric fields, magnetic fields, and thermal motion. Collision and Doppler broadened line profiles extend far from line centers (e.g. Voight profile, see also Chap. 3.2.2 continuum absorption). The resulting absorption feature is illustrated in Fig. 3.4.

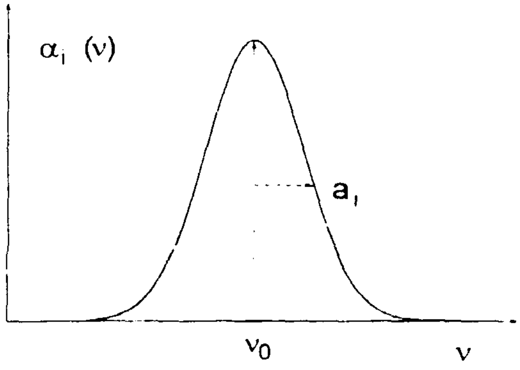

Fig.3.4: Spectral absorption coefficient of an absorption line.

The strength of the i'th absorption line is defined as the entire area under the absorption curve $\alpha_i(\upsilon)$. Thus,

$$S_i = \int_0^\infty \alpha_i^{ML}(\upsilon)\, d\upsilon. \tag{3.8}$$

The profile, or line-shape function, of the transition is defined as

$$g(\upsilon, \upsilon_0; a_i), \tag{3.9}$$

where a_i is the half-width at half maximum and υ_0 is the line center wavenumber. Thus, the absorption coefficient of a single line can be broken down into two factors, the line strength and the line-shape profile given by

$$\alpha_i^{ML}(\upsilon)=S_i g(\upsilon,\upsilon_0;a_i). \qquad (3.10)$$

The definition of S_i requires the line-shape profile to be normalized as

$$1=\int_0^{\infty} g(\upsilon,\upsilon_0;a_i). \qquad (3.11)$$

Of course, no molecule has only one spectral line, and a sum over all spectral lines must be made to compute the total absorption as a function of frequency. Therefore,

$$\alpha^{ML}(\upsilon)=\sum_i \alpha_i^{ML}(\upsilon)=\sum_i S_i g(\upsilon,\upsilon_i). \qquad (3.12)$$

Fig. 3.5 shows an example of CO absorption coefficients as a function of wavenumber [5].

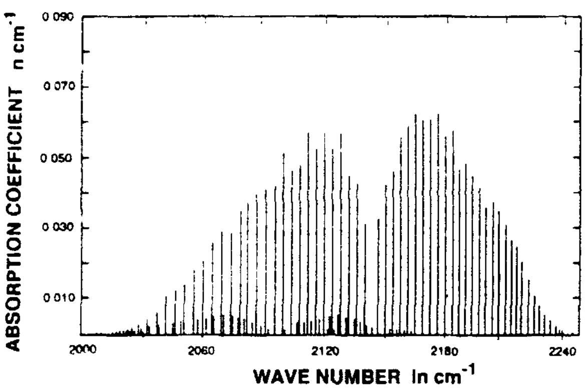

Fig.3.5: Carbon-monoxide absorption spectrum for P_{CO} = 3 Torr and T = 295 K [1].

3.2.2 Continuum Absorption

In addition to molecular absorption by discrete absorption lines, there exists a slowly varying component of molecular absorption in the atmosphere caused mainly by molecular clusters. This absorption plays an essential role particularly in "window" regions where absorption by discrete lines is small.

It is difficult to separate the cluster molecular absorption from absorption in the distant wings of strong discrete absorption lines. For practical reasons far wing absorption and cluster absorption are combined and called "continuum" absorption. In regions of more substantial line absorption, the problem reduces to that of deciding how far into the wings of each line to assume individual line contributions and how much of the experimentally observed absorption to model as a "continuum". Two significant absorption features, treated as continuum absorption are of particular significance in atmospheric window regions will be described in the following.

The main continuum absorption $\alpha^{MC}(\upsilon)$ is caused by H_2O in the 7 - 14 µm band (a minor one near 4 µm) and can be approximated according to

$$\alpha^{MC}(\upsilon,T)=C_s(\upsilon,T)P_s+C_n(\upsilon,T)P_n \qquad (3.12a)$$

where $C_s(\upsilon, T)$ is a self-broadening coefficient due to collisions of water molecules with other water molecules, $C_n(\upsilon, T)$ is a nitrogen broadening coefficient due to collisions of water molecules with air (primarily nitrogen) molecules, P_s is the partial pressure (in atmospheres) of water vapor and P_n is the partial pressure of the remainder of the atmosphere (primarily nitrogen) [6].Fig. 3.6 gives an example of the impact of the H_2O continuum on the absorption coefficient at 4.0 µm and 10.6 µm for different atmospheric models (see part B of this lecture).

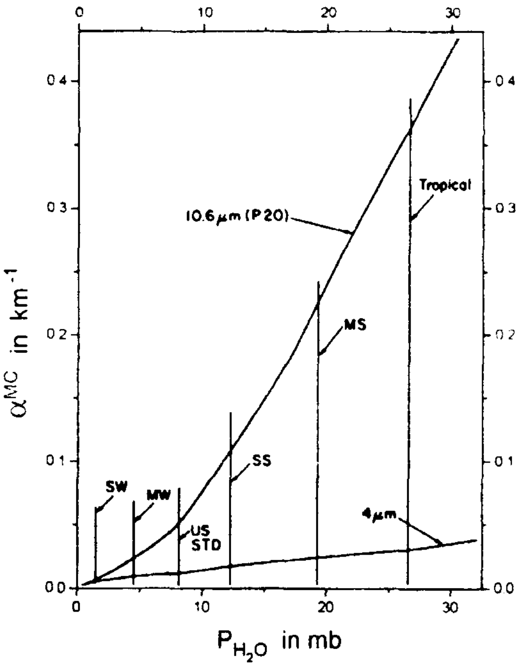

Fig.3.6: Absorption coefficients due to the water vapor continuum [6].

Fig. 3.6 shows that especially for warm humid areas (Tropical) the absorption due to the H_2O continuum is much higher at 10.6 µm compared to 4 µm. Because of the considerable lack of experimental data, related to the physical complexity of the origin of the continuum absorption, there is still some uncertainty in the calculations (see lecture B, Chap. 2, LOWTRAN).

3.2.3 Molecular Scattering

Scattering by molecules is a result of the dipole moment that is synchronously induced by the incident radiation. It is described by the spectral volume scattering function $\beta_\lambda^M(\varphi)$ according to

$$\beta_\lambda^M(\varphi) = \frac{dI_\lambda(\varphi)}{E_\lambda \cdot dV}, \qquad (3.13)$$

with

$dI_\lambda(\varphi)$ = spectral radiant intensity (Wsr^{-1}),

φ = angle with respect to original direction,

E_λ = spectral irradiance (Wm^{-2}),

dV = volume element (m^3).

The spectral scattering coefficient β_λ^M, covering all losses from all molecules in dV follows by integration according to

$$\beta_\lambda^M = 2\pi \int_0^{2\pi} \beta_\lambda^M(\varphi) \sin\varphi \, d\varphi, \qquad (3.14)$$

if unpolarized radiation is assumed, e. g. if rotational symmetry is present.

For all wavelengths λ considered here the diameter d of the atmospheric molecules ($d \approx 10^{-4}$ μm) is much smaller than λ, molecular scattering can be handled as Rayleigh scattering [7] with

$$\beta_\lambda^M(\varphi) \approx (1 + \cos^2\varphi), \qquad (3.15)$$

and

$$\beta_\lambda^M \approx \frac{1}{\lambda^4}. \qquad (3.16)$$

The λ^{-4} dependence of β_λ^M results in the fact, that Rayleigh scattering can be neglected at wavelength larger than about 1.3 μm. In the visible range, where molecular absorption usually can be neglected, molecular scattering determines the maximum visual range V_N, the so called Rayleigh visibility:

$$V_N = \frac{3.912}{\sigma} = 337\,km, \qquad (3.17)$$

which is equivalent to a transmittance of 0.02, see Eq. 3.5.

3.3 Aerosol Extinction

The spectral aerosol extinction coefficient σ_λ^A is difficult to evaluate. This is basically caused by the complexity of the atmospheric aerosols, which can consist of dust and combustion products, salt particles, industrial pollutants, living organisms and, the most important, water droplets. These particles are further characterised in terms of size distributions, spatial constituent distributions, humidity effects etc.

Mie theory can be used to derive absorption and scattering coefficients α_λ^A and β_λ^A for spherical particles if the complex refractive index and the number density and size distribution are known [8]. Every irregularity in particle size gives however strong changes [9].

Atmospheric aerosol is present in every state of the atmosphere but with a highly variable concentration in time and in space. The size distribution ranges in a large interval of radii for natural particles between about 10^{-3} μm up to 10^{+2} μm and can have a considerable complexity.

Moreover many particles of natural aerosols, which are a mixture of water soluble and insoluble components, are subjected to strong changes in size when relative humidity changes [10].

The spectral aerosol extinction coefficient can be written as

$$\sigma_\lambda^A = \int_0^\infty Q_{ext}(r, \lambda, m)\, \pi r^2\, n(r)\, dr, \qquad (3.18)$$

where Q_{ext} is the so called Mie Efficiency factor of a particle with radius r at wavelength λ (size parameter $s = 2\pi \; r/\lambda$) and refractive index m, and $n(r)$ is the aerosol size distribution function. According to absorption and scattering contributions, Q_{ext} can be separated into

$$Q_{ext} = Q_{abs} + Q_{scat}, \qquad (3.19)$$

what results after integration according to Eq. 3.18 in α_λ^A and β_λ^A. Fig. 3.7 shows Q_{ext} as a function of the size parameter s for different refractive indices [11]. The pronounced resonance effect at $s \cong 7$ for non absorbing particles is reduced by

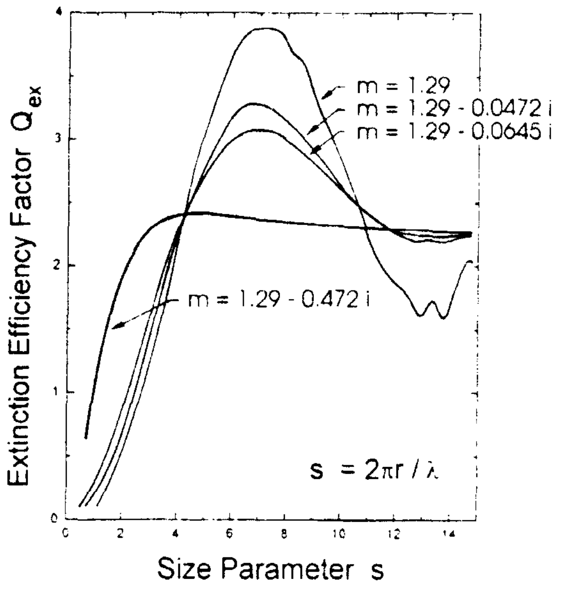

Fig. 3.7: Mie extinction efficiency factor Q_{ex} as a function of the size parameter for different refractive indices [11].

increasing the imaginary part of the refractive index. The high variable size distributions *n(r)* have to be in situ measured or approximated by aerosol models. Fig. 3.8 shows three examples of measured and predicted size distributions from the rural FfO aerosol model [11]. Other widely used models will be described in part B of this lecture.

Fig. 3.9 shows an example of aerosol extinction coefficients as a function of wavelengths for a continental aerosol at a visibility of 23 km [13]. Fig. 3.9 shows that under such meteorological conditions the aerosol extinction coefficient is a decreasing function with wavelength except a few resonances areas (e.g. near 10 μm) caused by aerosol absorption. With the introduction of the Mie angular scattering efficiency function F (r, λ, m, φ) the phase function for aerosol scattering $\beta_\lambda^A(\varphi)$ can be expressed as:

$$\beta_\lambda^A(\varphi) = \int_{r_1}^{r_2} F(r,\lambda,m,\varphi)\,\pi r^2\, n(r)\,dr. \qquad (3.20)$$

Fig. 3.10 is an example of calculated phase functions for measured aerosol size distributions for low and high visibilities for two wavelengths [12]. Very pronounced is the strong forward scattering peak at 0.55 μm compared to 10.6 μm: Fig. 3.9 also shows that the relation between forward- and back scattering is increasing with decreasing visibility.

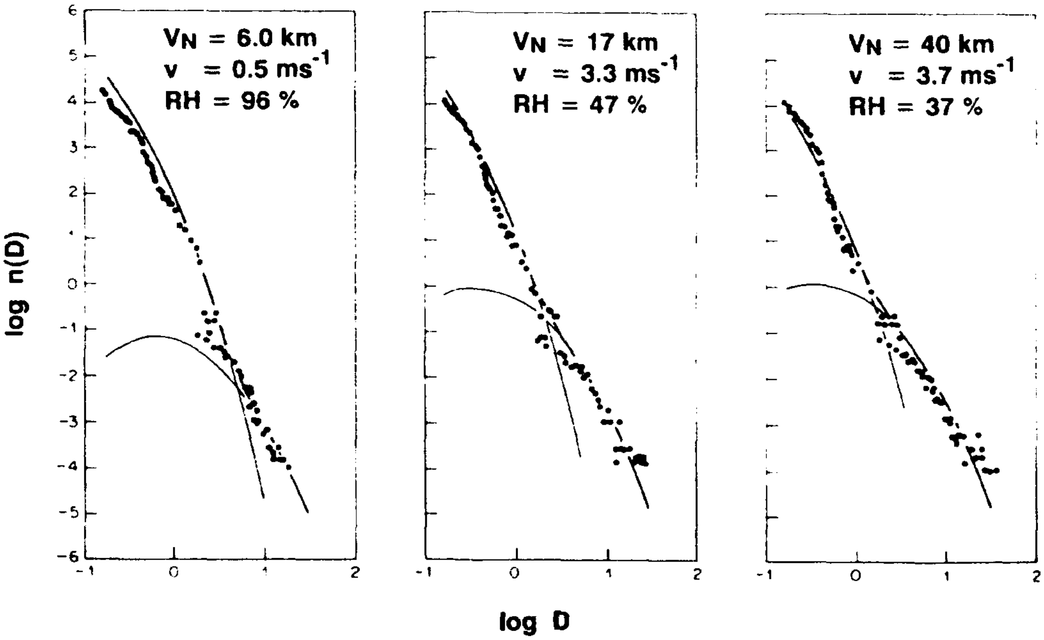

Fig. 3.8: Three examples comparing measured aerosol size distributions (log n(D)) and predicted size distributions from the rural FfO model, for different situations as indicated by the visual range V_N (with 5 % threshold), wind speed v and RH (D in μm; n(D) in cm^{-3} μm^{-1}) [12].

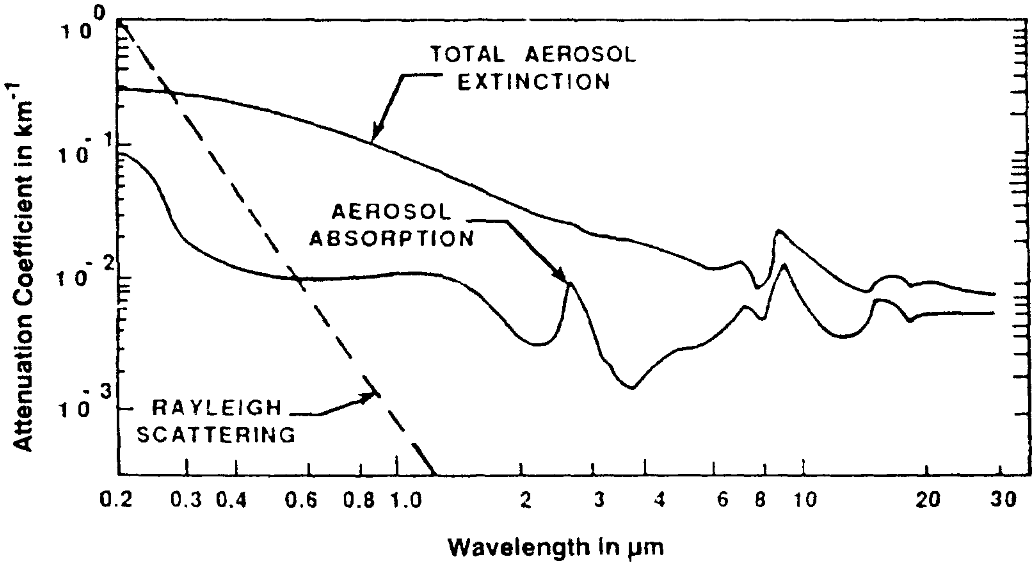

Fig. 3.9: Aerosol absorption and extinction coefficients for 23 km visiblity and a continental aerosol model [13].

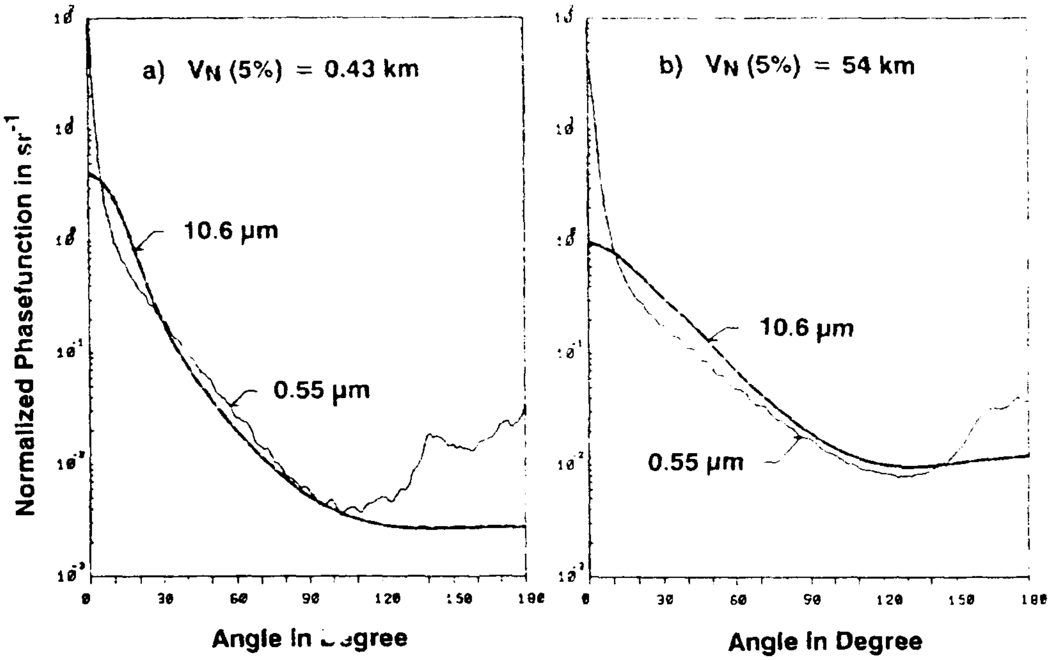

Fig. 3.10: Calculated phase function from measured aerosol size distributions for $\lambda = 0.55$ µm and $\lambda = 10.6$ µm and for visibilties of 430 m (a) and 54 km (b) [12].

3.4 Rain Extinction

Raindrops are many times larger than the wavelengths of interest here. As a result there is no wavelength dependent scattering. In this case the extinction efficiency factor can be approximated ($Q_{abs}=0$) as

$$Q_{ext} \approx 2\pi r^2 , \tag{3.21}$$

which is twice the geometrical scattering cross section. Analysis of measured raindrop size distributions $n(r)$ shows that they can be expressed in the general form [14]

$$n(r) = N_0 \cdot \exp - 2\Lambda r . \tag{3.22}$$

Marshall-Palmer determined $N_0 = 0.08$ cm and $\Lambda = 41.R^{-0.21}$ cm with R rain rate in mm h^{-1}.

The integration according Eq. 3.18 results in the rain extinction coefficient σ_λ^R

$$\sigma_\lambda^R \approx 0.365 R^{0.63} , \tag{3.23}$$

or in the general form

$$\sigma_\lambda^R \approx A \cdot R^B . \tag{3.24}$$

The constants A and B where experimentally determined by different researches for different rain types, see Table 3.1 [15, 16].

Type of Rain	**N_0 (mm^{-1} m^{-3})**	**Λ (mm^{-1})**	**A**	**B**
Marshall-Palmer	8,000	4.1 $R^{-0.21}$	0.365	0.63
Drizzle (Joss and Waldvogel)	30,000	5.7 $R^{-0.21}$	0.509	0.63
Widespread (Joss and Waldvogel)	7,000	4.1 $R^{-0.21}$	0.319	0.63
Thunderstorm (Joss and Waldvogel)	1,400	3.0 $R^{-0.21}$	0.163	0.63
Thunderstorm (Sekhon and Srivastava)	7,000 $R^{0.37}$	3.8 $R^{-0.14}$	0.401	0.79

Table 3.1: Parameter to determine the extinction coefficient of different rain types.

3.5 Extinction Statistics

For system considerations e. g. for statistical system performance analysis extinction statistics for areas of interest are desirable. We select here as an example laser statistics of Nd:YAG (1.06 µm) and CO_2 (10.6 µm) laser radiation based on data from the NATO project OPAQUE for the German station Birkhof in Southern Germany [17]. The extinction coefficients are calculated for the Nd:YAG laser radiation from measured visibility data (aerosol part) and from measured meteorological data (molecular part using FASCODE, see part B of this lecture); for the CO_2 laser radiation from measured 8 - 12 µm broad band transmittance values (aerosol part) and from measured meteorological data (molecular part using FASCODE). The exact method used for these calculations is explained in [17]. Fig. 3.11 and 3.12 show the Nd:YAG and CO_2 extinction coefficients respectively as a function of the month of the year for specified cumulative probabilities. These Figures show that the probability follow extinction values is best from April to September. Within that time the variation of extinction values is much higher for the Nd:YAG laser radiation than for CO_2. The reason is that visibility variations at visibilties larger that about 5 km does effect Nd:YAG - much more than CO_2 laser radiation. Another interesting fact is that the CO_2 laser extinction values never reach the very low values of Nd:YAG laser radiation in this time period. This is caused by the fact that CO_2 laser extinction has an H_2O absorption term (especially continuum absorption, see chapter 3.2.2) which is limiting the CO_2 extinction values during the high absolute humidity period in summer. The molecular absorption at Nd:YAG laser radiation can be neglected.

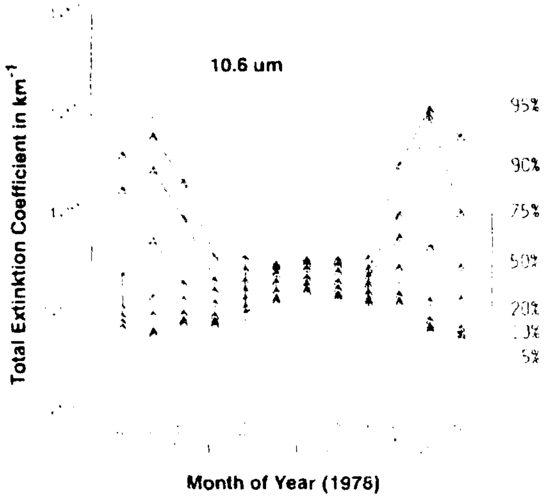

Fig. 3.11: Nd:YAG laser extinction coefficient extrapolated from OPAQUE visual extinction data as a function of month of year for specified cumulative probabilities of occurrence. (c.p.o.)., (from bottom to top: 5, 10, 20, 50, 75, 90, 95 %). Based on data collected at the German OPAQUE station Birkhof [17].

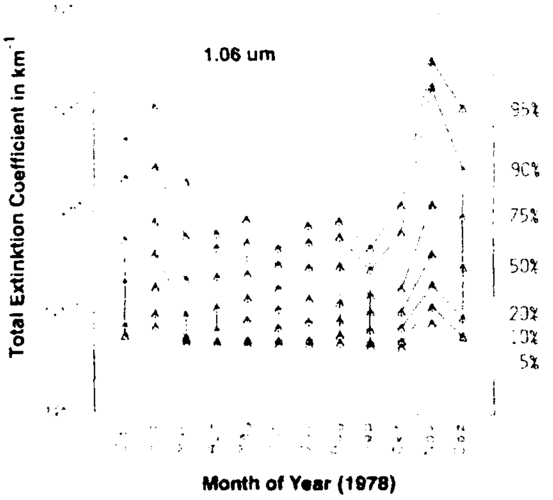

Fig. 3.12: CO_2 laser extinction coefficient extrapolated from OPAQUE 8 - 13 μm transmittance data as a function of month of year for specified cumulative probabilities of occurrence. (from bottom to top: 5, 10, 20, 50, 75, 90, 95 %). Based on data collected at the German OPAQUE station Birkhof [17].

3.6 Propagation through Atmospheric Optical Turbulence

Wind turbulence and convection induces random irregularities in the atmosphere's index of refraction. In passing through these irregularities, optical wavefronts become distorted. As more sophisticated EO systems are developed details of the propagation medium that had previously been ignored become important. Optical turbulence is such a subject area. In the next chapters first atmospheric turbulence and than optical effects of turbulence are described.

3.6.1 Atmospheric Turbulence

The structure of turbulence is described by statistical fluctuations in air velocity. Two basic mechanisms are responsible for velocity turbulence: wind shear and convection. As a result, eddy air currents are produced. For instance air blown over obstacles breaks up into eddies, the largest of which being determined by the size of the obstacle. Due to viscosity if the energy in the eddy exceeds a critical level determined by the Reynold's number, the velocity fluctuations within the eddy are no longer stable, and the eddy breaks up into smaller eddies. Further break-up occurs until the eddy is reduced to sufficiently small size where viscous effects become dominant thereby dissipating the available energy into heat.

The refractive index .. for air or the refraction number N is given as

$$N = (n-1)10^6 \approx \frac{77.6\,P}{T} + \frac{0.584\,P}{T\lambda^2} - 0.06\,P_{H_2O}. \tag{3.25}$$

where P is the atmospheric pressure, T is the temperature and P_{H_2O} is the H_2O partial pressure. Eq. (3.25) shows, that both wavelengths and humidity dependence of N is weak in the spectral band of relevance here. If pressure and humidity fluctuations are neglected a simple relation between refractive index and temperature fluctuation can be derived ($\lambda \;= 10\,\mu m$):

$$\delta n = -79\,P\frac{\delta T}{T^2}10^{-6}. \tag{3.26}$$

For strong turbulence with $\delta T \approx 1\,K$ the refractive index fluctuation is $\delta n \approx 10^{-6}$.

The spatial refractive index spectrum of atmospheric turbulence can be divided into three ranges. The first range, the so called "production range", contains the largest eddies. These eddies are directly formed by turbulent friction and convection. However as soon as these eddies appear they become dynamically unstable and decay into smaller eddies which again are unstable and decay. The spectral range of this cascade is called "inertial subrange". The largest size of eddies belonging to this range is of the order of the height above the ground and is called "outer scale" L_0. In contrast to the eddies in the production range, those of the inertial subrange are isotropic. The cascade ends when the eddies reach sizes in the order of some millimeters. Now diffusion and viscous shear effectively level out the turbulent fluctuations. This last spectral range is called "dissipation range". For refractive index, the eddy size marking the transition between inertial range and dissipation range is called "inner scale" l_0.

For spatial wavenumbers κ in the inertial subrange the refractive index spectrum has a very simple form. If n denotes the refractive index of air, here at locations x and x + r, the ratio of the structure function D_n (see below) and the 2/3 power of the distance r is independent of r

$$D_n(x,r)=\left\langle\left[n(x+r)-(x)\right]^2\right\rangle=C_n^2(x)r^{2/3}. \qquad (3.27)$$

The brackets $\langle\ \rangle$ indicate an ensemble average. C_n^2 is called "structure constant" of refractive index fluctuations. It can be shown that the structure constant can be identified with the spectral amplitude T_n of the (three-dimensional) refractive index spectrum

$$T_n(\kappa)=0.033C_n^2\kappa^{-11/3}. \qquad (3.28)$$

Since most optical systems are sensitive to turbulence eddies in the inertial range, C_n^2 is the most important quantity for the description of optically relevant refractive index turbulence. However, some optical systems are also sensitive to wavenumbers smaller than 2 π/L_0, or larger than 2 π/l_0.

For $\kappa >$ 2 π/l_0, in the production range, the turbulence spectrum is anisotropic, and the spectral density takes smaller values than would be expected assuming a continuation of the inertial range. However in the real atmosphere the observed spectral behaviour is quite complicated. For 2 π/L_0, in the dissipation range, the spectrum deceased rapidly with spatial wavenumber. A variety of different models for the description of this decay is found in the literature. Among these, two spectra are commonly used for wave propagation application: the spectrum of Tatarskii [18] and the spectrum of Hill [19]. The latter contains free parameters which were carefully fitted to experimental data. Even though there are differences in the complexity and accuracy of the models for the dissipation range, experience has shown that for most applications these differences can be neglected and that the models are quite reliable.

Fig. 3.13 shows an idealized refractive index spectrum. In the large wavenumber region both the Tatarskii spectrum and the Hill spectrum are plotted. In the small wavenumber region, the Tatarskii curve was extended according to the von Kármán spectrum. The largest differences with real refractive index spectra are expected here.

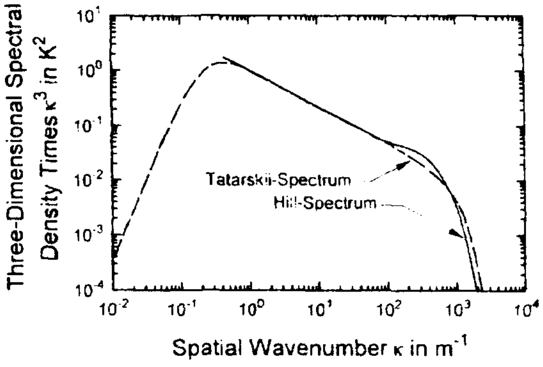

Fig. 3.13: Examples for three-dimensional model spectra of refractive index. Both the spectrum after Tatarskii [18] and the spectrum after Hill [19] are plotted for an inner scale value of 5 mm. The Hill model does not include an outer scale effect, the Tatarskii model uses the von Kármán formulation, here for an outer scale of 5 m.

We can summarize that the refractive index spectrum is generally described by three parameters: - the structure constant C_n^2, the inner scale l_0 and the outer scale L_0. However often C_n^2 is the only really relevant parameter of these. Fig. 3.14 shows as an example measured C_n^2 values versus time of the day [21].

Because refractive index fluctuations are mainly caused by temperature fluctuations a temperature structure function and a temperature structure constant C_T^2 can be defined according to Eq. 3.27. The relation between both structure constants is

$$C_n=\frac{77.6\,P}{T^2}\left(1+\frac{0.00753}{\lambda^2}\right)10^{-6}\,C_T. \qquad (3.29)$$

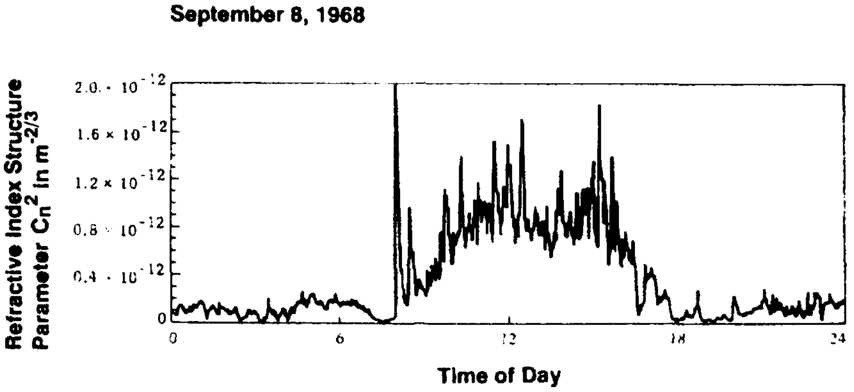

Fig. 3.14: Refractive index structure parameter versus time of day. The measurements were derived from temperature-structure-function measurements made with vertical spacings of 0.01 m at an elevation of 2 m [21].

3.6.2 Optical Effects of Turbulence

Optical effects of turbulence are manifold and widely described in the literature [1, Vol. 2 and Ref. there]. Generally one can distinguish between effects on intensity and effects on phase. Depending on the dominant turbulence scale size and beam diameter we can identify two cases that lead to different effects. For instance, if the scale sizes at all points along the beam path are larger than the beam diameter, the turbulence cells act as very weak lenses that deflect the beam as a whole in a random way, leaving the beam diameter essentially unaltered. This is shown schematically in Fig. 3.15a. The resulting beam displacement from the initial beam direction is known as beam wander. For imaging systems this would result in image motion. When the scale sizes (or cell dimensions) are smaller than the diameter of the beam, diffraction and refraction of the beam takes place and the beam's intensity profile is smeared out and as a rule markedly distorted. This effect, schematically illustrated in Fig. 3.15b, is refered to as beam breathing and scintillation. For imaging systems this would result in image degradation. Depending on the characteristics of the turbulence and the beam dimensions, both cases may be observed simultaneously.

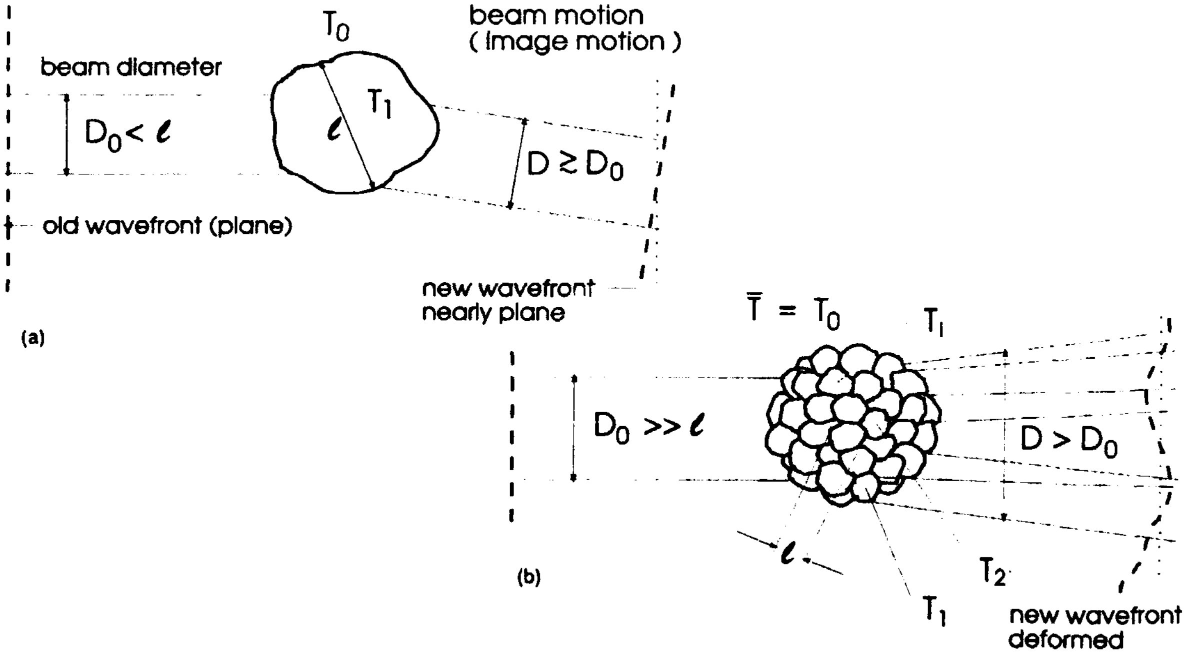

Fig. 3.15: Laser beam deflection by turbulence cells that are larger than the beam diameter (a) and laser beam break up by turbulence cells that are smaller than the beam diameter (b).

In contrast to molecular or particle extinction, turbulence does not reduce the average light intensity. Instead, a quasi random modulation takes place with frequencies between several and several hundreds of Hertz depending on the configuration of the system and the atmospheric state. The modulation of intensity is called scintillation and is well known for star light. Scintillation especially disturbs the transmission of time coded signals as with optical communication or guidance system, LIDARs or range finders. The strength of scintillation is usually described by the normalizied variance of the intensity σ_I^2. In theories often the log-amplitude variance σ_x^2 is regarded. For weak scintillation ($\sigma_x^2 < 0.3 \ldots 0.5$) both quantities can be related according to

$$\sigma_x^2 = 1/4\ln(\sigma_I^2 + 1) \approx \frac{1}{4}\sigma_I^2. \qquad (3.30)$$

The intensity variance for path length L and wavelength λ can be given for $l_0 << (\lambda L)^{1/2}$ for a plane wave [18] as

$$\sigma_x^2(L) = 0.56k^{7/6}\int_0^L C_n^2(x)(L-x)^{5/6}dx, \qquad (3.31)$$

and for a spherical wave as

$$\sigma_x^2(L) = \qquad (3.32)$$
$$0.56k^{7/6}\int_0^L C_n^2(x)\left(\frac{x}{L}\right)^{5/6}(L-x)^{5/6}dx.$$

In these equations the source is at x = 0 and the observer at x = L. Because k = 2 π/λ is increasing with shorter wavelength, optical turbulence effects are decreasing with wavelength.

Fig. 3.16 shows the log-amplitude standard deviation σ_x at four lengths (50, 310, 500 and 1000 m) compared to the refractive index structure parameter C_n versus time of the day [21]. Fig. 3.16 shows the so called saturation phenomenon. Only on the 50 m path the linear relation between C_n and σ_x is pronounced over the full day.

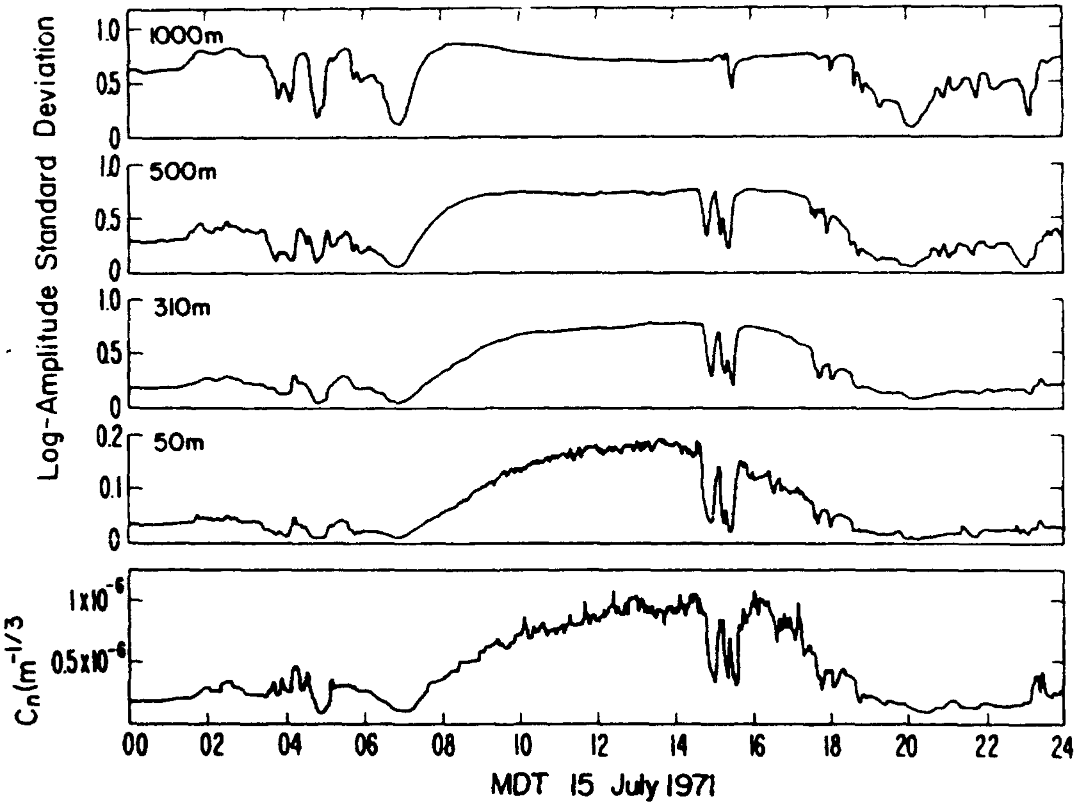

Fig. 3.16: Variance of the log-amplitude standard deviation σ_x at each of four path lengths compared to the refractive index structure parameter C_n [20].

Together with the fluctuations of intensity there occur those of phase. Turbulence distorts the wavefronts and thus causes a nonlinear propagation. Especially heterodyne laser systems and high resolution imaging devices suffer from this: Spatial structures become disordered, images move and become blurred. This impact can be quantified e. g. by an optical transferee function (OTF) which describes the effect of atmospheric turbulence on the resolution of an optical imaging system. The OTF represents a selective weighting of the object's spatial frequency spectrum, see Fig. 3.17.

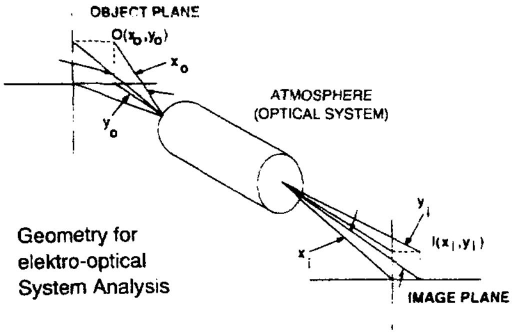

Fig. 3.17: Impact of optical transfer function on imaging through the atmosphere.

Fried [22] has derived an expression for the OTF of the atmosphere, which is dependent on the strength of atmospheric turbulence. Others, after using this theoretical model and comparing it to experimental results, have concluded that a good agreement exists between theory and experiment [23], see Fig. 3.18.

The model by Fried for spherical waves is given by the expression [4]

$$OTF = e^{-\left\{21.62\, C_n^{2}\, R \lambda^{-1/3} f_s^{5/3} \left(1-\alpha\left(f_s \lambda / D_0\right)^{1/3}\right)\right\}} \tag{3.33}$$

where

C_n^2	is the refractive index structure parameter,
R	is the range or path length,
λ	is the wavelength,
f_s	is the angular spatial frequency in cycles/rad,
D_0	is the diameter of aperture,

α = 0 for a long-term OTF

α = 1/2 for a far-field, short-term OTF

α = 1 for a near-field, short-term OTF

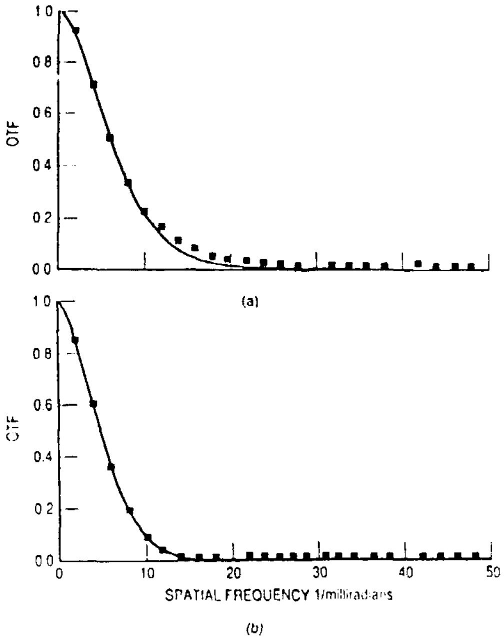

Fig. 3.18: Comparision of thermal measurements of short- and long-term optical transfer function: (a) short-term OTF, (b) long-term OTF for

λ = 0.488 µm

R = 18.8 km

D_0 = 0.4572 m

C_n = $9.5 \cdot 10^{-8}\ m^{-2/3}$ [23].

Equation (3.20) gives the OTF expression of the atmosphere limited in general to two cases: short term and long term.

The short-term OTF is a short-exposure OTF, in which the image is obtained over a short time interval. If a series of short-term OTFs are taken from a point source, there would be beam spreading and beam wandering effects at the image plane caused by atmospheric turbulence. The average short-term OTF is obtained by shifting the center of the area of each point spread function (PSF) to a common point and then averaging and taking the Fourier transforms of the successive PSFs. The shifts required to center the image are known as image wander to beam wander. This averaging procedure has the effect of centering the image and removing the beam wander, and the short-term OTF is often called the beam spread.

The long-term OTF is obtained from a long exposure time, so that every turbulence configuration has been taken into account on a single exposure. Average long-term OTF is therefore the same as that of a single long exposure, and there is no need for the shifting process discussed previously. Long-term OTF, therefore, refers to both the beam spread (short-term OTF) and beam wander.

Phase fluctuations also reduce the coherence of lights and thus limit the performance of coherent detection techniques. Moreover, laser beam propagation is affected by beam spread and wander.

Today theories are available which reliably predict many optical turbulence effects from a statistically known refractivity field. This is widely analogous to the situation with aerosol, where the extinction and scattering can be computed from the sizes, shapes and the compositions of the particles. However, as with the aerosol, the main problem in the prediction of turbulence effects in a real environment is the difficulty to predict the propagation medium: the atmosphere. This is why modelling of the atmospheric turbulent refractive index filed has become more and more important. In part B of the lecture some models will be discussed.

3.7. Nonlinear Propagation

When a high-energy laser (HEL) beam propagates through the atmosphere, a small portion of the energy is absorbed by certain molecules and particulate matter in the air. The absorbed energy heats the air, causing it to expand and form a distributed thermal lens along the atmospheric path that, in turn, spreads, bends, and distorts the laser beam. This self-induced effects is called "thermal blooming" and, since it can limit the maximum power that can be efficiently transmitted through the atmosphere, is one of the most serious nonlinear problems encountered in the propagation of high-energy laser radiation in the atmosphere. A variety of thermal blooming effects are relevant for high-energy laser beams in the atmosphere. Many of these effects have been studied extensively and a number of detailed review articles have been written [1, Vol. 2 and Ref. there].

To illustrate the problem we consider a high energy CW laser beam propagating horizontally in an absorbing medium where the absorption coefficient α^M and the cross-wind speed υ are uniform. As the air moves across the beam the temperature increases due to the absorbed energy from the laser beam. This causes the density of the air and also the refractive index, which is proportional to the density, to decrease as the air moves across the beam. The temperature and refractive-index variations across the beam center along the wind direction are shown in Fig. 3.19.

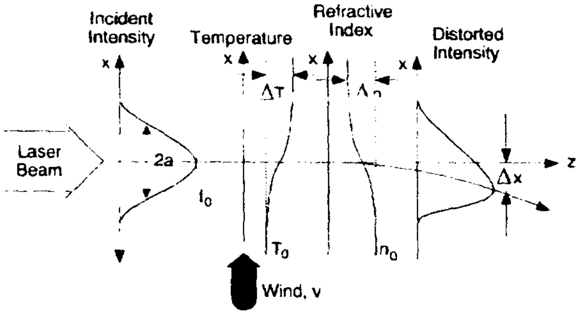

Fig. 3.19: Diagram of the steady-state thermal-blooming problem with wind [1].

4. Conclusions

It is essential that EO systems engineers understand in addition to specific sensor capabilities the impact of background radiation and propagation phenomena on the overall EO system performance. This is essential even for optimized application of the advanced modelling tools described in part B of this lecture.

It is impossible to explain in depth and fully comprehensive all specific details which play a role in system performance analysis. The selection of described topics is rather based on experience with atmospheric sensor evaluation and adaptation to atmospheric restrictions.

Acknowledgement

The assistance of L.H. Boehme in drafting most of the Figures is gratefully acknowledged. Parts of this basic lecture has been taken from referenced literature.

Literature

[1] Accetta, I.S., D.L. Schumaker, Executive Editiors, The Infrared & Electro-Optical Systems Handbook, ERIM/SPIE (Volumes 1 - 7) (1993).

[2] Seyrafi, K., Electro-Optical Systems Analysis, Electro-Optical Research Company, Los Angeles (1990).

[3] Pinson, L.J., Electro Optics, John Wiley & Sons, New York (1985).

[4] Seyrafi, K., Hovanessian, S.A., "Introduction to Electro-Optical Imaging and Tracking Systems", Artec House, Boston (1993).

[5] Clough, S.A., Kneizys, F.X., Shettle, E.P., and Anderson, G.P., "Atmospheric Radiance and Transmittance: FASCOD2", Sixth Conference on Atmospheric Radiation, May 13-16, 1986, American Meteorological Society, Boston, MA (1987).

[6] Clough, S.A., Kneizys, F.X., and Davies, R., "Line shape and water vapor continuum", Atmospheric Reserach 23 (1989).

[7] McCartney, E.J., "Optics of the Atmosphere: Scattering by Molecules and Particles", John Wiley & Sons, New York (1976).

[8] Bohren, C.F., Hoffmann, D.R., "Absorption and Scattering of Light by Small Particles", Wiley-Interscience, New York (1983).

[9) Barber, P., Yeh, C., "Scattering of Electromagnetic Waves by Arbitrary Shaped Dielectric Bodies, Appl. Opt. 14 (1975).

[10] Shettle, E.P., Fenn, R.W., "Models for the Aerosols of the Lower Atmosphere and Effects of Humidity Variations on their Optical Properties", Air Force Geophysics Laboratory Report AFGL-TR-79-0214 (1979).

[11] Kerker, M., "The Scattering of Light and Other Electromagnetic Radiation", Academic Press, New York (1969).

[12] Höhn, D.H., Steffens, W., Kohnle, A., "Atmospheric IR Propagation", Infrared Phys. Vol. 25, No. 1/2 (1985).

[13] McClatchey, R.A., Selby, J.E., Environmental Report, AFGL-TR-74-460 (1974).

[14] Marshall, J. S., Palmer, W. M. K., "The distribution of raindrops with size", J. Met. Vol. 5 (1948).

[15] Joss, J., Waldvogel, A., "Raindrop size distributions and sampling size errors", J. Atm. Sci., Vol. 26 (1969).

[16] Kneizys, F.X., Shettle, E.P., Gallery, W.O., Chetwynd, J.H., Abreu, L.W., Selby, J.E.A., Clough, S.A., Fenn, R.W., "Atmospheric Transmittance/Radiance: Computer Code LOWTRAN 6", Air Force Cambridge Research Laboratory, Report AFGL-TR-83-0187 (1985).

[17] Clement, D., Höhn, D.H., Jessen, W., Kohnle, A., "Atmospheric Performance Statistics for IR Broad-Band and Laser Systems Based upon OPAQUE Data", AGARD Conf. Proceedings No. 454 (1989).

[18] Tatarskii , V. F., Wave Propagation in a Turbulent Medium, Dover Publications, New York (1971).

[19] Hill, R. J., "Spectra of fluctuations in refractivity, temperature, humidity, and the temperature-humidity cospectrum in the inertial and dissipation ranges", Radio Science 13, No. 6 (1978).

[20] Strohbehn, J.W., Laser Beam Propagation in the Atmosphere, Springer-Verlag, Vol. 25 (1978).

[21] Lawrence, R.S., Ochs, G.R., Clifford, S.F., J. Opt. Soc. Am. Vol. 64, No. 6 (1970).

[22] Fried, D.L., "Optical Radiation through a Randomly Inhomogeneous Medium for Very Long and Very Short Exposures", I. Opt. Soc. Amer., Vol. 56 (1966).

[23] Crittenden, E.C., et. al., "Effects of Turbulence on Imaging through the Atmosphere", SPIE Vol. 142 (1978).

Electro-optics: Propagation from IR to UV and Sensor Considerations

Part B: Tools for Exploitation of Propagation Conditions and System Range Performance

Anton Kohnle
FGAN-Forschungsinstitut für Optik (FfO), Doc. 1994/48
Schloss Kressbach, D-72072 Tübingen, Germany

ABSTRACT

During the last decade powerful modelling tools for the assessment and exploitation of propagation conditions together with range performance models for military systems have become available.

After a theoretical description of the propagation environment together with relevant effects on system performance (part A of this lecture) some of the most common used models are described here. For atmospheric transmittance/ radiance calculations these are LOWTRAN, MODTRAN, and FASCODE developed and maintained by the Phillips Laboratory, Geophysics Directorate. For system performance calculations these are EOSAEL developed and maintained by the U.S. Army Research Laboratory, NIRATAM developed by the NATO research study group AC/243 (Panel 04/RSG.06) and maintained by ONTAR Corp., ACQUIRE (FLIR 92) developed and maintained by the U.S. Army Night Vision and Electro-Optics Directorate and TRM 2 developed and maintained by FGAN-Forschungsinstitut für Optik (FfO).

1. INTRODUCTION

During the last decade powerful modelling tools for the assessment and exploitation of propagation conditions together with range performance models for military systems have become available. It is impossible to explain in depth and fully comprehensive all available tools in such a lecture. A selection of models is made, based on experience with sensor evaluation and adaptation to atmospheric conditions.

Due to the large number of parameters involved in optical transmission through the atmosphere, numerical calculations of atmospheric transmission is an unavoidable process. The aim of the numerical calculation is to predict with a high degree of accuracy the transmittance through the atmosphere, given a path, atmospheric conditions, wavelength, and a set of measured or predicted meteorological parameters. The computer codes applied here are transmission models or computational techniques implemented in computer programs that generate the transmittance or a transmittance spectrum, given the necessary input by the user.

Three numerical methods for atmospheric transmission calculations widely in use are LOWTRAN, MODTRAN and FASCODE, developed at the Air Force Geophysics Laboratory (AFGL), Hanscom AFB, Ma., USA, with is now the Phillips Laboratory, Geophysics Directorate. FASCODE contains the molecular database HITRAN and is a high-resolution transmission code, whereas LOWTRAN is a low-resolution transmission code, and MODTRAN offers medium resolution. As new measurements became available and better understanding of the extinction process were reached, FASCODE and LOWTRAN were modified and updated in the last 15 years.

Once LOWTRAN became available other computer models, more specially designed to simulate tactical battlefield situations, could be built around it. Such is the case for EOSAEL (Electro-Optical Systems Atmospheric Effects Library) designed by the U.S. Army Atmospheric Sciences Laboratory which is now the U.S. Army

Research Laboratory. EOSAEL offers many different modules for calculating the effects of battlefield-induced contaminants like smoke, high explosive dust, and vehicular dust. Various other modules are concerned with the effects of turbulence and with absorption and backscattering of laser radiation, effects of clouds and so forth. For many military and civilian applications the infrared radiative emission from aircrafts and missiles are mandatory. The computer code NIRATAM developed by a NATO study group AC/243 (Panel 04/RSG.06) predicts IR radiation of aircrafts in natural surroundings. This code is being maintained by ONTAR Corp., USA. The extension of the code to missile signatures is presently being performed in NATO study group RSG.18 of the same Panel.

Prediction of range performance of a sensor for a given task is essential especially for mission planning despite from sensor development and environmental adaptation. Different models based on Johnson's criteria for perception tasks have became available. The most recent one is FLIR 92 which has been developed by the U.S. Army Night Vision and Electro-Optics Directorate.

2. LOWTRAN Atmospheric Transmission Code

LOWTRAN is a computer code that estimates atmospheric transmittance at low resolutions over a wide spectral interval. This transmission model has great computer efficiency, flexibility, and reasonable accuracy for broadband systems applications. The main features of LOWTRAN are described in the next 6 Chapters.

2.1 General Overview

Since its conception, the LOWTRAN computer program has been used widely by workers in many fields of atmosphere-related science, first as a tool for predicting atmospheric transmissions (LOWTRAN 2 [1], LOWTRAN 3 [2], and LOWTRAN 3B [3]) and later for atmospheric background radiance and transmittance calculations (LOWTRAN 4 [4], LOWTRAN 5 [5], and LOWTRAN 6 [6]) for any given geometry from 0.25 µm to 28.5 µm (i.e., from 350 to 40,000 cm^{-1}). Fig. 2.1 shows the result of a LOWTRAN sample calculation of atmospheric spectral transmittance for a 2 km horizontal path. The latest version of the computer code is LOWTRAN 7 [7, 8]. With LOWTRAN 7, the wavelength range has now been expanded to cover from 0.2 µm in the ultraviolet to the millimeter wave region (0 - 50,000 cm^{-1}). The computer program was designed as a simple and flexible band model that will allow fast, reasonably accurate, low-resolution atmospheric transmittance and radiance calculations to be made over broad regions of the spectrum for any required atmospheric path geometry. LOWTRAN 7 includes all of the important physical mechanisms (with the exception of turbulence) that affect atmospheric propagation and radiance. LOWTRAN has proved valuable for the development and evaluation of many optical systems working in ultraviolet, visible, and infrared parts of the spectrum.

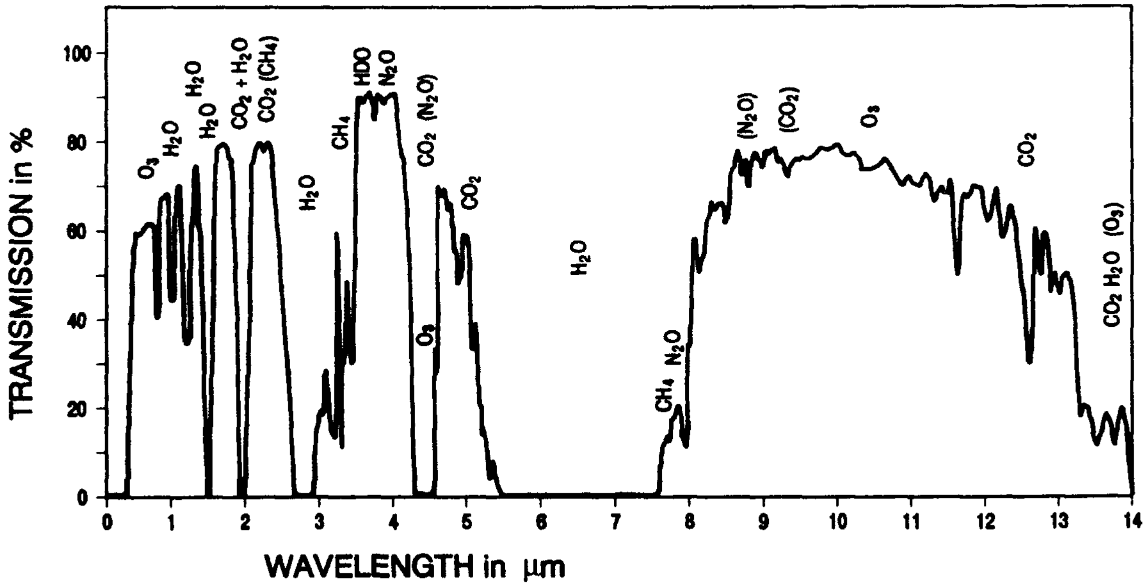

Fig. 2.1: Atmospheric transmission for a horizontal path length of 2 km, absolute humidity 8.5 gm^{-3}, visibility 15 km, and rural aerosol.

Fig. 2.2 shows the new capabilities of LOWTRAN 7 in the UV region. Given is the calculated atmospheric spectral transmission between 0.2 and 0.4 µm wavelength for a horizontal path length of 4 km at sea level for a visibility of 5 km and rural aerosol. Also shown in Fig. 2.2 are the different attenuating components essential in this spectral region.

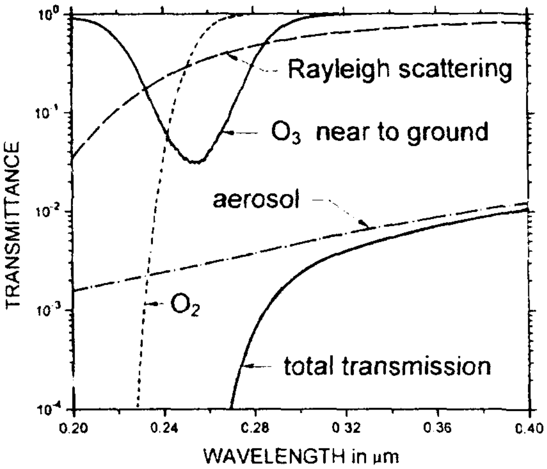

Fig. 2.2: Atmospheric transmittance calculated using LOWTRAN 7 for a horizontal path length of 4 km at sea level, rural aerosol, and visibility of 5 km.

Fig. 2.3 gives a LOWTRAN 7 sample calculation for different horizontal path lengths in the far infrared [12]. Markedly is the strong attenuation beyond 14 µm. Fig. 2.4 shows a comparison of LOWTRAN 6 and 7 calculations with measurements of the Technion, Israel [12]. It is obvious that LOWTRAN 7 results are much closer to the measurements than LOWTRAN 6.

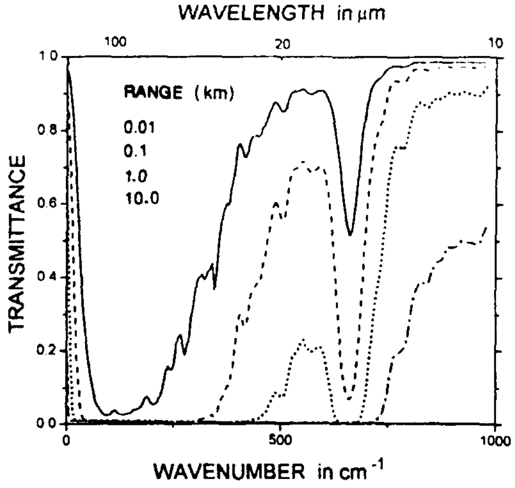

Fig. 2.3: Atmospheric transmittance for horizontal path lengths varying from 0.01 to 10 km at sea level (Midlatitude Summer atmosphere, 23 km rural aerosol) [12].

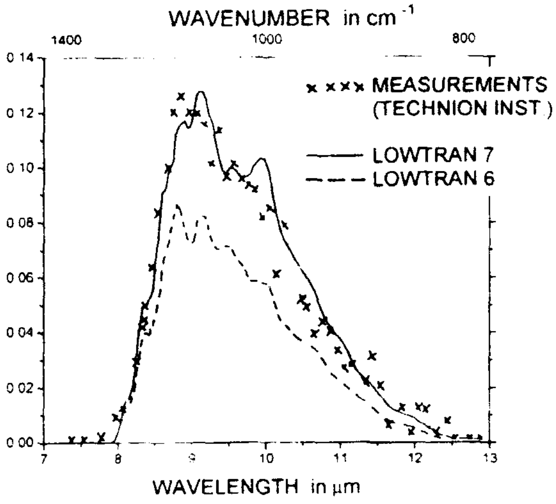

Fig. 2.4: Comparison of LOWTRAN 6 and 7 calculations with a 8.6 km atmospheric transmittance measurement in the 7 - 14 µm region at sea level (for recorded meteorological conditions) [12].

2.2. Fundamentals of LOWTRAN 7

The LOWTRAN 7 computer program allows the user to calculate the atmospheric transmittance, atmospheric background thermal radiance, single-scattered and earth-reflected solar and lunar radiance, direct solar irradiance, and multiple-scattered solar and thermal radiance at a spectral resolution of 20 cm^{-1} in steps of 5 cm^{-1} from 0 to 50,000 cm^{-1}; i.e. for wavelengths in excess of 0.2 µm. The total atmospheric transmittance is treated as the product of the individual transmittances due to:

1. molecular absorption,
2. molecular scattering,
3. aerosol, fog, rain, and cloud extinction (scattering and absorption).

The transmittance due to molecular absorption is further subdivided into more components and is now calculated as the product of the separate transmittances due to:

1. H_2O, O_3, CO_2, N_2O, CO, CH_4, O_2, NO, NO_2, NH_3, SO_2, HNO_3,
2. H_2O continuum (over the entire spectrum),
3. N_2 continuum (in the 2000 - 2700 cm^{-1} region).

A selection of atmospheric aerosol models is given in LOWTRAN 7; these are divided into altitude regions corresponding to the boundary layer (0 - 2 km), troposphere (2 - 10 km), stratosphere and upper atmosphere (10 - 120 km). The boundary layer models include rural, urban, maritime, tropospheric, a Navy maritime, and a desert aerosol. Representative aerosol models also are included for the troposphere and upper atmospheric regions. Two fog models are included together with a selection of rain and cloud models. The user also has the option to substitute other aerosol models or measured values.

The six reference atmospheric geographical and seasonal models for tropical, midlatitude summer and winter, subarctic summer and winter, and the U.S. standard atmosphere, which provided temperature, pressure, H_2O, and O_3 concentrations as a function of altitude from 0 to 100 km in LOWTRAN 6, have now been extended in LOWTRAN 7 to include density and N_2O, CO, and CH_4 mixing ratio variability with altitude. The remaining six molecular species are each described by a single vertical profile. When adding meteorological data to LOWTRAN 7, the user is given much greater flexibility in the choice of units that will be accepted by the program. Spherical earth geometry is assumed, and refraction and earth curvature effects are included in the atmospheric slant path calculations. The main structure of the LOWTRAN 7 code split up into different subroutines is shown in Fig. 2.5. A detailed explanation of the capabilities of these subroutines is given in [8].

2.3 Transmission Functions

In LOWTRAN 7 a single parameter band model which describes the molecular absorption component of the atmospheric transmittance is used [9]. For this approach, a double exponential transmission function is assumed where the average transmittance τ over a 20 cm^{-1} spectral interval is given for a center wavenumber υ by

$$\tau(\upsilon) = \exp\left[-C(\upsilon)\,U(P/P_0)^n(T_0/T)^m\right]^a \qquad (2.1)$$

where the parameters C, a, m, and n were determined from line-by-line calculations using FASCODE 2 [10] with the HITRAN 86 [11] molecular line parameter data base where the results were degraded in resolution to 20 cm^{-1} (full width at half maximum). Average values of a, m, and n were determined for discrete spectral regions for each of the following molecular species: H_2O, CO_2, O_3, N_2O, CO, CH_4, and O_2 as well as the trace gases NO, NO_2, NH_3 and SO_2.

Separate transmission functions are used for each of the molecular species in LOWTRAN 7, allowing the user the option of varying the relative mixing ratios of the gases, which was not possible with LOWTRAN 6 and its predecessors. Treating the transmittances of each molecule separately should also improve the accuracy of LOWTRAN in overlap regions between strong absorption bands of different molecules: e.g., CO_2 and N_2O in the 4.5 μm region.

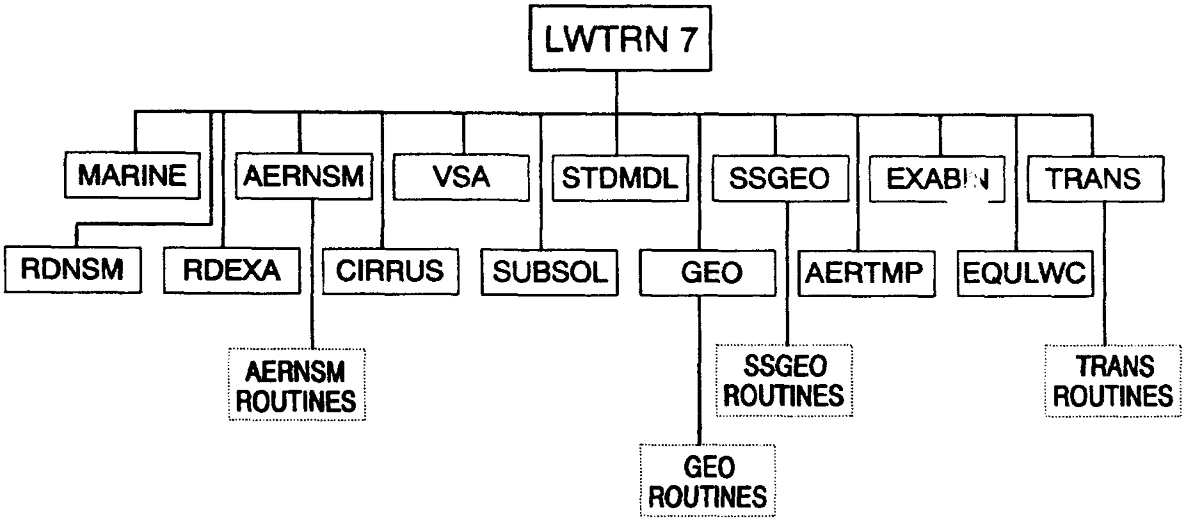

Fig. 2.5: LOWTRAN 7 main program structure. The boxes enclosed by dashes are modules of subroutines for calculations of non-standard models [8].

2.4 Boundary Layer Aerosol Models

The boundary layer aerosol models include those representative of rural, urban, maritime, and desert environments, as well as fog models. Most of these models include a dependence on the relative humidity, and in the case of the maritime and desert models a dependence on the prevailing winds.

The effects of relative humidity become increasingly important as the atmosphere approaches saturation. The effect of increasing relative humidity is for the particles to grow through the accretion of water, which also means a change in the composition and effect refractive index of the aerosol particle.

The size distributions of atmospheric particulates are commonly represented by analytic functions. The most commonly used of these are the log-normal distribution:

$$n(r) = \frac{dN(r)}{dr} = \sum_{i=1}^{2} \frac{N_i}{\ln(10) r \sigma_i \sqrt{2\pi}} \exp\left[-\frac{(\log r - \log r_i)^2}{2\sigma_i^2} \right] \tag{2.2}$$

where N(r) is the cumulative number density of particles of radius r, σ_i is the standard deviation, r_i is the mode radius, and N_i is the total number for the i^{th} mode. The mode number here is 2.

Typical characteristics and sizes for the boundary layer models are given in Table 2.1, [13], where the size parameters refer to the log-normal size distribution (Eq. 2.2). The precise values of the parameters will change with variations in the relative humidity, and in the case of maritime aerosols with variations in wind speed and duration of time since the air mass was over land [14].

Aerosol Model	Size Distribution			Type
	N_i	r_i	σ_i	
Rural	0.999875 0.000125	0.03 0.5	0.35 0.4	Mixture of Water Soluble and Dust-Like Aerosols
Urban	0.999875 0.000125	0.03 0.5	0.35 0.4	Rural Aerosol Mixtures with Soot-Like Aerosols
Maritime Continental Origin	0.99	0.03	0.35	Rural Aerosol Mixture
Oceanic Origin	0.01	0.3	0.4	Sea Salt Solution in Water
Tropospheric	1.0	0.03	0.35	Rural Aerosol Mixture

Table 2.1: Representative sizes and compositions for boundary layer aerosol models.

Given the size distribution and complex refractive index for the atmospheric aerosols their radiative properties can be determined from Mie scattering calculations. Fig. 2.6 illustrates the extinction coefficients for the rural aerosol model as a function of wavelength for several relative humidities. Fig. 2.7 shows the angular scattering function (often referred to as the phase function) for marine aerosols for several wavelengths.

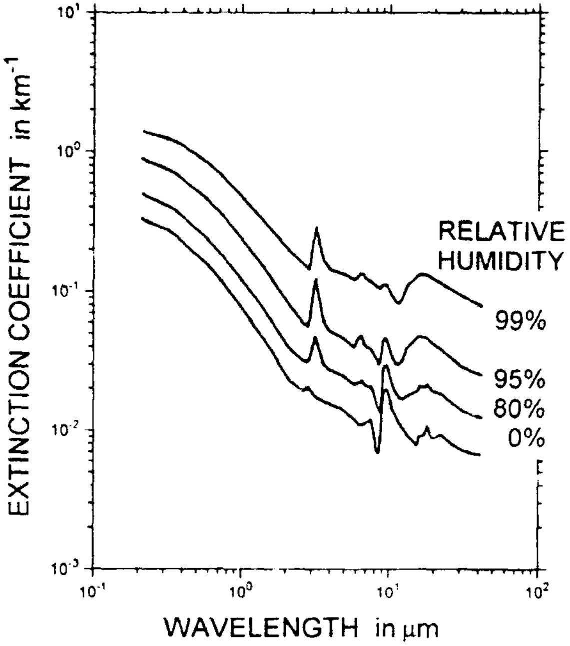

Fig. 2.6: Extinction coefficients vs wavelength for the rural aerosol model with different relative humidities and a number density of 15.0 cm^{-3}.

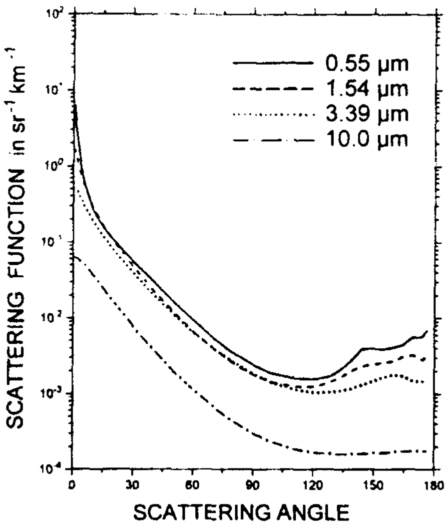

Fig. 2.7: Angular scattering function for the Shettle & Fenn (1979) maritime aerosol model with a relative humidity of 80 % and a number density of 4.0 cm^{-3} for several wavelengths.

The aerosol, fog, rain, and cloud model absorption and scattering coefficients in LOWTRAN 6 were extended to the millimeter wavelength region in LOWTRAN 7. In addition, the Navy maritime aerosol model was modified to improve its wind speed dependence for the large particle component. The background stratospheric model also has been updated to utilise more recent refractive index and size distribution measurements.

A new desert aerosol model has been added, which includes a wind speed dependence. LOWTRAN 7 will now modify the aerosol altitude profiles to account for elevated ground level cases.

The five cloud models contained in FASCODE 2 have been added to LOWTRAN 7; these correspond to cumulus, stratus, alto-stratus, stratocumulus, and nimbostratus. Two new cirrus models with more realistic wavelength dependences and separate scattering, absorption, and asymmetry parameters also have been incorporated into LOWTRAN 7.

2.5 Radiance calculations

LOWTRAN 7 also offers the possibility of radiance calculations including atmospheric self-emission, solar and/or lunar radiance single scattered into the path, direct solar irradiance through a slant path to space, and multiple scattered solar and/or self-emission radiance into the path. Fig. 2.8 show the impact of multiple scattering on the radiance looking straight down from 20 km for a solar zenith angle of 60°.

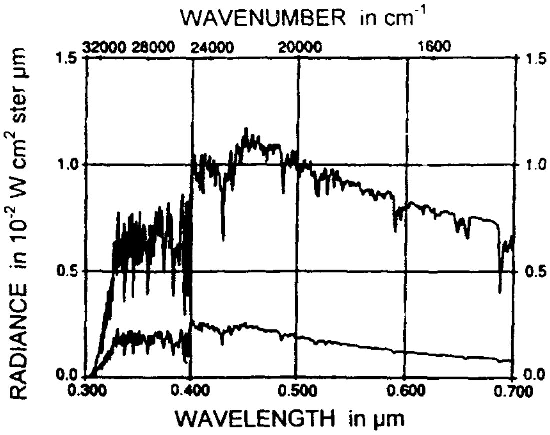

Fig. 2.8: Slant-path radiance calculation for an observer at 20-km altitude looking straight down. The solar zenith angle is 60 deg. The 1976 U.S. standard atmosphere is used with the rural aerosol model. The lower curve is the radiance due to single scatter and the upper curve includes multiple scatter, thus emphasizing its importance.

2.6 LOWTRAN Input Options

Table 2.1 gives a summary of LOWTRAN inputs and relevant options.

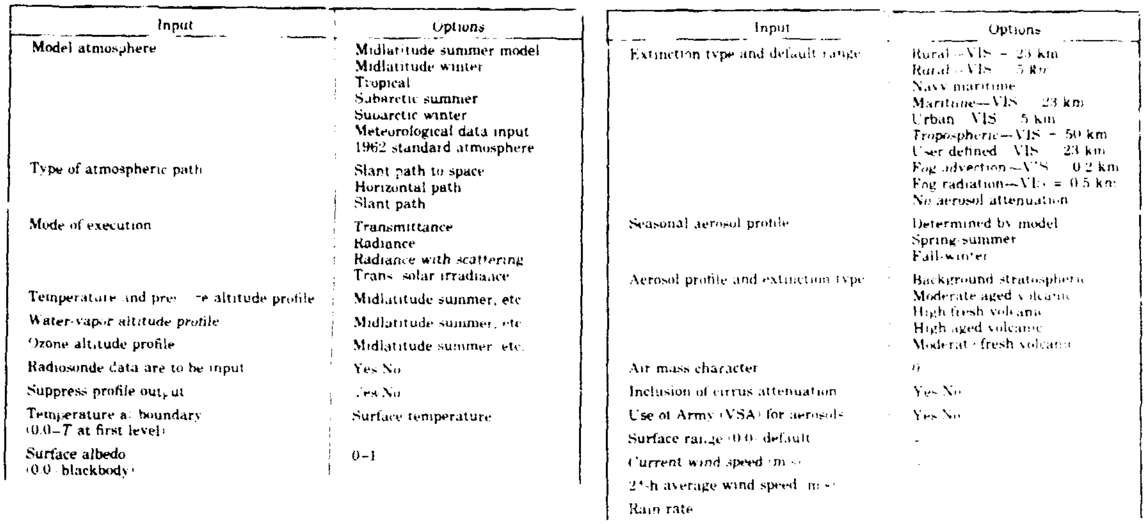

Input	Options
Model atmosphere	Midlatitude summer model Midlatitude winter Tropical Subarctic summer Subarctic winter Meteorological data input 1962 standard atmosphere
Type of atmospheric path	Slant path to space Horizontal path Slant path
Mode of execution	Transmittance Radiance Radiance with scattering Trans. solar irradiance
Temperature and pressure altitude profile	Midlatitude summer, etc
Water-vapor altitude profile	Midlatitude summer, etc
Ozone altitude profile	Midlatitude summer, etc.
Radiosonde data are to be input	Yes/No
Suppress profile output	Yes/No
Temperature at boundary (0.0–T at first level)	Surface temperature
Surface albedo (0.0 blackbody)	0–1
Extinction type and default range	Rural—VIS = 23 km Rural—VIS = 5 km Navy maritime Maritime—VIS = 23 km Urban—VIS = 5 km Tropospheric—VIS = 50 km User defined—VIS = 23 km Fog advection—VIS = 0.2 km Fog radiation—VIS = 0.5 km No aerosol attenuation
Seasonal aerosol profile	Determined by model Spring-summer Fall-winter
Aerosol profile and extinction type	Background stratospheric Moderate aged volcanic High fresh volcanic High aged volcanic Moderate fresh volcanic
Air mass character	0
Inclusion of cirrus attenuation	Yes/No
Use of Army (VSA) for aerosols	Yes/No
Surface range (0.0 default)	-
Current wind speed (m/s)	-
24-h average wind speed (m/s)	
Rain rate	

Table 2.1: LOWTRAN inputs and relevant options.

3. MODTRAN Atmospheric Transmittance Code

MODTRAN (MODerate resolution LOWTRAN) [16] is a radiative transfer model with a spectral resolution of 2 cm^{-1} (FWHM) which has been developed based on the LOWTRAN 7 model. MODTRAN is identical to LOWTRAN except it contains an other band model. In MODTRAN the molecular transmittance τ from lines originating within a spectral interval $\Delta\nu$ is determined according to

$$\tau = \left(\frac{2}{\Delta\upsilon}\int_0^{\Delta\upsilon/2} e^{-sug(\upsilon)}\,d\upsilon\right)^n , \tag{3.1}$$

where g (υ) is a line shape function, u is the absorber amount, and s and n are functions of the absorption coefficient. The latest version is MODTRAN2, released 1992. Fig. 3.1 shows a comparison of MODTRAN and LOWTRAN calculations for a slant path from 5 to 10 km height. Initial validation studies, based on comparisons to FASCODE 2, indicate no significant discrepancies at 2 cm^{-1} resolution, FWHM. MODTRAN can be used to calculate atmospheric radiance at upper altitudes, specifically for any path in which the LTE (local thermodynamic equilibrium) approximation is valid. Molecular absorption is modelled as a function of both temperature and pressure for twelve molecular species - water vapor, carbon dioxide, ozone, nitrous oxide, carbon monoxide, methane, oxygen, nitric oxide, sulf dioxide, nitrogen dioxide, ammonia and nitric acid. MODTRAN also has multiple scattering contributions.

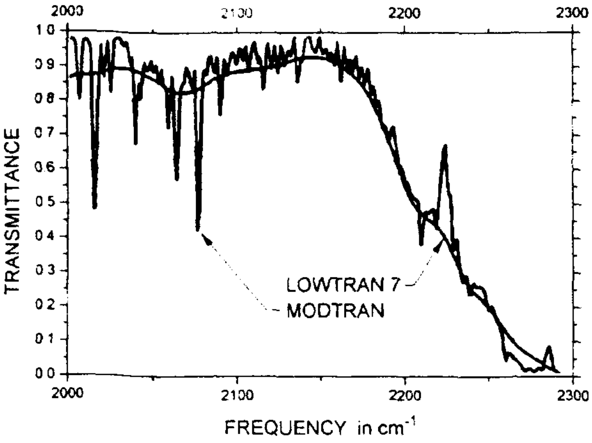

Fig. 3.1: Atmospheric transmittance for a slant path from 5 to 10 km at 15° from zenith and through the U.S. standard atmosphere with no haze. The solid curve was calculated with MODTRAN at 2 cm^{-1} spectral resolution, and the dotted curve with the regular LOWTRAN 7 at 20 cm^{-1} resolution [16].

4. FASCODE Atmospheric Transmission Code

For studies involving the propagation of very narrow optical band width radiation, for example, lasers, the high resolution atmospheric transmission code FASCODE, also developed and maintained by the Phillips Laboratory, Geophysics Directorate, Hanscom AFB, Ma., can be applied. Characterization of the aerosol and molecular continuum in FASCODE is much the same as that for LOWTRAN. The spectral molecular transmission is calculated by a line-by-line monochromatic calculation method. These resolution calculations require a detailed database e. g. HITRAN of spectral-line parameters. The Geophysics Directorate is the center for establishing and maintaining the HITRAN database [11].

4.1 HITRAN Data Base

The molecular spectroscopic database, known under acronym HITRAN, has been in existence for two decades to provide the necessary fundamental parameters to represent molecular properties in atmospheric spectroscopic analysis. The Phillips Laboratory, Geophysics Directorate is the center for relevant work concerning this data base. Fig. 4.1 gives an overview of absorption line strengths of a subset of HITRAN gases versus wavenumber up to 1000 cm^{-1}. The HITRAN 1986 database is a line-by-line compilation of 348,043 spectral-line parameters (e.g., line position, strength, half-width, lower energy level, etc.) representing 28 different molecules of atmospheric importance [15]. Table 4.1 shows the parameter format used to organize the data base. Each molecule is identified by a number and a set of quantities (see Table 4.1 and descriptions there). A new edition of HITRAN became available in March 1992 [18] with major updates. This current edition contains over 70 Mbyte of high-resolution data for transitions of 31 species and their atmospheric significant isotopic variants. It is available also on optical CD-ROM.

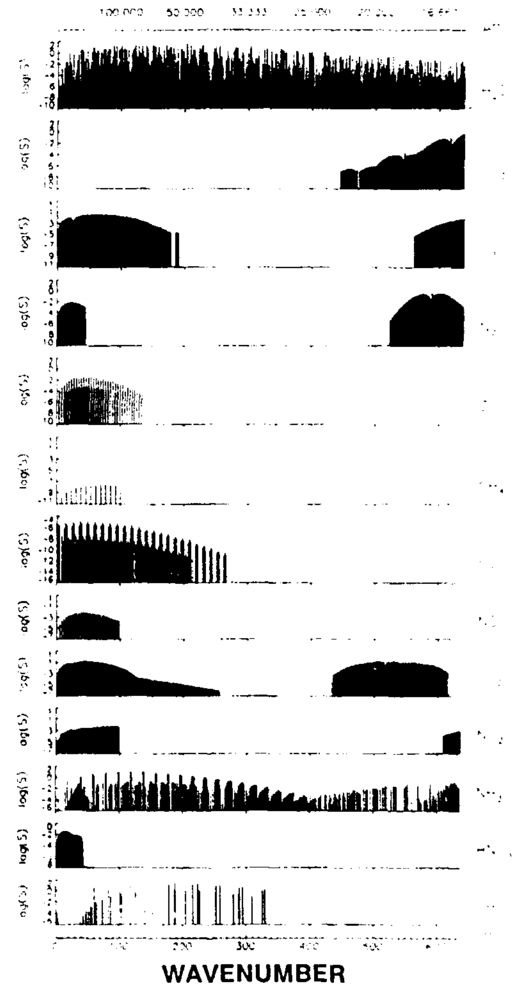

Fig. 4.1: Absorption line strengths of AFGL gases versus wavenumber up to 1000 cm^{-1}.

```
 iso   Frequency  Intensity
 Mo        ν           S'          R        γ    γs        E"     n  δ or y  v' v"     Q'        Q"      IER  IREF
-------------------------------------------------------------------------------------------------------------------
 31   800.276500 4.316E-25 3.777E-07.0599.0000 1162.00600.76 0.00000  2   12418 6   2517 9    382   0
281   800.287000 2.270E-23 4.717E-05.0750.0000 1483.94700.50 0.00000  2   117 7     18 7      381   0
101   800.301900 4.680E-23 2.421E-07.0630.0000  105.93600.50 0.00000  2   1 8 4 4   - 9 3 7   - 84  0
 31   800.304700 1.286E-24 1.131E.05.0618.0000 1636.93510.76 0.00000  2   159 951   58 850    382   0
 31   800.322500 1.243E-23 1.274E-06.0610.0000  720.65800.76 0.00000  2   11615 1   1614 2    382   0
101   800.322700 1.840E-22 2.195E-06.0630.0000  277.86000.50 0.00000  2   126 224   -25 125   - 84  0
 23   800.326900 5.380E-26 2.668E-05.0793.1103 1326.41920.75 0.00000  8   3              R 13  186   0
271   800.332030 1.100E-22 3.212E-02.1000.0000 2354.24000.50 0.00000 19   14             4  8  382   0
101   800.361600 1.910E-22 2.278E-06.0630.0000  277.80700.50 0.00000  2   126 224   +25 125   + 84  0
 31   800.379600 6.380E-24 6.554E-07.0602.0000  707.21200.76 0.00000  2   11515 1   1514 2    382   0
101   800.416400 5.300E-23 1.025E-05.0630.0000  851.01800.50 0.00000  2   145 244   +44 143   + 84  0
271   800.416750 1.330E-22 2.035E-02.1000.0000 2221.36110.50 0.00000 19   14             3  8  382   0
 31   800.434100 4.273E-25 2.225E-05.0618.0000 1982.04700.76 0.00000  3   2501040   49 941    382   0
 22   800.444000 6.390E-26 1.396E-04.0653.0846 1844.81880.75 0.00000  8   3              R 38  186   0
101   800.447000 5.180E-23 1.002E-05.0630.0000  851.04100.50 0.00000  2   145 244   -44 143   - 84  0
 21   800.451200 3.210E-26 1.731E-05.0661.0872 2481.56150.75 0.00000 14   6              P 37  186   0
-------------------------------------------------------------------------------------------------------------------
```

FORMAT (I2, I1, F12, 1P2E10.3, 0P2F5.4, F10.4, F4.2, F8.5, 2I3, 2A9, 3I1, 3I2)
= 100 characters per transition

This format corresponds as follows:

Mo	—I2	—Molecule number
iso	—I1	—Isotope number (1—most abundant, 2—second, etc.)
ν	—F12.6	—Frequency in cm^{-1}
S'	—E10.3	—Intensity in cm^{-1}/(molecules cm^{-2}) @ 296 K
R	—E10.3	—Transition probability in debyes^2 (presently lacking internal partition sum)
γ	—F5.4	—Air-broadened half-width (HWHM) in cm^{-1}/atm^{-1} @ 296 K
γ_s	—F5.4	—Self-broadened half-width (HWHM) in cm^{-1}/atm^{-1} @ 296 K
E''	—F10.4	—Lower-state energy in cm^{-1}
n	—F4.2	—Coefficient of temperature dependence of air-broadened half-width
y	—F8.5	—Shift of transition due to pressure (presently empty; some coupling coefficients inserted)
v'	—I3	—Upper-state global quanta index
v''	—I3	—Lower-state global quanta index
Q'	—A9	—Upper-state local quanta
Q''	—A9	—Lower-state local quanta
IER	—3I1	—Accuracy indices for frequency,* intensity, and half-width
IRef	—3I2	—Indices for lookup of references for frequency, intensity, and half-width (not presently used)

Table 4.1: Example of spectroscopic data contained in the 1986 HITRAN data base [15].

4.2 Line-by-Line Computation

FASCODE uses a special form to calculate the optical depth (extinction coefficient times path length) k(υ) as a function of wavenumber υ, assuming superposition of the contributions from individual spectral transitions, given by

$$k(\upsilon) = \upsilon \tanh(hc\upsilon / 2kT) \sum_i W_i S_i(T)\left[f(\upsilon, \upsilon_i) + f(\upsilon, -\upsilon_i)\right] \tag{4.1}$$

where W_i is the column density for the molecular species i (mol cm^{-2}) with transition wavenumber υ_i (cm^{-1}) and S_i (mol cm^{-2}) is the intensity at temperature T, approximate to the FASCODE line shape $f(\upsilon, \upsilon_i)$. The necessary molecular line parameters are taken from the HITRAN data base, see Table 4.1.

4.3 FASCODE 2 Calculations

FASCODE 2 is available also from ONTAR Corp. Brookline, Ma., USA, as PC-Version. This is a menu-driven package that allows line file generation, creation of the input file for FASCODE, execution of the transmission calculations, and subsequent plotting of results. Fig. 4.2 shows the spectral transmission for an entire range of 850 to 1100 cm^{-1} of a sample calculation for a 100 km long slant path from an altitude of 6.096 km down to ground. Fig. 4.3 shows the spectral transmission in the vicinity of the P(20) line of the CO_2 laser (10.591 µm) for the same conditions and Fig. 4.4 shows the spectral transmission in the vicinity of the P(20) ^{13}C-isotope-based CO_2 laser (11.15 µm). It is obvious that at 11.15 µm the transmission is markedly better than at 10.591 µm.

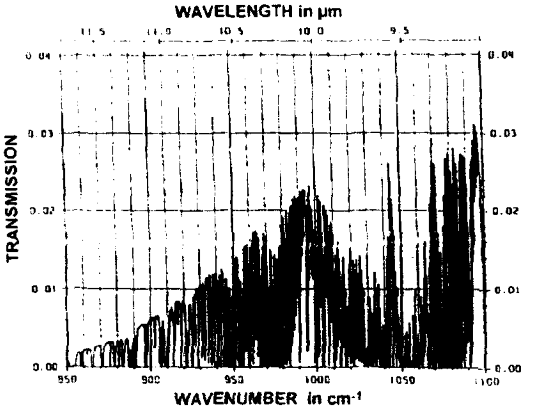

Fig. 4.2: FASCODE transmission estimates in the 850 to 1100 cm^{-1} range for a 100 km slant path from an altitude of 6.096 km down to ground.

Molecular profile	Midlatitude summer
Path description	6.096 km - ground
Path length	100 km
Path type	Short
Aerosol profile	Maritime, 23 km visibility
No clouds or rain	

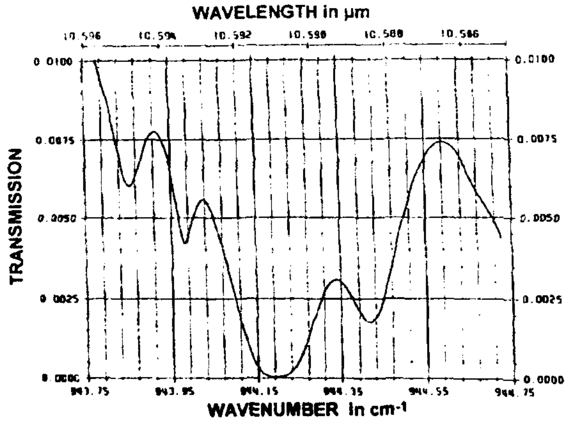

Fig. 4.3: FASCODE transmission estimates for the same conditions as in Fig. 4.2 in the vicinity of 10.591 µm (CO_2 laser, P(20) line).

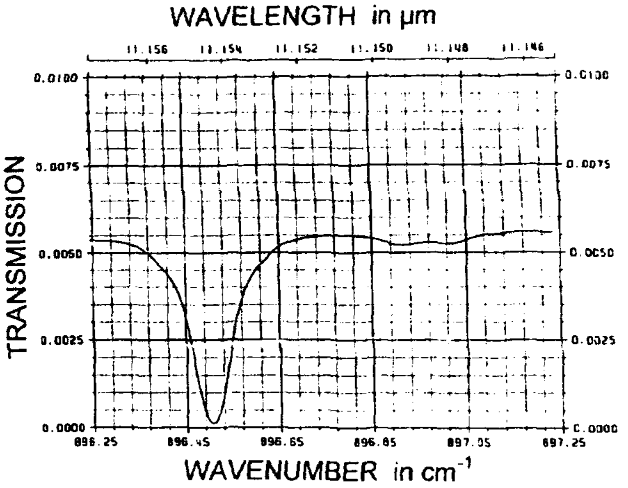

Fig. 4.4: FASCODE transmission estimates for the same conditions as in Fig. 4.2 in the vicinity of 11.15 µm (^{13}C-isotope-based CO_2 laser, P(20) line).

5. Electro-Optical Systems Atmospheric Effects Library (EOSAEL)

The Electro-Optical Systems Atmospheric Effects Library (EOSAEL) is a comprehensive library of computer codes specifically designate to simulate tactical battlefield situations. EOSAEL has been designed and steadily updated by the U.S. Army Atmospheric Sciences Laboratory, White Sands, NM, which is now the Army Research Laboratory. EOSAEL is a state-of-the-art computer library comprised of fast-running theoretical, semi-empirical, and empirical computer programs (called modules) that mathematically describe various aspects of electromagnetic propagation in battlefield environments. The modules are connected through an executive routine but often are exercised individually. The modules are more engineering oriented than first-principles. The philosophy is to include modules that give reasonably accurate results with the minimum in computer time for conditions that may be expected on the battlefield. EOSAEL models comprise clear air transmission, transmission through natural and man-made obscurants, turbulence, multiple scattering, contrast and contrast transmission, and others.

The latest Version of EOSAEL is EOSAEL 92 [20] which contains unchanged, upgraded, obsolete, and new models compared to the predecessor EOSAEL 87 [19]. Table 5.1 gives an overview of the present modules and their functions.

EOSAEL 92 is available to U.S. Department of Defence (DoD) specified allied organisations and DoD authorized contractors at no cost from the U.S. Army Research Laboratory.

To give an insight into the capabilities of EOSAEL a sample calculation using the model Plume is performed [21]. This model produces a time series of fire plume images with a time resolution of 1 second for the visual and IR spectral regions. The images are calculated based on spatially simulated variations of wind speed and wind direction, of heat and mass output and of turbulent flows. The "observer" is an imager with a rectangular field of view comprised of an n by m matrix of square pixels and with a defined angular resolution. Fig. 5.1 shows a set of contour plots of visual transmittance for a series of times after the start of a fire.

	Name	Calculations
same as	NMMW	mmW transmission and backscattering
EOSAEL 87	CLTRAN	cloud transmission
"	COPTER	obscuration due to helicopter lofted snow and dust
"	GRNADE	self-screening
"	MPLUME	missile smoke plume obscuration
"	OVRCST	contrast transmission
"	FCLOUD	contrast transmission through clouds
"	ILUMA	natural illumination under realistic weather conditions
"	FASCAT	atmospheric scattering
"	LASS	large area screening systems applications
"	GSCAT	single scattering of visible radiation through Gaussian clouds
"	NOVAE	nonlinear aerosol vaporization and breakdown effects
"	RADAR	millimeter wave system performance
upgraded models	LOWTRAN	atmospheric transmittance and radiance
"	LZTRAN	laser transmission
"	KWIK	munition expenditure
"	XSCALE	natural aerosol extinction
"	TARGAC	target acquisition
"	COMBIC	combined obscuration model for battlefield-induced contaminants
new models	FASCODE	high resolution atmospheric transmittance and radiance
"	NBMSCAT	multiple scattering in near forward direction
"	UVTRANS	ultraviolet transmission

Table 5.1: EOSAEL 92 modules compared to EOSAEL 87 [20].

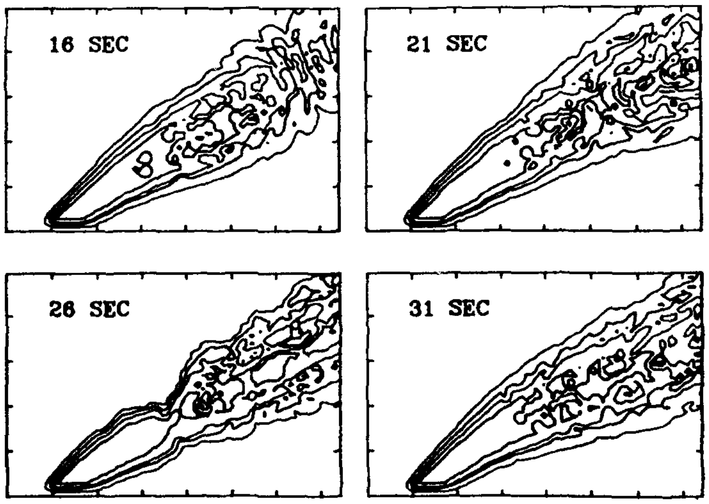

Fig. 5.1: A set of contour plots of transmittance for a series of times after the start of the fire. The contours represent thirty percent changes in transmittance from a minimum of five percent to a maximum of ninety-five percent.

6. NATO InfraRed Air TArget Model NIRATAM

For many military and civilian applications the Infrared (IR) radiative emission from aircraft and missiles must be calculated. NIRATAM (NATO InfraRed Air TArget Model) is a computer model, which predicts IR radiation of an aircraft in its natural surroundings [22].

6.1 Model Description

The model takes into account IR-radiation emitted from different sources:

1. hot engine parts of the tail pipe and the air intakes,
2. combustion gases in the plume, in particular H_2O, CO_2, CO and carbon particles,
3. skin of the airframe, due to
   - thermal emission resulting from aerodynamic heating and internal heat sources,
   - reflected ambient radiation from the sky, the ground and solar reflection.

The importance of these individual components to the total IR radiation depends on the propulsion system, its operational mode, geometry, the temperature and optical properties of the surfaces and flight and ambient conditions. The aircraft is considered in conjunction with the background because not only the fuselage signature is influenced by the surrounding environment but the detectable aircraft signature image is actually its contrast to the background radiation.

NIRATAM determines the influence of:

- atmospheric transmission and emission between target and observer,
- direct observed homogeneous background represented by the sky or the earth or optionally, measured background scenes from imaging sensors can be inserted,
- spectral response and spatial resolution of a sensor.

The NIRATAM code has been developed through international co-operation within NATO Research and Study Group AC/243 (Panel 04/RSG.06). NIRATAM is available for specified users as PC-Version from ONTAR Corp.

Fig. 6.1 shows typical sources of radiation comprising jet aircraft target signature. The relative spectral radiant intensity of the respective components is shown in Fig. 6.2 [1].

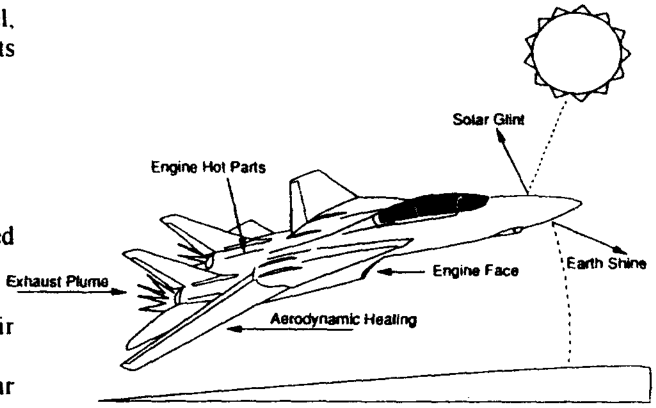

Fig. 6.1.: Typical sources of radiation comprising a target signature.

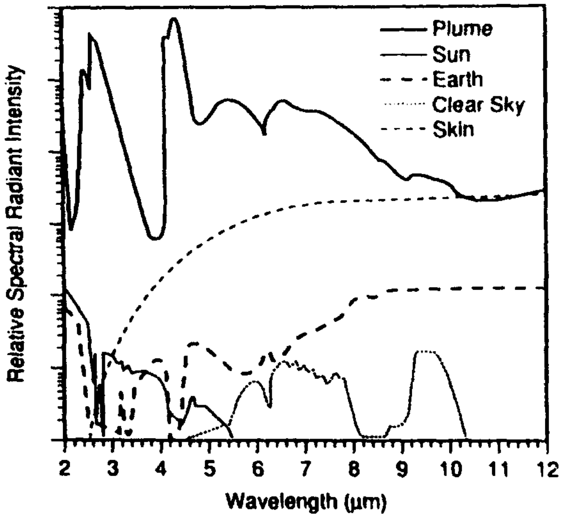

Fig. 6.2: The relative magnitude of typical target signature components versus wavelength for a jet aircraft at 90-deg aspect, M 1.2 airspeed.

6.2 Model Code Structure

An overview of the code structure is given as a simplified flow diagram in Fig. 6.3. As preparation the three-dimensional (3-D) representation of the surface of the air target and the exhaust plume have to be generated.

The main program consists of two essential parts. The first part deals with preparation for the emission/transmission calculations for each pixel in the scene. During initialisation the user specified input data, the plume file, band model data and the polygon file for the target surface are read. The projection of the 3D-target surface on a plane is performed.

After these preparatory stages, the IR radiance of each pixel is calculated. Depending on how the window in the observer plane is subdivided, parallel Lines-of-Sight (LOS) are directed towards the target at intervals specified in the input. The LOS may intercept the target surface, the plume and the hot engine parts or the background, thus drawing the corresponding modules and subroutines. If the LOS interacts with the plume, the path is divided into layers and emission and transmission of the gas layers is calculated using a molecular band model. Spectral co-adding or multiplication of all possible radiation sources and transmission parts results in the total spectral radiance of a LOS. Spectral and spatial integration are performed to obtain a thermal image and the spectral distribution.

Output is available in three basic forms, for line printer and/or data sets, namely:

- thermal Image, as array of pixels, in radiant intensity and equivalent blackbody temperature,
- spectral Radiant Intensity, local LOS and total scene, wavenumber and wavelength scale, all spectra analysed for contribution of each radiating component (skin, engine, plume, atmosphere, background),
- integrated Radiant Intensity in spectral bands and cumulated integrals of all spectra.

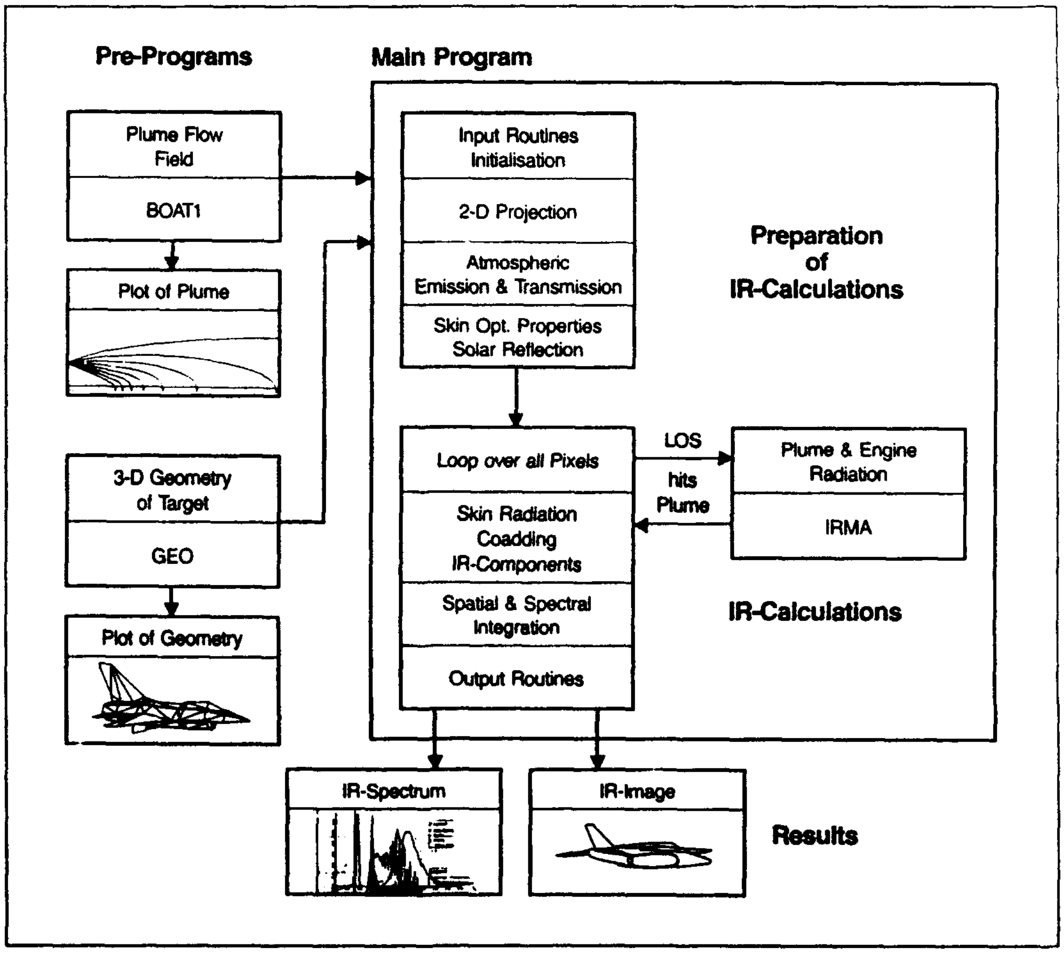

Fig. 6.3: Simplified flow diagram of NIRATAM.

These quantities can be given with and without atmospheric and background effects.

Fig. 6.4 shows a thermal image of a jet airplane calculated with NIRATAM in the spectral band 3 - 5 µm.

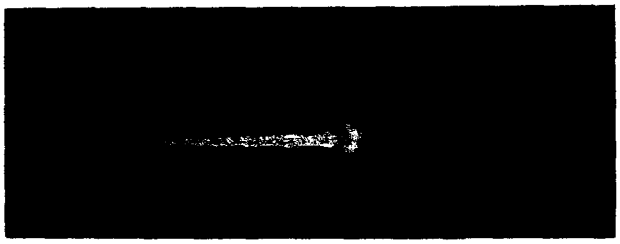

Fig. 6.4: Thermal image calculated by NIRATAM, spectral band 3 - 5 µm, gray-scale representation in radiance values.
Number of rows = 145, number of columns = 450, pixel size = 3 cm x 3 cm, distance = 300 m, altitude = 150 m AGL, speed = 0.6 Mach, aspect angle OTA (Off-Tail-Angle) = 30°, elevation angle = 0°.

6.3 Model Applications

The model can be used for experimental or theoretical studies and more detailed operational research studies, e.g. sensor evaluation against air targets. Typical applications are prediction of the IR-signature for unmeasurable aircraft, e.g. future aircraft under development. The model is also useful in the study of the effectiveness of IR-guided missiles, target detection probability and the result of passive countermeasures, e.g. camouflage and reduction of IR-emission.

7. Range Performance Models

Prediction of range performance of a sensor requires appropriate use of object signatures, background signatures, atmospheric attenuation, hardware performance and human recognition criteria. We concentrate here on thermal imagers (FLIR). Fig. 7.1 shows the different elements necessary for electro-optical system modelling.

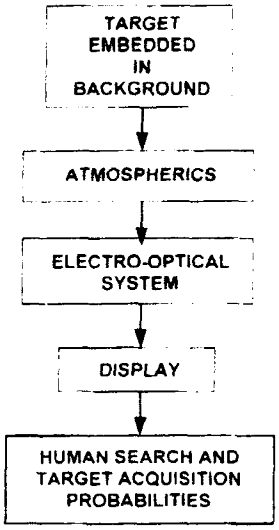

Fig. 7.1: Elements of electro-optical systems modelling.

To characterize the performance of thermal imagers as a whole some quantitative measures have to be introduced.

7.1 Sensor Performance Measures

For a thermal imager the capability to resolve small temperature differences is a quality number. A quantity called noise equivalent temperature difference (NETD) has been introduced as quantitative measure for this. It may be defined as the blackbody target-to-background temperature difference in a standard test pattern that produces a peak-to-rms-noise ratio of unity at the output of the sensor electronic.

NETD is a single value rather than a curve and may be used for rough estimates of the signal-to-noise ratio (SNR) from a FLIR for large targets:

$$SNR \approx \Delta T/NETD, \qquad (7.1)$$

where ΔT is the "received" temperature difference. Most good FLIRs can be expected to have NETD values of a few tenths of a degree Kelvin.

Besides thermal resolution spatial resolution of the thermal imager is an essential factor. This is quantified by the modulation transfer function (MTF) of the imager. This is a sine wave amplitude response to a sine wave input intensity for a particular spatial frequency. The spatial frequency is defined as

$$\upsilon_x = \frac{1}{\theta_x} = 10^3 \frac{R}{T_x} \, (cycles\, mrad^{-1}) \qquad (7.2)$$

where R = observation distance in m
T_X, θ_X = linear (in m) and angular (in rad) period of sine wave input intensity.

Fig. 7.2 gives a qualitative interpretation of the MTF for increasing spatial frequencies.

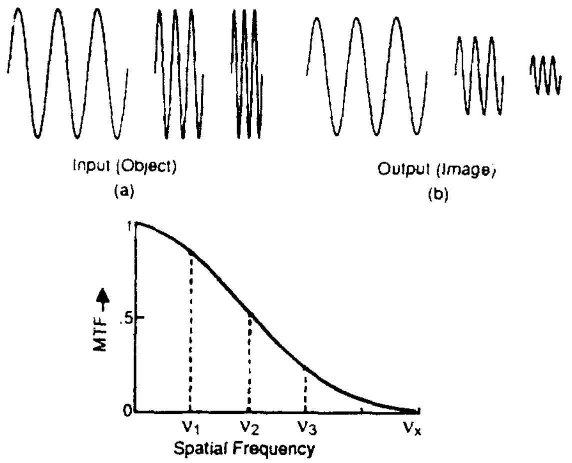

Fig. 7.2: Modulation transfer function. (a) Input signal for three different spatial frequencies, (b) output for the three frequencies, and (c) MTF is the ratio of output-to-input modulation.

In part A of this lecture we introduced the optical transfer function OTF. The relation between the OTF and the MTF can be expressed for horizontally and vertically spatial frequencies υ_X and υ_Y as

$$OTF\left(\upsilon_x,\upsilon_y\right) = MTF\left(\upsilon_x,\upsilon_y\right)\exp\left[i\,PTF\left(\upsilon_x,\upsilon_y\right)\right]. \quad (7.3)$$

This shows that the OTF is a complex function whose modulus is a sine wave amplitude response function (MTF) and whose argument is called phase transfer function (PTF).

The most widely used FLIR system performance measure is the minimum resolvable temperature difference MRTD. This quantity is measured using a test pattern like that shown in Figure 7.3. Blackbody radiation is assumed from the hotter bars and cooler background. Starting from 0, the temperature difference is increased until the largest bar pattern can just be confidently resolved by an observer with normal vision viewing the display. This temperature difference becomes the MRTD value for that lowest spatial frequency. Then the temperature difference is increased again until the next largest bar pattern can be resolved, and so on. In this manner a curve of MRTD versus spatial frequency is mapped out. Typically it would appear as shown in Figure 7.4.

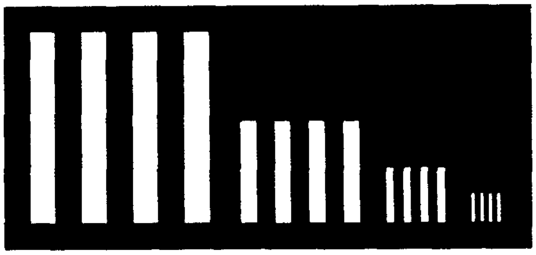

Fig. 7.3: Test pattern for sensor MRTD determination.

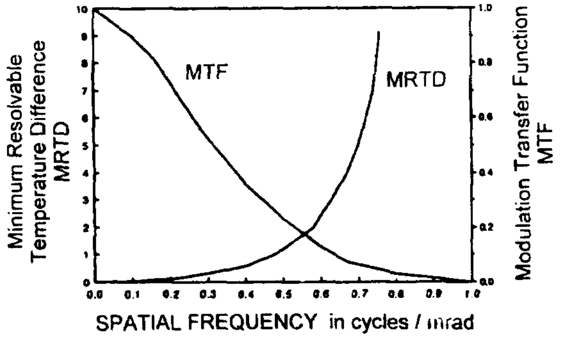

Fig. 7.4: Typical FLIR MTF and MRTD curves.

This procedure shows, that a human observer is involved in this process and that assumptions must be made concerning e.g. the SNR value required for a given probability of recognition.

An exact formula for the MRTD is given in STANAG 4350. Approximately the MRTD as a function of the spatial frequency υ_x can be given as

$$MRTD(\upsilon_x) = \tag{7.4}$$

$$\frac{\pi \cdot k_T \cdot F^2}{\sqrt{14 \cdot \tau_0 W(T) D^*}_{\lambda P}} \frac{r}{MTF_{tot}(\upsilon_x)} \cdot \sqrt{\frac{FOV}{n A_D t_e \eta_{sc}}}$$

with

k_T:	S/N-level of the eye, $k_T = 2.25$,
F:	F-number of the optics,
τ_0:	transmittance of the optics,
W(T):	weighted ($R_n(\lambda)$) differential radiance,
$R_n(\lambda)$:	normalized detector responsivity,
$D^*_{\lambda p}$:	peak spectral. detectivity,
FOV:	field-of-view,
MTF_{tot}:	overall MTF,
n:	number of detector elements,
A_D:	detector area,
t_e:	eye integration time,
η_{sc}:	scan efficiency.

7.2 Static Performance Prediction Methodology [25]

In the late 1950s John Johnson investigated the relationship between the ability of an observer to resolve bar targets through an imaging device and their ability to perform the tasks of detection, recognition, and identification of military vehicles through the same imager, known as the "equivalent bar pattern approach".

In this approach the number of cycles N required across the targets critical dimension was determined for various discrimination tasks. Based on various field tests later, the probability of performing a particular task has been analyzed what let to the so called "target transfer probability function" [1]. Table 7.1 is a combination between the transfer probability and the number of necessary resolvable cycles across a target to perform a specified task. The minimum resolvable temperature difference MNTD (υ_x), see Chapter 7.1, determines the temperature difference ΔT which can be resolved by a human observer for a given spatial frequency υ_x. From this relation the range performance of a FLIR can be calculated according to STANAG 4347.

	Number of Resolvable Cycles across Target		
Probability	*Detection*	*Recognition*	*Identification*
1.0	1.5–3	9–12	18–24
.95	1–2	6–12	12–16
.80	.75–1.5	4.5–6	9–12
.50	.5–1	3–4	6–8
.30	.375–.75	2.25–3	4.5–6
.10	.25–.5	1.5–2	3–4
.02	.125–.25	.75–1	1.5–2

Table 7.1: Number of resolvable cycles across a target and probability to perform a specified task.

For some practical reasons in determining the range performance of a system the spatial frequency dependent MRTD (υ_x) is transferred by pure geometrical considerations to a range R depended function called "minimum necessary temperature difference" MNTD (R) for a specified task and for specified probabilities to perform the task, see Table 7.1. Using this concept the performance ranges of a FLIR can be determined from the calculated or measured MNTD (R) curves for the tasks detection, classification, recognition and identification of a target for a determined probability to perform the task e.g. 50 % or 90 % ATΔ is the effective temperature difference. The relevant ranges are determined by the intersection points of the MNTD (R) curves with the range dependent effective temperature difference curve ΔT(R) seen by the sensor at distance R from the target with initial temperature difference ΔT(0) to the background. The initial temperature difference is reduced as a function of distance caused by atmospheric extinction, see part A of this lecture. This procedure is explained in Fig. 7.5.

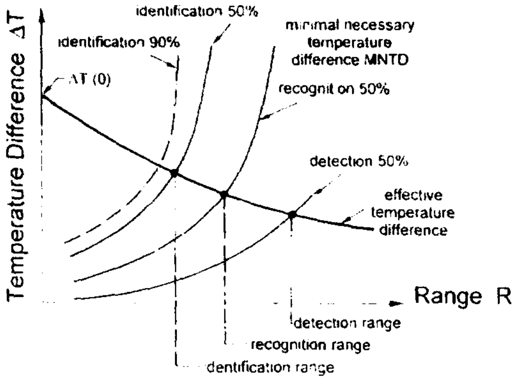

Fig. 7.5: Schematic for range determination of a FLIR from the effective temperature difference ΔT at the observation point and the minimal necessary temperature difference MNTD for detection, classification, recognition, and identification for 50 % probability to perform the task. For comparison the 90 %-curve for identification is given.

7.3 Static Performance Models

The U.S. Army Night Vision and Electro-Optics Directorate (NVEOD) has produced several end-to-end sensor performance models that have been widely used. These include the 1975 static performance model for thermal viewing scanning systems (also widely known as the Ratches model [25]) the 1990 thermal imaging systems performance model (also known as FLIR 90) with a two-dimensional minimum resolvable temperature MNTF representation and the 1992 updated version FLIR 92 which includes also staring infrared sensors [26], sampling effects and three-dimensional noise contributions. FLIR 92 calculated MRTD values are presently validated against measured MRTD values of different sensors. Fig. 7.6 shows the results for measured and calculated horizontal MRTD curves for a staring PtSi camera. The error bars in Fig. 7.6. indicate 95 % confidence intervals for the MRTD measurements [26].

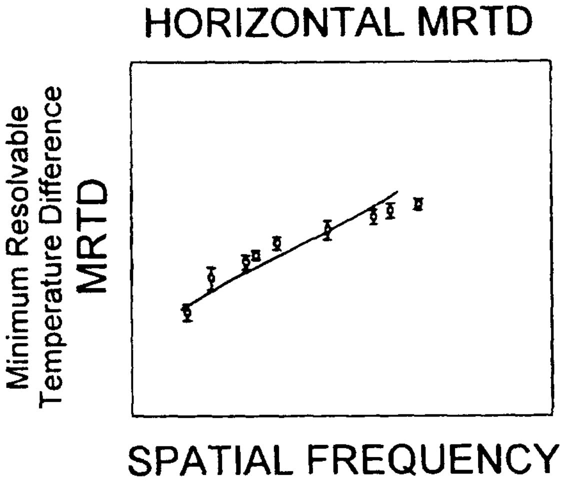

Fig. 7.6: Comparison of FLIR 92 calculated horizontal MRTD curve for a PtSi camera with a measured one. Error bars indicate 95 % confidence intervals for MRTD measurements.

7.4. Range Performance Models

ACQUIRE is as computer program designed by the U.S. Army NVEOD to generate range performance predications based on the sensor performance parameters calculated by the FLIR 92 sensor performance model. This program can also be used as a stand-alone analysis tool, using sensor parameters from other sources such as measured MRTD values.

ACQUIRE uses MRTD data, target characteristics and atmospheric conditions to predict probability of successfully accomplishing various acquisition tasks as a function of range, using Johnson's cycle criteria.

A very similar program which contains sensor performance calculations and range calculations is the TRM 2 model of the FGAN-FfO [27]. The input of this program are specified values for

optics,
image formation,
detectors,
electronics,
frequency boost,
display,
synchronisation and stabilisation,
observer performance,
Johnson criteria and target specification,
atmospheric.

The output is the horizontal, vertical and averaged MRTD as a function of spatial frequency and the range performance (detection, recognition, identification) for specified probability values. Table 7.2 is a typical range performed output of TRM 2 for a sample calculation.

```
          Input File      : HYPO.EIN
          Output File       HYPO.AUS
          Day and Time of Run : 10-MAY-94  09:10:33


     FOV                  [mrad^2] =  87.00 x 52.00
     Target Size            [m^2] =   2.30 x  2.30
     Delta T of Target        [K] =    2.00
     tau0                         =    1.00


     a) Ranges for 50% Probability

     Extinction Coefficient    0.20 km^-1   1.00 km^-1

     Detection                 7862. m      3869. m
     (1.00 lp/target)
     Recognition               3008. m      2276. m
     (3.00 lp/target)
     Identification            1509. m      1309. m
     (6.00 lp/target)

     b) Ranges for 90% Probability

     Extinction Coefficient    0.20 km^-1   1.00 km^-1

     Detection                 5064. m      3127. m
     (1.70 lp/target)
     Recognition               1817. m      1537. m
     (5.00 lp/target)
     Identification             892. m       819. m
     (10.00 lp/target)
```

Table 7.2: Output of FGAN-FfO TRM 2 sample calculation.

8. Conclusions

Modelling tools for atmospheric propagation and system range performance analysis have been developed and steadily improved in resent years based on extensive validations using new high resolution measurements and theoretical adaptations together with enlarged computer capabilities. Nevertheless there is still some work to do in extending these models or establishing new models for further coverage of needs concerning both empirical/statistical planning methods and deterministic operational decision aids.

Acknowledgement

The assistance of L.H. Boehme in drafting most of the Figures is gratefully acknowledged. Parts of this basic lecture has been taken from referenced literature.

Literature

[1] Selby, J.E.A., and McClatchey, R.A., Atmospheric Transmittance from 0.25 to 28.5 μm: Computer Code LOWTRAN 2, AFCRL-TR-72-0745, AD A763721, 1972.

[2] Selby, J.E.A., and McClatchey, R.A., Atmospheric Transmittance from 0.25 to 28.5 μm: Computer Code LOWTRAN 3, AFCRL-TR-75-0255, AD A017734, 1975.

[3] Selby, J.E.A., Shettle, E.P., and McClatchey, R.A., Atmospheric Transmittance from 0.25 to 28.5 μm: Supplement LOWTRAN 3B, AFGL-TR-76-0258, AD A040701, 1976.

[4] Selby, J.E.A., Kneizys, F.X., Chetwynd, Jr., J.H., and McClatchey, R.A., Atmospheric Transmittance/Radiance: Computer Code LOWTRAN 4, AFGL-TR-78-0053, AD A058643, 1978.

[5] Kneizys, F.X., Shettle, E.P., Gallery, W.O., Chetwynd, Jr., J.H., Abreu, L.W. Selby, J.E.A., Fenn, R.W., and McClatchey, R.A., Atmospheric Transmittance/Radiance: Computer Code LOWTRAN 5, AFGL-TR-80-0067, AD A058643, 1980.

[6] Kneizys, F.X., Shettle, E.P., Gallery, W.O., Chetwynd, Jr., J.H., Abreu, L.W. Selby, J.E.A., and Fenn, R.W., Atmospheric Transmittance/Radiance: Computer Code LOWTRAN 6, AFGL-TR-83-0187, AD A137796, 1983.

[7] Kneizys, F.X., Shettle, E.P., Abreu, L.W. Chetwynd, Jr., J.H., Anderson, G.P., Gallery, W.O., Selby, J.E.A., and Clough, S.A., Users Guide to LOWTRAN 7, AFGL-TR-88-0177, AD A206773, 1988.

[8] Kneizys, F.X., Shettle, E.P., Abreu, L.W. Chetwynd, Jr., J.H., Anderson, G.P., Gallery, W.O., Selby, J.E.A., and Clough, S.A., Users Guide to LOWTRAN 7 Model, in preparation.

[9] Pierluissi, J.H., and Maragoudakis, C.E., Molecular Transmission Band Models for LOWTRAN, AFGL-TR-86-0272, AD A180655, 1986.

[10] Clough, S.A., Kneizys, F.X., Shettle, E.P., and Anderson, G.P., Atmospheric Radiance and Transmittance: FASCODE 2, Sixth Conference on Atmospheric Radiation, May 13-16, 1986, American Meteorological Society, Boston, MA, 1987.

[11] Rothman, L.S., Gamache, R.R., Goldman, A., Brown, L.R., Toth, R.A., Pickett, H.M., Poynter, R.L., Flaud, J.-M., Campy-Peyret, C., Barbe, A., Husson, N. Rinsland, C.P., and Smith, M.A.H., The HITRAN Database: 1986 Edition, Appl. Opt., 26: 4058-4097, 1987.

[12] Kneizys, F.X., Anderson, G.P., Shettle, E.P., Abreu, L.W., Chetwynd, Jr., J.H., AGARD Conference Proceedings Nr. 454, 1990.

[13] Shettle, E.P., Models of Aerosols, Clouds and Precipitation for Atmospheric Propagation Studies, AGARD Conference Proceedings No. 454, 1990.

[14] Gathmann, S.G., Optical Properties of the Maritime Aerosol as Predicted by the Navy Aerosol Model, Opt. Eng. 22, 1983.

[15] Rothman, L.S., et. al., The HITRAN Data base: 1986 Edition, Appl. Opt. 26, 1987.

[16] Beck, A., Bernstein, L.S., Robertson, D.C., MODTRAN: A Moderate Resolution Model for LOWTRAN 7, Final Report, Spectral Sciences, Inc., Burlington, MA, 1989.

[17] Anderson, G.P., et. al., MODTRAN2: Suitability for Remote Sensing, SPIE Vol. 1968, 1993.

[18] Rothman, L.S., The HITRAN Molecular Database: Enhancement for Remote Sensing, SPIE Vol. 1968, 1993.

[19] Shirkey, R.C., Duncan, L.D., and Niles, F.E., 1987: EOSAEL87 Volume 1 Executive Summary, ASL-TR-0221-1, U.S. Army Atmospheric Sciences Laboratory, White Sands Missile Range, New Mexico 88002-5501.

[20] Wetmore, A.E., EOSAEL92, Proceedings of the 13th Annual EOSAEL Conference, U.S. Army Research Laboratory, White Sands Missiles Range, New Mexico 88002-5501.

[21] Bruce, D., A realistic model for battlefield fire plume simulation, SPIE Vol. 1486, 1991.

[22] Beier, K., Färber, R., Infrared Radiation Model NIRATAM, Deutsche Forschungsanstalt für Luft- und Raumfahrt, Oberpfaffenhofen, Publ. DLR NE-OE, 1992.

[23] Waldmann, G., Watton, J., Electro-Optical Systems Performance Modelling, Artec House, 1992.

[24] Lloyd, J.M., Thermal Imaging Systems, Plenium Press, New York, 1975.

[25] Ratches, J.A., Static Performance Model for Thermal Imaging Systems, Optical Engineering 15, 1976.

[26] Scott, L., d'Agostino, J., NVEOD FLIR92 Thermal Imaging Systems Performance Model, SPIE Vol. 1689, 1992.

[27] Beutelschiess, J., Wittenstein, W., Schubert, W., Benutzeranleitung für den Computercode zum Thermischen Reichweitenmodell TRM2 des FfO, FGAN-FfO, Schloss Kressbach, Tübingen, Report 1988/89.

Relevance of Decision Aids to the New NATO Strategy

Juergen H. Richter
Ocean and Atmospheric Sciences Division
NCCOSC RDTE DIV 54
53570 SILVERGATE AVE
SAN DIEGO CA 92152-5230
USA

1. SUMMARY

Changes in the North Atlantic Treaty Organizations's (NATO) strategy, force structure and weapons acquisition are reviewed. Propagation assessment and environmental decision aids that mitigate or exploit atmospheric effects are an important component for a smaller, more flexible, and more efficient allied defense. Examples of decision aids are presented and future direction of some of the efforts is discussed.

2. INTRODUCTION

The collapse of the Soviet Union and the dissolution of the Warsaw Pact caused a change of NATO's strategy and force structure. The new strategy emphasizes crisis management rather than countering a monolithic threat. The new force structure relies on smaller forces, increased mobility, lower overall readiness, more flexibility, multi-national forces, and rapid augmentation capability. These changes are coupled with declining defense budgets which, more than ever, make optimum utilization of all resources critically important. Many military systems such as communications, surveillance, navigation, electronic warfare, and weapons rely on electromagnetic (including electrooptical) propagation in the earth's environment. Mitigation and exploitation of environmental effects through proper propagation assessment and the development of environmental decision aids are crucial components in achieving the goals of the post Cold War NATO.

3. NEW NATO STRATEGY

The new NATO strategy is based on a number of documents whose content is summarized in the Initial Planning Guidance for AGARD Technical Panels (1993). Relevant portions are quoted in the following.

NATO's focus has changed from a monolithic threat to crisis management. Emphasis on countering specific threats has shifted to dealing with a wide spectrum of potential risks including the proliferation of weapons of mass destruction and their delivery systems, disruptions in the flow of vital resources, terrorism and sabotage, and ethnic rivalries. Concurrently, NATO member defense budgets are declining steeply. Overall, the European security architecture is more dynamic than during the Cold War era.

The characteristics of NATO's new force structure include: smaller forces, increased mobility, lower overall readiness, more flexibility, multi-national forces, and rapid augmentation capability. There are three basic components: main defense forces, augmentation forces and reaction forces. The main defense and augmentation forces will be at a lower state of readiness than prior to the dissolution of the Warsaw Pact. Reaction forces will be at a higher state of readiness.

Weapons acquisition is also changing. Modern, potent weapons are widely available and widely deployed. Concurrently, NATO members are reducing the quantity of weapons bought. There is less pressure to field advanced technology weapons, fewer resources for research and development, and more competition for scarce resources. However, there is more time to develop systems and produce prototypes. Procurement emphasis will be on low risk, high payoff systems. Cost, producibility, reliability, durability, ease of use, and environmental impact are becoming more important.

What has not changed is the fundamental need for weapons that are superior in terms of lethality, survivability, operability, and flexibility. A wide range of broad aerospace research activities must be continued to enable the development of improved weapons. Primary aerospace research areas should include all weather day-night operations, all weather day-night precision munitions with longer stand-off-ranges, missile defense, better identification systems, better sensors and information processing, and advanced weapons such as directed energy and non-lethal weapons.

What is new is a shift in emphasis on certain force characteristics and capabilities that increase their relative importance in achieving NATO's strategy. Areas of increased attention include: improved flexibility through better command and control and weapons capabilities, better mobility, improved situational awareness, and better training techniques.

Areas of interest, mission needs and related technology thrusts
The following identifies areas of interest and corresponding mission needs/technology thrusts where propagation assessment and decision aids will directly support and enhance the successful accomplishment of the new NATO strategy.

Improved Flexibility
Mission need: Multi-role aircraft with night/all weather capability and wider operating envelopes. *Technology thrusts:* Improved sensors, weapons and interface, displays, and C^3I.

Mission need: More precise night/all weather and stand-off weapons to attack both mobile and fixed targets. *Technology thrusts:* Improved sensors and guidance systems.

Mobility
Mission need: More mobile and deployable tactical air sensors. *Technology thrust:* More effective weapons (sensors, guidance).

Improved Situational Awareness
Mission need: Improved reconnaissance/surveillance systems, sensors, and platforms with emphasis on better resolution, deeper coverage, and all-weather day/night operation. *Technology thrusts:* Multi-spectral sensors, space sensors, and image and signal processing.

Mission need: Identification of friend or foe on the ground and in the air. *Technology thrusts:* Non-cooperative target recognition and multi-spectral target analysis.

Improved Training Techniques
Mission need: Virtual synthetic battlefields for exercises. *Technology thrusts:* Distributed interactive simulation networks, wideband communications, and advanced displays.

In the above areas of interest, propagation assessment and associated decision aids can make significant contributions. For example, night and all weather operations are critically dependent on electromagnetic and electrooptical sensors and their performance in adverse environments. Non-cooperative target recognition and multi-spectral analysis must take the propagation environment into account. Synthetic battlefields would not be realistic if propagation effects like natural and man-made obscurants would not be included. In the following,

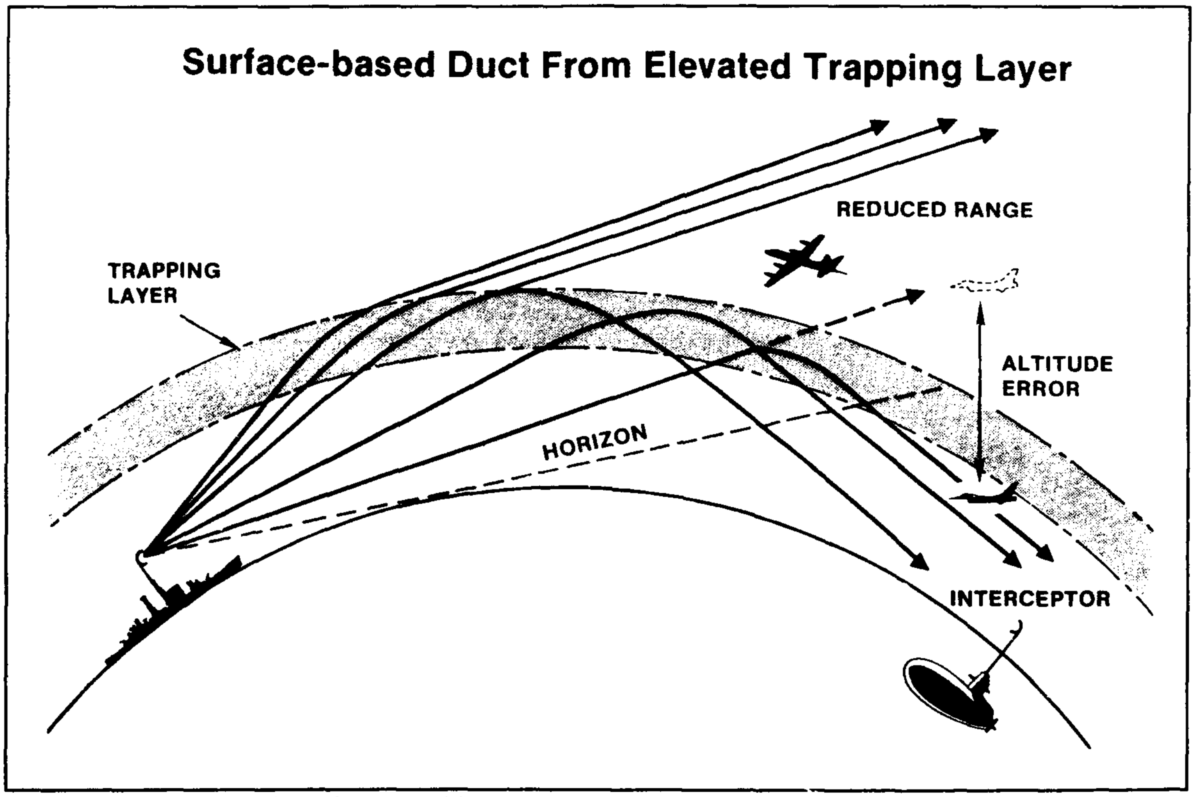

Figure 1. Radio propagation effects caused by atmospheric refractive layers.

examples are given that illustrate the operational importance of propagation effects.

4. PROPAGATION EFFECTS AND DECISION AIDS

Performance assessment and prediction for military systems are critical for their optimum use. This is illustrated for radiowave propagation in the lower atmosphere where, especially over the ocean, refractive layers may cause anomalous propagation conditions. Figure 1 shows how such a surface-based duct may alter the radar coverage for a shipboard radar. The radar signals may propagate far beyond the normal horizon and permit extended coverage. At the same time, signals may be intercepted at unexpectedly large ranges. Above the layer trapping the electromagnetic energy, there may be a "hole" in radar coverage which can be exploited by an intruding aircraft or missile. In the case of a height-finder radar for which altitude is derived from the elevation angle of a narrow-beam radar, significant altitude errors may be encountered. Figure 2 shows the dramatic effect of a surface-based duct on jamming operations and illustrates how knowing the environment can be used to military advantage. Figure 2 consists of two photographs of a shipboard radar display during operations off the southern California coast. The fact that the radar senses the coast line and several islands beyond its "normal" radar horizon indicates the presence of a surface-based duct. The left radar display was taken when a jamming aircraft flew high above the duct but only 26 nmi away. The radar is jammed over a very narrow angle along the radial to the jammer. The right radar display shows the jamming aircraft at more than twice the distance away from the ship but now at a low altitude of only 500 ft which is within the duct. Under standard atmospheric conditions, the ship's radar should not be affected by the jammer since it is far beyond the horizon. However, as one can see from the right side of figure 2, the duct channels the jamming energy very efficiently and the ship's radar is jammed over a wide range of angles (i.e., through radar sidelobes).

The scientific understanding and the ability to model anomalous propagation effects must be made available to the operational military community in a manner that can be readily used. This has been accomplished with the increased availability of computers and display technology. An early example of a stand-alone propagation assessment system for shipboard use is the Integrated Refractive Effects Prediction System (IREPS) (Hitney and Richter, 1976). This system provides radio and radar propagation assessment in a marine environment. Several tactical decision aids (TDAs) were developed. An example of a TDA is shown in figure 3 for determining attack aircraft flight altitudes. The left side of figure 3 schematically displays a radar detection envelope under standard atmospheric conditions. An attack aircraft would avoid detection by flying low. The right side of figure 3 shows the radar detection envelope for ground-based ducting conditions when radar coverage may be greatly extended. Since a low flying aircraft would be detected at long ranges, a flight altitude just above the duct would best facilitate penetration without detection. This TDA and others have become an integral part of military operations and demonstrate the success of translating the effect of complex geophysical conditions into military doctrine.

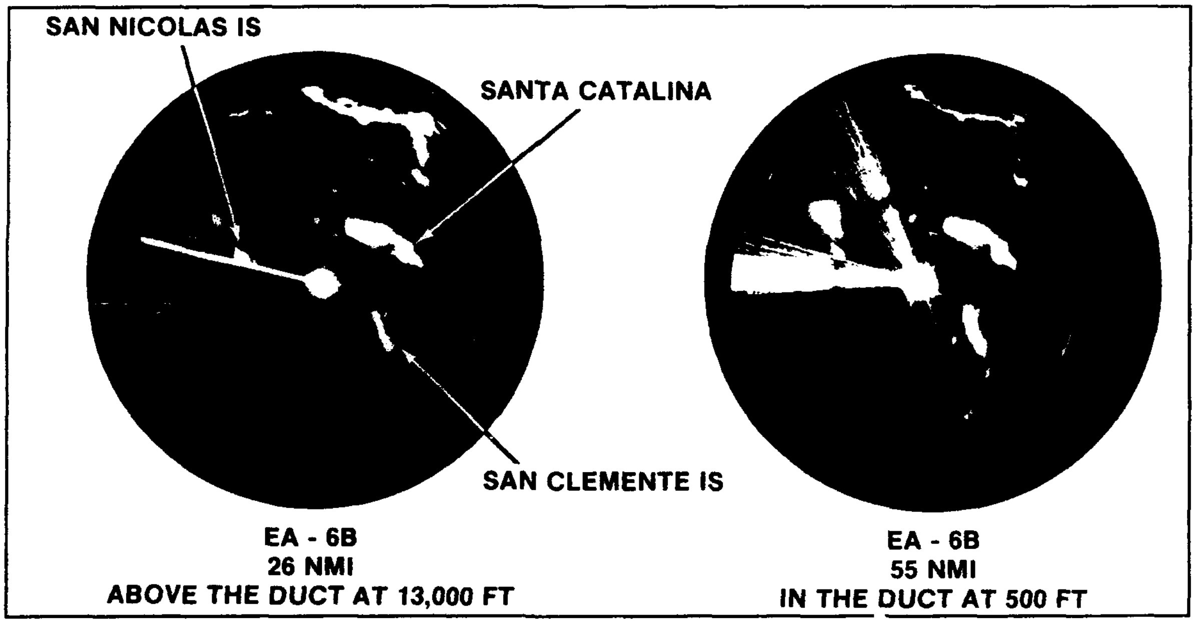

Figure 2. Jamming effectiveness under atmospheric ducting conditions (540 ft surface-based duct).

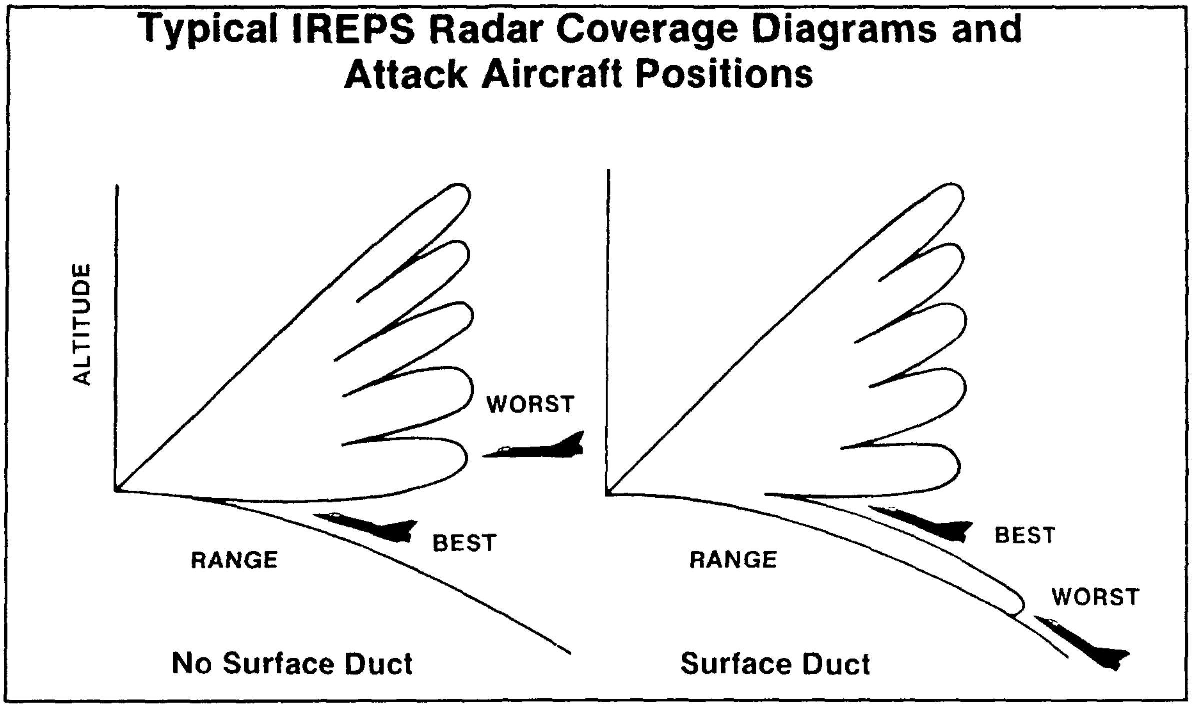

Figure 3. Flight altitudes for attack aircraft for different atmospheric ducting conditions.

Another propagation assessment system became widely used for the assessment of high-frequency (hf) propagation and is called PROPHET (Richter et al., 1977). Long-range propagation for the hf frequency band (2-40 MHz) is determined by the structure of the ionosphere which is influenced by solar radiation. Prediction of hf

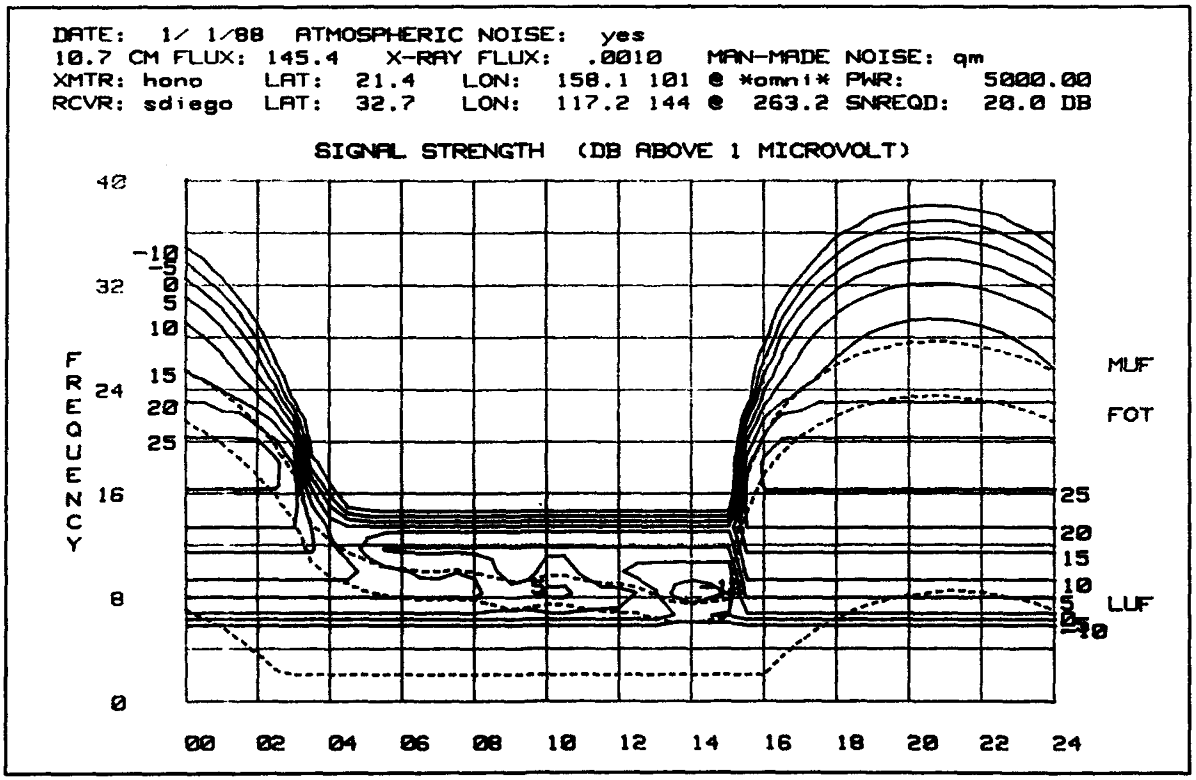

```
DATE:   1/ 1/88  ATMOSPHERIC NOISE:   yes
10.7 CM FLUX: 145.4    X-RAY FLUX:   .0010   MAN-MADE NOISE: qm
XMTR: hono     LAT:   21.4    LON:   158.1 101 @ *omni* PWR:      5000.00
RCVR: sdiego   LAT:   32.7    LON:   117.2 144 @   263.2 SNREQD:   20.0 DB
```

Figure 4. Signal strength contours for high-frequency propagation coverage.

propagation conditions requires a complex mix of analytical and empirical models. An example of a PROPHET product is shown in figure 4. Signal-strength contours are plotted for a 24-hour time period as a function of frequency. This display is for a specific propagation path (Honolulu to San Diego) and depends on solar radiation and ambient electromagnetic noise. The communications operator can determine from this display which frequency to use to suit specific communications requirements (MUF is maximum usable frequency, FOT is frequency of optimum transmission, LUF is lowest usable frequency). The hf-frequency spectrum will remain of importance to the military community in spite of advances in satellite communications for two reasons. First, it remains a back-up in case of satellite communications denial and, second, many countries (let alone terrorists and drug-traffickers) do not have satellite resources and rely on hf. HFDF (high-frequency direction finding) is, therefore, another important and very successful application of PROPHET and its derivatives devoted specifically to this purpose.

While IREPS and PROPHET were developed as stand-alone systems, the complexity of modern warfare necessitated their incorporation into command and control systems. The high-level military decision maker must have real-time access to accurate environmental data which include the propagation environment. An example is Tactical Environmental Support System (TESS) developed by the United States Navy which provides meteorological and oceanographic data to command and control systems (figure 5). TESS accepts forecast models from central sites, receives real-time meteorological and oceanographic satellite data and uses locally generated models and observations. TESS can either provide electromagnetic propagation data and TDAs directly or transfer properly formatted environmental input data to the respective components of command and control systems. Similarly, hf propagation assessment has been incorporated into frequency management systems.

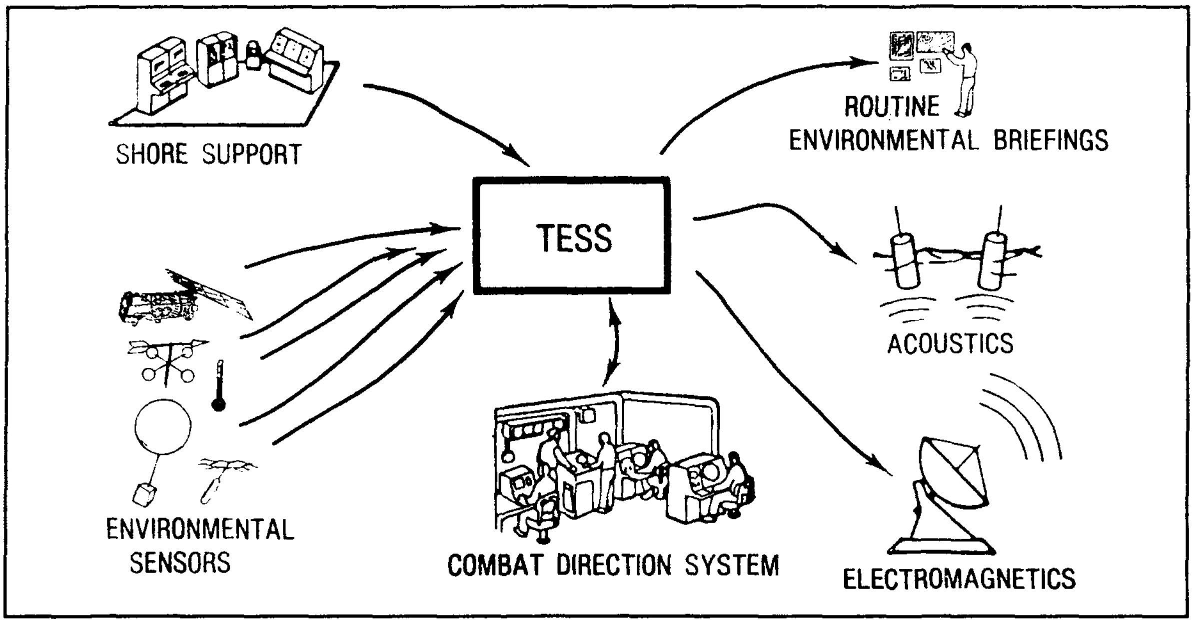

Figure 5. Information flow for the Tactical Environmental Support System (TESS).

5. FUTURE DIRECTIONS

Tropospheric Radio Propagation

Operational assessment of anomalous radio propagation is usually made under the assumption that the atmosphere is horizontally homogeneous. This assumption is based on a physical reason since the atmosphere, in particular over ocean areas, is horizontally much less variable than vertically. Horizontal homogeneity also implies temporal persistence. Propagation forecasts are often based on persistence, i.e., it is assumed that present conditions will not change significantly in the near future. There are, however, conditions for which horizontal inhomogeneity may be important, for example at air mass boundaries, in coastal regions or over complex terrain. Therefore, future efforts will address both propagation assessment for horizontally varying refractivity conditions and propagation over terrain.

The major problem of operational assessment of propagation in inhomogeneous refractivity conditions is not the propagation modeling part but the timely availability of the temporal and spatial structure of the refractivity field. There are presently no sensing capabilities available which could be used operationally and the outlook is not very good. There is some hope of success in two areas: use of satellite sensing techniques to describe the three dimensional refractivity field and improvement of numerical mesoscale models that are adequate for this purpose. Since entirely rigorous solutions are unlikely to be available soon, empirical data have to be used as well as expert systems and artificial intelligence techniques. In addition, improved direct and remote ground-based refractivity sensing techniques need to be developed. Radiosondes and microwave refractometers will remain the major sources for refractivity profiles. Profiling lidars may supplement techniques under clear sky conditions and their practicability will be further investigated. There is, presently, little hope that radiometric methods can provide profiles with sufficient vertical resolution to be useful for propagation assessment. There is, however, some hope that radars themselves can eventually be used to provide refractivity profiles.

Long Wave Propagation

So far, propagation in the frequency range below the hf band has not been discussed. It is often referred to as long wave propagation and a number of military applications, especially for strategic use, occupy frequencies in this band. Propagation of long waves over great-circle paths in a homogeneous ionosphere is well understood. Less understood are the effects of propagation over non-great-circle paths, the effects of inhomogeneous ionospheric conditions caused by energetic particle precipitation, sporadic E, electron density ledges and nonreciprocal propagation phenomena. Another area in need of attention is the improvement of atmospheric noise prediction codes. Finally, the often extensive computer time required by longwave propagation codes should be shortened through more efficient algorithms and faster numerical techniques.

High-Frequency Propagation

Empirical data bases are used in short wave propagation modeling and assessment work. These data bases need improvement in both accuracy and spatial/temporal coverage. Profile inversion techniques which are used to derive electron density profile parameters give non-unique answers and need to be refined. Short-term ionospheric fluctuations and tilts are becoming increasingly important for modern geolocation and surveillance systems. An intensive measurement and modeling effort is required to understand and predict such phenomena. Some of the physics of solar-ionospheric interactions and the time scales involved are still poorly understood and require further research. Existing short wave propagation assessment systems are based on simple models. Future systems will need sophisticated models and extensive validation procedures. With increased computer capability, more complex models can be executed fast enough for near-real-time applications. Also, the increasing use and availability of oblique and vertical incidence sounders make this data source an attractive additional input for assessment systems. This would make it possible to update the various ionospheric parameters used in the models which form the basis of these assessment systems. In addition, the availability of computer networks should allow the development of regional, near-real-time models based on a net of sounder measurements.

Transionospheric propagation predictions are limited by the accuracy of total electron content (TEC) values. Much of the difficulty arises from geomagnetic storm effects, traveling ionospheric disturbances, lunar/tidal effects, and other temporal/spatial phenomena. The best and only major improvement over monthly TEC climatology predictions can be obtained by real data observations not more than a few hours old taken where the TEC-time-delay correction is required. Present theories are inadequate to predict these temporal deviations from quiet ionospheric behavior, and efforts to improve those deficiencies are recommended.

Climatological models for transionospheric propagation predictions need more and better data for improved spatial resolution. In addition, parameters from the neutral atmosphere and the magnetosphere may provide insight into the reasons for the complexity in the spatial/temporal variability of TEC. For the proper use of more spatially-dense data, future ground-based observation networks must have standard format, calibration, editing, processing and interpretation techniques.

Ionospheric scintillations are caused by various plasma instabilities. Approximate stochastic solutions to the propagation problem describe quantitatively the scintillation phenomenon when the statistical properties of the irregularities are known. Morphological models of scintillation have been built to predict the scintillation occurrence and strength as a function of geographical, geophysical and solar parameters. Since ionospheric scintillation can be a limitation to various space-based systems, empirical models have been made available for system design. However, the solar and geomagnetic dependence of scintillation is still not fully understood and requires more attention in the future. Multi-technique measurements have proved very productive and should be the experimental approach for future modeling efforts.

For hf ground-wave propagation assessment, the approximate models now utilized should be replaced by more complex and comprehensive prediction models. This should improve the accuracy of assessment and would avoid the discontinuity at frequencies where a change in approximate models is now made. New software should allow for a nonstandard atmosphere and for sections with different ground electrical properties.

Millimeter-Wave and Electrooptical (EO) Propagation

Figure 6 shows atmospheric attenuation for frequencies

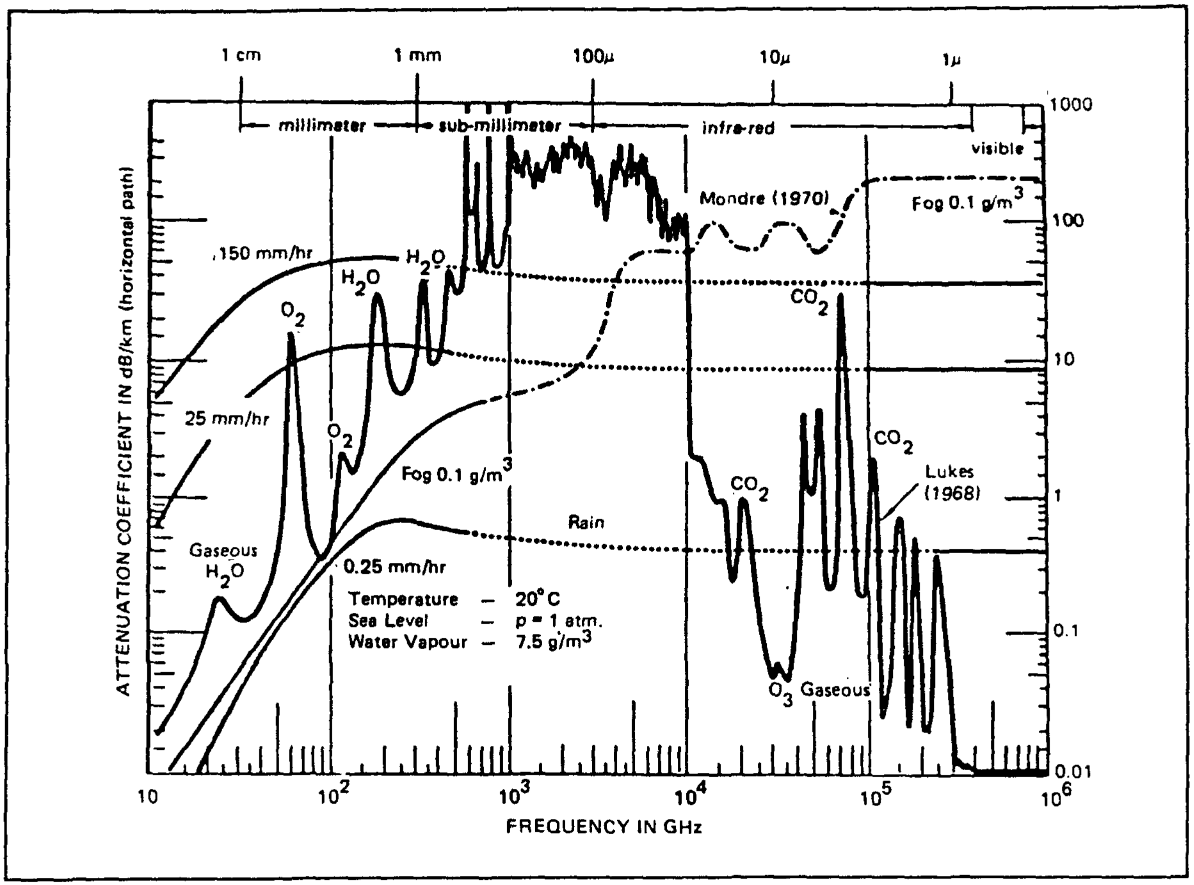

Figure 6. Attenuation coefficients for frequencies above 10 GHz.

above 10 GHz. Molecular absorption and extinction from aerosol particles (haze, fog, clouds, rain, snow etc.) play a major role. The solid curve in the figure denotes molecular absorption which rapidly increases above 10 GHz with alternating peaks and valleys. Of particular interest is the valley just below 100 GHz which offers still acceptably low attenuation rates for many applications. What makes the frequency range between 90 - 100 GHz attractive is that the relatively small wavelength (approximately 3 mm) permits narrow antenna beams for small apertures. The major advantage of mm-waves over other frequencies in the infrared or optical region is that mm-waves are less affected by hazes, fogs, smokes and clouds and are also capable of penetrating foliage. They are also strongly affected by atmospheric refractivity. In the case of near-surface ocean propagation, the so-called evaporation duct dramatically increases signal levels. For example, 94 GHz signal levels for a 41 km propagation link in the southern California off-shore area are commonly enhanced by 60 dB (Anderson, 1990). Intense mm-wave measurement and analysis efforts are presently being conducted under the sponsorship of the Defense Research Group of NATO.

Molecular absorption decreases for frequencies above 10 THz but is, again, characterized by peaks and valleys. There are several such valleys in the infrared band and molecular absorption is very low for the visible band. EO systems are sensor and weapon systems which rely on electromagnetic radiation in the infrared, visible and ultraviolet wavelength bands. They are of specific importance to military operations because they permit pointing accuracies and covertness not achievable at radio wavelengths. Unfortunately, they are significantly more dependent on the properties of the propagation medium than radio wavelengths. This critical dependency controls their deployment and requires a precise knowledge of the effects of the propagation environment on their performance.

Figure 7 illustrates .ospheric parameters influencing the performance of a Forward Looking Infrared (FLIR) system operating in a marine environment. The primary atmospheric parameters affecting the propagation of radiation in the (EO) bands are: aerosol extinction, molecular absorption, turbulence and refraction. Aerosol extinction is the sum of scattering and absorption by atmospheric aerosols. Shape, chemical composition, and size distribution of atmospheric aerosols are dependent on a number of other, often unknown, parameters (such as air mass origin, relative humidity, wind, etc.) and are difficult to measure and model. Molecular absorption is

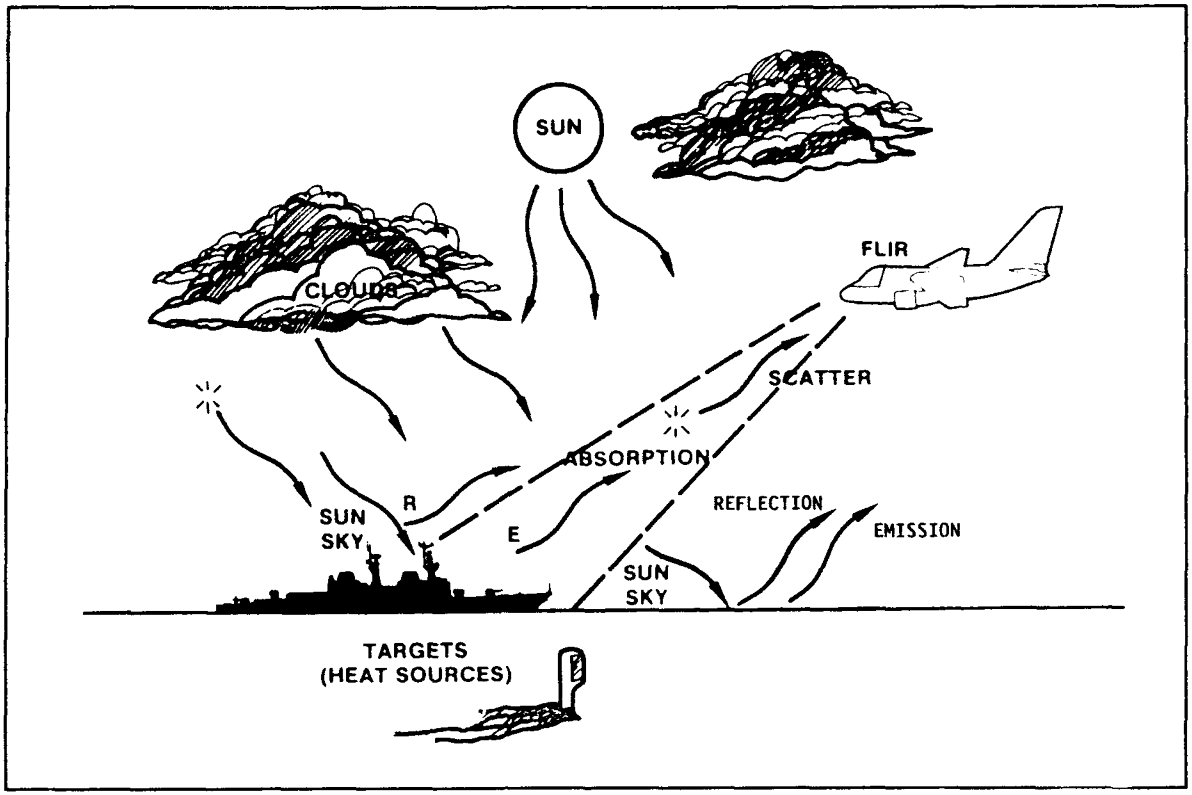

Figure 7. Parameters affecting FLIR (Forward Looking Infrared) performance.

probably the best understood of the above parameters and, for practical purposes, can be accurately predicted. Atmospheric turbulence is primarily due to temperature fluctuations and may cause beam wander, scintillations and image blurring. Atmospheric refraction may significantly shorten or extend horizon ranges for near-surface geometries which is an important factor in the detection of low-flying anti-ship missiles.

Besides the atmospheric parameters which control propagation, use of some EO sensors requires a knowledge of additional environmental factors. Surveillance systems (such as FLIRs and Infrared Search and Track Systems or IRSTs) sense the temperature difference or contrast temperature between the target and the background. The background temperature is often a complex function of emissivity of the background (atmosphere, sea surface, ice, ground), path radiance and reflections from the sky or other sources. In addition, clutter from sun-glint or cloud edges may mask targets or produce false alarms.

Environmental factors affecting EO systems must be known for both the design of such systems and their optimum operational deployment. Design of new EO systems and planning of military operations require good statistical data bases while their actual use necessitates accurate information of the conditions present. Therefore, models need to be developed and validated which relate atmospheric EO parameters to commonly available meteorological data. An example is an aerosol model based on temperature, humidity and wind observations. A particularly challenging task is the development of new sensing techniques for both in-situ and satellite use. Among various approaches are lidars (laser radars), radiometric techniques and a variety of devices which measure angular scattering from aerosols.

Finally, comprehensive technologies have been developed using fibers to transmit EO signals. These technologies are dominated by commercial applications but there are significant military uses that make fiber optics an important concern for AGARD. An example is use of ultra-low loss fibers to guide missiles or to remotely control vehicles.

6. CONCLUSIONS

Electromagnetic propagation assessment is crucial in the development of sensor and weapon systems, in military planning and for real-time operations and, in connection with operational decision aids, has an important role in the new NATO strategy. Propagation assessment supports the NATO-identified areas of interest in improved flexibility, mobility, improved situational awareness, and improved training techniques. Above all, propagation assessment and related decision aids allow more effective and efficient use of available resources. Many challenging tasks remain in all regions of the electromagnetic spectrum. Promising areas for emerging applications are mm-wave and EO wavelength bands. A major concern is the timely and accurate description of the propagation environment. Increasingly sophisticated signal processing techniques will be required for jam-resistant, noisy and congested electromagnetic environments. For military operations, electromagnetic propagation assessment must be an integral part of command and control systems.

7. ACKNOWLEDGEMENT

This work was supported by the Office of Naval Research.

8. REFERENCES

AGARD, Initial Planning Guidance for AGARD Technical Panels, AGARD ltr 14 Sep 1993

Anderson, K.D., 94 GHz propagation in the evaporation duct, IEEE Trans. Ant. and Prop., Vol. 38, No. 5, pp. 746-753, 1990

Hitney, H.V., and J.H. Richter, Integrated Refractive Effects Prediction System (IREPS), Nav. Eng. J., Vol. 88, No. 2, pp. 257-262, 1976

Richter, J.H., I.J. Rothmuller, and R.B. Rose, PROPHET: real time propagation forecasting terminal, Proc. 7th Technical Exchange Conference, Published by ASL, WSMR NM 88002, pp. 77-81, 1977

Effects of Hydrometeors and Atmospheric Gases at SHF/EHF

K.H. Craig
Radio Communications Research Unit
Rutherford Appleton Laboratory
Chilton, Didcot, OX11 0QX
U.K.

1 SUMMARY

The presence of rain on a propagation path can cause severe attenuation in the SHF and EHF frequency bands, reducing the performance of communications and radar systems. Rain, snow and ice can also gives rise to scatter, causing radar clutter and the potential for interference to, and an increased probability of intercept of, communications links. The structure of precipitation and cloud is discussed, and an overview of the physics of scatter of electromagnetic waves by rain is given. This is followed by a description of practical, statistical methods for the prediction of rain attenuation on terrestrial, radar and satcom systems, and simple cross section models for radar clutter and bistatic scatter.

Atmospheric gases absorb energy from electromagnetic waves because of molecular resonances at particular frequencies in the SHF and EHF bands. The mechanisms are discussed and practical prediction procedures for the calculation of gaseous attenuation given.

2 INTRODUCTION

Rain and atmospheric gases can affect the performance of communications and radar systems. The most complex and variable component is water: depending on temperature and concentration, it can occur in the gaseous, liquid or solid phase. Rain and other forms of precipitation (snow and hail) together with suspended liquid or frozen water in the form of fog, cloud or ice crystals are generically referred to as "hydrometeors".

Hydrometeors absorb and scatter electromagnetic waves, and therefore, if present along a communications or radar path, can lead to:

- attenuation of the signal, resulting in a reduction of radar detection and communication ranges;
- backscatter from rain cells, giving rise to rain clutter returns on radar systems;
- coupling of the transmission path to a second receiver via bistatic scatter from rain cells common to the two communications paths, causing interference or an increased intercept probability.

In the gaseous state, water vapour and other atmospheric components strongly absorb electromagnetic energy at particular frequencies, and this gives rise to attenuation at these frequencies.

All the effects mentioned become more significant as the frequency increases, and can generally be ignored at frequencies below 3 GHz. The primary concern here is the operation of radar and communications systems in the SHF (3–30 GHz, 10–1 cm wavelength) and EHF (30–300 GHz, 10–1 mm wavelength) bands. Above 300 GHz the effects of hydrometeors and atmospheric gases are also very important: these are discussed in the lectures devoted to electrooptics.

3 HYDROMETEORS

The effect of hydrometeors on a radar or communication path depends on the system geometry, frequency, and the types of particles present. In general, more than one type of hydrometeor can occur simultaneously along a radio or radar path. In particular a satcom link will often encounter rain over the lower part of the path and snow and ice at greater heights.

Because of the complexity and variability of the rainfall process, and the consequent lack of knowledge of the detailed structure of rainfall along a specific path at a specific time, practical prediction models for the effects of hydrometeors on radio systems tend to be statistical in nature, based on information such as the rainfall rate distribution at the ground. However, these statistical models are founded on physical principles, and in recent years advances in remote sensing by meteorological radars have increased our understanding of the structure of rain, and the way in which it affects radiowave propagation.

The effect of hydrometeors on the attenuation or scattering of an electromagnetic wave is determined by (a) the attenuation and scattering properties of a single hydrometeor particle; (b) the distribution of particle types, sizes and shapes within a rain cell; (c) the distribution of rain cells along the propagation path. Before presenting the statistical models, therefore, the structure of rain and the other hydrometeor types is discussed, followed by an overview of the physics of scattering by particles.

3.1 Structure of precipitation and cloud

3.1.1 Rain cell structure and rainfall rates

One of the most obvious observations about rain is that very different types of rainfall occurs, depending on the climate and local weather. For example, in temperate climates, stratiform rain gives rise to widespread rain or drizzle of long duration, although the rain rates are generally quite low, while convective rain is usually of short duration, but can be quite intense, particularly during a thunderstorm. In tropical climates, long periods of very intense rainfall can occur.

Figure 1 shows two views of typical stratiform rain in the UK, obtained from the Chilbolton Advanced Meteorological Radar [1], operating at 3 GHz. On the left is a plan-position indicator (PPI) view out to a radius of 80 km surrounding the radar, the darker colours indicating the higher levels of backscatter from the hydrometeors. On the right is a range-height indicator (RHI) view along the 315° radial of the PPI. Note the uniform and widespread nature of the rain. The dark band between 1.5 and 2 km height in the RHI is the *melting*

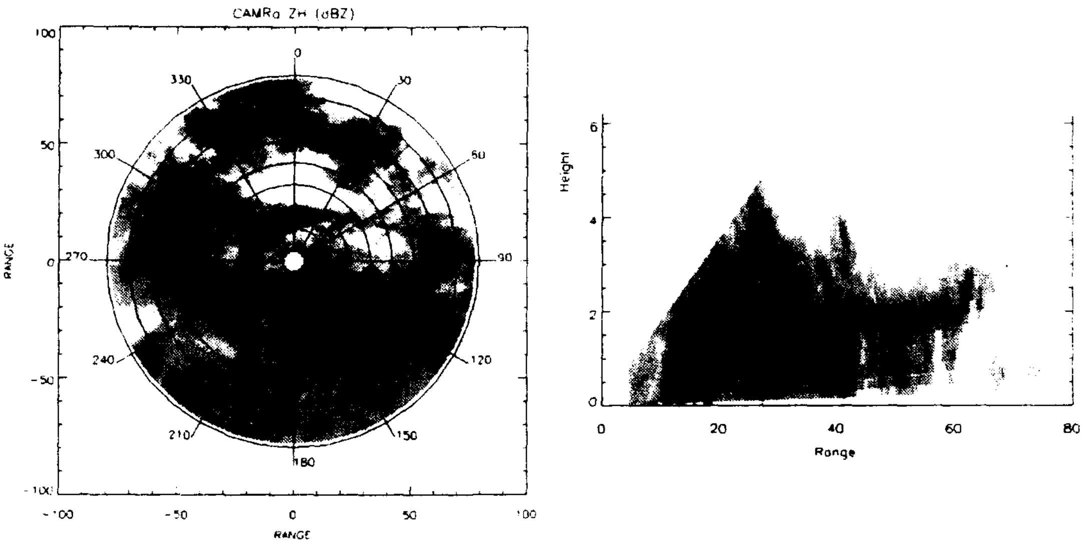

Figure 1: Radar views of stratiform rain

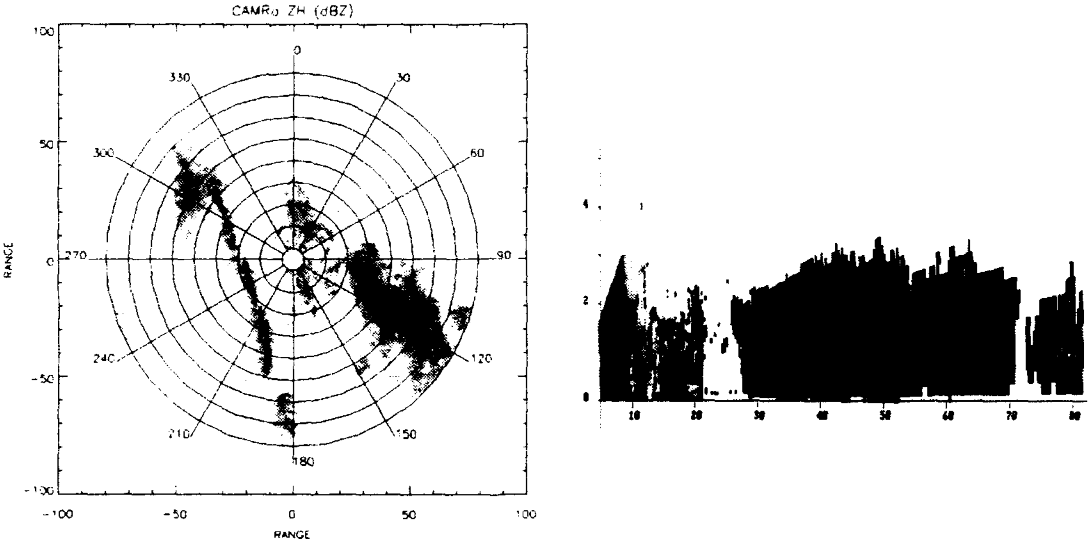

Figure 2: Radar views of convective rain

layer; above this height, the water is in the solid state (ice). The melting layer is also visible in the PPI as a poorly-defined ring at the radius where the radar beam (which is inclined at 1.5° elevation to the horizontal) intercepts the layer. The melting layer is discussed in more detail later.

In contrast Figure 2 shows a typical convective event. The PPI shows a line of rain cells associated with a weather front on the left of the picture, and convective activity to the right. The RHI was taken along the 115° radial of the PPI, and is very different from the stratiform event: the individual rain cells are more intense and localised, there is a clear "top" to the convective activity, and there is no evidence of a melting layer. (The scatter visible at ranges less than 20 km is not due to rain at all, but to ground clutter in the vicinity of the radar. Note also that the dark colours at the top of the rain do not represent high levels of backscatter, but are an artefact due to the monochrome reproduction of a colour radar image).

Figures 1 and 2 have shown something of the variability of the spatial structure of different types of rain cells. It is also important to know for any particular climate the percentage of the time that different rain types will be encountered. The simplest indicator of this is the rainfall rate distribution measured at the ground.

Rainfall statistics are of course available from measurements made on a regular basis by the world-wide network of meteorological stations. Unfortunately these measurements are more concerned with total rainfall *amounts* than with rainfall *rates* and rainfall rates derived from these generally have integration times of the order of one hour. This is unsatisfactory since the intense rain events that give rise to the most severe problems for radiowave propagation may last for only a few minutes or less.

However, rain rate measurements using fast response rain gauges (typically with integration times of one minute) have been made by radio engineers world-wide, and the International Telecommunication Union (ITU) has published global maps of rain climatic zones [2]. Figure 3 shows the rainfall intensity exceeded for a given percentage of the time in three of these zones (Arctic: zone A; Temperate: zone E; Tropical: zone P). The Arctic and Tropical zones represent the

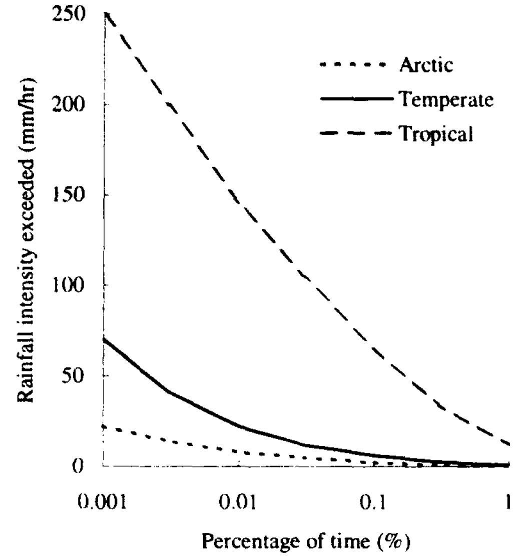

Figure 3: Typical rainfall rate distributions for three climates

extremes of low and high intensity rainfall, respectively. Note the fairly obvious facts that in any climate, the duration of intense rain is much less than that of weak rain, and that rain only occurs at all for a few percent of the time in most climates.

The rainfall rate distributions shown in Figure 3 are median annual distributions. It has to be borne in mine that rainfall patterns can vary widely from year to year, and that there will be seasonal variations within the year. These issues are discussed in Section 3.5.

3.1.2 Raindrop size distributions

In rain, the drops are not all of the same size or shape. They range in size from less than 0.1 mm to greater than 1 mm. The relative mix of small and large drop sizes depends on the rain type and rainfall rate, and is described statistically by means of the *drop size distribution*. This distribution is central to the calculation of physical quantities such as rainfall rate, attenuation and radar scatter cross section.

The effects of gravity, air resistance and surface tension cause the larger drops to become more elongated in the horizontal than in the vertical direction (oblate spheroids) as they fall. The degree of oblateness is directly proportional to the size of the drops: those with a diameter smaller than 1 mm are virtually spherical, while 8 mm diameter drops have an axial ratio of about 0.5.

The drop size distribution function $N(D)$ is defined such that $N(D)dD$ is the number of drops per cubic metre with drop diameters between D and $D + dD$. (Since the larger drops are not exactly spherical, D is strictly defined as the equivalent diameter of an equivolumetric sphere).

Measurements of rain drop sizes in several types of rain all show a drop size distribution strongly biased towards the smaller drop sizes. The most widely used model of the drop size distribution is the Marshall-Palmer distribution [3]:

$$N(D) = N_o \exp(-\Lambda D) \qquad (1)$$

The quantity Λ decreases with rain rate R, and the distribution can be written in terms of rain rate using the empirical relationship:

$$\Lambda = 41\, R^{-0.21} \qquad (2)$$

with Λ given in cm^{-1} and R in mm/hr. A typical value of N_o is $8\times10^4\ \mathrm{m}^{-3}\mathrm{cm}^{-1}$.

Because of the rain rate dependence of Λ, the ratio of the number of large drops to the number of small drops increases as the rain rate increases. Table 1 gives typical values for the Marshall-Palmer distribution. Note also that the total number of drops per unit volume increases as the rain rate increases.

Rain type	Percentage of small drops (diam < 0.1 mm)	Percentage of large drops (diam > 1 mm)
Light rain (1 mm/hr)	34	2
Moderate rain (5 mm/hr)	25	5
Heavy rain (25 mm/hr)	19	12
Intense rain (100 mm/hr)	14	21

Table 1: Rain drop sizes in the Marshall-Palmer distribution

Other raindrop size distributions exist in the literature. The Laws and Parsons distribution [4] is a numerically tabulated distribution, similar in form to the Marshall-Palmer except that it has slightly fewer small drops. Gamma and log-normal distributions have also been used: these provide a natural cut-off at the small drop sizes.

No single model of drop size distribution is adequate to describe all rain-related phenomena. Different propagation quantities at different frequencies are sensitive to different ends of the distribution, and accurate predictions may require a careful consideration of the best distribution for the application. However, the Marshall-Palmer distribution has generally been found to be satisfactory for statistical predictions in the upper SHF band: in practical calculations, any fine structure in the drop size distributions and variations in the large scale structure of a rain cell tend to be averaged out by the integration over the distribution and along the path.

3.1.3 Snow, hail and ice

Snow consists of aggregated ice crystals, with large flakes forming only at temperatures just below freezing. In stratiform rain, large snow flakes occur up to a few hundred metres above the melting level, but at greater heights, single ice crystals are the main constituent. Dry snow has little effect on radio waves (its very low density structure having an effective permittivity close to unity).

Hail is formed by the accretion of supercooled cloud droplets, giving rise to large, high density particles of spherical (or conical) shape. Although the effective permittivity of hail is larger than that of snow, hail is only weakly attenuating, certainly at SHF frequencies.

Ice crystals form at high altitude. Although the attenuation effects are weak, they can be important for satcom systems. This is because ice crystals are very non-spherical, and so give rise to significant depolarisation effects. Ice crystals tend to form either "plates" (diameters reaching 5 mm in the dendritic form) or "needles" and "prisms" (with lengths around 0.5 mm). The relative importance of these types varies with temperature. Computations of electromagnetic scattering from ice crystals often approximate their shapes by very oblate or prolate spheroids.

3.1.4 Melting layer

In stratiform rain, partially melted snowflakes exist in a height interval of about 500 m around the 0°C isotherm. In this melting layer, the particles are large and have a large effective permittivity because of the high water content. Due to their relatively small fall velocity, they also have a high density. This means that the melting layer can produce very significant scattering of electromagnetic waves. The melting layer is clearly visible in Figure 1. The height of the 0°C isotherm depends on latitude and season, ranging from 4–5 km at the equator to ground level at the poles.

On a radar RHI display, the enhanced backscatter at the melting layer is sometimes referred to as the "bright band", because of its enhanced intensity on the radar screen. The backscatter from the melting layer is typically 10–15 dB higher than at heights immediately above or below the layer. The melting layer is even more obvious in Figure 4, which shows the same RHI view as in Figure 1; the difference is that the cross-polar signal is displayed here (i.e. the intensity of the vertically polarised backscatter return from the rain cell, with a horizontally transmitted radar pulse) rather than the copolar signal. The large, non-spherical particles and canting due to tumbling in the melting layer causes significant depolarisation of the backscattered signal. Figure 4 gives a good impression of the variation that can occur in the height of the melting layer.

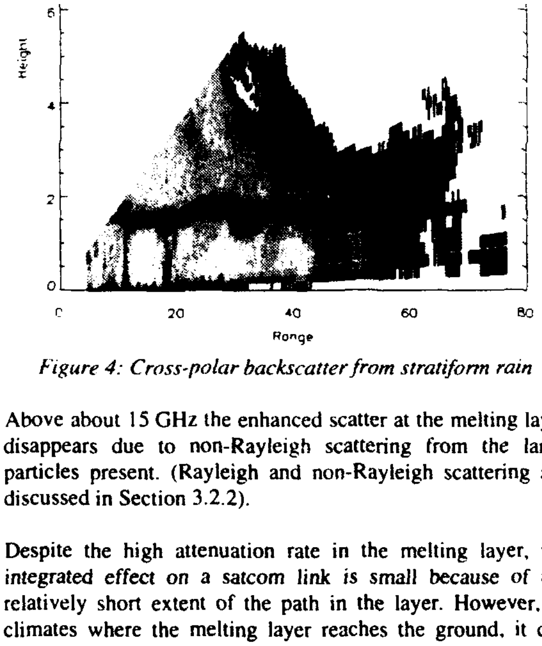

Figure 4: Cross-polar backscatter from stratiform rain

Above about 15 GHz the enhanced scatter at the melting layer disappears due to non-Rayleigh scattering from the large particles present. (Rayleigh and non-Rayleigh scattering are discussed in Section 3.2.2).

Despite the high attenuation rate in the melting layer, the integrated effect on a satcom link is small because of the relatively short extent of the path in the layer. However, in climates where the melting layer reaches the ground, it can cause very significant attenuation on terrestrial communications links.

3.1.5 Cloud and fog

The liquid water content of non-precipitating clouds and fog is low: it varies from 0.05 gm^{-3} in stratiform clouds to about 1 gm^{-3} in cumulonimbus, and from 0.05 gm^{-3} in medium fog (visibility of the order of 300 m) to 0.5 gm^{-3} in thick fog (visibility of the order of 50 m).

The droplet sizes are also small (less than 100 μm). For both these reasons, the effect of clouds and fog is negligible at frequencies below 100 GHz.

3.2 Physics of single particle scatter

When electromagnetic energy propagates through a medium containing an ensemble of particles, such as water droplets, energy is removed from the beam. Two mechanisms are involved:

(i) scatter removes energy from the beam by redistributing this energy in other directions;
(ii) absorption removes energy from the beam by converting it to heat (i.e. the temperature of the particles increases).

The attenuation of the beam caused by the combination of these two mechanisms is referred to as "extinction". Thus extinction (and therefore both scatter and absorption) is the quantity relevant to the attenuation of a communications or radar signal due to propagation through rain. On the other hand, the calculation of rain clutter cross sections, or of interference levels due to bistatic scatter, are principally concerned with the scattering of energy out of the direct path, although some absorption of the scattered signal will also occur.

Although propagation through rain cells involves a very large number of scatterers, the total power absorbed or scattered by the ensemble of rain drops in a rain cell can be obtained by summing the contributions of each individual drop incoherently. In this section we consider the basic physics of single particle scattering and absorption.

Consider a plane electromagnetic wave with electric field E_{in}, incident on a particle. The scattered field E_{sca} is related to E_o by the dimensionless scattering function, $S(\theta,\varphi)$ [5]:

$$E_{sca} = E_o\, S(\theta,\phi)\, \frac{\exp(ikr)}{-ikr} \tag{3}$$

r is the radial distance from the particle to the observation point; θ and φ are the scattering angles in a spherical coordinate system centred on the particle with the z-axis aligned with the direction of propagation.

It follows that the *intensity* of the scattered wave (defined as the energy flux per unit area) I_{sca} is related to the incident intensity I_o by:

$$I_{sca} = I_o \frac{|S(\theta,\phi)|^2}{k^2 r^2} \tag{4}$$

A plot of $|S(\theta,\phi)|^2$ as a function of θ (normalised to the value in the forward direction) gives the scattering diagram of the particle. The forward scatter direction is $\theta = 0°$ while the backscatter direction is $\theta = 180°$.

It is useful to define a scattering *cross section* C_{sca} for the particle: the total energy scattered in all directions is equal to the energy of the incident wave falling on the area C_{sca}. Cross sections for absorption C_{abs} and extinction C_{ext} can de defined similarly, and it follows from the above that:

$$C_{ext} = C_{sca} + C_{abs} \tag{5}$$

Discussion of the problem is simplified by introducing dimensionless quantities:

(i) the particle size is normalised by dividing it by a multiple of the wavelength λ. For spherical particles, the "size" can be taken to be the particle radius a. For non-spherical particles, the "size" is normally taken to be the radius of an equivolumetric sphere. The most convenient dimensionless quantity, known as the *size parameter*, x, is defined by:

$$x = k\,a \qquad (6)$$

where k is the wavenumber (equal to $2\pi/\lambda$). The size parameter can be interpreted as the number of wavelengths contained in the particle's circumference.

Note that the particle ***radius*** is used in scattering theory, while the particle ***diameter*** was used in the raindrop size distributions. The factor of two will be unimportant in the qualitative discussion, although care needs to be taken in quantitative calculations.

(ii) the cross sections are normalised by dividing by the geometrical cross section of the particle. For spherical particles of radius a this is πa^2. These normalised, dimensionless, cross sections are called *efficiency factors*, denoted by Q_{ext}, Q_{sca} and Q_{abs} for extinction, scattering and absorption, respectively:

$$Q = C / \pi a^2 \qquad (7)$$

Obviously:

$$Q_{ext} = Q_{sca} + Q_{abs} \qquad (8)$$

It is straightforward to show that the efficiency factors are simply related to the scattering function $S(\theta,\varphi)$:

$$\begin{aligned} Q_{ext} &= \frac{4}{x^2}\Re\{S(0)\} \\ Q_{sca} &= \frac{1}{\pi x^2}\int |S(\theta,\phi)|^2 d\Omega \qquad (9) \\ Q_{abs} &= Q_{ext} - Q_{sca} \end{aligned}$$

$\Re\{S(0)\}$ denotes the real part of the forward ($\theta = 0°$) scattering function. The integral in the expression for Q_{sca} is taken over the whole 4π solid angle surrounding the particle.

For radar applications, we can also define an efficiency factor for backscattering:

$$Q_{back} = \frac{4}{x^2}|S(180°)|^2 \qquad (10)$$

This definition gives a backscatter cross section that is greater by a factor of 4π than the differential scattering cross section for scattering into a unit solid angle around the backscattering direction. The latter definition would be more natural here, and would be consistent with the expression for Q_{sca} given in eqn (9). Unfortunately, the traditional radar definition of cross section is normalised differently from that used in scattering theory. Further discussion of this awkward point is given in [6, page 121]. We use the *radar* definition of cross section in eqn (10).

There is a large literature on the evaluation of $S(\theta,\varphi)$ for various shapes and sizes of particle. Here it suffices to consider some aspects of the classical problem of scatter from a spherical particle, for which analytical solutions exist. Further details will be found in [5,6]. Various numerical methods have been developed in recent years to model scatter from oblate and prolate spheroidal, and more general shaped, raindrops; these include solutions by point matching [7], T-matrix methods [8], integral equation methods [9] and separation of variables [10]; a review of these methods is given in [11].

In the above, it has been assumed for simplicity that there is only a single scattering function $S(\theta,\varphi)$ for a particle. However, the electromagnetic field is actually a vector quantity: the electric field vector lies in the plane perpendicular to the direction of propagation and its direction defines the polarisation of the field. Since there are two mutually orthogonal polarisation states (usually taken to be horizontal and vertical, or right and left hand circular) $S(\theta,\varphi)$ is actually a 2×2 matrix. The four components of this *amplitude scattering matrix* relate the amplitude of one particular polarisation state of the scattered field to one particular polarisation state of the incident wave. For a spherical particle, this matrix is diagonal, and there is no coupling between the different polarisations. There are then two scattering functions (S_1 and S_2) to be considered, one for each polarisation state. The generic term $S(\theta,\varphi)$ will be used in the discussion below when polarisation effects are not important.

The evaluation of $S(\theta,\varphi)$ is non-trivial in general, even for a spherical particle. The scattering function and the cross sections depend on frequency, for two reasons: (a) the refractive index of water is frequency dependent; (b) for a given particle size, the size parameter is a function of frequency.

3.2.1 Refractive index of water

Figure 5 shows the dependence of the refractive index n of water on frequency at a temperature of 20°C. The high values of refractive index arise from the polar nature of the water molecule. (The figures confirm the well-known fact that the dielectric constant of water has a value of 80 at low frequencies: the dielectric constant is equal to n^2.) It is important to observe that n is complex: $n = \Re[n] + i\Im[n]$. The peak in $\Im[n]$ around 20 GHz can be regarded as the 22 GHz water vapour absorption line (see Section 4.1 below) greatly broadened in the liquid state.

A plane wave travelling in a medium of complex refractive index n is attenuated as it propagates. The field intensity is attenuated by a factor of $\exp(-2\pi\Im[n])$ in travelling through a depth of one free space wavelength. Thus in the 3–300 GHz range, the attenuation rate is greater than 40 dB/wavelength

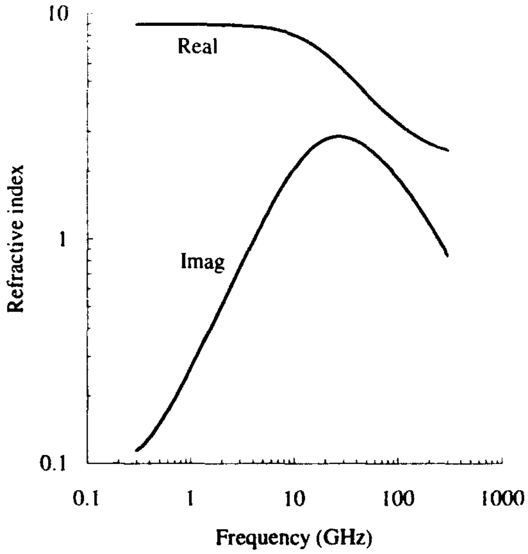

Figure 5: Refractive index of water at a temperature of 20°C

for rain at a temperature of 20°C. This shows that waves penetrating raindrops at 300 GHz (1 mm wavelength) and above are well-attenuated within the diameter of the drop. This condition is satisfied down to wavelengths of at least 0.01 mm, but of course, drops are transparent at optical frequencies, where $\Im[n]$ reaches a minimum.

The refractive index of water is temperature dependent. At the frequencies of interest, the effect of increasing temperature in the range 0 to 30°C is to translate the real and imaginary refractive index curves to the right along the frequency axis. This means that below about 30 GHz, $\Im[n]$ decreases with increasing temperature, while above 30 GHz, the opposite is true.

The refractive index of ice is very different from water in the liquid state. $\Re[n]$ is very close to 1.78 over the entire frequency range shown, while at 0°C, $\Im[n]$ falls from 0.025 at 300 MHz to 0.0002 at 300 GHz; at -20°C these values are about a factor of 5 smaller. Thus the attenuation of radio waves by ice is very small.

3.2.2 Scattering regions

The dependence of $S(\theta,\varphi)$ on particle size is illustrated in Figure 6. This shows the scattering, absorption and extinction efficiencies as a function of the particle size parameter. The calculation was made using the refractive index of water at 3 GHz (8.86 + 0.75 i). Although the curves are different for particles with different refractive indices, the efficiency factors (or cross sections) for all particles show the same general features. In particular, note that the extinction efficiency is equal to the sum of the scattering and absorption efficiencies, in agreement with eqn (8).

Three distinct regions are identifiable in Figure 6, and in each of these different scatter approximations may be applied in order to simplify the calculation of scattering cross sections:

(i) for size parameters $x \ll 1$ the efficiency factors fall off rapidly with decreasing x (note the logarithmic scales); this is the Rayleigh scattering region;

(ii) for $x \gg 1$, the efficiency factors are independent of x; this is the optical region;

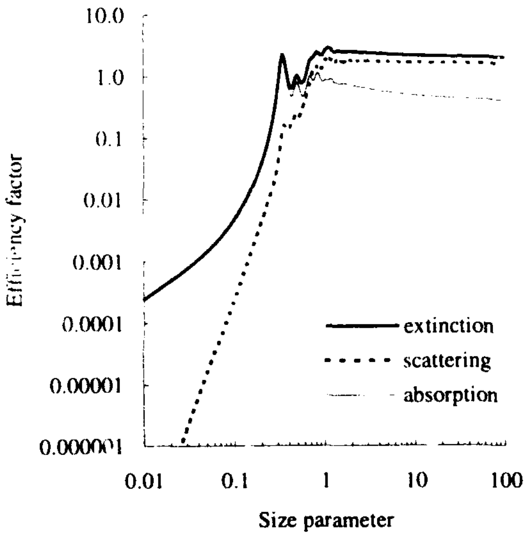

Figure 6: Efficiency factors for extinction, scattering and absorption, illustrating the different scattering regions

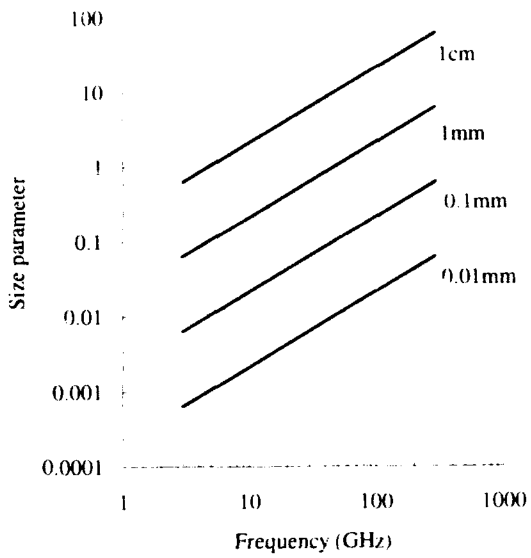

Figure 7: Size parameter as a function of particle radius and frequency

(iii) for intermediate sizes of x, the behaviour of the efficiency factor is complicated; this is the resonance, or Mie scattering, region.

The efficiency factor curves and the scattering regions of Figure 6 should, strictly speaking, be interpreted in terms of varying particle size at a fixed frequency or wavelength, and not as a function of frequency for a fixed particle size. This is because the calculations have been performed for a specific value of refractive index, which is frequency dependent. However, a graph of efficiency factor as a function of frequency does show the same scattering regions as in Figure 6, and the same general principles apply.

In order to relate Figure 6 to actual raindrop sizes and frequencies of interest, Figure 7 gives the size parameter as a

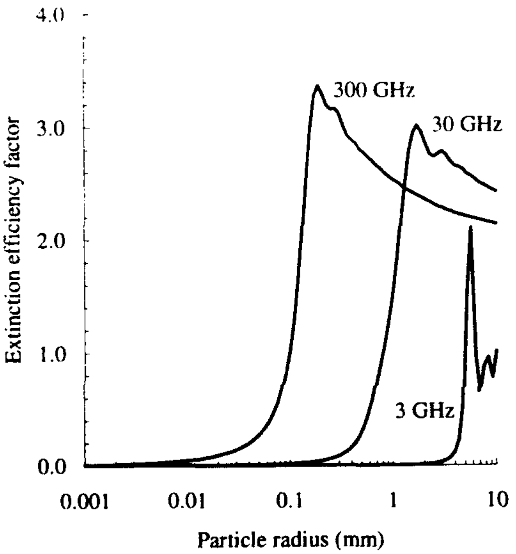

Figure 8: Extinction efficiencies as a function of particle radius and frequency

function of particle radius and frequency.

It is seen that at the lower SHF frequencies (3–10 GHz) all raindrop, cloud and fog particles have size parameters less than 1, and scattering is entirely in the Rayleigh region. On the other hand, at EHF frequencies, the larger raindrops lie in the Mie scattering region, although the smaller raindrops, and cloud and fog particles, can still be described by Rayleigh scattering.

This is further illustrated in Figure 8, where the extinction efficiency curves are given at 3, 30 and 300 GHz. In this Figure, the efficiency factor is shown on a linear scale to emphasise the variations in the resonance region.

3.2.3 Rayleigh scattering region

We have seen that the Rayleigh scattering region is the most important one at the frequencies of interest. Rayleigh scattering is named after Lord Rayleigh who wrote a seminal paper in 1871 [12] which explained (among other things) the reason for the blue colour of the sky in terms of light scattering. Although Rayleigh's derivation only applied to non-absorbing particles, the name is now applied generally to all small particle scattering.

If a particle is much smaller than the wavelength of the incident electromagnetic field, the field can be considered uniform and static (that is, it has a constant value) throughout the volume of the particle. (Strictly speaking, this requires that $|n|x << 1$ as well as $x << 1$ to exclude, for example, the case of significant absorption across the diameter of a single drop, and the Rayleigh region is normally defined by these two conditions.) This field induces a dipole moment in the particle proportional to the magnitude of the incident field, and the particle re-radiates like a dipole antenna. The scattering function for this dipole radiation is:

$$S(\theta) = ik^3\alpha\, f(\theta) \qquad (11)$$

where α is the *polarisability* of the particle, which for a spherical particle of radius a and refractive index n is:

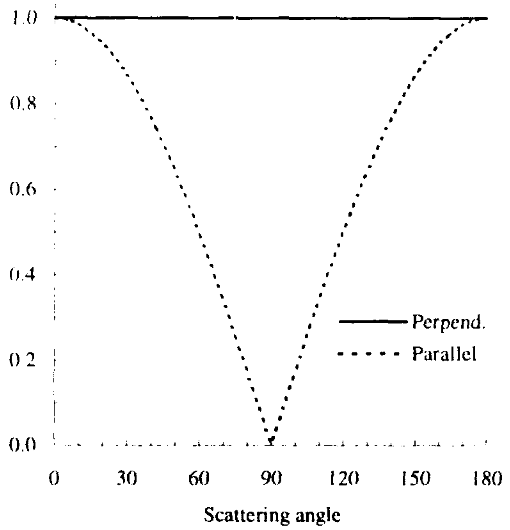

Figure 9: Rayleigh scattering diagram for perpendicular and parallel polarisation

$$\alpha = \frac{n^2-1}{n^2+2}a^3 \qquad (12)$$

$f(\theta)$ gives the variation of $S(\theta)$ with scattering angle and depends on polarisation.

In the plane perpendicular to the direction of polarisation (for example, in the horizontal plane for a vertically polarised wave), $f(\theta) = 1$, while in the plane parallel to the plane of polarisation, $f(\theta) = \cos\theta$, characteristic of dipole radiation. The scattering diagram ($|S(\theta)|^2$ normalised to the forward direction) is given in Figure 9. Note the null at 90° for parallel polarisation. This means, for example, that a horizontally polarised emission will be much less detectable than a vertically polarised one by a receiver on a path at right angles to the direction of propagation and which is coupled to the emitter by rain scatter, assuming that Rayleigh scattering dominates.

From eqns (9) and (10) it is a simple matter to derive efficiency factors which are valid to leading order in the size parameter x:

$$\begin{aligned} Q_{ext} &= 4x\Im(\hat{n}) \\ Q_{sca} &= \frac{8}{3}x^4|\hat{n}|^2 \\ Q_{abs} &= 4x\Im(\hat{n}) \qquad (13) \\ Q_{back} &= 4x^4|\hat{n}|^2 \\ \hat{n} &= \frac{n^2-1}{n^2+2} \end{aligned}$$

These expressions are very simple, but have important consequences:

- to leading order in x, Q_{sca} and Q_{back} vary as x^4 while Q_{abs} and Q_{ext} vary as x. This means that the scattering cross sections are always negligible compared to the absorption cross section for sufficiently small values of x although, for a weakly absorbing particle (one for which $\Im(n)$ is very small), this asymptotic behaviour may not occur until very small values of x. However, Figure 6 shows that absorption does dominate over scattering at SHF frequencies.
- Q_{abs} is equal to Q_{ext}. This is only true to leading order. Since $Q_{ext} = Q_{sca} + Q_{abs}$ (eqn (8)), there must be differences at higher orders in x; a proper treatment of these higher order terms requires Mie theory (see below).
- the expressions for Q_{sca} and Q_{back} appear to show that the backscatter cross section is *greater* than the total scattering cross section! This apparent paradox is due to the different (radar) normalisation used in Q_{back} compared to the other efficiency factors.

The scattering efficiencies are proportional to x^4. If $(n^2-1)/(n^2+2)$ is a weak function of frequency over a band of interest, this leads to an important conclusion: the Rayleigh scattering *cross sections* (total and backscatter) of a spherical particle (which are obtained from the scattering *efficiencies* by multiplying by the particle's physical cross section πa^2) are *proportional* to the *sixth* power of the particle's diameter and *inversely proportional* to the *fourth* power of wavelength. This simple observation leads to the following:

- because of the D^6 dependence on rain drop diameter D, the small number of large drops in a distribution of different sizes will contribute most to the scattered signal.
- if radiation comprising a band of frequencies is incident on a distribution of particles which are small compared to the wavelength, the shortest wavelengths are scattered most—this is precisely the case for white light scattered by dust particles in the atmosphere, and explains why the colour of the sky (seen by scattered light) is blue.

Consideration of the quantity $\hat{n} = (n^2-1)/(n^2+2)$ in eqn (13) shows an important difference between the properties of water and ice:

- $|\hat{n}|^2$ for both water and ice is approximately constant throughout the SHF/EHF range, with a ratio between the two of about 5. For similarly sized particles, therefore, the scatter and backscatter cross sections of water and ice are of the same order of magnitude.
- the value of $\Im(\hat{n})$ for water increases with frequency, while that of ice decreases with frequency throughout the SHF/EHF range, the value for ice being between one and four orders of magnitude smaller than for water. Thus the absorption and extinction cross sections for ice are much smaller than for water.

The practical consequence is that while the ice above the melting layer may appear as "bright" as the rain below the layer on a meteorological radar (seen in backscatter), the ice will not contribute significant attenuation on a satellite path, and only the attenuation on the path below the melting layer need be considered.

3.2.4 Optical scattering region

The optical region is so-called because the method of geometrical optics can be used to obtain the extinction and scattering efficiencies, and the angular distribution of the scattered electromagnetic field. At SHF and EHF frequencies, hydrometeor particles are never sufficiently large for scattering to be truly optical (see Figure 8), and the optical region need not be discussed in detail. Scattering of light by rain drops occurs in the optical region.

The most obvious fact about the optical region is that the extinction efficiency approaches the limiting value 2 as the size parameter increases (see Figure 6):

$$\lim_{x\to\infty} Q_{ext}(x,n) = 2 \qquad (14)$$

Thus the extinction cross section is *twice* the geometrical cross section of the particle. This appears paradoxical since in the optical limit a particle is expected to act as an opaque screen, removing an amount of energy from the incident field equal to the intensity of the field times the geometrical cross section of the particle.

The explanation is that diffraction at the edge of the particle (which is not taken into account in geometrical optics) removes an additional amount of energy from the forward direction exactly equal to the geometrical cross section. Care needs to be taken in interpreting this result. Most of the energy diffracted out of the forward direction is confined within a narrow cone of half angle $\psi \cong 10/x$ about the forward direction. Only if the acceptance angle of the detector of the scattered energy (i.e. the beamwidth of the receiver at RF frequencies) is much less than this half angle (say, $\psi_{acc} < 1/2x$) will the full extinction in the forward direction be realised. With larger acceptance angles the measured value of Q_{ext} will tend to 1 since the diffracted energy will be captured by the detector.

The angular distribution of scattered energy can be obtained by tracing geometrical "rays" through the particle, taking account of transmissions and multiple reflections. A graph of the scattering function as a function of scatter angle θ will have sharp peaks corresponding to the directions at which rays exit the particle after 0, 1, 2, ... internal reflections. This behaviour is very different from the behaviour in the Rayleigh region, where the scattering function is either constant or various smoothly as a function of θ (Figure 9). The best illustration of this effect is the rainbow, caused by reflections of sunlight by rain drops: the *primary* bow is formed by rays that have undergone a single internal reflection, while the *secondary* bow is formed by rays that have undergone two internal reflections. The colours of the rainbow are due to the refractive index of the water varying slightly with the wavelength of the light, giving rise to slightly different reflection angles for the different colours.

3.2.5 Mie scattering region

The Mie region is the most complex to model. Because the particle size is comparable with the wavelength, resonances occur within the particle: these are evident in the oscillatory portions of Figure 8. (The oscillations are strongest at 3 GHz where the phase angle of the refractive index is smallest.) The problem was formally solved by Mie in 1908 [13] by expanding the incident and scattered fields in terms of spherical harmonics and applying Maxwell's equations.

Computer programs are available for the rapid evaluation of Mie scattering on desk top computers (for example, see [6]). Because these implement a rigorous, numerical solution to the problem, they give results in the Rayleigh and optical regions as well. However, a separate treatment of these regions is worthwhile, as it gives more physical insight into the problem, and the approximate formulae are often adequate and preferable to a numerical solution.

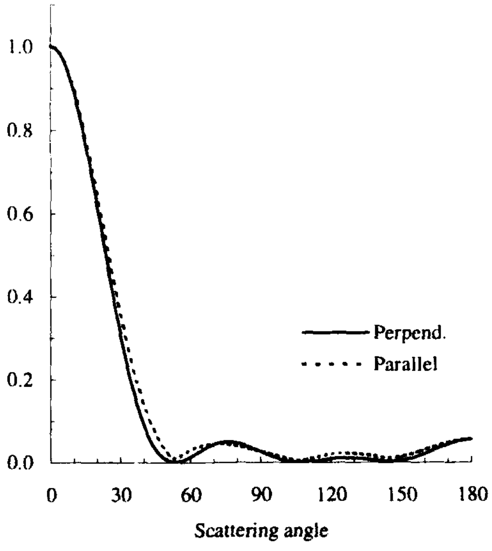

Figure 10: Mie scattering diagram for perpendicular and parallel polarisation

An example of the angular distribution of scattered energy is shown in Figure 10, for a 1 mm diameter spherical ice particle at 300 GHz (although recall that ice particles are generally very non-spherical). Note the dominance of forward scatter, and the "sidelobes" in the scatter pattern, compared to the Rayleigh region (Figure 9). More and more of the scattered energy becomes concentrated in the forward direction as the size parameter increases.

3.3 Attenuation and scatter from distributions of particles

The combined effect of all the raindrops in the rain cell is obtained by incoherently summing the contribution of each drop, taking account of the incident field at each drop, and the (empirically measured) statistical distribution of particle sizes in the cell. This is possible because each drop scatters independently of the others, and (at least in the frequency range of interest here) the effects of multiple scattering are small.

Recall that the drop size distribution function $N(D)$ is defined such that $N(D)dD$ is the number of drops per cubic metre with drop diameters between D and $D + dD$. The scattering and attenuating effect of a distribution of particles can therefore be expressed in terms of scattering and extinction cross sections *per unit volume* as:

$$C^d = \int C(D)\, N(D)\, dD \tag{15}$$

where $C(D)$ has been used to denote a cross section for a particle with diameter D and the integration is taken over all D. The superscript d is used to indicate that the cross sections are per unit volume of the *distribution*.

When Rayleigh scattering dominates, a simple relationship exists between the cross sections $C(D)$ and the particle diameters D (eqn (13)). In terms of the practical quantities η_s (the radar scatter cross section per unit volume, related to C_{sca} or C_{back}) and γ_R (the attenuation rate in dB/km, related to C_{ext}), eqn (15) shows that:

$$\begin{aligned} \eta_s &\propto f^4 |\hat{n}|^2 \int D^6\, N(D)\, dD \\ \gamma_R &\propto f\, \Im(\hat{n}) \int D^3\, N(D)\, dD \end{aligned} \tag{16}$$

where only terms depending on D and the frequency f have been retained.

The rainfall rate R (in mm/hr) is also expressible as an integral over the drop size distribution:

$$R \propto \int V(D)\, D^3\, N(D)\, dD \tag{17}$$

where $V(D)$ is fall velocity for a particle of diameter D.

Since simple analytical forms for the drop size distribution $N(D)$ exist (see Section 3.1.2), and the form of $V(D)$ is known, eqns (16) and (17) enable relationships to be derived relating the propagation quantities η_s and γ_R to the rainfall rate R. Many (hundreds) of such relationships have appeared in the literature (each differing slightly in the distributions assumed, or in the empirically determined constants used), but one of the most widely used forms is:

$$\eta_s, \gamma_R = a R^b \tag{18}$$

(the a and b are of course different for η_s and γ_R and they also depend on frequency through the f and $\hat{n}$ -dependent terms in eqn (16)). This form is used in the practical attenuation and scatter models described below.

3.4 System implications

The principal cause of rain-induced system degradation on a communications link is fading due to rain attenuation: this reduces the wanted signal level, and decreases the available system margin. The margin can be reduced further if interference is received from unwanted signals, reducing the signal-to-interference ratio of the link; this can be caused by scatter from rain cells common to both the wanted and unwanted signal paths. Incoherent interference from a broadband digital signal effectively increases the noise floor of the receiver.

[illegible] of radar, rain attenuation is still important. [illegible] more significant problem is the effect of backscatter from rain cells lying on the path between the radar and the target. This rain *clutter* can significantly reduce the probability of detection of a target.

For communications links and radar systems alike, rain can compromise the security of the system. Bistatic scattering from rain cells located within the antenna beam of the radio or radar antenna may be detectable by a surveillance receiver with an antenna beam which also illuminates the rain cells, giving rise to an increased probability of intercept.

A complete assessment of system performance should, of course, include other sources of propagation degradation as well as hydrometeors. Gaseous absorption is discussed below. Clear-air effects (such as multipath and ducting) are discussed elsewhere.

3.5 Statistical prediction methods

So far the discussion has been mainly concerned with the basic physics of scatter from a single particle or distribution of particles. In most practical cases where a prediction of rain attenuation or scatter is required, detailed information on the structure of the rain causing the system degradation will not be available. This is particularly true at the system design stage. In this case, the interest is not in how much attenuation or scatter will there be on a particular link at a particular time, but rather in the operational reliability of the proposed link.

The effect of propagation on the degradation of system performance is normally expressed statistically in terms of the probability (or more specifically, the percentage of the time) that a given attenuation loss or scattered signal level will be exceeded. For high availability systems, an outage of 0.01% or even 0.001% of the time may be significant; high capacity satcom systems may be considered to be in this category. On the other hand, some systems (such as radar systems and field communications) may be able to tolerate higher levels of outage, perhaps as high as 0.1% or 1%, and are considered to be low availability systems. In any case, the basic statistic is the cumulative probability distribution of some reliability measure obtained from (or predicted by models based on) long-term results. Because the occurrence and intensity of rain varies on a seasonal basis, and because there is also significant year-to-year variability, "long-term" in this context means a period of several years. Statistics derived on this basis are usually referred to as "long-term average annual".

If statistical predictions are required for a link that is to be established for only a short period, average annual statistics may not be very useful. An alternative is to obtain monthly statistics for the location of interest: that is, cumulative distributions based on data for a given calendar month, averaged over a period of several years. In particular the concept of the "worst-month" (the calendar month that gives the worst system degradations) has proved useful as a means of accounting for annual variations in the weather. A procedure for converting between average annual and worst-month statistics is given in [14]. However, it is important to note that year-to-year variations can be large, and any statistical prediction must be interpreted with care if it is to be used in the planning of links of short duration.

For reference, the time periods corresponding to various time percentage of the year and the month are given below (d = day, h = minute, m = minute and s = second):

Percentage of:	1%	0.1%	0.01%	0.001%
Year	3.6 d	8.8 h	53 m	5.3 m
Month	7.2 h	43 m	4.3 m	26 s

In the civil sector, the need for planning of communications systems (both for reliability and for the frequency planning and coordination of systems sharing the same frequency bands) has led the ITU-R (formerly known as the CCIR) to recommend statistical prediction procedures for the use of Administrations. These planning procedures are based on physical principles, but often incorporate semi-empirical parameters that describe the statistical characteristics of the meteorology of the different regions of the world. These parameters are derived from extensive sets of data collected over many years from operational links and experimental campaigns.

Practical prediction methods, based mainly on the relevant ITU-R Recommendation, are given in the following sections.

3.6 Practical attenuation models

Despite the large variability of rainfall types encountered even within a single climate, it has been found that a few readily obtainable parameters concerning the rainfall pattern at a given location are sufficient for practical attenuation models. These include:

(i) the rainfall rate distribution at the ground, which describes the amount and relative proportions of high and low intensity rain;
(ii) the effective rain height, defined by the 0° isotherm, above which attenuation is negligible;
(iii) a path reduction factor to account for the limited horizontal extent of rain cells.

The relevant ITU-R recommended procedure for attenuation due to hydrometeors are given in Rec 530 [15] for terrestrial line-of-sight systems, and in Rec 618 [16] for Earth-space systems. The models are based on the expression for the path attenuation A (in decibels) in terms of the specific attenuation of rain γ_R (dB/km) and an effective path length d_{eff} (km):

$$A = \gamma_R d_{eff} \tag{19}$$

The calculation of d_{eff} and the method used to obtain results at various time-percentages differ for terrestrial and Earth-space paths. However, the calculation of γ_R is common to both methods and is given first.

The specific attenuation due to rain γ_R (dB/km) is obtained from the rain rate R (mm/hr) using the power-law relationship of eqn (18):

$$\gamma_R = a R^b \tag{20}$$

The frequency-dependent coefficients a and b have been obtained from scatter calculations and assumed drop size distributions [17]. They are given graphically in Figure 11. Both a and b are polarisation dependent (because of the tendency of large raindrops to be oblate spheroidal, rather than spherical, in shape), the values for horizontal polarisation being slightly larger than those for vertical polarisation; the differences are small (the two curves for a being indistinguishable in Figure 11) and can be ignored for most purposes; if needed, the coefficients for horizontal, vertical and circular polarisation can be obtained from [17].

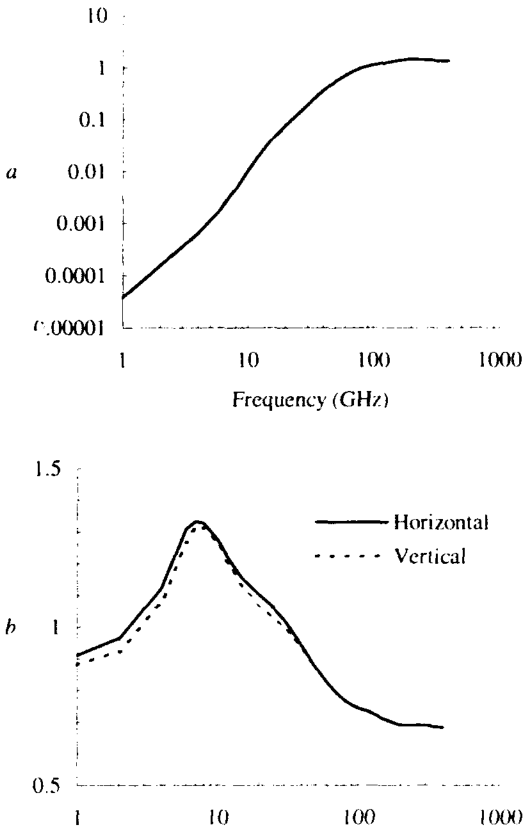

Figure 11: Coefficients required for estimating the specific attenuation due to rain

It is clear from the graph of a that for a given rain rate, the attenuation rate increases rapidly with frequency up to around 100 GHz (since at these frequencies, Rayleigh scattering dominates); above this, both a and b vary only slowly, and the attenuation rate is almost independent of frequency above 100 GHz (where the large particles that dominate attenuation lie in the Mie scattering region).

Table 2 shows the attenuation rates evaluated at specific frequencies for various rain types (horizontal polarisation). Although the figures appear quite low at 10 GHz and below, it should be noted, for example, that the belt of moderate to heavy rain ahead of a warm front can extend for 100 km or more (see Figure (2)) and this can very significantly reduce the detection ranges of radars operating around 10 GHz.

For clouds or fog consisting entirely of small droplets (generally less than 100 μm), the Rayleigh approximation is valid and the specific attenuation γ_c (dB/km) can be expressed

Frequency (GHz)	3	10	30	100
Light rain (1 mm/hr)	< 0.01	0.01	0.2	1.1
Moderate rain (5 mm/hr)	< 0.01	0.08	1.0	3.7
Heavy rain (25 mm/hr)	< 0.01	0.6	5.0	12.2
Intense rain (100 mm/hr)	0.04	3.6	20.6	34.3

Table 2: Specific attenuation (dB/km) for rain

in terms of the liquid water content of the cloud or fog per unit volume M (g/m3) [18]:

$$\gamma_c = K_l \, M \tag{21}$$

The specific attenuation coefficient K_l (given in units of dB/km per g/m^3) is temperature dependent, and is shown in Figure 12 for temperatures of 0°C and 20°C. The 0°C curve should be used for cloud. The liquid water content of fog is typically about 0.05 gm^{-3} for medium fog (300 m visibility) and 0.5 gm^{-3} for thick fog (50 m visibility).

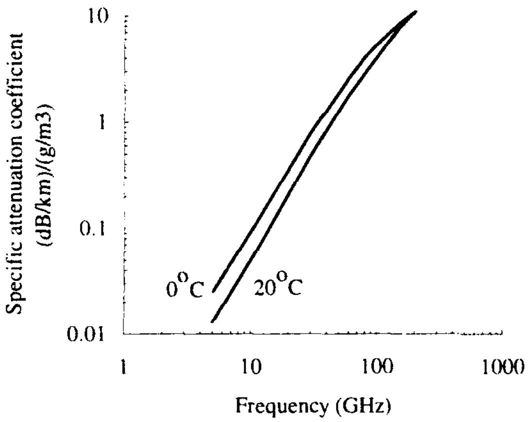

Figure 12: Specific attenuation by water droplets in cloud and fog

Eqn (19) together with eqns (20) or (21) could be used for deterministic predictions of rain attenuation if the actual rain rate and the path length through the rain were known. This is unlikely to be so, however, and in any case the rain rate and the extent of the rain cells along the propagation path is likely to be very variable. For this reason, the effective path length d_{eff} is normally considered to be a statistical parameter, and the long term cumulative distribution of rain fading are derived from the 0.01% rain rate.

3.6.1 Terrestrial links

The first step in calculating the cumulative distribution of attenuation is to obtain the level of path attenuation exceeded for 0.01% of the time $A_{0.01}$ (in decibels) from eqns (19) and (20):

$$A_{0.01} = a\, R_{0.01}^{b}\, d_{eff} \tag{22}$$

The 0.01% rain rate $R_{0.01}$ should be taken from local sources of long term measurements if available; otherwise it can be taken from global climatic maps given in [2]. (See also Section 3.1.1).

The effective path length d_{eff} is obtained from the actual path length d by means of a reduction factor that accounts for the fact that the longer the path, the less likely it is for the path to be filled with rain:

$$d_{eff} = \frac{1}{1 + d / d_0}\, d \tag{23}$$

The quantity d_0 is a rain rate dependent factor that accounts for the fact that more intense rainfall is likely to occur in smaller rain cells:

$$d_0 = 35 \exp(-0.015\, R_{0.01}) \tag{24}$$

In this expression, the value of $R_{0.01}$ should be limited to a maximum of 100 mm/hr; d_0 is given in km.

Figure 13 shows the effective path length as a function of the actual path length for various values of $R_{0.01}$. The reduction is seen to be quite significant, and at the higher rain rates the effective path length is almost constant and independent of the actual path length.

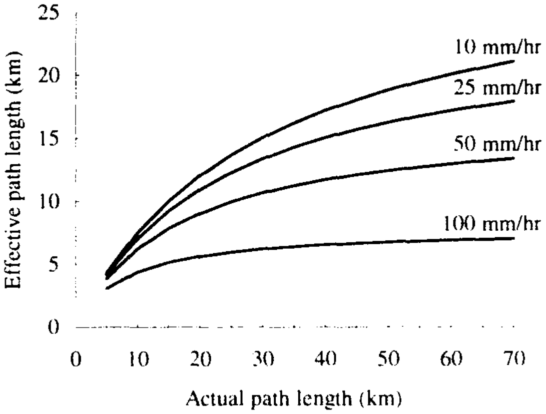

Figure 13: Effective path lengths for various 0.01% rain rates

Once $A_{0.01}$ has been estimated, the level of attenuation A_p exceeded for any other time percentage p (and hence the cumulative distribution of rain fading) within the range 1% to 0.001% can be deduced:

$$A_p = A_{0.01} \times 0.12\, p^{-(0.546 + 0.043 \log_{10} p)} \tag{25}$$

Figure 14 shows this scaling factor graphically.

Note that the values of attenuation A calculated above refer to a *one-way path*. These values should be doubled in the case of a radar (*two-way path*).

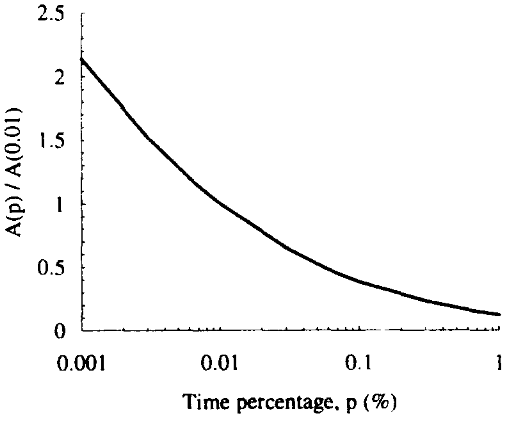

Figure 14: Scaling factor A_p / $A_{0.01}$

The prediction procedure is considered to be valid in all parts of the world at least for frequencies up to 40 GHz and path lengths up to 60 km.

3.6.2 Earth-space links

The prediction procedure relevant to satcom links is similar to that for terrestrial links, but is complicated by the fact that an elevated path through the atmosphere will experience a variety of rain types at different heights in the atmosphere. The geometry is shown in Figure 15. Since attenuation by ice particles is very low, the height of the 0°C isotherm effectively defines the maximum height at which rain attenuation occurs.

Statistically, the mean *effective* rain height h_R (in km) can be taken to be simply a function of latitude ϕ, as shown in Figure 16. (This curve is not quite the same as the 0°C isotherm curve, as some corrections have been included to take account of the different rain types at different latitudes.)

Given the effective rain height h_R and the station height above mean sea level h_s (in km) the slant path length below the rain height L_s (in km) can be calculated from simple straight line geometry for satellite elevation angles θ greater than 5°. Below this angle, a correction for refractive bending should be included:

$$L_s = \begin{cases} \dfrac{(h_R - h_s)}{\sin\theta} & \theta \geq 5° \\[2ex] \dfrac{2(h_R - h_s)}{\sqrt{\left(\sin^2\theta + \dfrac{2(h_R - h_s)}{R_e}\right)} + \sin\theta} & \theta < 5° \end{cases} \qquad (26)$$

R_e is the effective Earth radius, which can be taken to be 8500 km.

The effective path length d_{eff} is obtained from the slant path length L_s by means of a reduction factor in a similar fashion to the terrestrial path calculation (eqn (23)):

$$d_{eff} = \frac{1}{1 + L_s \cos\theta / d_o} L_s \qquad (27)$$

The $\cos\theta$ factor gives the horizontal projection of the slant path length; d_o is the same factor as for terrestrial paths (eqn (24)).

The level of path attenuation exceeded for 0.01% of the time $A_{0.01}$ can now be calculated from eqn (22), and the level of attenuation A_p exceeded for any other time percentage p within the range 1% to 0.001% from eqn (25) as before.

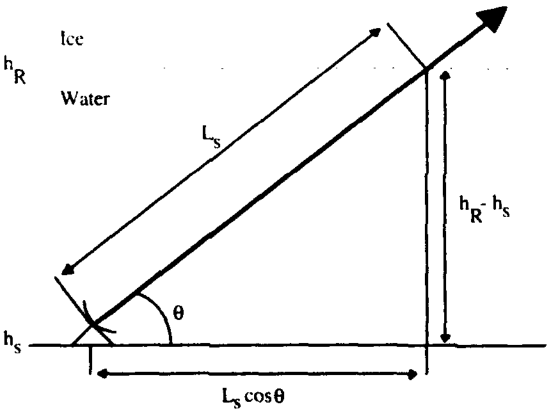

Figure 15: Earth-space satellite path geometry

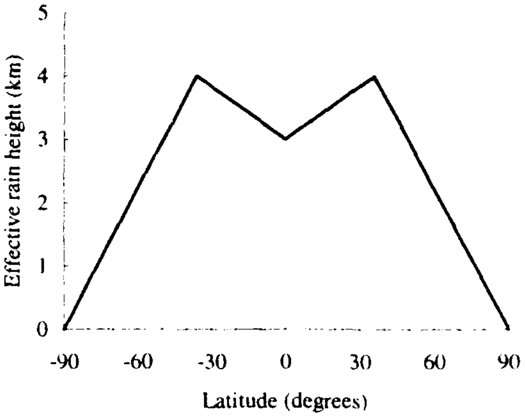

Figure 16: Effective rain height as a function of latitude

The methods of this section can also be used to estimate the rain attenuation loss on a path between a radar with elevation angle θ and an airborne target. The attenuation values should be doubled (for a two-way path). Note that the calculation of L_s given in eqn (26) is only appropriate if the target lies above the rain height; otherwise L_s should be taken simply as the radar–target distance.

3.7 Practical scatter models

The effect of rain scatter on a radar or communication system is determined by the bistatic radar equation. The power P_r^{scat} received by scatter from a target (located at a distance d_r from the receiver) is related to the power P_t emitted by the transmitter (at a distance d_t from the target) by:

$$P_r^{scat} = P_t \frac{G_t G_r \lambda^2}{(4\pi)^3 d_t^2 d_r^2} \sigma \qquad (28)$$

G_t and G_r are the transmitter and receiver antenna gains, λ is the wavelength, and σ is the target cross section. For a normal monostatic radar, $d_t = d_r$ and $G_t = G_r$.

In the case of scattering from rain, σ is obtained by integrating η_s (the radar cross section per unit volume) over the volume of the rain cells falling within the beam of the radar or radio antenna. Strictly, this integration should also include the G and d terms in eqn (28) if these vary significantly over the scatter volume. However, it is often a good approximation to write simply:

$$\sigma = \eta_s V \qquad (29)$$

where V is the scatter volume as defined by the extent of the rain cells and the antenna beam geometry.

V can be quite difficult to determine accurately. At short ranges from a radar, V will be defined by the radar resolution cell, which is given approximately by:

$$\frac{\pi}{4} d_r^2 \theta_h \theta_v \frac{c\tau}{2} \qquad (30)$$

where θ_h and θ_v are the horizontal and vertical beamwidths of the radar antenna, τ is the radar pulse duration, and c is the velocity of light. At longer ranges, or in intense rainfall, V will tend to be limited by the horizontal and vertical extent of the rain cell rather than the radar resolution cell.

3.7.1 Clutter

Backscattering of radar signals from rain gives rise to rain clutter. In the Rayleigh region (which applies at SHF and the lower EHF frequencies), the radar scatter cross section per unit volume η_s is proportional to the fourth power of frequency and the sixth power of raindrop diameter (eqn (16)), while V depends on the extent of the rain cells and the antenna beamwidth. Thus

- clutter is much more significant at higher frequencies: the clutter cross section at 10 GHz is over 100 times that at 3 GHz.
- the clutter return is dominated by the relatively small number of large drops in the rain cell. Heavy rain gives a strong return because it contains larger particles than light rain. In particular, returns from fog are insignificant at frequencies less than 10 GHz.
- clutter is less of a problem for a radar using a narrow beam and short range gates.

The radar cross section (RCS) of rain clutter, σ_c (expressed in decibels relative to 1 m², dBsm) can be estimated from the expression:

$$10\log_{10}\sigma_c = -22 + 40\log_{10} f + 16\log_{10} R + 10\log_{10} V \qquad (31)$$

where the frequency f is in GHz, the rainfall rate R is in mm/hr and V is in cubic kilometres. This expression assumes a relationship between η_s and R of the form given in eqn (18) with $b = 1.6$, derived for stratiform rain.

Table 3 gives rain clutter cross sections for a radar operating *in the low SHF band, assuming the values of V shown: these* are typical figures based on eqn (30) for a range of 10 km. Comparing with typical target cross sections for missiles (< 0 dBsm) and small aircraft (< 10 dBsm), it is seen that rain clutter can effectively prevent the detection of such targets.

	3 GHz	10 GHz
Scatter volume V (km³)	1	0.1
Light rain (1 mm/hr)	-3	8
Moderate rain (5 mm/hr)	8	19
Heavy rain (25 mm/hr)	19	30

Table 3: Radar cross sections (dBsm) of rain clutter at 10 km range

Circular polarisation is often used to enhance the target to (rain) clutter ratio. The reason is that a circularly polarised wave is reflected from a spherical raindrop with the opposite sense of rotation, and this reflected signal is rejected by the radar antenna (which will only accept the same sense of polarisation as it is designed to transmit). On the other hand the target, being a complex reflector, will return reflected energy more or less equally divided between the two senses of *polarisation. Unfortunately rejection of clutter is imperfect:*

(i) since large raindrops are not spherical the scattered signal will contain both senses of polarisation (see Figure (4)).
(ii) reflections from the Earth's surface alter the sense of polarisation.
(iii) the antenna isolation against opposite sense polarisation is never perfect.

In practice, circular polarisation cancellation of clutter echoes is rarely better than 20 dB, and can be as low as 10 dB in heavy rain. It has been found that slightly elliptical polarisation can improve the clutter cancellation (by up to 10 dB) in heavy rain. Good results require careful adjustment of the polarisation in real time, as the optimum polarisation depends on the detailed structure of the rain cell.

3.7.2 Bistatic scatter

Bistatic scatter from rain can cause interference on a communications link, or can lead to an increased probability of intercept of a communications or radar emission. Because of the potential risk of interference via rain scatter between terrestrial radio links and Earth-space services in the civil sector, ITU-R Rec 452 [19] contains a procedure for rain scatter interference. The procedure is based on eqn (28) evaluated under particular assumptions of rain cell structure and antenna beam geometries, and makes allowance for rain attenuation along the scatter path, and for non-Rayleigh scattering effects above 10 GHz. The procedure is somewhat complicated, and the reader is referred to [19] for details.

Instead, a very simple rule-of-thumb can be given for the ratio of the signal level received via bistatic rain scatter to the signal level that would be received in free space over a path of the same length as the scatter path. In free space, the signal power P_r^{fs} received at the terminals of an antenna of gain G_r after propagating a distance d through free space from a transmitter of power P_t and antenna gain G_t is:

$$P_r^{fs} = P_t\frac{G_t G_r \lambda^2}{(4\pi)^2 d^2} \qquad (32)$$

where λ is the wavelength. Taking the ratio of the bistatic scattered power given by eqn (28) to P_r^{fs}, assuming the simple path geometry $d_t = d_r = d/2$, and expressing the result in decibels gives:

$$10\log_{10}(P_r^{scat} / P_r^{fs}) = 10\log_{10}\sigma - 20\log_{10} d - 59 \qquad (33)$$

where $10\log_{10}\sigma$ is given in dBsm and the path length d is given in km. An estimate of $10\log_{10}\sigma$ can be obtained from the backscatter clutter cross section $10\log_{10}\sigma_c$, eqn (31).

For example, at 10 GHz on a 20 km (two-way) scatter path during heavy rain, $10\log_{10}\sigma_c = 30$ dBsm (from Table 3), and the scattered signal is 55 dB below the free space level that would result from boresight-to-boresight coupling between the transmitter and receiver. Strictly, account should also be taken of the scattering diagram $|S(\theta)|^2$ (Figure 9) which is included in the bistatic scatter cross section (cf. eqn (10) for backscatter), but this is not really justified at this level of approximation In any case, the scattering diagram rarely shows as strong an angle dependence as Figure 9 once it has been integrated over the full drop size distribution [20].

It is important to appreciate that a signal arriving via rain scatter will be incoherent and randomly fluctuating in both amplitude and phase on a timescale of milliseconds. The time delay spread between the scatter paths from all the individual rain drops may be in the order of microseconds. Thus any signal of more than a few tens of kHz bandwidth is unlikely to be intelligible after being scattered by rain although its presence will be detectable.

4 ATMOSPHERIC GASES

In the absence of hydrometeors or other particles, the atmosphere can be considered to be a continuous dielectric medium with complex refractive index n. The value of n is determined by the molecular constituents of the air, principally nitrogen, oxygen, carbon dioxide and water vapour. It deviates from its vacuum value of unity because of (a) the polarisability of these molecules due to the incident electromagnetic field, and (b) quantum mechanical molecular resonances.

The deviation of n from unity is very small in absolute terms, a typical value being 1.0003 at the Earth's surface. Because of the closeness of n to unity, it is usual to work with the refractivity, N, defined by:

$$N = (n-1)\times 10^6 \qquad (34)$$

N is dimensionless, but for convenience is measured in "N-units". The value of N at the Earth's surface is therefore about 300 N-units.

The molecular polarisability only contributes to the real part of N, and the contribution is independent of frequency in the SHF and EHF frequency bands. The variation of N with position is responsible for the refraction of radio waves. N depends on the pressure P (hPa), the absolute temperature T (K) and the partial pressure of water vapour e (hPa):

$$N = 77.6\frac{P}{T} + 3.73\times 10^5\frac{e}{T^2} \qquad (35)$$

This is derived from the Debye formula [21] for the polarisability of molecules. The second (wet) term is due to the polar (i.e. with a strong permanent electric dipole moment) water vapour molecules, while the first (dry) term is due principally to the non-polar nitrogen and oxygen molecules. The constants are empirically determined, based on experimental measurements [22]. An excellent discussion of eqn (35) is given in [23].

The effects of variations in N on the refraction of radio waves are very important for the performance of radar and communications systems, and are discussed fully in a separate lecture.

4.1 Attenuation mechanisms

The effects of quantum mechanical molecular resonances are limited to narrow frequency bands at SHF and EHF frequencies. Their contribution to the refractive index (less than 2 N-units) is relatively small compared to the contribution of molecular polarisability (eqn (35)). However, of critical importance is that the resonances contribute both a real *and an imaginary* part to N, the imaginary part being due to gaseous absorption. While the real part can generally be ignored, the imaginary part gives rise to attenuation of the electromagnetic waves. Indeed the specific attenuation rate γ (dB/km) is simply related to the imaginary part of N by:

$$\gamma = 0.182\, f\, \Im(N) \qquad (36)$$

where f is the frequency in GHz.

Only oxygen and water vapour have resonance lines below 350 GHz. The oxygen molecule has a permanent magnetic dipole moment due to paired electron spins. Changes in orientation of the combined electron spin relative to the orientation of the rotational angular momentum give rise to a closely spaced group of "spin-flip" or hyperfine transitions near 60 GHz, and a single line at 119 GHz. The water molecule has a permanent electric dipole moment, and rotations of the molecule with quantised angular momentum give rise to spectral lines at 22, 183 and 325 GHz.

Calculations of gaseous attenuation are made by summing the effects of each individual resonance line, taking into account the frequency, strength and width of each line. Spectroscopic parameters for the lines have been published by Liebe et. al. [24]. The contribution of each line depends on the pressure, temperature and (especially for water vapour absorption) on the water vapour pressure (or water vapour density). Liebe has implemented his algorithms as a computer program, MPM. Figure 17 shows the attenuation rate per kilometre at ground level (1013 hPa, 15°C) due to dry air and water vapour, calculated using MPM. In the case of water vapour, a water vapour density of 7.5 g/m^3 was assumed; the graph can easily be scaled to other values since the specific attenuation is proportional to the water vapour density.

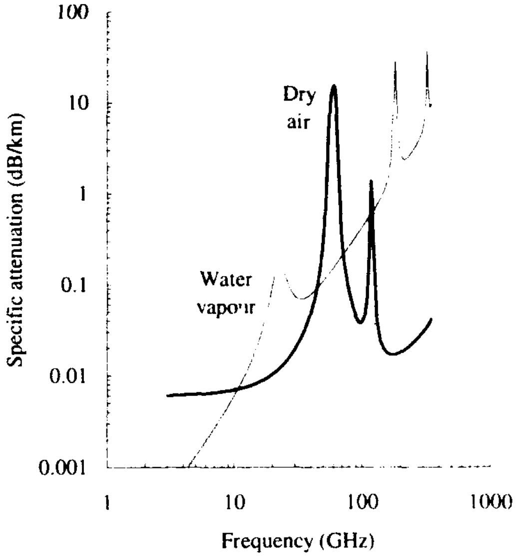

Figure 17: Specific attenuation due to atmospheric gases

It will be observed that the absorption does not fall to zero away from the resonance lines. The dry air continuum arises from the non-resonant Debye spectrum of oxygen below 10 GHz and a pressure-induced nitrogen attenuation above 100 GHz. The absorption spectrum of water vapour has very intense lines in the far infra-red region and the low frequency tails of these lines are seen as the sloping baseline of the water vapour spectrum in Figure 17. The wet continuum also contains an "anomalous" contribution to account for the fact that measurements of water vapour attenuation are generally in excess of those theoretically predicted, the effect being most noticeable in the wings of the spectral lines where the expected attenuation is small.

The 50–70 GHz region contains a complex of more than 30 oxygen resonance lines. These are not visible in Figure 17 because near sea-level, the spectral lines are greatly widened by pressure (collision) broadening, and merge together. Absorption rates exceed 10 dB/km between 57 and 63 GHz, and this limits the ranges over which transmissions can be received to within a few kilometres. The 60 GHz band thus offers potential for secure, short range communications.

At altitudes above about 15 km, the pressure is sufficiently low that the 60 GHz line is clearly resolved into several closely spaced components. This is illustrated in Figure 18 for pressure levels of 1013, 40, and 20 hPa, corresponding to approximate heights above sea level of 0, 20 and 23 km.

Between the resonant lines, the absorption rate can fall below 0.1 dB/km. This leads to the possibility of long range communication between high altitude aircraft or satellites that is secure from detection at the surface of the Earth.

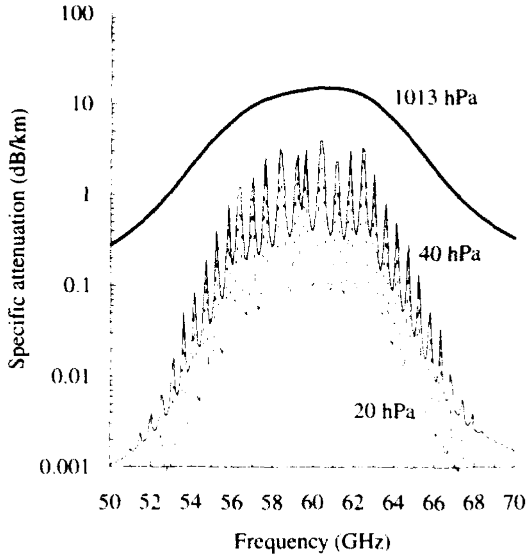

Figure 18: Specific attenuation due to oxygen at various atmospheric pressures

4.2 Practical attenuation models

In practice, the effects of gaseous absorption are negligible at frequencies below 10 GHz, particularly when compared to other propagation impairments that are likely to be encountered. Above 10 GHz, an allowance for gaseous absorption should be made.

For a terrestrial link near the surface of the Earth, the total gaseous attenuation A_g (dB) on a path length d (in km) is simply:

$$A_g = (\gamma_o + \gamma_w)\, d \tag{37}$$

γ_o and γ_w are the specific attenuations (dB/km) at the surface for dry air and water vapour, respectively, obtained from Figure 17 for the frequency of interest.

For an Earth-space link, the calculation is slightly more complicated, since account needs to be taken of the variation of absorption with height in the atmosphere. The total slant path gaseous attenuation through the atmosphere A_g (dB) for a path elevation angle θ *greater than* 10° is:

$$A_g = \frac{\gamma_o h_o \exp(-h_s / h_o) + \gamma_w h_w}{\sin\theta} \tag{38}$$

In this expression,

(i) h_s is the height (km) of the Earth station above mean sea level.

(ii) γ_o and γ_w are the specific attenuations (dB/km) *at the surface* for dry air and water vapour, respectively, obtained from Figure 17 for the frequency of interest; formulae for calculating γ_o and γ_w, taking account of temperature and water vapour density, are given in [25].

(iii) h_o and h_w are the "equivalent heights" (km) for dry air and water vapour, respectively [25]. For frequencies below 57 GHz, $h_o = 6$ km, while h_w can be determined from

$$h_w = h_{w0}\left(1 + \frac{3.0}{(f - 22.2)^2 + 5}\right) \tag{39}$$

$h_{w0} = 1.6$ km in clear weather and 2.1 km in rain.

At frequencies above 57 GHz, or for path elevation angles θ *less than* 10° (when allowance should be made for refractive bending in the atmosphere) the more detailed expressions given in [16] or [25] should be used.

The attenuation caused by gaseous absorption is not constant, principally due to the fact that both water vapour density and its vertical profile are quite variable from place to place and from day to day (the oxygen contribution being relatively constant). The methods of [16] and contour maps of water vapour density [26] can be used to estimate distributions of gaseous attenuation if required. The variations in atmospheric attenuation exceeded for large percentages of the time (when no rain is present) are important for low-availability systems. Measurements in Europe in the 11 GHz band have shown that seasonal variations in the monthly median level of total attenuation do not exceed 0.1 dB, and that the total attenuation exceeded for 20% of the worst month is less than 0.2 dB above the monthly median value.

5 CONCLUSIONS

Simple prediction methods are available for the effects of hydrometeors and atmospheric gases on communications and radar systems at SHF and EHF. These are based on fundamental physical principles, and use input parameters that are readily available from local meteorological measurements, or from global maps that have been prepared by the ITU for civil communications systems.

These methods can be used both at the system planning stage when statistical predictions are required, and to improve the accuracy of real-time prediction tools when operating in the presence of rain.

6 ACKNOWLEDGEMENTS

The author wishes to thank his colleagues John Goddard and Jun Tan of the Radar Group at the Radio Communications Research Unit for providing the rain radar pictures used in this paper.

7 REFERENCES

[1] Goddard J.W.F., Eastment, J.D. and Thurai, M., "The Chilbolton Advanced Meteorological Radar: a tool for multi-disciplinary atmospheric research, *IEE Elec. and Eng. J.*, 6, 77–86, 1994.

[2] ITU-R Recommendation 837, "Characteristics of precipitation for propagation modelling", 1992-CCIR Recommendations, RPN series, Propagation in Non-Ionised Media, Geneva, 1992.

[3] Marshall, J.S. and Palmer, W.McK, "The distribution of raindrops with size", *J. Meteorol.*, 5, 165–166, 1948.

[4] Laws, J.O. and Parsons, D.A., "The relation of raindrop-size to intensity", *Trans. Amer. Geophys. Union*, 24, 452–460, 1943.

[5] van de Hulst, H.C., "Light scattering by small particles", Dover Publications Inc., New York, 1981, (ISBN 0-486-64228-3).

[6] Bohren, C.F., and Huffman, D.R., "Absorption and scattering of light by small particles", John Wiley & Sons, New York, 1983, (ISBN 0-471-05772-X).

[7] Oguchi, T. and Hosoya, Y., "Scattering properties of oblate raindrops and cross-polarisation of radio waves due to rain: Calculations at microwave and millimetre

wave regions", *J. Radio Res. Lab. Jpn*, 21(105), 191–259, 1974.

[8] Barber, P.W. and Yeh, C., "Scattering of electromagnetic waves by arbitrarily shaped dielectric bodies", *Appl. Opt.*, 14(12), 2864–2872, 1975.

[9] Uzunoglu, N.K., Evans, B.G. and Holt, A.R., "Evaluation of the scattering of an electromagnetic wave from precipitation particles by the use of Fredholm integral equations", *Electron. Lett.*, 12(12), 312–313, 1976.

[10] Asano, S. and Yamamoto, G., "Light scattering by spheroidal particles", *Appl. Optics*, 14(1), 29–49, 1975.

[11] Holt, A.R., "The scattering of electromagnetic waves by single hydrometeors", *Radio Science*, 17(5), 929–945, 1982.

[12] Rayleigh, Lord, "On the light from the sky, its polarisation and colour", *Philos. Mag.*, 41, 107–120, 274–279, 1871.

[13] Mie, G., "Beitrage zur Optik trüber Medien speziell kolloidaler Metallösungen, *Ann. Phys.*, 25, 377–445, 1908.

[14] ITU-R Recommendation 841, "Conversion of annual statistics to worst-month statistics", 1992-CCIR Recommendations, RPN series, Propagation in Non-Ionised Media, Geneva, 1992.

[15] ITU-R Recommendation 530-4, "Propagation data and prediction methods required for the design of terrestrial line-of-sight systems", *ibid.*, 1992.

[16] ITU-R Recommendation 618-2, "Propagation data and prediction methods required for the design of Earth-space telecommunications systems", *ibid.*, 1992.

[17] ITU-R Recommendation 838, "Specific attenuation model for rain for use in prediction methods", *ibid.*, 1992.

[18] ITU-R Recommendation 840, "Attenuation due to clouds and fog", *ibid.*, 1992.

[19] ITU-R Recommendation 452-5, "Prediction procedure for the evaluation of microwave interference between stations on the surface of the Earth at frequencies above about 0.7 GHz", *ibid* 1992.

[20] COST 210 Final Report, "Influence of the atmosphere on interference between radio communications systems at frequencies above 1 GHz", *EUR 13407*, Commission of the European Communities, Annex 2.19, 1991.

[21] Debye, P., "Polar molecules", Dover Publ., 89–90, 1957.

[22] Smith, E.K. and Weintraub S., "The constants in the equation for atmospheric refractive index at radio frequencies", *Proc. IRE*, 41, 1035–1037, 1953.

[23] Bean, B.R. and Dutton, E.J., "Radio meteorology", National Bureau of Standards Monograph 92, Chapter 1, 1966.

[24] Liebe, H.J., Hufford, G.A. and Cotton, M.G., "Propagation modeling of moist air and suspended water/ice particles at frequencies below 1000 GHz", *in* "Atmospheric propagation effects through natural and man-made obscurants for visible to mm-wave radiation", AGARD-CP-542, Paper 3, 1993.

[25] ITU-R Recommendation 676-1, "Attenuation by gases in the frequency range 1–350 GHz", *ibid.*, 1992.

[26] ITU-R Recommendation 836, "Surface water vapour density", *ibid.*, 1992.

REPORT DOCUMENTATION PAGE

1. Recipient's Reference	**2. Originator's Reference** AGARD-LS-196	**3. Further Reference** ISBN 92-836-1004-0	**4. Security Classification of Document** UNCLASSIFIED

5. Originator Advisory Group for Aerospace Research and Development
North Atlantic Treaty Organization
7 rue Ancelle, 92200 Neuilly-sur-Seine, France

6. Title
Propagation Modelling and Decision Aids for Communications, Radar and Navigation Systems

7. Presented on 4-5 October 1994 in Ottawa, Canada, 10-11 October 1994 in Lisbon, Portugal, and 13-14 October 1994 in The Hague, The Netherlands

8. Author(s)/Editor(s) Various	**9. Date** September 1994
10. Author's/Editor's Address Various	**11. Pages** 184

12. Distribution Statement There are no restrictions on the distribution of this document. Information about the availability of this and other AGARD unclassified publications is given on the back cover.

13. Keywords/Descriptors

Wave propagation
Ionospheric propagation
Ground wave propagation
Decision making
Decision aids
Software tools
Communication and radio systems
Radar systems
Navigation systems
Systems engineering
Predictions
Mathematical models

14. Abstract

In recent years, a number of powerful, flexible, modelling tools for the assessment and exploitation of propagation conditions have become available. Rapid advances in mini and microcomputer technology have put complex models with sophisticated user interfaces at the disposal of the non-specialist user. These range from system design tools to near real-time operational and tactical decision aids that include models and databases of the necessary environmental parameters. Prediction tools are required for communications, radar and navigation applications, and cover the frequency spectrum from ELF to optical.

The lectures will concentrate on the prediction tools, but will also cover the background required to understand the models used. The emphasis will be on frequencies from HF to optical. Topics will include the ionosphere, ground wave propagation, terrain diffraction, refractive effects, hydrometeors, atmospheric gases, electro-optics and the sensing of radiometeorological parameters. Both empirical/statistical system planning methods, and more theoretically based deterministic operational decision aids will be covered.

This Lecture Series, sponsored by the Sensor and Propagation Panel of AGARD, has been implemented by the Consultant and Exchange Programme.

AGARD Lecture Series 196
Advisory Group for Aerospace Research and Development, NATO
PROPAGATION MODELLING AND DECISION AIDS FOR COMMUNICATIONS, RADAR AND NAVIGATION SYSTEMS
Published September 1994
184 pages

In recent years, a number of powerful, flexible, modelling tools for the assessment and exploitation of propagation conditions have become available. Rapid advances in mini and microcomputer technology have put complex models with sophisticated user interfaces at the disposal of the non-specialist user. These range from system design tools to near real-time operational and tactical decision aids that include models and databases of the necessary environmental parameters. Prediction tools are

AGARD-LS-196

Wave propagation
Ionospheric propagation
Ground wave propagation
Decision making
Decision aids
Software tools
Communication and radio systems
Radar systems
Navigation systems
Systems engineering
Predictions
Mathematical models

AGARD Lecture Series 196
Advisory Group for Aerospace Research and Development, NATO
PROPAGATION MODELLING AND DECISION AIDS FOR COMMUNICATIONS, RADAR AND NAVIGATION SYSTEMS
Published September 1994
184 pages

In recent years, a number of powerful, flexible, modelling tools for the assessment and exploitation of propagation conditions have become available. Rapid advances in mini and microcomputer technology have put complex models with sophisticated user interfaces at the disposal of the non-specialist user. These range from system design tools to near real-time operational and tactical decision aids that include models and databases of the necessary environmental parameters. Prediction tools are

AGARD-LS-196

Wave propagation
Ionospheric propagation
Ground wave propagation
Decision making
Decision aids
Software tools
Communication and radio systems
Radar systems
Navigation systems
Systems engineering
Predictions
Mathematical models

AGARD Lecture Series 196
Advisory Group for Aerospace Research and Development, NATO
PROPAGATION MODELLING AND DECISION AIDS FOR COMMUNICATIONS, RADAR AND NAVIGATION SYSTEMS
Published September 1994
184 pages

In recent years, a number of powerful, flexible, modelling tools for the assessment and exploitation of propagation conditions have become available. Rapid advances in mini and microcomputer technology have put complex models with sophisticated user interfaces at the disposal of the non-specialist user. These range from system design tools to near real-time operational and tactical decision aids that include models and databases of the necessary environmental parameters. Prediction tools are

AGARD-LS-196

Wave propagation
Ionospheric propagation
Ground wave propagation
Decision making
Decision aids
Software tools
Communication and radio systems
Radar systems
Navigation systems
Systems engineering
Predictions
Mathematical models

AGARD Lecture Series 196
Advisory Group for Aerospace Research and Development, NATO
PROPAGATION MODELLING AND DECISION AIDS FOR COMMUNICATIONS, RADAR AND NAVIGATION SYSTEMS
Published September 1994
184 pages

In recent years, a number of powerful, flexible, modelling tools for the assessment and exploitation of propagation conditions have become available. Rapid advances in mini and microcomputer technology have put complex models with sophisticated user interfaces at the disposal of the non-specialist user. These range from system design tools to near real-time operational and tactical decision aids that include models and databases of the necessary environmental parameters. Prediction tools are

AGARD-LS-196

Wave propagation
Ionospheric propagation
Ground wave propagation
Decision making
Decision aids
Software tools
Communication and radio systems
Radar systems
Navigation systems
Systems engineering
Predictions
Mathematical models

required for communications, radar and navigation applications, and cover the frequency spectrum from ELF to optical.

The lectures will concentrate on the prediction tools, but will also cover the background required to understand the models used. The emphasis will be on frequencies from HF to optical. Topics will include the ionosphere, ground wave propagation, terrain diffraction, refractive effects, hydrometeors, atmospheric gases, electro-optics and the sensing of radiometeorological parameters. Both empirical/statistical system planning methods, and more theoretically based deterministic operational decision aids will be covered.

This Lecture Series, sponsored by the Sensor and Propagation Panel of AGARD, has been implemented by the Consultant and Exchange Programme.

ISBN 92-836-1004-0

required for communications, radar and navigation applications, and cover the frequency spectrum from ELF to optical.

The lectures will concentrate on the prediction tools, but will also cover the background required to understand the models used. The emphasis will be on frequencies from HF to optical. Topics will include the ionosphere, ground wave propagation, terrain diffraction, refractive effects, hydrometeors, atmospheric gases, electro-optics and the sensing of radiometeorological parameters. Both empirical/statistical system planning methods, and more theoretically based deterministic operational decision aids will be covered.

This Lecture Series, sponsored by the Sensor and Propagation Panel of AGARD, has been implemented by the Consultant and Exchange Programme.

ISBN 92-836-1004-0

required for communications, radar and navigation applications, and cover the frequency spectrum from ELF to optical.

The lectures will concentrate on the prediction tools, but will also cover the background required to understand the models used. The emphasis will be on frequencies from HF to optical. Topics will include the ionosphere, ground wave propagation, terrain diffraction, refractive effects, hydrometeors, atmospheric gases, electro-optics and the sensing of radiometeorological parameters. Both empirical/statistical system planning methods, and more theoretically based deterministic operational decision aids will be covered.

This Lecture Series, sponsored by the Sensor and Propagation Panel of AGARD, has been implemented by the Consultant and Exchange Programme.

ISBN 92-836-1004-0

required for communications, radar and navigation applications, and cover the frequency spectrum from ELF to optical.

The lectures will concentrate on the prediction tools, but will also cover the background required to understand the models used. The emphasis will be on frequencies from HF to optical. Topics will include the ionosphere, ground wave propagation, terrain diffraction, refractive effects, hydrometeors, atmospheric gases, electro-optics and the sensing of radiometeorological parameters. Both empirical/statistical system planning methods, and more theoretically based deterministic operational decision aids will be covered.

This Lecture Series, sponsored by the Sensor and Propagation Panel of AGARD, has been implemented by the Consultant and Exchange Programme.

ISBN 92-836-1004-0

NATO ✢ OTAN

7 RUE ANCELLE • 92200 NEUILLY SUR SEINE

FRANCE

Télecopie (1)47.38.57.99 • Telex 610 176

DIFFUSION DES PUBLICATIONS

AGARD NON CLASSIFIEES

Aucun stock de publications n'a existé à AGARD. A partir de 1993, AGARD détiendra un stock limité des publications associées aux cycles de conférences et cours spéciaux ainsi que les AGARDographies et les rapports des groupes de travail, organisés et publiés à partir de 1993 inclus. Les demandes de renseignements doivent être adressées à AGARD par lettre ou par fax à l'adresse indiquée ci-dessus. *Veuillez ne pas téléphoner.* La diffusion initiale de toutes les publications de l'AGARD est effectuée auprès des pays membres de l'OTAN par l'intermédiaire des centres de distribution nationaux indiqués ci-dessous. Des exemplaires supplémentaires peuvent parfois être obtenus auprès de ces centres (à l'exception des Etats-Unis). Si vous souhaitez recevoir toutes les publications de l'AGARD, ou simplement celles qui concernent certains Panels, vous pouvez demander à être inclu sur la liste d'envoi de l'un de ces centres. Les publications de l'AGARD sont en vente auprès des agences indiquées ci-dessous, sous forme de photocopie ou de microfiche.

CENTRES DE DIFFUSION NATIONAUX

ALLEMAGNE
Fachinformationszentrum,
Karlsruhe
D-76344 Eggenstein-Leopoldshafen 2

BELGIQUE
Coordonnateur AGARD VSL
Etat-major de la Force aérienne
Quartier Reine Elisabeth
Rue d'Evere, 1140 Bruxelles

CANADA
Directeur du Service des renseignements scientifiques
Ministère de la Défense nationale
Ottawa, Ontario K1A 0K2

DANEMARK
Danish Defence Research Establishment
Ryvangs Allé 1
P.O. Box 2715
DK-2100 Copenhagen O

ESPAGNE
INTA (AGARD Publications)
Pintor Rosales 34
28008 Madrid

ÉTATS-UNIS
NASA Headquarters
Code JOB-1
Washington, D.C. 20546

FRANCE
O.N.E.R.A. (Direction)
29, Avenue de la Division Leclerc
92322 Châtillon Cedex

GRÈCE
Hellenic Air Force
Air War College
Scientific and Technical Library
Dekelia Air Force Base
Dekelia, Athens TGA 1010

ISLANDE
Director of Aviation
c/o Flugrad
Reykjavik

ITALIE
Aeronautica Militare
Ufficio del Delegato Nazionale all'AGARD
Aeroporto Pratica di Mare
00040 Pomezia (Roma)

LUXEMBOURG
Voir Belgique

NORVÈGE
Norwegian Defence Research Establishment
Attn: Biblioteket
P.O. Box 25
N-2007 Kjeller

PAYS-BAS
Netherlands Delegation to AGARD
National Aerospace Laboratory NLR
P.O. Box 90502
1006 BM Amsterdam

PORTUGAL
Força Aérea Portuguesa
Centro de Documentação e Informação
Alfragide
2700 Amadora

ROYAUME-UNI
Defence Research Information Centre
Kentigern House
65 Brown Street
Glasgow G2 8EX

TURQUIE
Millî Savunma Başkanliği (MSB)
ARGE Dairesi Başkanliği (MSB)
06650 Bakanliklar-Ankara

Le centre de distribution national des États-Unis ne détient PAS de stocks des publications de l'AGARD.

D'éventuelles demandes de photocopies doivent être formulées directement auprès du NASA Center for AeroSpace Information (CASI) à l'adresse ci-dessous. Toute notification de changement d'adresse doit être fait également auprès de CASI.

AGENCES DE VENTE

NASA Center for
AeroSpace Information (CASI)
800 Elkridge Landing Road
Linthicum Heights, MD 21090-2934
États-Unis

ESA/Information Retrieval Service
European Space Agency
10, rue Mario Nikis
75015 Paris
France

The British Library
Document Supply Division
Boston Spa, Wetherby
West Yorkshire LS23 7BQ
Royaume-Uni

Les demandes de microfiches ou de photocopies de documents AGARD (y compris les demandes faites auprès du CASI) doivent comporter la dénomination AGARD, ainsi que le numéro de série d'AGARD (par exemple AGARD-AG-315). Des informations analogues, telles que le titre et la date de publication sont souhaitables. Veuiller noter qu'il y a lieu de spécifier AGARD-R-nnn et AGARD-AR-nnn lors de la commande des rapports AGARD et des rapports consultatifs AGARD respectivement. Des références bibliographiques complètes ainsi que des résumés des publications AGARD figurent dans les journaux suivants:

Scientific and Technical Aerospace Reports (STAR)
publié par la NASA Scientific and Technical
Information Division
NASA Headquarters (JTT)
Washington D.C. 20546
États-Unis

Government Reports Announcements and Index (GRA&I)
publié par le National Technical Information Service
Springfield
Virginia 22161
États-Unis
(accessible également en mode interactif dans la base de
données bibliographiques en ligne du NTIS, et sur CD-ROM)

Imprimé par le Groupe Communication Canada
45, boul. Sacré-Cœur, Hull (Québec), Canada K1A 0S7

Figure 9: Rayleigh scattering diagram for perpendicular and parallel polarisation

inversely proportional to the *fourth* power of wavelength. This simple observation leads to the following:

AGARD

NATO OTAN

7 RUE ANCELLE • 92200 NEUILLY-SUR-SEINE

FRANCE

Telefax (1)47.38.57.99 • Telex 610 176

DISTRIBUTION OF UNCLASSIFIED AGARD PUBLICATIONS

AGARD holds limited quantities of the publications that accompanied Lecture Series and Special Courses held in 1993 or later, and of AGARDographs and Working Group reports published from 1993 onward. For details, write or send a telefax to the address given above. *Please do not telephone.*

AGARD does not hold stocks of publications that accompanied earlier Lecture Series or Courses or of any other publications. Initial distribution of all AGARD publications is made to NATO nations through the National Distribution Centres listed below. Further copies are sometimes available from these centres (except in the United States). If you have a need to receive all AGARD publications, or just those relating to one or more specific AGARD Panels, they may be willing to include you (or your organisation) on their distribution list. AGARD publications may be purchased from the Sales Agencies listed below, in photocopy or microfiche form.

NATIONAL DISTRIBUTION CENTRES

BELGIUM
Coordonnateur AGARD — VSL
Etat-major de la Force aérienne
Quartier Reine Elisabeth
Rue d'Evere, 1140 Bruxelles

CANADA
Director Scientific Information Services
Dept of National Defence
Ottawa, Ontario K1A 0K2

DENMARK
Danish Defence Research Establishment
Ryvangs Allé 1
P.O. Box 2715
DK-2100 Copenhagen Ø

FRANCE
O.N.E.R.A. (Direction)
29 Avenue de la Division Leclerc
92322 Châtillon Cedex

GERMANY
Fachinformationszentrum
Karlsruhe
D-76344 Eggenstein-Leopoldshafen 2

GREECE
Hellenic Air Force
Air War College
Scientific and Technical Library
Dekelia Air Force Base
Dekelia, Athens TGA 1010

ICELAND
Director of Aviation
c/o Flugrad
Reykjavik

ITALY
Aeronautica Militare
Ufficio del Delegato Nazionale all'AGARD
Aeroporto Pratica di Mare
00040 Pomezia (Roma)

LUXEMBOURG
See Belgium

NETHERLANDS
Netherlands Delegation to AGARD
National Aerospace Laboratory, NLR
P.O. Box 90502
1006 BM Amsterdam

NORWAY
Norwegian Defence Research Establishment
Attn: Biblioteket
P.O. Box 25
N-2007 Kjeller

PORTUGAL
Força Aérea Portuguesa
Centro de Documentação e Informação
Alfragide
2700 Amadora

SPAIN
INTA (AGARD Publications)
Pintor Rosales 34
28008 Madrid

TURKEY
Millî Savunma Başkanliği (MSB)
ARGE Dairesi Başkanliği (MSB)
06650 Bakanliklar-Ankara

UNITED KINGDOM
Defence Research Information Centre
Kentigern House
65 Brown Street
Glasgow G2 8EX

UNITED STATES
NASA Headquarters
Code JOB-1
Washington, D.C. 20546

The United States National Distribution Centre does NOT hold stocks of AGARD publications.

Applications for copies should be made direct to the NASA Center for AeroSpace Information (CASI) at the address below.
Change of address requests should also go to CASI.

SALES AGENCIES

NASA Center for
AeroSpace Information (CASI)
800 Elkridge Landing Road
Linthicum Heights, MD 21090-2934
United States

ESA/Information Retrieval Service
European Space Agency
10, rue Mario Nikis
75015 Paris
France

The British Library
Document Supply Centre
Boston Spa, Wetherby
West Yorkshire LS23 7BQ
United Kingdom

Requests for microfiches or photocopies of AGARD documents (including requests to CASI) should include the word 'AGARD' and the AGARD serial number (for example AGARD-AG-315). Collateral information such as title and publication date is desirable. Note that AGARD Reports and Advisory Reports should be specified as AGARD-R-nnn and AGARD-AR-nnn, respectively. Full bibliographical references and abstracts of AGARD publications are given in the following journals:

Scientific and Technical Aerospace Reports (STAR)
published by NASA Scientific and Technical
Information Division
NASA Headquarters (JTT)
Washington D.C. 20546
United States

Government Reports Announcements and Index (GRA&I)
published by the National Technical Information Service
Springfield
Virginia 22161
United States
(also available online in the NTIS Bibliographic
Database or on CD-ROM)

Printed by Canada Communication Group
45 Sacré-Cœur Blvd., Hull (Québec), Canada K1A 0S7

ISBN 92-836-1004-0